Volume 7 Issue 1 (2021) · ISSN 2424-7723

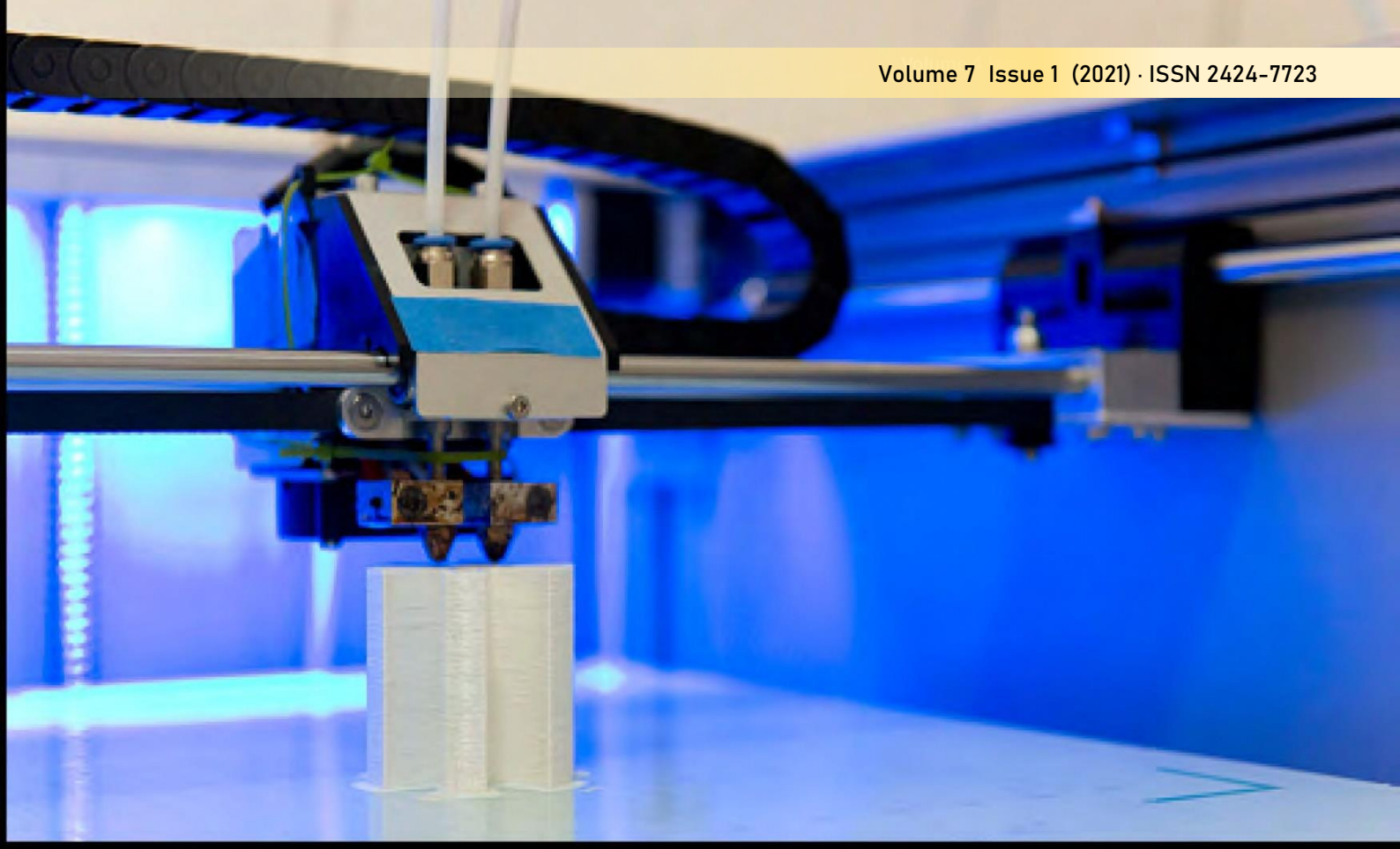

# INTERNATIONAL JOURNAL OF BIOPRINTING

WHIOCE PUBLISHING PTE. LTD.
PROVIDING
FIRST-CLASS SCIENTIFIC INFORMATION
FOR TOP SCHOLARS

Volume 7 Issue 1 • 2021
ISSN 2424-7723 (print) ISSN 2424-8002 (online)

# INTERNATIONAL JOURNAL OF BIOPRINTING

**Editor-in-Chief**

**Chee Kai Chua**

*Singapore University of Technology and Design, Singapore*

WHIOCE PUBLISHING PTE. LTD.

Volume 7 | Issue 1 | 2021 | Page 1 – 145 |

International Journal of Bioprinting

https://ijb.whioce.com/index.php/int-j-bioprinting

# CONTENTS

PERSPECTIVE ARTICLE

# Application of Machine Learning in 3D Bioprinting: Focus on Development of Big Data and Digital Twin

**Jia An[1], Chee Kai Chua[2], Vladimir Mironov[3]***

[1]Singapore Centre for 3D Printing, School of Mechanical and Aerospace Engineering, Nanyang Technological University, 50 Nanyang Avenue, Singapore 639798
[2]Engineering Product Development, Singapore University of Technology and Design, 8 Somapah Road, Singapore 487372
[3]3D Bioprinting Solutions, 68/2 Kashirskoe Highway, Moscow, Russian Federation 115409

**Abstract:** The application of machine learning (ML) in bioprinting has attracted considerable attention recently. Many have focused on the benefits and potential of ML, but a clear overview of how ML shapes the future of three-dimensional (3D) bioprinting is still lacking. Here, it is proposed that two missing links, Big Data and Digital Twin, are the key to articulate the vision of future 3D bioprinting. Creating training databases from Big Data curation and building digital twins of human organs with cellular resolution and properties are the most important and urgent challenges. With these missing links, it is envisioned that future 3D bioprinting will become more digital and *in silico*, and eventually strike a balance between virtual and physical experiments toward the most efficient utilization of bioprinting resources. Furthermore, the virtual component of bioprinting and biofabrication, namely, digital bioprinting, will become a new growth point for digital industry and information technology in future.

**Keywords:** 3D bioprinting; Complexity; Machine learning; Big data; Digital twin

***Correspondence to:** Vladimir Mironov, 3D Bioprinting Solutions, 68/2 Kashirskoe highway, Moscow, Russian Federation 115409; vladimir.mironov54@gmail.com

**Received:** January 8, 2021; **Accepted:** January 18, 2021; **Published Online:** January 29, 2021

**Citation:** An J, Chua CK, Mironov V., 2021, Application of Machine Learning in 3D Bioprinting: Focus on Development of Big Data and Digital Twin. *Int J Bioprint*, 7(1):342. http://doi.org/10.18063/ijb.v7i1.342

## 1. Introduction

Recently, there is surge in scientific publications regarding the application of machine learning (ML) to bioprinting-relevant researches such as medical imaging and segmentation, optimization of bioinks or bioprinting process as well as *in vitro* parametric studies, which are well reviewed in Yu and Jiang[1], Ng *et al*.[2]. Both recent articles focused on the benefits and potential of ML but missed a clear portrait of what future bioprinting looks like. This perspective article is, therefore, written as an extension of previous reviews, focusing on a vision of future three-dimensional (3D) bioprinting enabled by ML.

ML is a collection of computational methods of discovering approximate mathematical functions of the real world based on historical data (**Figure 1**). Given a set of input (X) and output (Y) data, humans are usually able to find a relationship between X and Y as a function of Y(X). If the input has multiple variables ranging from $X_0$ to $X_n$ and the output $Y_0$ to $Y_n$, humans will be easily overwhelmed by the complexities. However, computer algorithms can replace human to "inspect" the input and output and "guess" an approximate function among them. This approximate function generated by the algorithms is called ML model. The more input and output data there are, the more accurate the ML model becomes. This approach is known as mapping or supervised learning. In contrast, in grouping or unsupervised learning, the output (Y) is not given, the computer algorithms must figure out the output on its own, such as a pattern, a cluster, or a relationship in the input data ($X_0$, $X_1$,… $X_n$). Therefore, this approach is best for uncovering hidden patterns or relationships in data. Another approach in ML is reinforcement learning, in which both input ($X_0$, $X_1$ … $X_n$) and output ($Y_0$, $Y_1$… $Y_n$) are known, the algorithms (or agent) are

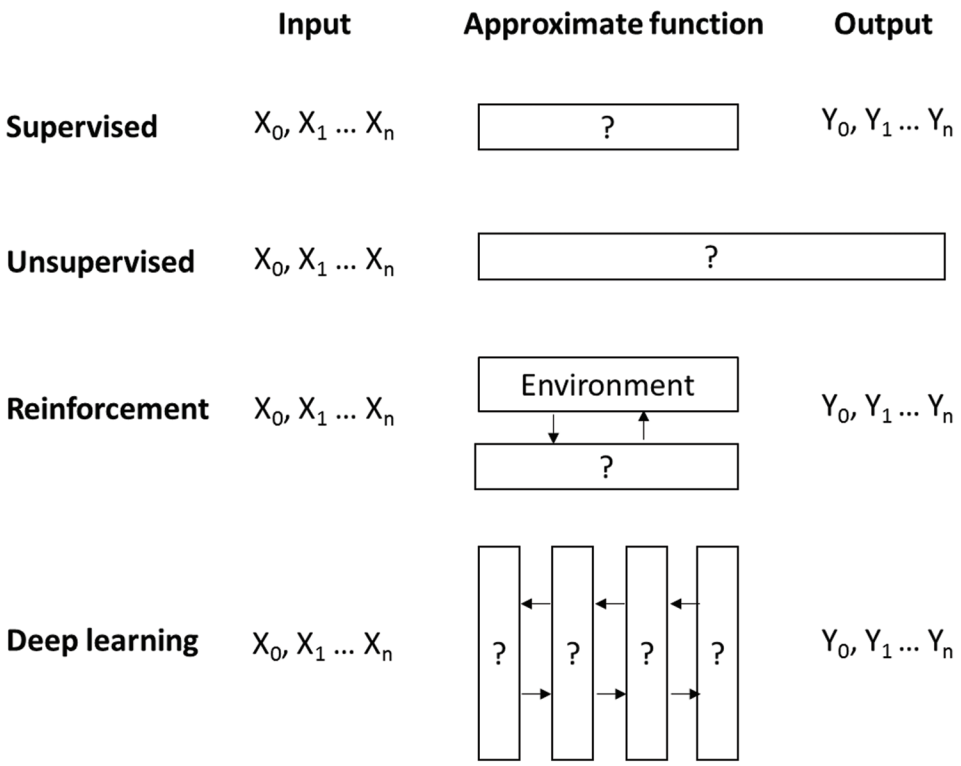


**Figure 1.** Example methods in machine learning.

to find the functions between X and Y like in supervised ML, but through a dynamic interaction with another test algorithm called environment. The environment rewards or punishes the agent's trial and error learning so that the ML model becomes more and more accurate in predication by maxing the reward. Another similar method is deep learning, in which the trained learning algorithms have multiple hidden layers and are always applied to new datasets instead of dynamically adjusting agent's actions from the continuous feedback. Above are example methods in ML. In fact, learning is quite a broad topic and several techniques have already been used in 3D printing in general[3,4].

## 2. Complexities in bioprinting

In general, ML models are preferred when complexities arise, because they can account for factors or conditions not considered in traditional mathematical models, that is, they tend to be more robust in the real-world context in terms of predication. Bioprinting coming across ML is inevitable for the reason of complexities. The complexities of bioprinting span across the entire process chain, namely, pre-processing, processing, and post-processing (**Figure 2**). In pre-processing, it is challenging to perform segmentation of tissue images at a single cell level and reconstruct them into a 3D tissue model with cross-scale cellular resolution and tissue properties. ML is, therefore, needed because of multiscale complexities of representing biological tissue models. In addition, ML can also help predict the compatibility of dissimilar materials used in bioprinting[5,6]. In processing and post-processing, it is almost impossible to perform wet experiments when the number of changing parameters exceeds a certain number, for example, ten parameters. ML is, therefore, needed because of multiparameter complexity of finding optimal protocol of bioprinting. Here, it is envisioned that ML coupled with Big Data, will solve the multiscale and multiparameter complexities and transform present 3D bioprinting into future 3D bioprinting, which is "heavily virtual" in nature.

## 3. *In silico* experiment and big data

*In silico,* experiment such as digital fabrication and computational study is believed to be a key innovation driver and play a major role in the new era of tissue engineering[7,8]. Although the current challenge is creating more realistic virtual experiment with satisfactory accuracy, there are various methods such as statistical tools and techniques that can be combined with first-principles simulations to solve it[9]. In the case of bioprinting, ML has already been used to optimize the printability of bioinks and drastically reduced the number of experiments from thousands of possible combinations[10]. Moreover, various mathematical models on bioink printability have been developed as

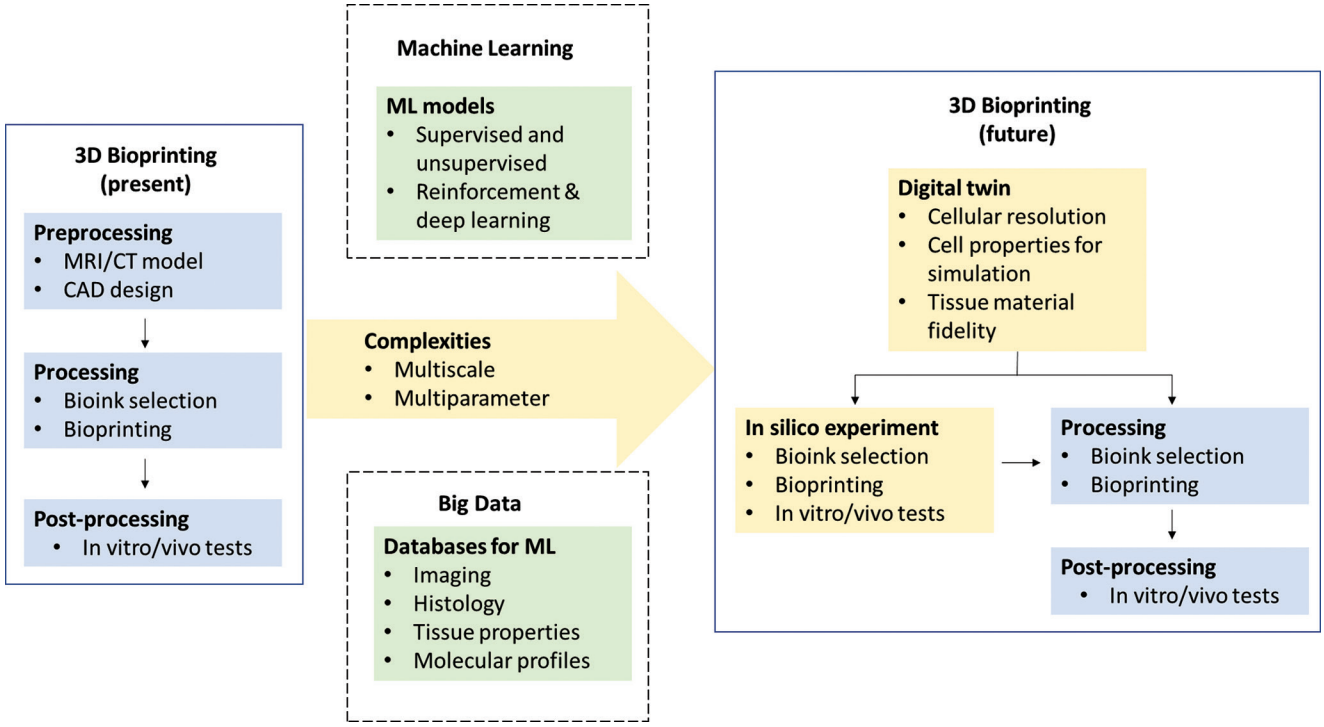


**Figure 2.** A vision for future bioprinting.

recently reviewed in Zhang *et al*.[11], Schwab *et al*.[12]. These mathematical models are useful for construction of virtual bioprinting process. ML models have also been used in *in vitro* study for identification of cell signature genes out of complex gene expression profiles among different cell groups[13,14]. Another *in vitro* example is virtual histological staining, which bypasses the lengthy and laborious process for tissue preparation. Researchers used deep learning to transform autofluorescence images of tissue into images equivalent to histologically stained tissue[15], and achieved blending of multiple stains by assigning each stain at the pixel level[16,17]. Furthermore, mathematical models and ML models, which help us understand the complexities of biological systems and extract new biological knowledge from complex experimental datasets, are expected to bring tissue engineering much closer to clinical reality[18]. Collectively, the above evidence of virtual experiments in either processing or post-processing of bioprinting suggests that we will see more *in silico* experiments with ML in bioprinting in future.

However, ML cannot be performed without Big Data about modern clinical imaging of organs, histology, immunohistochemistry, biomechanical properties of tissue and organs, molecular profiles of cell, tissue, and organs (genomics and proteomics) function and so on. Big Data can be structured, unstructured or semi-structured and it is much more than traditional databases[19]. For ML purposes, the first step is collection of Big Data or Big Data curation. The sources of big data for bioprinting are huge and diverse, it could be all types of diagnostic images stored in hospital databases, all types of experimental data in worldwide laboratories and research centers, all the "omics" databases already established in past years, or simply the vast scientific literature. Standard and open-access databases with meaningful and valuable training datasets specifically targeting for bioprinting must be created from Big Data curation. A recent example is the construction of a web-based nanomaterial database through Big Data curation, which contains 705 unique nanomaterials, and the annotation of nanostructures generates 2142 nanodescriptors for modeling and ML, but more importantly, the database is publicly available[20]. Another example is geoscience databases, which is large and ideal for ML and automated geoscience analysis[21]. In fact, numerous experimental data and various materials directly related to bioprinting have been generated over past years, making bioprinting a potentially a data-driven research, but so far there is limited database created specifically for bioprinting. In future, we hope to see more developments in this area, in line with the development of databases for 3D printing. Perhaps it may be even possible to predict new bioprinting discoveries by exploiting the current literature alone without relying on experts' opinions[22].

## 4. Digital twin of human organ

On the other hand, design process in 3D bioprinting must be organized around the concept of digital twins of organs

and virtual shadow. Creating such cell-level twins of organs requires high quality tissue specimens and advanced imaging and 3D reconstruction methods. Fortunately, the Human BioMolecular Atlas Program from Institute of Health in the United States[23], which aims to develop an open and global framework to create 3D molecular and cellular atlas of the human body, may enable the building of an integrated tissue map across scales. However, as pointed out in Campos and De Laporte[8], digital tissues should not only enable architectural replication of native tissues but also be biologically functional. This would require the capability of assigning fidelitous tissue materials to the digital twin and a profound understanding of individual and collective behaviors of cells. Cell-based mathematical models and software[24], which have been extensively used in computational biology, may be useful tools for modeling cell and tissue properties and behaviors to enable the simulation of biological functions of the virtual tissue and organs. In fact, from the economic point of view, an alternative but efficient method should be one that directly converts current magnetic resonance imaging (MRI)/confidence interval-based 3D models into cell-based models, that is, cells and tissue properties are intelligently assigned to a virtual organ model with spatial accuracy and material diversity by artificial intelligent algorithms. Slicing of the digital twin for layer-by-layer bioprinting should also be intact cell-based and matching extrusion layer thickness, which is very different from common slicing in 3D printing. Another alternative further empowering our imagination is *in vivo* cellular imaging such as MRI[25], which can map the anatomic locations of specific cells within living tissue. Given that ML has been successfully used for recognition of cell phenotype[26], it might be reasonable to imagine "*in vivo* 3D scan" of a patent-specific live tissue model into a digital twin with cellular resolution. Nevertheless, the immediate impact of the digital twins of organs on bioprinting is that the *in vivo* performance of physical bioprinting such as preclinical as well as clinical studies must collect information with specially designed assay, biosensor, and so on for updating original model in the form of digital twin. Furthermore, the cell-level digital twins together with physical 3D bioprinting could also revolutionize biology fundamentally by building tissues from scratch to explore entirely new cell configurations for cell cross-talks and cellular morphogenesis[27]. This would help provide new insights into the challenging question: "Print me an organ! Why we are not there yet?" which was recently raised in Ng *et al*.[28].

## 5. Other aspects of the future

In future, it is necessary to include the development of correspondent infrastructures such as education and training specialists and development and adaptation of software and computational power and so on. Interestingly, ML had been applied to nanotechnology to develop nanocomputing hardware that can boost artificial-intelligence-based applications[29]. It could be a reciprocal advancement to expect in future. Another topic worth watching is ML-based programmable design for 4D printing[30], as it is relevant to 4D bioprinting, a method in which bioprinted tissues transform shape, size, or pattern over time[31]. Aside from academy, the industry also expects a bright future for use of artificial intelligence in 3D bioprinting. For example, in 2019 Procter and Gamble partnered with a biotechnology company Aether to develop AI 3D Bioprinter[32].

## 6. Toward digital bioprinting

Application of ML in bioprinting and biofabrication will induce dramatic transformation and bioprinting will became a part of digital industry and information technology[33,34]. What could be done to implement these forthcoming transformations? First, bioprinting community must attract experts in computer sciences, mathematical modeling, computer simulations, and ML. Second, special efforts must be done for generation, assembly and maintaining of desirable Big Data. Maintaining and up-dating of such databases are essential. Third, digital organ twins based on sophisticated mathematical modeling and advanced software will become a new type of knowledge presentation, accumulation, and compaction in bioprinting. Finally, during transition from empiric to digital approach bioprinting will enter in digital era and it will become not descriptive but rather predictive technology increasingly based on virtual or *in silico* experiments.

## 7. Conclusion

In our opinion, when applying ML to bioprinting the most important and urgent challenges are: (1) To build training databases for ML from Big Data curation and (2) to build digital twins of human tissue/organs. The goal is to achieve a predictive power of digital twin of human tissue/organ based on Big Data which is close to virtual crash test in automobile industry. Ultimately, we hope to see a standard bioprinting simulation practice in future to reduce or replace present 3D bioprinting studies. We envision that future 3D bioprinting will become more digital and *in silico*, and eventually strike a balance between virtual and physical experiments to maximize the efficiency of bioprinting resource utilization. In future, digital bioprinting will become a new growth point for digital industry and information technology.

## References

1. Yu C, Jiang J, 2020, A Perspective on Using Machine Learning in 3D Bioprinting. *Int J Bioprinting*, 6:95.

https://doi.org/10.18063/ijb.v6i1.253

2. Ng WL, Chan A, Ong YS, *et al*., 2020, Deep Learning for Fabrication and Maturation of 3D Bioprinted Tissues and Organs. *Virtual Phys Prototyp*, 15:340–58.
3. Meng L, McWilliams B, Jarosinski W, *et al*., 2020, Machine Learning in Additive Manufacturing: A Review. *JOM*, 72:1–15.
4. Goh G, Sing S, Yeong W, 2020, A Review on Machine Learning in 3D Printing: Applications, Potential, and Challenges. *Artif Intell Rev*, 54:63–94. https://doi.org/10.1007/s10462-020-09876-9
5. Hamid OA, Eltaher HM, Sottile V, *et al*., 2020, 3D Bioprinting of a Stem Cell-laden, Multi-material Tubular Composite: An Approach for Spinal Cord Repair. *Mater Sci Eng C*, 2020:111707. https://doi.org/10.1016/j.msec.2020.111707
6. Lee JM, Sing SL, Yeong WY, 2020, Bioprinting of Multimaterials with Computer-aided Design/Computer-aided Manufacturing. *Int J Bioprint*, 2020:245. https://doi.org/10.18063/ijb.v6i1.245
7. Geris L, Papantoniou I, 2019, The Third Era of Tissue Engineering: Reversing the Innovation Drivers. *Tissue Eng Part A*, 25:821–6. https://doi.org/10.1089/ten.tea.2019.0064
8. Campos DF, De Laporte L, 2020, Digitally Fabricated and Naturally Augmented *In Vitro* Tissues. *Adv Healthc Mater*, 2020:2001253. https://doi.org/10.1002/adhm.202001253
9. Barnard AS, 2014, *In silico* veritas. *ACS Nano*, 8:6520–5.
10. Ruberu K, Senadeera M, Rana S, *et al*., Coupling Machine Learning with 3D Bioprinting to Fast Track Optimisation of Extrusion Printing. *Appl Mater Today*, 22:100914. https://doi.org/10.1016/j.apmt.2020.100914
11. Zhang Z, Jin Y, Xu C, *et al*., 2018, Evaluation of Bioink Printability for Bioprinting Applications. *Appl Phys Rev*, 5:041304.
12. Schwab A, Levato R, D'Este M, *et al*., 2020, Printability and Shape Fidelity of Bioinks in 3D Bioprinting. *Chem Rev*, 120:11028–55. https://doi.org/10.1021/acs.chemrev.0c00084
13. Arai F, Stumpf PS, Ikushima YM, *et al*., 2020, Machine Learning of Hematopoietic Stem Cell Divisions from Paired Daughter Cell Expression Profiles Reveals Effects of aging on Self-Renewal. *Cell Syst*, 11:640–52. https://doi.org/10.1016/j.cels.2020.11.004
14. Cilloni D, Petiti J, Campia V, *et al*., 2020, Transplantation Induces Profound Changes in the Transcriptional Asset of Hematopoietic Stem Cells: Identification of Specific Signatures Using Machine Learning Techniques. *J Clin Med*, 9:1670. https://doi.org/10.3390/jcm9061670
15. Rivenson Y, Wang H, Wei Z, *et al*., 2019, Virtual Histological Staining of Unlabelled Tissue-Autofluorescence Images via Deep Learning. *Nat Biomed Eng*, 3:466. https://doi.org/10.1038/s41551-019-0362-y
16. Zhang Y, de Haan K, Rivenson Y, *et al*., 2020, Digital Synthesis of Histological Stains Using Micro-Structured and Multiplexed Virtual Staining of Label-free Tissue. *Light*, 9:1–13. https://doi.org/10.1038/s41377-020-0315-y
17. Rivenson Y, de Haan K, Wallace A, *et al*., 2020, Emerging Advances to Transform Histopathology Using Virtual Staining. *BME Front*, 2020:9647163. https://doi.org/10.34133/2020/9647163
18. MacArthur BD, Stumpf PS, Oreffo RO, 2020, From Mathematical Modeling and Machine Learning to Clinical Reality. In: Lanza R, Langer R, Vacanti J, editors. Principles of Tissue Engineering. 5th ed., Ch. 2. Academic Press, Cambridge, Massachusetts, pp. 37–51. https://doi.org/10.1016/b978-0-12-818422-6.00001-0
19. What is the Structure of Big Data? 2019. Available from: https://www.magnimindacademy.com/blog/what-is-the-structure-of-big-data#:~:text=Big%20data%20structures%20can%20be,look%20at%20them%20in%20detail. [Last accessed on 2020 Dec 25].
20. Yan X, Sedykh A, Wang W, *et al*., 2020, Construction of a Web-based Nanomaterial Database by Big Data Curation and Modeling Friendly Nanostructure Annotations. *Nat Commun*, 11:1–10. https://doi.org/10.1038/s41467-020-16413-3
21. Bergen KJ, Johnson PA, de Hoop MV, *et al*., 2019, Machine Learning for Data-driven Discovery in Solid Earth Geoscience. *Science*, 363:eaau0323. https://doi.org/10.1126/science.aau0323
22. Clauset A, Larremore DB, Sinatra R, 2017, Data-Driven Predictions in the Science of Science. *Science*, 355:477–80. https://doi.org/10.1126/science.aal4217
23. Consortium H, 2019, The Human Body at Cellular Resolution: The NIH Human Biomolecular Atlas Program. *Nature*, 574:187. https://doi.org/10.1038/s41586-019-1629-x
24. Hoehme S, Drasdo D, 2010, A Cell-based Simulation Software for Multi-Cellular Systems. *Bioinformatics*, 26:2641–2. https://doi.org/10.1093/bioinformatics/btq437
25. Rogers WJ, Meyer CH, Kramer CM, 2006, Technology Insight: *In Vivo* Cell Tracking by Use of MRI. *Nat Clin Pract*

*Cardiovasc Med*, 3:554–62.

26. Sommer C, Gerlich DW, 2013, Machine Learning in Cell Biology-Teaching Computers to Recognize Phenotypes. *J Cell Sci*, 126:5529–39. https://doi.org/10.1242/jcs.123604
27. Daly AC, Prendergast ME, Hughes AJ, *et al*., 2021, Bioprinting for the Biologist. *Cell*, 184:18–32. https://doi.org/10.1016/j.cell.2020.12.002
28. Ng WL, Chua CK, Shen YF, 2019, Print me an Organ! Why we are not there yet. *Prog Polym Sci*, 97:101145. https://doi.org/10.1016/j.progpolymsci.2019.101145
29. Sacha GM, Varona P, 2013, Artificial Intelligence in Nanotechnology. *Nanotechnology*, 24:452002. https://doi.org/10.1088/0957-4484/24/45/452002
30. Hamel CM, Roach DJ, Long KN, *et al*., 2019, Machine-learning Based Design of Active Composite Structures for 4D Printing. *Smart Mater Struct*, 28:065005. https://doi.org/10.1088/1361-665x/ab1439
31. An J, Chua CK, Mironov V, 2016, A Perspective on 4D Bioprinting. *Int J Bioprint*, 2:02003.
32. Jackson B, 2019, Aether to Develop Ai 3D Bioprinter in Agreement with Procter and Gamble. Available from: https://www.3dprintingindustry.com/news/aether-to-develop-ai-3d-bioprinter-in-agreement-with-procter-gamble-149405. [Last accessed on 2020 Dec 20].
33. Rezende RA, Kasyanov V, Mironov V, *et al*., 2015, Organ Printing as an Information Technology. *Proc Eng*, 110:151–8.
34. Dernowsek JD, Rezende RA, Lopes da Silva JV, 2-17, The Role of Information Technology in the Future of 3D Biofabrication. *J 3D Print Med*, 1:63–74.

REVIEW ARTICLE

# 3D Composite Bioprinting for Fabrication of Artificial Biological Tissues

**Yi Zhang, Bin Wang, Junchao Hu, Tianyuan Yin, Tao Yue, Na Liu, Yuanyuan Liu***

School of Mechatronic Engineering and Automation, Shanghai University, Shanghai 200444, China

**Abstract:** Three-dimensional (3D) bioprinting is an important technology for fabricating artificial tissue. To effectively reconstruct the multiscale structure and multi-material gradient of natural tissues and organs, 3D bioprinting has been increasingly developed into multi-process composite mode. The current 3D composite bioprinting is a combination of two or more printing processes, and oftentimes, physical field regulation that can regulate filaments or cells during or after printing may be involved. Correspondingly, both path planning strategy and process control all become more complex. Hence, the computer-aided design and computer-aided manufacturing (CAD/CAM) system that is traditionally used in 3D printing system is now facing challenges. Thus, the scale information that cannot be modeled in the CAD process should be considered in the design of CAM by adding a process management module in the traditional CAD/CAM system and add more information reflecting component gradient in the path planning strategy.

**Keywords:** 3D composite bioprinting; Biofabrication; Computer-aided design and computer-aided manufacturing; Multiscale structure; Physical field control

***Correspondence to:** Yuanyuan Liu, School of Mechatronic Engineering and Automation, Shanghai University, Shanghai 200444, China; yuanyuan_liu@shu.edu.cn

**Received:** June 20, 2020; **Accepted:** September 9, 2020; **Published Online:** December 4, 2020

**Citation:** Zhang Y, Wang B, Hu J, *et al*., 2021, 3D Composite Bioprinting for Fabrication of Artificial Biological Tissues. *Int J Bioprint,* 7(1):299.http://doi.org/10.18063/ijb.v7i1.299

## 1. Introduction

Driven by clinical needs, tissue engineering, bio-fabrication, and additive manufacturing have been deeply intersected, and this multi-disciplinary intersection effectively promotes the rapid development of three-dimensional (3D) bioprinting technology. 3D bioprinting not only inherits the principle of additive manufacturing but also has obvious particularity in printing ink and printing object. Specifically, the "ink" for 3D bioprinting refers mostly to biological materials, cells, drugs, growth factors, etc.[1,2] The ideal printing process needs to effectively fabricate items that imitate the structure and composition of natural biological tissues and organs as well as take into account the regulation of the behavior of printed biological tissues/organs in the later cultivation and growth process[3,4].

It is well known that 3D bioprinting is divided into the following types: Material extrusion (mechanical/pneumatic extrusion)[5-7], material jetting (inkjet, microvalve-based, laser-assisted, electrohydrodynamic printing)[8-11], and vat polymerization (stereolithography, digital light processing, and two-photon polymerization)[12-14]. Each printing process is unique for its characteristics. Since natural tissues, such as the heart, nerves, and blood vessels, tend to have unique anisotropic fiber structures of exceptionally rich internal components[15], it is quite difficult to fabricate a bioconstruct that features multi-scale and heterogeneous microstructures using a single-step printing process[16]. Therefore, an increasing number of researches have begun to integrate two or more printing processes with different forming principles to prepare complex biological structures or functional scaffolds, which is also the origin of 3D composite bioprinting. In fact, 3D composite bioprinting has become a research hotspot in the field of artificial biological tissue and organ construction. The current 3D composite bioprinting not only features a combination of two or more printing processes but also

often involves physical field regulation that can regulate filaments or cells during or after printing.

It should be pointed out that the steps of multi-physical field regulation are often adopted in the process of 3D composite bioprinting to form micro-scale structure inside the macro-scale 3D printing structure. Correspondingly, the computer-aided design and computer-aided manufacturing (CAD/CAM) software for 3D composite bioprinting are different from the traditional 3D printing system. In other words, the CAM software for 3D composite bioprinting should be able to combine the scale information that cannot be modeled in CAD software with the modellable information from the CAD software, presenting new challenges to the design of 3D composite bioprinting system.

## 2. The process of 3D composite bioprinting

The intention of 3D composite bioprinting is to effectively overcome the limitations of a single-step printing process and ensure the inclusion of multiscale heterogeneous characteristics in the final construction by the integration of multiple process technologies. However, according to the status quo of research, two principles are very important for good integration: (i) The material structure formed by different printing processes can form a good composite interface and (ii) the integration of different printing processes has engineering realizability in the system implementation.

### 2.1. Combination of extrusion printing and dynamic crosslinking

Extrusion printing is the most typical and common process method. It uses air pressure or mechanical force as the driving energy to controllably extrude bioink, and by the spatial motion of the platform and the print nozzle, different two-dimensional patterns can be depicted and stacked to form a 3D structure. In extrusion printing, materials with different viscosity can be used as bioink. The highly viscous materials can be extruded to form continuous fibers, while the lower ones can be applied to obtain discrete droplets. Therefore, various materials are available for extrusion printing which are beneficial for manufacturing structures with good mechanical properties. Recently, many studies on 3D composite bioprinting based on extrusion printing have been carried out and the most representative is the combination of dynamic crosslinking technologies, which specifically refer to a class of technologies that can achieve various degrees of crosslinking in extrusion printing process through online control of process parameters or dynamic adjustment of external physical field.

At present, by adding temperature gradient in the process of extrusion printing, printing technologies and equipment with the capacity of imposing different temperature conditions have been developed[17-20]. Direct extrusion of biomaterials such as gel, slurry, particle, and filament that represent temperature-dependent phase transition is the main operating mode and the printing path can be obtained from conventional 3D modeling, slicing, and path planning methods and software. One research hotspot in this field is to improve the mechanical properties and biocompatibility of the printed construct at the same time using a composite printing system which combines the printing processes under different temperature field; some progress has already been made. Chen *et al.* built a hierarchical construct by alternately depositing the Wharton's jelly mesenchymal stem cells-coated polydopamine (PDA)-coated calcium silicate/polycaprolactone (PCL) fibers and HUVECs-laden hydrogel in a composite printing system combining melt extrusion, normal temperature extrusion, and electrospray processes to obtain a bone scaffold with good mechanical properties and the ability to promote angiogenesis and osteogenesis[21]. Mekhileri *et al.* designed a singularization device that was capable of capturing and extruding a single microtissue of hydrogel spheroid with more than 80% accuracy. The integrated system of this device with melt extrusion equipment was capable of precisely delivering a single microstructure to a specific position in the scaffold during the printing process, thereby realizing the preparation of complex hierarchical bioconstruct **(Figure 1A)**[22].

In addition, the introduction of ionic crosslinking and coaxial nozzle enables the extrusion process to effectively construct vessels like microchannels[23-26]. Dynamic reactive extrusion printing technology, which has shown good potential in the realization of cell printing under room temperature, is a growing research interest. Narayanan *et al.* produced meniscus by printing human adipose-derived stem cells (hASCs) with polylactic acid (PLA) fibers and alginate hydrogel. Previous studies indicated that the composite fiber structure enhanced cell proliferation and promoted extracellular matrix (ECM) secretion and chondrogenic differentiation **(Figure 1B)**[27]. Tabriz *et al.* prepared a 3D cellular biological structure by extruding pre-crosslinked sodium alginate into calcium ion bathing. After that, the structural stability was further enhanced by barium ion crosslinking **(Figure 1C)**[28]. Lozano *et al.* printed 3D brain-like structures composed of discrete layers of primary cortical neural cells with a coaxial nozzle. The result showed that the cortical cells inside the structure could develop into 3D neuronal networks in <5 days[29]. Wang *et al.* prepared *in vitro* glioma model by coaxially extruding materials into the calcium chloride ($CaCl_2$) solution. The shell consisted of sodium alginate and glioma stem cells (GSC23), while the cell suspension containing glioma cell U118 was taken as the core material. The experimental results showed that

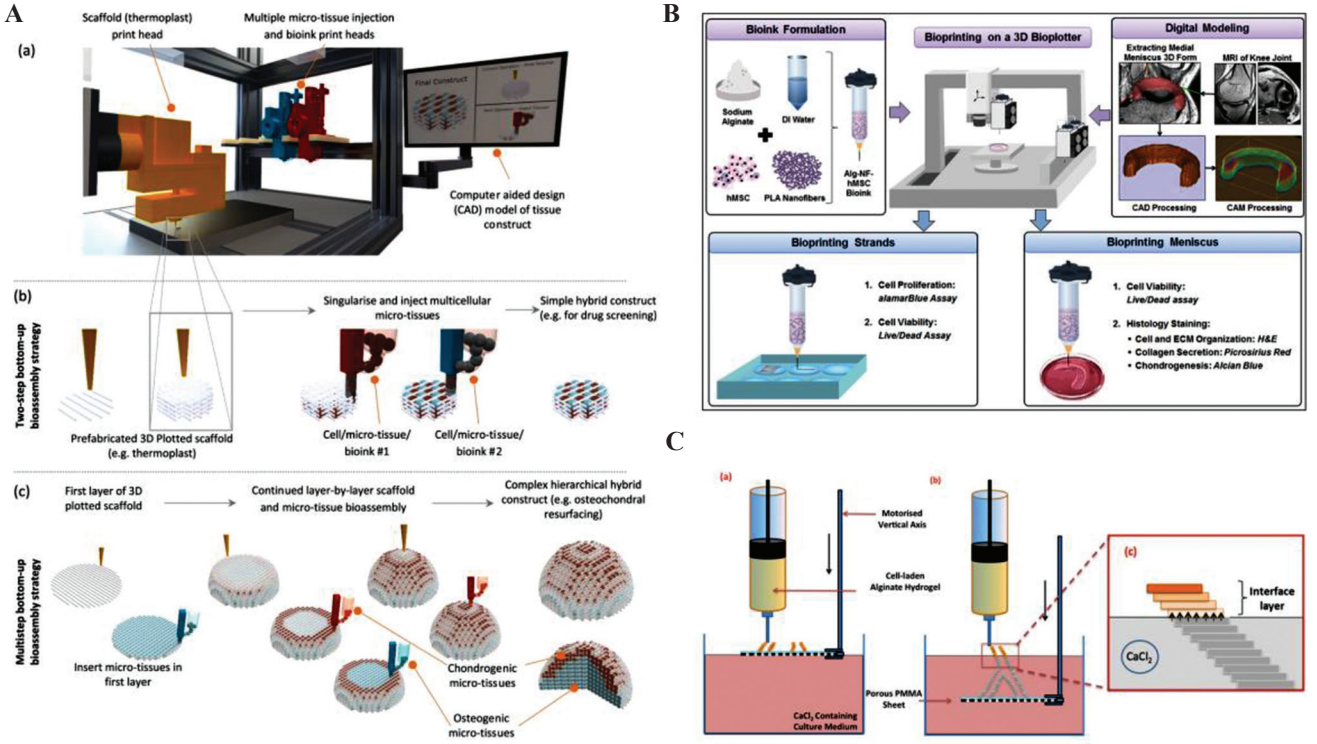


**Figure 1.** Fabrication of bioconstruct through the composite forming technology by combining extrusion printing with dynamic crosslinking. (A) Complex hierarchical construct made by the integrated system combining melt extrusion and singularization printing (from ref.[22] licensed under Creative Commons Attribution 3.0 license). (B) Meniscus printing based on the extrusion of bioink containing polylactic acid (PLA) fibers, human adipose-derived stem cells, and alginate, and crosslinking by $CaCl_2$ (Reprinted with permission from Narayanan LK, Huebner P, Fisher MB, *et al.*, 2016, 3D-Bioprinting of Polylactic Acid (PLA) Nanofiber–Alginate Hydrogel Bioink Containing hASCs. *ACS Biomater. Sci. Eng.*, 2(10):1732–1742[27]. Copyright © 2016 American Chemical Society). (C) Vascular structure formed by stacking pre-crosslinking alginate patterns and subsequently enhanced by adding $Ba^{2+}$ (from ref.[28] licensed under Creative Commons Attribution 3.0 license).

the glioma model prepared by this method could mimic the glioma microenvironment and had enhanced drug resistance[30].

In summary, the integration of dynamic crosslinking means is an important driving force for the development of extrusion printing technology; especially, the combination of coaxial extrusion printing and materials with ionic crosslinking properties gives great advantages in the construction of vessel-like structures. Compared with the existing two-dimensional lamellar microchannel manufacturing technology, this method has obvious advantages and potentials in the integration forming process with living cells. Besides, the vessel-like constructs made by this method can better mimic the tubular structure and is more convenient for 3D bioprinting. In addition, the aforementioned dynamic crosslinking technology usually achieves various degrees of crosslinking in the whole extrusion printing process through online control of process parameters or dynamic adjustment of the external physical field. Hence, this kind of method accords with the characteristics of the above-mentioned 3D composite bioprinting.

## 2.2. Combination of electrohydrodynamics and extrusion printing

Electrohydrodynamics refers to the dynamics of electrically charged fluid, which constitute the basis of electrospinning, material jetting, and electrostatic direct writing. The process of electrospinning, electrospray, or electrostatic direct writing is achieved similarly by applying a voltage between the nozzle and the receiving plate. However, due to different material properties, the resultant forces formed on the charged fluid surface are different, resulting in different shapes of material after they leave the nozzle.

Compared with other methods, electrospinning is more widely used to fabricate tissue engineering scaffolds because the structure made by electrospinning resembles ECM. However, the electrospinning structure does not have enough mechanical properties and cannot form a 3D structure with a certain thickness; therefore, many researchers start to combine electrospinning with extrusion printing. Besides, some of the research results pointed out that electrostatic direct writing can

generate micron-scale fibers and properly control the fiber deposition position. However, electrostatic direct writing encounters challenges when constructing thick structures[31]. According to recent studies, the composite forming process based on electrospinning/electrostatic direct writing and extrusion printing has emerged as a powerful technique in the field of developing new scaffolds, including vessel, bone, and skin.

Among various attempts, the most representative one lies in the preparation of the artificial blood vessel, which contains the integration of micro-nano fibers generated by electrospinning and the macrostructure formed by extrusion printing to mimic the multilayer structure of the blood vessel wall and regulate the mechanical properties[32-36]. Wu *et al.* utilized melt extrusion printing and electrospinning to prepare a bi-layered vascular graft with 3D interconnected circumferential microchannels. The bi-layered structure was fabricated by casting and electrospinning poly(l-lactic acid-co-ε-caprolactone) while the microchannels in the inner layer were formed by sacrificing the extruded sugar fiber[37]. By combining electrospinning with melt extrusion printing process, Lee *et al.* proposed a fabrication method of building a composite artificial vessel which using electrospinning PCL membranes with highly-aligned fiber surface as the inner layer and extruding PCL grid structure as the outer layer. After PDA coating and vascular endothelial growth factor immobilization, this vessel scaffold achieved good mechanical properties and biocompatibility[38]. Due to the tubular structure of the artificial blood vessel, most of the composite printing process in this field can adjust the properties by controlling the rotation of the receiving axis instead of the planning printing path by CAD/CAM.

In the field of bone and skin-repairing, the composite fabrication method containing electrospinning, electrostatic direct writing, and extrusion printing has drawn lots of attention as it is capable of controllably shaping both macro and micro characteristics[39-42]. The core idea of this kind of technology is to take advantage of the respective characteristics of different processes. Extrusion printing, capable of forming mesoscale filaments, is chosen to provide mechanical support for the scaffold. Meanwhile, the microstructure formed by sub-10-micrometer fibers can be readily manufactured by electrohydrodynamic processes. Along with the development of this technology and increasing fulfilment of various application requirements, this method has begun using materials with different attributes. At the same time, with the improvement of technology, the number of cross-scale features is progressively increasing, putting this technology to great advantages for manufacturing bioconstructs with stable mechanical properties and controllable cell distribution. Recently, for the 1st time, de Ruijter *et al.* verified the hydrogel extrusion printing and electrostatic direct writing composite forming system. The system can achieve the preparation of bioconstructs with stable mechanical properties as well as controllable cell distribution[43]. Rajzer *et al.* used fused deposition modeling (FDM) and electrospinning to prepare a kind of layered scaffold for the reconstruction of nasal cartilage and subchondral bone. The upper layer of the scaffold was made of osteogenon-gelatin by electrospinning to promote cell adhesion and proliferation. The lower layer of the scaffold was prepared by printing poly-L-lactide with FDM. The porous grid structure could not only provide the mechanical strength for the scaffold as well as convenient *in vivo* fixation of the implant but also promote the tissue growth and the penetration of gelatin[44]. Diloksumpan *et al.* proposed a method to prepare bone cartilage scaffold by composite technology. In this method, PCL framework was constructed by melt electrowriting and then the printable calcium phosphate-based materials (pCaP) subchondral bone was directly built on the PCL layer by extrusion printing. After that, the cartilage was prepared by injecting methacryloyl-modified gelatin (GelMA) into the former framework. The experimental results showed that the PCL framework improved the interfacial shear strength between GelMA and pCaP by 6.5 times. Furthermore, the PCL grid embedded in GelMA increases the compression stiffness of the cartilage layer, increasing its resemblance to the natural one **(Figure 2)**[45].

The composite forming method combining extrusion printing and electrospinning has been proven to be able to effectively prepare the scaffold with a multiscale pore structure, which has obvious advantages in realizing the composite forming of multiscale micro-nano structures. However, most of the existing research results are still limited in the use of biomaterials to prepare artificial regeneration scaffolds while the research on the direct printing of cells, growth factors, and scaffolds materials to achieve the composite forming of active biological structures is still at the stage of exploration.

## 2.3. Combining cell printing and hybrid additive/subtractive manufacturing

Cell printing technology has advantages in achieving direct cell assembly, but most of the technologies with high cell printing resolution are often unable to directly construct large-scale complex biostructures[46-49]. For this reason, tackling this bottleneck requires combining them with scaffold printing technologies. Due to the complexity of the vascularization process, the use of artificial biological tissue is limited to clinical application at present[50-53]. It is necessary take into account the requirements of cell metabolism in the process of preparing biological structures and the role of scaffold materials, cells, and growth factors from macro, meso, and micro scales[54-56]. In this context, as hybrid additive/subtractive

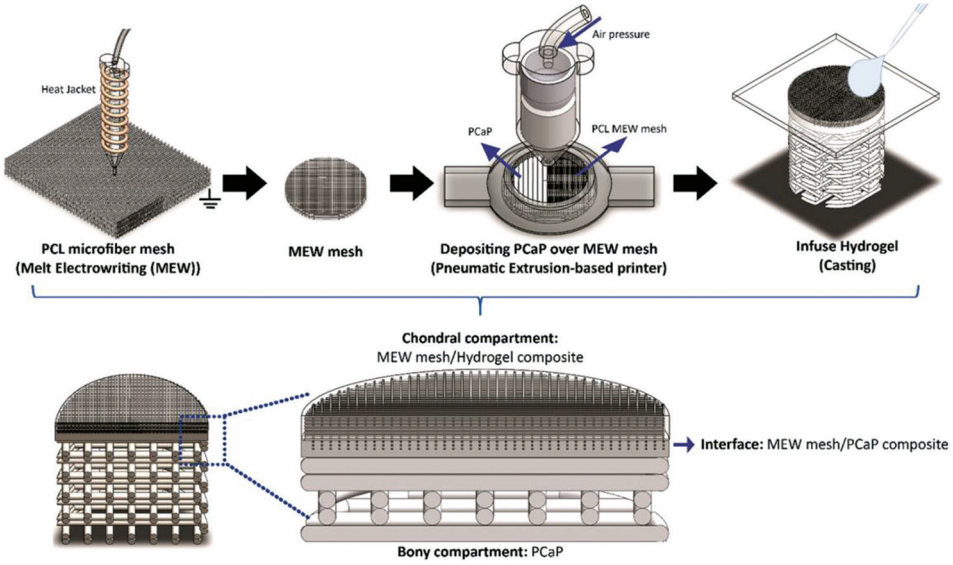


**Figure 2.** Manufacture of bioconstruct using composite forming technology that combines electrohydrodynamics and extrusion printing. Bone cartilage scaffolds are successively made by three processes – melt electrowriting, fused deposition modeling, and hydrogel casting (from ref.[45] licensed under Creative Commons Attribution 4.0 license).

manufacturing has already archived many positive results in the preparation of prevascularized tissues[57-61], the composite forming technology combining cell printing and hybrid additive/subtractive manufacturing is applied to the manufacture of biological structure.

At present, in the process of the preparation of biostructures, the composite forming technology combining cell printing with hybrid additive/subtractive manufacturing has been able to initially realize the structural shaping in different scales and the position control of different materials and cells, which proves it to be a potential technical means to construct heterogeneous biostructures with a multiscale vascular network. Kim *et al.* used extrusion printing to form human preadipocytes, human dermal fibroblasts, and gelatin to construct subcutaneous tissue, dermis, and vascular channels between them, respectively. After that, primary human epidermal keratinocytes were ink-jetted on the surface of the dermis to form the epidermis layer to complete the manufacture of the vascularized full-layer skin model *in vitro*. Compared with the *in vitro* skin model only with the epidermis or dermis layer, the cell morphology and functional expression markers in the dynamically cultured, vascularized full-thickness skin model were similar to those in the natural one and can better simulate the complexity of real skin[62]. Kang *et al.* proposed an integrated tissue–organ printer for human-scale organ manufacturing, which uses PCL and F-127 as the structural support frame while composite of gelatin, fibrin, hyaluronic acid, and glycerin as the cell carrier. Through the integrated printing of these materials, the method could fabricate vascularized tissue structures that resemble the size and stable mechanical structure of human organs[63]. Noor *et al.* verified the possibility of making a personalized vascularized heart patch with no immune response by capitalizing on multi-head extrusion printing with the patient's cells and acellular matrix. On this basis, through the combination of embedded printing, the fabrication of a human heart with natural structure characteristics was achieved **(Figure 3)**[64].

In summary, hybrid additive/subtractive manufacturing has been proven to have great potential in the construction of vessel-like microchannel structure, highlighting its significance in the formation of vascularized bioconstructs using cell printing technology. The printing of sacrificial materials into the whole biological structure not only helps provide mechanical support in the manufacturing process but also is important for the construction of microchannel structures.

## 2.4. 3D composite bioprinting integrated with light, magnetic and acoustic field control

As 3D bioprinting not only constructs structures that mimic the structure and component distribution of natural biological tissues and organs but also take into account the regulation of cell behavior in the printing process, the research of combining non-contact field regulation technology, such as light, magnetism, and sound, with traditional 3D bioprinting technology has attracted more attention, especially in combination with environmentally responsive intelligent materials.

Some innovative research results have been achieved recently. Yang *et al.* combined the external DC electric

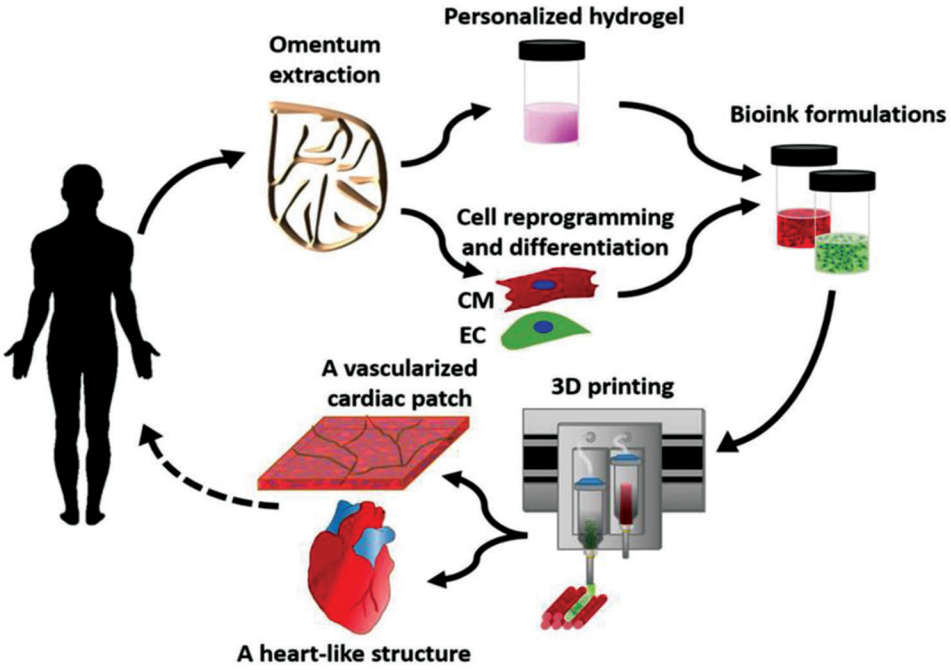


**Figure 3.** Manufacture of bioconstructs using the composite forming process of cell printing and hybrid additive/subtractive manufacturing. This example shows the preparation of personalized perfusable cardiac patches and cellularized human heart using multi-head extrusion printing of autologous stem cells and acellular matrix (from ref.[64] licensed under Creative Commons Attribution 4.0 license).

field and the photocuring mask projection process so that the modified multiwalled carbon nanotubes (mwcnt-s) embedded in the photosensitive resin could be controllably arranged by the electric field imposed. The tensile test shows that the arrangement of mwcnt-s will produce anisotropic elastic modulus, which is higher in the direction parallel to mwcnt-s, but lower in the vertical one. Using this approach, a reinforced artificial meniscus with carbon nanotubes aligned in the circumferential and radial directions was fabricated[65]. Chansoria *et al.* developed an ultrasound-assisted bio 3D printing technology that used the standing bulk acoustic wave produced by an ultrasonic alignment chamber around the printing platform to arrange the cells in the printed structure to construct single or multi-layer anisotropic cell structure **(Figure 4A)**[66]. Kirillova *et al.* performed two-dimensional extrusion printing with methacrylated alginate or methacrylated hyaluronic acid on the glass substrate. By taking advantage of the photo-crosslinking gradient between the upper and lower surface of the structure, the printed film would have a self-folding behavior to form a tubular structure of which the internal diameter could achieve as low as 20 μm[67].

Thus, it can be observed that multi-physics field control has unique advantages in improving printing flexibility. Although some studies have not yet been applied in the field of biological manufacturing, it can be predicted from the latest technical characteristics analysis that these methods will provide new solutions for biological manufacturing. Kokkinis *et al.* proposed a "5D" printing method. By integrating the printhead with component mixing function as well as rotating magnetic field in the extrusion printing system, the composite system allowed additional control over component concentration and orientation of magnetic particles, which realized the printing of the structures with anisotropic texture arrangement **(Figure 4B)**[68]; Kim *et al.* added a magnetic coil around the extrusion printing nozzle to achieve the desired orientation of ferromagnetic particles contained in the materials. This method could pattern the magnetic polarity of the printed filament so that fast transformations between complex 3D structures through magnetic actuation could be realized[69].

## 3. 3D composite bioprinting system

With the continuous development of 3D printing technology for biological purposes, the research of bio-CAD/CAM/3D printing forming system is also progressing. However, it should be pointed out that most of the early research on biological manufacturing is based on commercial 3D printers, and some commercial CAD/CAM software has been widely used. The representative software includes Makerbot proposed by Makerbot, which is a slicing software customized for Makerbot printer; Xbuilder of Xery 3D printing technology, a Chinese software supporting STL, G-Code, obj, and other formats; Cura developed by Ultimaker, which has a high degree of integration and the best support for Ultimaker's

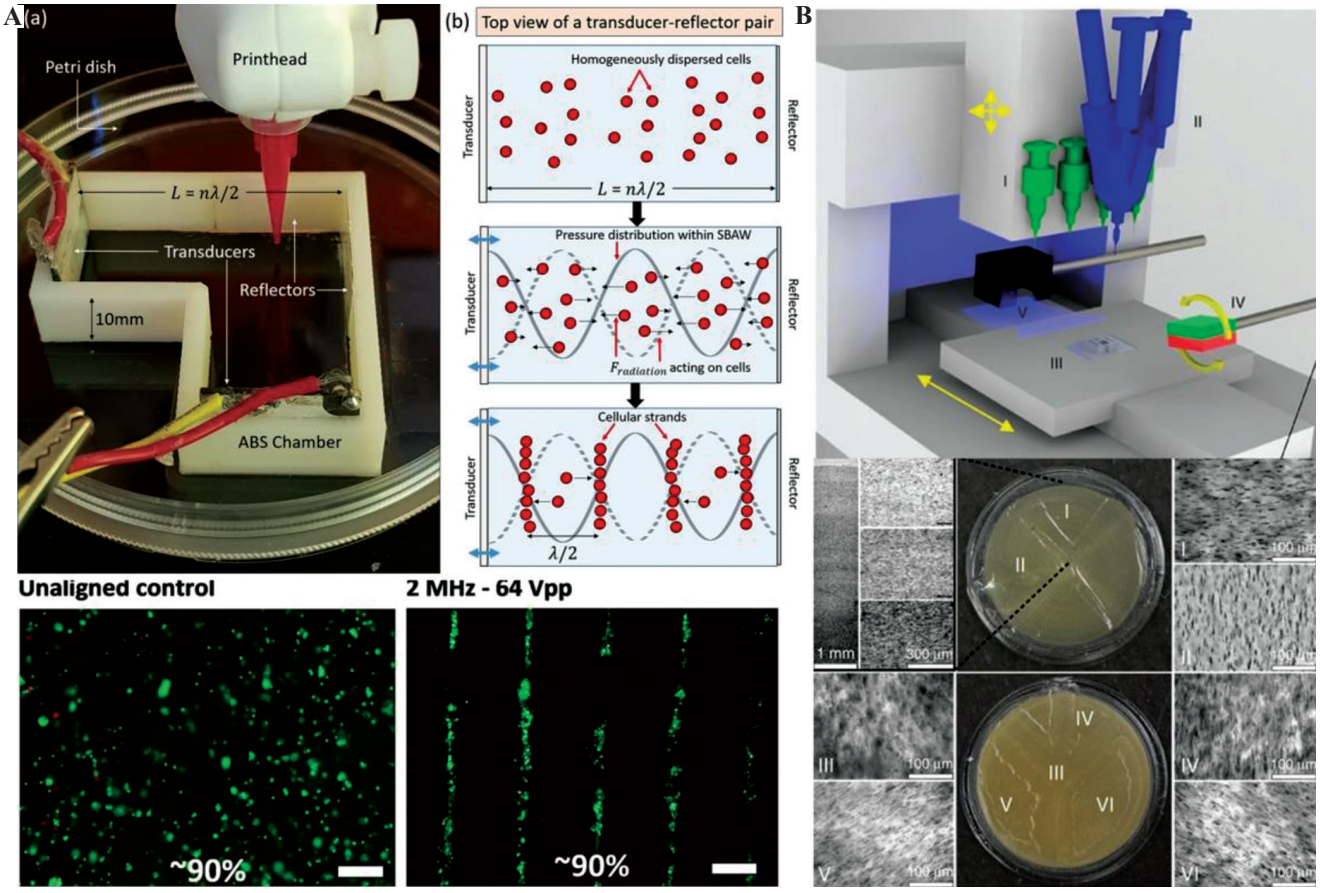


**Figure 4.** Bio-composite printing assisted by non-contact field regulation technology. (A) The ultrasonic-assisted extrusion printing with the capacity of no-contact cell arrangement based on the acoustophoretic principle (from ref.[66] licensed under Creative Commons Attribution 4.0 license). (B) The extrusion printing system combined with the external magnetic field and material component mixing printhead for adjusting the material concentration and particle orientation during printing procedure (from ref.[68] licensed under Creative Commons Attribution 4.0 license).

products; Skeinforge, an open-source program composed of Python scripts that can convert 3D models into G-Code files. Focusing on the needs of medical applications, the Magics developed by Materialise is the most representative program, as Magics can process not only the CAD model generated through 3D model reconstruction by Mimics but also the general CAD data output by the CAD/Re software system. The generated model files by Magics are saved in STL format and can be fabricated by a rapid prototyping machine.

With the continuous improvement in biomanufacturing and 3D bioprinting technology, the application field has also expanded from the preparation of biological scaffolds to cell printing, cell assembly, construction of complex biological structures, etc., which make the technical route based on industrial 3D printers no longer meet the demand. Many research institutions develop corresponding bio-CAD/CAM/3D printing systems for specific bioprinting processes. Shim *et al.* combined air pressure extrusion with piston extrusion to prepare a multi-nozzle extrusion printing platform that is suitable for 3D printing of various materials[70]. The NovoGen MMX bioprinter of Organovo has two printheads for printing cell-laden materials and cell-free materials. Two vials housed on the instrument can adjust the temperature of materials. Besides, the device is also equipped with a laser calibration device to calibrate the position of the micropipette[71]. Whatley *et al.* developed a 3D additive manufacturing equipment to prepare the biomimetic elastic intervertebral disk scaffold[72]. The 3D bioprinting system of RegenHU uses air pressure for the extrusion of materials to satisfy the requirements of biological fabrication. The printer has strong adaptability and is easy to operate. The inlet air pressure can be adjusted according to different viscosity of the materials so that the fabrication of bioconstruct consisting of multi-materials can be carried out. The 3D-Bioplotter printing platform of EnvisionTec has high mobile precision and multiple printheads. The printheads have embedded heating modules and can be swiftly changed. A high-

resolution camera is used to position the nozzle while the z-axis sensor can accurately control the height between the nozzle and the receiving platform. Lu *et al.* used CAD software to design the 3D model of the internal micropore structure of the bionic bone scaffold and fabricated it based on the path planned by an independently developed path planning software[73]. Yan *et al.* put forward the low-temperature 3D bioprinting technology and equipment and made a number of achievements in the preparation of bone scaffolds[74]. Liu *et al.* introduced the inertial force injection (AVIFJ) and extrusion printing composite forming system, which can achieve precise deposition of droplets containing a single cell and the printing of cell-laden hydrogel[75]. Xie *et al.* introduced a printing system, which integrates extrusion printing and electrospinning for forming structures with micro-nano scale features. The system had a micro-level printing resolution to meet the requirements of forming exquisite complex cross-scale structures[76]. Liu *et al.* proposed and preliminarily provided the test platform of the bio-CAD/CAM/3D composite printing technology, abbreviated as a composite forming test platform[77,78].

It can be found that combining the process with micro-nano forming precision and 3D bioprinting effectively solves the problem of limited precision and the inability of forming micro-scale structures inside the structure, which are evident in the formation process of traditional 3D printing. This feature makes the corresponding bio-CAD/CAM process different from the traditional CAD/CAM, that is, the biological CAM process needs to merge the scale information that cannot be modeled in the CAD process with the information from the CAD process. In addition, the composite forming process, which combines printing technology and micro-nano forming technology, often integrates multiple physical fields, cross-linked reaction, and other effects so as to effectively regulate the interface effect in the composite structure which make the prepared scaffold satisfy the requirements of cell attachment and growth while taking into account the structural controllability and mechanical properties. These also call out challenges upon the corresponding printing system and the designation of the CAD/CAM function module. To solve these problems, Liu Yuanyuan *et al.* from Shanghai University proposed a type of a composite forming system consisting of multiple functional subsystems with which the bio-CAD/CAM software system was studied. The system designed the automatic processing flow and detail implementer method that encompass the following: Obtaining STL models of injury tissue from manual designs or medical imaging modalities reconstruction, generating printing path information and drive file containing processing information by post-processing. Importantly, an approach of adding process management module which innovates the bio-CAD/CAM system and realizes the use of bio-CAM processing for fabricating structures which could not be modeled in the CAD processing was put forward **(Figure 5)** [79].

In summary, for tissue engineering scaffold printing, the CAD/CAM system for 3D bioprinting is the same as the traditional 3D printing system if the scale of the printing structure is single or common and the material used is suitable for the current mainstream 3D printing technology and system. Otherwise, if the goal of printing is to assemble components such as cells, drugs, biomaterials, etc., both path planning strategy and process control can become more complex. Hence, it is necessary to add a process management module in a traditional CAD/CAM system and supplement with more information reflecting component gradient in the path planning strategy. Besides, it should be pointed out that at present, the 3D composite bioprinting system proposed by different institutions involves different processes, so there will be differences in the scope of applicable materials and specific application objects. As for the index advantage analysis from the engineering and technology perspectives, the detailed parameter comparison is not available at present because most of the systems are not commercial.

## 4. Discussion and prospects

According to the researches and demands for tissue engineering and regenerative medicine, the core issue of the regeneration of tissue and organ by biofabrication technologies lies in the effective assembly and behavior regulation of cells. A typical way of cell assembly is using the biodegradable scaffolds with autologous stem cells seeded and then co-cultured on it *in vitro*. After that, the scaffold can be planted *in vivo* to repair the injured tissue and organ. In this context, to ensure the effective adhesion of the inoculated cells and further realize the accurate positioning and reasonable distribution of cells or cell clusters, the solution of precisely controlling the components and microstructures of scaffolds as required has become an important goal of the development of 3D printing technologies and equipment. Another route is the technology of direct assembly of cells which is capable of precisely depositing living cells in the spatiotemporal dimension. Although great progress has been made in this field in obtaining a 3D biological structure, its shortcomings still lie in the manufacturing efficiency, achievable scale, and complexity of the structure; these problems pose new challenges to the biological printing process and equipment technology.

In such a context, the research interest in 3D composite bioprinting based on the integration of two or more printing processes with different forming principles is gradually intensifying **(Table 1)**. 3D

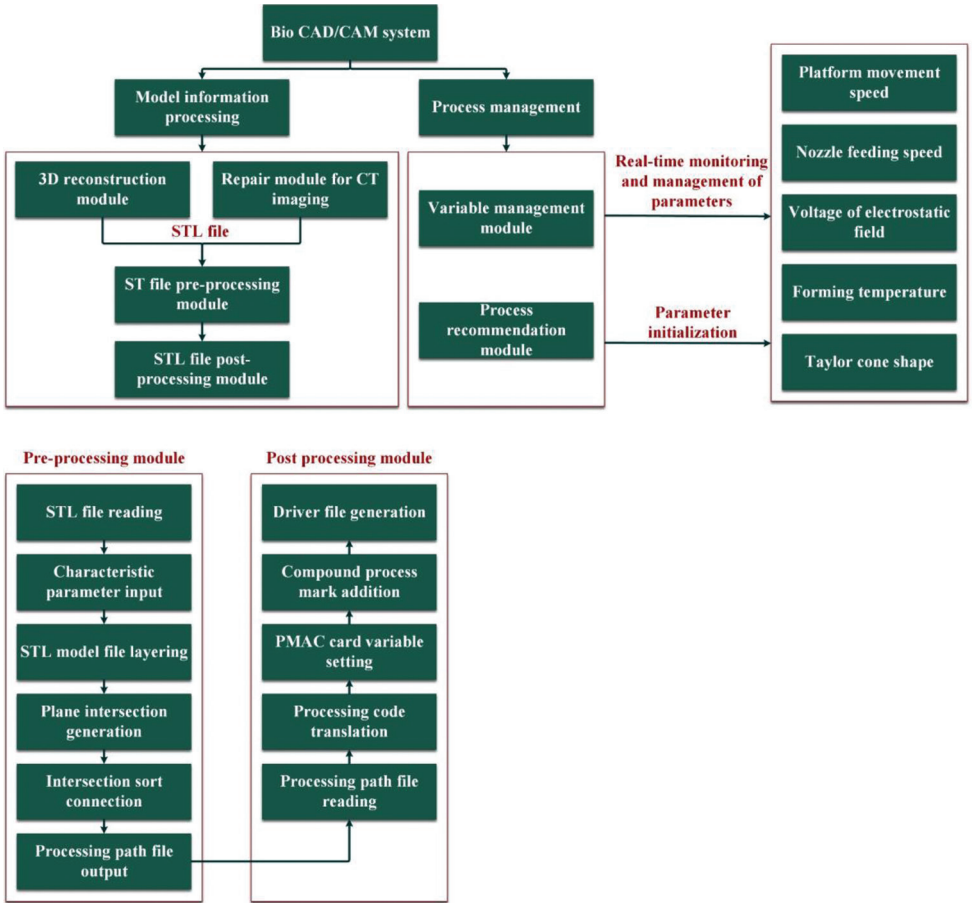


**Figure 5.** Software composition and model information processing flow of the bio-computer-aided design/computer-aided manufacturing/3D composite printing system.

**Table 1.** Current efforts toward 3D composite bioprinting

| Combined processes | | Main characteristics | References |
|---|---|---|---|
| Phase transition through temperature gradient | Extrusion printing | Improve the mechanical properties and biocompatibility of the printed construction at the same time | [21,22] |
| Ionic crosslinking | Extrusion printing | Provide more fabrication flexibility by controlling ion diffusion and material extrusion speed; perform cell printing under room temperature; effectively construct vessels like microchannels | [27-30] |
| Electrohydrodynamics | Extrusion printing | Fabricate scaffolds with good mechanical properties and large scales, and the structure can mimic natural extracellular matrix on the micro-nano scale; effectively prepare the scaffolds with a multiscale pore structure | [37,38,43-45] |
| Cell printing | Hybrid additive/ subtractive manufacturing | Construct vascularized bio constructs with certain mechanical strength and complex microstructure | [62-64] |
| Physical field control | Extrusion printing | Improve printing flexibility, especially with environmentally responsive intelligent materials; regulate materials and cells in the printing process | [65-69] |

composite bioprinting is a combination of two or more printing processes, and it may often involve physical field regulation that can regulate filaments or cells during or after printing.

Some research results in the field of tissue damage repairing demonstrated a technology with broad application prospects. For example, 3D composite bioprinting which combines extrusion forming with electrospinning technology has been proven to be able to effectively prepare tissue scaffold with a multiscale pore structure, showing obvious advantages in the formation of multi-scale micro-nano composite structure. Besides, hybrid additive/subtractive manufacturing has been proven to have great potential in the construction of vessel-like microchannel structure, which is of great significance in the formation of vascularized bioconstructs. Moreover, the printing of sacrificial materials into the whole biological structure not only helps provide mechanical support in the manufacturing process but also is very important for the construction of microchannel structures. On the other hand, the 3D composite bioprinting integrated with light, magnetic, and acoustic field control would have a greater development potential if it is combined with environmentally responsive smart materials. Recently, some innovative research achievements have been made, such as the manufacture of artificial blood vessels. However, it is still limited by the difficulties in the construction of large-scale artificial regeneration tissue as well as repairing large area tissue damage. Furthermore, how to attain rapid vascularization of large-scale artificial regeneration tissue remains an urgent question to address.

In terms of 3D composite bioprinting process and system research, the printing process, whether extrusion printing, electrospinning or the existing 3D composite bioprinting technology, is being further integrated with the technologies such as direct cell assembly, dynamic cross-linking formation, cell behavior guiding, controlled drug-releasing, etc. as required. The constant expansion and enrichment of the research scope of 3D composite bioprinting promote further application and innovation of this technology in the field of tissue and organ repairing and regeneration. The existing interface problems in the integration of multiscale structure and multi-gradient components and in the technical feasibility of multi-process integration remain to be addressed in parallel with the continuous innovation of the 3D composite bioprinting process and system.

## Acknowledgments

This work was supported by grants from the National Natural Science Foundation of China (No. 61973206, 61703265, 61803250, 61933008) and Shanghai Science and Technology Committee Rising-Star Program (No. 19QA1403700).

## Conflict of interest

The authors declare no conflicts of interest.

## References

1. Groll J, Burdick JA, Cho DW, *et al*., 2018, A Definition of Bioinks and their Distinction from Biomaterial Inks [J]. *Biofabrication*, 11(1):013001. https://doi.org/10.1088/1758-5090/aaec52
2. Gungor-Ozkerim PS, Inci I, Zhang YS, *et al*., 2018, Bioinks for 3D Bioprinting: An Overview [J]. *Biomater Sci*, 6(5):915–46. https://doi.org/10.1039/c7bm00765e
3. Ng WL, Chua CK, Shen YF, 2019, Print Me An Organ! Why We Are Not There Yet [J]. *Prog Polym Sci*, 97:101145. https://doi.org/10.1016/j.progpolymsci.2019.101145
4. Ng WL, Chan A, Ong YS, *et al*., 2020, Deep Learning for Fabrication and Maturation of 3D Bioprinted Tissues and Organs [J]. Virtual Phys Prototyp 15(3):340–58
5. Ozbolat IT, Hospodiuk M, 2016, Current Advances and Future Perspectives in Extrusion-based Bioprinting [J]. *Biomaterials*, 76:321–43. https://doi.org/10.1016/j.biomaterials.2015.10.076
6. Emmermacher J, Spura D, Cziommer J, *et al*., 2020, Engineering Considerations on Extrusion-based Bioprinting: Interactions of Material Behavior, Mechanical Forces and Cells in the Printing Needle [J]. *Biofabrication*, 12(2):025022. https://doi.org/10.1088/1758-5090/ab7553
7. Gao G, Kim BS, Jang J, *et al*., 2019, Recent Strategies in Extrusion-Based Three-Dimensional Cell Printing toward Organ Biofabrication [J]. *ACS Biomater Sci Eng*, 5(3):1150–69. https://doi.org/10.1021/acsbiomaterials.8b00691
8. Gudapati H, Dey M, Ozbolat I, 2016, A Comprehensive Review on Droplet-based Bioprinting: Past, Present and Future [J]. *Biomaterials*, 102:20–42. https://doi.org/10.1016/j.biomaterials.2016.06.012
9. Ng WL, Lee JM, Yeong WY, *et al*., 2017, Microvalve-based Bioprinting Process, Bio-inks and Applications [J]. *Biomater Sci*, 5(4):632–47. https://doi.org/10.1039/c6bm00861e
10. Koch L, Brandt O, Deiwick A, *et al*. 2017, Laser-assisted Bioprinting at Different Wavelengths and Pulse Durations with a Metal Dynamic Release Layer: A Parametric Study [J]. *Int J Bioprint*, 3(1):42–53. https://doi.org/10.18063/ijb.2017.01.001
11. Onses MS, Sutanto E, Ferreira PM, *et al*., 2015, Mechanisms, Capabilities, and Applications of High-Resolution Electrohydrodynamic Jet Printing [J]. *Small*, 11(34):4237–66. https://doi.org/10.1002/smll.201500593

12. Ng WL, Lee JM, Zhou M, *et al*., 2020, Vat Polymerization-based Bioprinting Process, Materials, Applications and Regulatory Challenges [J]. *Biofabrication*, 12(2):022001. https://doi.org/10.1088/1758-5090/ab6034
13. Li W, Mille LS, Robledo JA, *et al*., 2020, Recent Advances in Formulating and Processing Biomaterial Inks for Vat Polymerization-Based 3D Printing [J]. *Adv Healthc Mater*, 9(15):2000156. https://doi.org/10.1002/adhm.202000156
14. Quan H, Zhang T, Xu H, *et al*., 2020, Photo-curing 3D Printing Technique and its Challenges [J]. *Bioact Mater*, 5(1):110–5.
15. Jun I, Han HS, Edwards JR, *et al*., 2018, Electrospun Fibrous Scaffolds for Tissue Engineering: Viewpoints on Architecture and Fabrication [J]. *Int J Mol Sci*, 19(3):745. https://doi.org/10.3390/ijms19030745
16. Liashenko I, Rosell-Llompart J, Cabot A, 2020, Ultrafast 3D Printing with Submicrometer Features Using Electrostatic Jet Deflection [J]. Nat Commun 11(1):753. https://doi.org/10.1038/s41467-020-14557-w
17. Wang C, Meng G, Zhang L, *et al*., 2012, Physical Properties and Biocompatibility of a Core-sheath Structure Composite Scaffold for Bone Tissue Engineering *In Vitro* [J]. *J Biomed Biotechnol*, 2012:579141
18. Kolesky DB, Homan KA, Skylar-Scott MA, *et al*., 2016, Three-dimensional Bioprinting of thick Vascularized Tissues [J]. *Proc Natl Acad Sci U S A*, 113(12):3179–84. https://doi.org/10.1073/pnas.1521342113
19. Skylar-Scott MA, Uzel SG, Nam LL, *et al*., 2019, Biomanufacturing of Organ-specific Tissues with High Cellular Density and Embedded Vascular Channels [J]. *Sci Adv*, 5(9):eaaw2459. https://doi.org/10.1126/sciadv.aaw2459
20. Wang W, Junior JR, Nalesso PR, *et al*., 2019, Engineered 3D Printed Poly(ε-caprolactone)/Graphene Scaffolds for Bone Tissue Engineering [J]. *Mater Sci Eng C*, 100:759–70. https://doi.org/10.1016/j.msec.2019.03.047
21. Chen YW, Shen YF, Ho CC, *et al*., 2018, Osteogenic and Angiogenic Potentials of the Cell-laden Hydrogel/Mussel-inspired Calcium Silicate Complex Hierarchical Porous Scaffold Fabricated by 3D Bioprinting [J]. *Mater Sci Eng C*, 91:679–87. https://doi.org/10.1016/j.msec.2018.06.005
22. Mekhileri NV, Lim KS, Brown GC, *et al*., 2018, Automated 3D Bioassembly of Micro-tissues for Biofabrication of Hybrid Tissue Engineered Constructs [J]. *Biofabrication*, 10(2):024103. https://doi.org/10.1088/1758-5090/aa9ef1
23. Gao Q, He Y, Fu JZ, *et al*., 2015, Coaxial Nozzle-assisted 3D Bioprinting with Built-in Microchannels for Nutrients Delivery [J]. *Biomaterials*, 61:203–15. https://doi.org/10.1016/j.biomaterials.2015.05.031
24. Andrique L, Recher G, Alessandri K, *et al*., 2019, A Model of Guided Cell Self-organization for Rapid and Spontaneous Formation of Functional Vessels [J]. *Sci Adv*, 5(6):eaau6562. https://doi.org/10.1126/sciadv.aau6562
25. Jia WT, Gungor-Ozkerim PS, Zhang YS, *et al*., 2016, Direct 3D Bioprinting of Perfusable Vascular Constructs Using a Blend Bioink [J]. *Biomaterials*, 106:58–68. https://doi.org/10.1016/j.biomaterials.2016.07.038
26. Millik SC, Dostie AM, Karis DG, *et al*., 2019, 3D Printed Coaxial Nozzles for the Extrusion of Hydrogel Tubes Toward Modeling Vascular Endothelium [J]. *Biofabrication*, 11(4):045009. https://doi.org/10.1088/1758-5090/ab2b4d
27. Narayanan LK, Huebner P, Fisher MB, *et al*., 2016, 3D-Bioprinting of Polylactic Acid (PLA) Nanofiber-Alginate Hydrogel Bioink Containing Human Adipose-Derived Stem Cells [J]. *ACS Biomater Sci Eng*, 2(10):1732–42. https://doi.org/10.1021/acsbiomaterials.6b00196
28. Tabriz AG, Hermida MA, Leslie NR, *et al*., 2015, Three-dimensional Bioprinting of Complex Cell Laden Alginate Hydrogel Structures [J]. *Biofabrication*, 7(4):045012. https://doi.org/10.1088/1758-5090/7/4/045012
29. Lozano R, Stevens L, Thompson BC, *et al*., 2015, 3D Printing of Layered Brain-like Structures Using Peptide Modified Gellan Gum Substrates [J]. *Biomaterials*, 67:264–73. https://doi.org/10.1016/j.biomaterials.2015.07.022
30. Wang X, Li X, Dai X, *et al*., 2018, Coaxial Extrusion Bioprinted Shell-core Hydrogel Microfibers Mimic Glioma Microenvironment and Enhance the Drug Resistance of Cancer Cells [J]. *Colloids Surf B Biointerfaces*, 171:291–9. https://doi.org/10.1016/j.colsurfb.2018.07.042
31. Abel SB, Ballarin FM, Abraham GA, 2020, Combination of Electrospinning with other Techniques for the Fabrication of 3D Polymeric and Composite Nanofibrous Scaffolds with Improved Cellular Interactions [J]. *Nanotechnology*, 31(17):172002. https://doi.org/10.1088/1361-6528/ab6ab4
32. Lee SJ, Heo DN, Park JS, *et al*., 2015, Characterization and Preparation of Bio-tubular Scaffolds for Fabricating Artificial Vascular Grafts by Combining Electrospinning and a 3D Printing System [J]. *Phys Chem Chem Phys*, 17(5):2996–9 https://doi.org/10.1039/c4cp04801f

33. Akentjew TL, Terraza C, Suazo C, *et al*., 2019, Rapid Fabrication of Reinforced and Cell-laden Vascular Grafts Structurally Inspired by Human Coronary Arteries [J]. *Nat Commun*, 10(1):3098. https://doi.org/10.1038/s41467-019-11446-9
34. Jungst T, Pennings I, Schmitz M, *et al*., 2019, Heterotypic Scaffold Design Orchestrates Primary Cell Organization and Phenotypes in Cocultured Small Diameter Vascular Grafts [J]. *Adv Funct Mater*, 29(43):1905987. https://doi.org/10.1002/adfm.201905987
35. Wang K, Zheng W, Pan Y, *et al*., 2016, Three-Layered PCL Grafts Promoted Vascular Regeneration in a Rabbit Carotid Artery Model [J]. *Macromol Biosci*, 16(4):608–18. https://doi.org/10.1002/mabi.201500355
36. Liu Y, Xiang K, Chen H, *et al*., 2015, Composite Vascular Repair Grafts via Micro-imprinting and Electrospinning [J]. *AIP Adv*, 5(4):041318. https://doi.org/10.1063/1.4906571
37. Wu P, Wang L, Li W, *et al*., 2020, Construction of Vascular Graft with Circumferentially Oriented Microchannels for Improving Artery Regeneration [J]. *Biomaterials*, 242:119922. https://doi.org/10.1016/j.biomaterials.2020.119922
38. Lee SJ, Kim ME, Nah H, *et al*., 2019, Vascular Endothelial Growth Factor Immobilized on Mussel-inspired Three-dimensional Bilayered Scaffold for Artificial Vascular Graft Application: *In Vitro* and *In Vivo* Evaluations [J]. *J Colloid Interface Sci*, 537:333–44. https://doi.org/10.1016/j.jcis.2018.11.039
39. Chen X, Ergun A, Gevgilili H, *et al*., 2013, Shell-core bi-layered Scaffolds for Engineering of Vascularized Osteon-like Structures [J]. *Biomaterials*, 34:8203–12. https://doi.org/10.1016/j.biomaterials.2013.07.035
40. Costa PF, Vaquette C, Zhang Q, *et al*., 2014, Advanced Tissue Engineering Scaffold Design for Regeneration of the Complex Hierarchical Periodontal Structure [J]. *J Clin Periodontol*, 41(3):283–94. https://doi.org/10.1111/jcpe.12214
41. Vaquette C, Fan W, Xiao Y, *et al*., 2012, A Biphasic Scaffold Design Combined with Cell Sheet Technology for Simultaneous Regeneration of Alveolar Bone/Periodontal Ligament Complex [J]. *Biomaterials*, 33(22):5560–73. https://doi.org/10.1016/j.biomaterials.2012.04.038
42. Kumar PT, Hashimi S, Saifzadeh S, *et al*., 2018, Additively Manufactured Biphasic Construct Loaded with BMP-2 for Vertical Bone Regeneration: A Pilot Study in Rabbit [J]. *Mater Sci Eng C*, 92:554–64. https://doi.org/10.1016/j.msec.2018.06.071
43. De Ruijter M, Ribeiro A, Dokter I, *et al*., 2019, Simultaneous Micropatterning of Fibrous Meshes and Bioinks for the Fabrication of Living Tissue Constructs [J]. *Adv Healthc Mater*, 8(7):1800418. https://doi.org/10.1002/adhm.201800418
44. Rajzer I, Kurowska A, Jabłoński A, *et al*., 2018, Layered Gelatin/PLLA Scaffolds Fabricated by Electrospinning and 3D Printing for Nasal Cartilages and Subchondral Bone Reconstruction [J]. *Mater Des*, 155:297–306. https://doi.org/10.1016/j.matdes.2018.06.012
45. Diloksumpan P, De Ruijter M, Castilho M, *et al*., 2020, Combining Multi-scale 3D Printing Technologies to Engineer Reinforced Hydrogel-ceramic Interfaces [J]. *Biofabrication*, 12(2):025014. https://doi.org/10.1088/1758-5090/ab69d9
46. Park JA, Lee HR, Park SY, *et al*., 2020, Self-Organization of Fibroblast-Laden 3D Collagen Microstructures from Inkjet-Printed Cell Patterns [J]. *Adv Biosyst*, 4(5):1900280. https://doi.org/10.1002/adbi.201900280
47. Kérourédan O, Bourget JM, Rémy M, *et al*., 2019, Micropatterning of Endothelial Cells to Create a Capillary-like Network with Defined Architecture by Laser-assisted Bioprinting [J]. *J Mater Sci Mater Med*, 30(2):28. https://doi.org/10.1007/s10856-019-6230-1
48. Kérourédan O, Hakobyan D, Rémy M, *et al*., 2019, *In Situ* Prevascularization Designed by Laser-assisted Bioprinting: Effect on Bone Regeneration [J]. *Biofabrication*, 11(4):045002. https://doi.org/10.1088/1758-5090/ab2620
49. Chen H, Liu Y, Hu Q, 2015, A Novel Bioactive Membrane by Cell Electrospinning [J]. *Exp Cell Res*, 338(2):261–6.
50. Redd MA, Zeinstra N, Qin W, *et al*., 2019, Patterned Human Microvascular Grafts Enable Rapid Vascularization and Increase Perfusion in Infarcted Rat Hearts [J]. *Nat Commun*, 10(1):584. https://doi.org/10.1038/s41467-019-08388-7
51. Clyne AM, Swaminathan S, Lantada AD, 2019, Biofabrication Strategies for Creating Microvascular Complexity [J]. *Biofabrication*, 11(3):032001. https://doi.org/10.1088/1758-5090/ab0621
52. Chandra P, Atala A, 2019, Engineering Blood Vessels and Vascularized Tissues: Technology Trends and Potential Clinical Applications [J]. *Clin Sci*, 133(9):1115–35. https://doi.org/10.1042/cs20180155
53. Rouwkema J, Khademhosseini A, 2016, Vascularization and Angiogenesis in Tissue Engineering: Beyond Creating Static

Networks [J]. *Trends Biotechnol*, 34(9):733–45. https://doi.org/10.1016/j.tibtech.2016.03.002

54. Kinstlinger IS, Miller JS, 2016, 3D-printed Fluidic Networks as Vasculature for Engineered Tissue [J]. *Lab Chip*, 16(11):2025–43. https://doi.org/10.1039/c6lc00193a
55. Miri AK, Khalilpour A, Cecen B, *et al*., 2019, Multiscale Bioprinting of Vascularized Models [J]. *Biomaterials*, 198:204–16. https://doi.org/10.1016/j.biomaterials.2018.08.006
56. Sharma D, Ross D, Wang G, *et al*., 2019, Upgrading Prevascularization in Tissue Engineering: A Review of Strategies for Promoting Highly Organized Microvascular Network Formation [J]. *Acta Biomater*, 95:112–30. https://doi.org/10.1016/j.actbio.2019.03.016
57. Daly AC, Pitacco P, Nulty J, *et al*., 2018, 3D Printed Microchannel Networks to Direct Vascularisation during Endochondral Bone Repair [J]. *Biomaterials*, 162:34–46. https://doi.org/10.1016/j.biomaterials.2018.01.057
58. Pimentel CR, Ko SK, Caviglia C, *et al*., 2018, Three-dimensional Fabrication of Thick and Densely Populated Soft Constructs with Complex and Actively Perfused Channel Network [J]. *Acta Biomater*, 65:174–84. https://doi.org/10.1016/j.actbio.2017.10.047
59. Negrini NC, Bonnetier M, Giatsidis G, *et al*., 2019, Tissue-mimicking Gelatin Scaffolds by Alginate Sacrificial Templates for Adipose Tissue Engineering [J]. *Acta Biomater*, 87:61–75. https://doi.org/10.1016/j.actbio.2019.01.018
60. Ji S, Almeida E, Guvendiren M, 2019, 3D Bioprinting of Complex Channels within Cell-laden Hydrogels [J]. *Acta Biomater*, 95:214–24. https://doi.org/10.1016/j.actbio.2019.02.038
61. Ouyang L, Armstrong JP, Chen Q, *et al*., 2020, Void-Free 3D Bioprinting for *In Situ* Endothelialization and Microfluidic Perfusion [J]. *Adv Funct Mater*, 30(1):1908349. https://doi.org/10.1002/adfm.201908349
62. Kim BS, Gao G, Kim JY, *et al*., 2019, 3D Cell Printing of Perfusable Vascularized Human Skin Equivalent Composed of Epidermis, Dermis, and Hypodermis for Better Structural Recapitulation of Native Skin [J] Adv. Healthcare Mater, 8(7):1801019. https://doi.org/10.1002/adhm.201801019
63. Kang HW, Lee SJ, Ko IK, *et al*., 2016, A 3D Bioprinting System to Produce Human-scale Tissue Constructs with Structural Integrity [J]. *Nat Biotechnol*, 34(3):312–9. https://doi.org/10.1038/nbt.3413
64. Noor N, Shapira A, Edri R, *et al*., 2019, 3D Printing of Personalized Thick and Perfusable Cardiac Patches and Hearts [J]. *Adv Sci*, 6(11):1900344. https://doi.org/10.1002/advs.201900344
65. Yang Y, Chen Z, Song X, *et al*., 2017, Biomimetic Anisotropic Reinforcement Architectures by Electrically Assisted Nanocomposite 3D Printing [J]. *Adv Mater*, 29(11):1605750. https://doi.org/10.1002/adma.201605750
66. Chansoria P, Shirwaiker R, 2019, Characterizing the Process Physics of Ultrasound-Assisted Bioprinting [J]. *Sci Rep*, 9(1):13889. https://doi.org/10.1038/s41598-019-50449-w
67. Kirillova A, Maxson R, Stoychev G, *et al*., 2017, 4D Biofabrication Using Shape-Morphing Hydrogels [J]. *Adv Mater*, 29(46):1703443. https://doi.org/10.1002/adma.201703443
68. Kokkinis D, Schaffner M, Studart AR, 2015, Multimaterial Magnetically Assisted 3D Printing of Composite Materials [J]. *Nat Commun*, 6(1):8643. https://doi.org/10.1038/ncomms9643
69. Kim Y, Yuk H, Zhao R, *et al*., 2018, Printing Ferromagnetic Domains for Untethered Fast-transforming Soft Materials [J]. *Nature*, 558(7709):274–9. https://doi.org/10.1038/s41586-018-0185-0
70. Shim JH, Lee JS, Kim JY, *et al*., 2012, Bioprinting of a Mechanically Enhanced Three-dimensional Dual Cell-laden Construct for Osteochondral Tissue Engineering Using a Multi-head Tissue/organ Building System [J]. *J Micromech Microeng*, 22(8):085014. https://doi.org/10.1088/0960-1317/22/8/085014
71. Marga F, Jakab K, Khatiwala C, *et al*., 2012, Toward Engineering Functional Organ Modules by Additive Manufacturing [J]. *Biofabrication*, 4(2):022001. https://doi.org/10.1088/1758-5082/4/2/022001
72. Whatley BR, Kuo J, Shuai C, *et al*., 2011, Fabrication of a Biomimetic Elastic Intervertebral Disk Scaffold Using Additive Manufacturing [J]. *Biofabrication*, 3(1):015004. https://doi.org/10.1088/1758-5082/3/1/015004
73. Chen Z, Li D, Lu B, *et al*., 2004, Fabrication of Artificial Bioactive Bone Using Rapid Prototyping [J]. *Rapid Prototyp J*, 10(5):327–33. https://doi.org/10.1108/13552540410562368
74. Liu L, Xiong Z, Yan Y, *et al*., 2007, Porous Morphology, Porosity, Mechanical Properties of Poly(α-hydroxy acid)-Tricalcium Phosphate Composite Scaffolds Fabricated by Low-temperature Deposition [J]. *J Biomed Mater Res Part A*, 82A(3):618–29.

https://doi.org/10.1002/jbm.a.31177

75. Liu TK, Pang Y, Zhou ZZ, *et al*., 2019, An Integrated Cell Printing System for the Construction of Heterogeneous Tissue Models [J]. *Acta Biomater*, 95:245–57. https://doi.org/10.1016/j.actbio.2019.05.052
76. Xie C, Gao Q, Wang P, *et al*., 2019, Structure-induced Cell Growth by 3D Printing of Heterogeneous Scaffolds with Ultrafine Fibers [J]. *Mater Des*, 181:108092. https://doi.org/10.1016/j.matdes.2019.108092
77. Liu D, 2012, Multiphysics Coupling Analysis and Experiment of Low-temperature Deposition Manufacturing and Electrospinning for Multi-scale Tissue Engineering Scaffold [J]. *J Mech Eng*, 48(15):137–43. https://doi.org/10.3901/jme.2012.15.137
78. Dali L, Jun G, Shuhui F, *et al*., 2012, On-line Monitor System for Nanoscale Fiber Manufacturing Based on Multi-featured Pattern Recognition [J]. *Opt Precis Eng*, 20(2):360–8. https://doi.org/10.37h88/OPE.20122002.0360
79. Liu Y. 2014, CAD/CAM System and Experimental Study of Biological 3D Printing Composite Process. *J Mech Eng*, 50(15):147. https://doi.org/10.3901/jme.2014.15.147

REVIEW ARTICLE

# 3D Printing Technologies in Metallic Implants: A Thematic Review on the Techniques and Procedures

**Shokouh Attarilar[1,2], Mahmoud Ebrahimi[3], Faramarz Djavanroodi[4,5], Yuanfei Fu[6], Liqiang Wang[2]*, Junlin Yang[1]***

[1]Department of Pediatric Orthopaedics, Xinhua Hospital Affiliated to Shanghai Jiao Tong University, School of Medicine, Shanghai, China
[2]State Key Laboratory of Metal Matrix Composites, School of Material Science and Engineering, Shanghai Jiao Tong University, Shanghai, China
[3]National Engineering Research Center of Light Alloy Net Forming, School of Materials Science and Engineering, Shanghai Jiao Tong University, Shanghai, China
[4]Department of Mechanical Engineering, College of Engineering, Prince Mohammad Bin Fahd University, Al Khobar, KSA
[5]Department of Mechanical Engineering, Imperial College London, London, UK
[6]Ninth People's Hospital, School of Medicine, Shanghai Jiao Tong University, Shanghai 200011, China

**Abstract:** Additive manufacturing (AM) is among the most attractive methods to produce implants, the processes are very swift and it can be precisely controlled to meet patient's requirement since they can be produced in exact shape, dimension, and even texture of different living tissues. Until now, lots of methods have emerged and used in this field with diverse characteristics. This review aims to comprehensively discuss 3D printing (3DP) technologies to manufacture metallic implants, especially on techniques and procedures. Various technologies based on their main properties are categorized, the effecting parameters are introduced, and the history of AM technology is briefly analyzed. Subsequently, the utilization of these AM-manufactured components in medicine along with their effectual variables is discussed, and special attention is paid on to the production of porous scaffolds, taking pore size, density, etc., into consideration. Finally, 3DP of the popular metallic systems in medical applications such as titanium, Ti6Al4V, cobalt-chromium alloys, and shape memory alloys are studied. In general, AM manufactured implants need to comply with important requirements such as biocompatibility, suitable mechanical properties (strength and elastic modulus), surface conditions, custom-built designs, fast production, etc. This review aims to introduce the AM technologies in implant applications and find new ways to design more sophisticated methods and compatible implants that mimic the desired tissue functions.

**Keywords:** Additive manufacturing; 3D printing techniques; Biometals; Implants; Porous scaffolds

***Correspondence to:** Liqiang Wang, State Key Laboratory of Metal Matrix Composites, School of Material Science and Engineering, Shanghai Jiao Tong University, Shanghai, China; wang_liqiang@sjtu.edu.cn. Junlin Yang, Department of Pediatric Orthopaedics, Xinhua Hospital Affiliated to Shanghai Jiao Tong University, School of Medicine, Shanghai, China; yjunlin@126.com

**Received:** August 28, 2020; **Accepted:** October 16, 2020; **Published Online:** December 9, 2020

**Citation:** Attarilar S, Ebrahimi M, Djavanroodi F, *et al*., 2021, 3D Printing Technologies in Metallic Implants: A Thematic Review on the Techniques and Procedures. *Int J Bioprint,* 7(1): 306. http://doi.org/10.18063/ijb.v7i1.306

## 1. Introduction

As the world's elderly population grows, the need for medical implants is rapidly growing. It is expected that the number of people aged 65 or above will increase to about 20% of the world population by 2050[1]. These elderly patients and other patients with bone fracture and failures need special cares, specifically those associated with rapid healing time, fast preparation of implants, and custom-built implants that are tailored to patients' fracture conditions. Furthermore, avoiding possible subsidiary issues arise from low-quality designs, stress-shielding effects, and infections. The traditionally manufactured implants have a lot of limitations, such as a time-consuming production process, low capability in

producing complex shapes, and difficulty to manufacture the custom-built designs. Hence, advance procedures are highly required to meet various demands from patients and healthcare market.

Three-dimensional printing (3DP) is an evolutionary technology and a branch of additive manufacturing (AM) methods that cover a range of applications in modern industries, including manufacturing of computer components, electricity, machinery, and digital control devices[2]. According to the AM principles and the use of special 3D bioprinters, human organs can be artificially produced[3] in the future, and the realization of this goal will be accompanied by a revolution in the healthcare system. These 3DP techniques have great potentials in producing porous and complex-shaped materials and components with very intricate internal structures. Therefore, 3DP technology enables fabrication of hierarchical materials with porous structure and mechanical properties (strength and elastic Young's modulus) very similar to natural bone and inhibits stress-shield effect in bone implants[4-6]. Moreover, 3DP technologies have some other advantages, including the ability in mass production, economic efficiency, low cost, repeatability, and shorter time to market[2]. In addition, 3D technology together with computer-aided design (CAD) technique[7] can be used in the production of completely patient-specific implants[8,9]. 3DP method developed rapidly and a variety of new techniques with many advantages were devised to cure the previous limitations. The first description about 3DP dates back to 1981 when Dr. Hideo Kodama fabricated a device that uses ultraviolet (UV) lights to harden polymers and create solid objects[10]. Although it was not commercialized, it was the first step to the conception of stereolithography (SLA) technique in 1983. Later, Charles Hull invented the first SLA machine[11]. In 1987, a selective laser sintering (SLS) process was patented, and the first commercial rapid prototyping printer entitled SLA-1 was sold 1 year later. Subsequently, fused deposition modeling (FDM) and laser AM (LAM) were introduced. Following the introduction of newly developed 3D printing techniques, Israeli scientists made a successful achievement in the fabrication of an entire heart with human cells in 2019[12], **Figure 1** schematically represents the 3DP history.

The 3DP process is performed sequentially based on the following steps: First, using the digital design software (SolidWorks, AutoCAD, Autodesk, etc.), 3D digital scanners, or other applications, the digital virtual version of the desired object is generated. Then, the 3D digital model is transformed into SLA or standard tessellation language (.STL) file format. The .STL file involves numerous triangulated facets that demonstrate the exact spatial coordinates (xyz) information of 3D model surfaces. A large

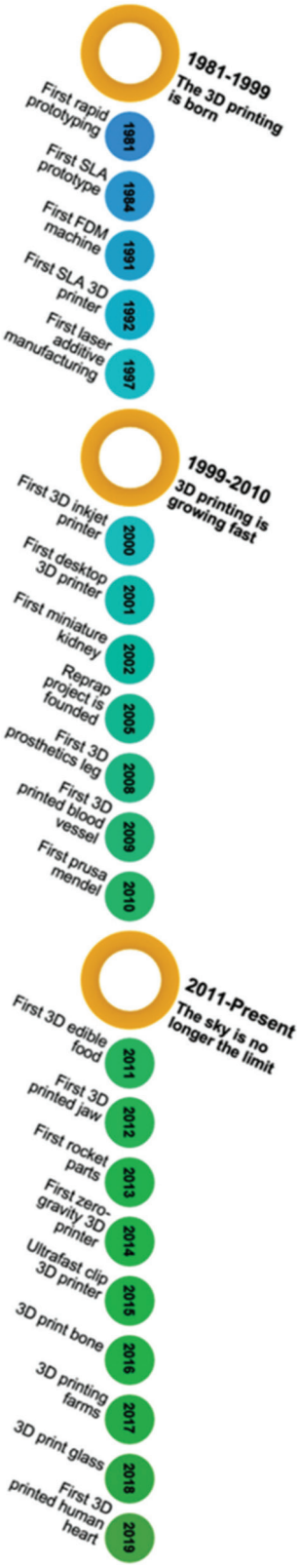


**Figure 1.** Timeline of 3D printing technologies.

number of triangles means more data points and higher resolutions. Third, by utilizing particular slicer software in

the 3D printer machine, the .STL file is converted into G file through slicing the designed model into 2D horizontal cross-section arrays in a size range of 25 – 100 μm. Then, the first layer of the 3D object is formed by the x-y movement of the printer head. Finally, the rest of the object was created through the incessant movement of the printer head in the z-direction; hence, the desired morphology can be deposited layer by layer on the first basal sheet as a substrate[13]. However, this printing procedure is highly dependent on the 3DP machine. The general production procedure is represented schematically in **Figure 2**.

3DP can utilize various types of materials such as ABS plastic, PLA, polyamide (nylon), glass filled polyamide, SLA materials (epoxy resins), silver, titanium, steel, wax, photopolymers and polycarbonate, cells, hydrogels, etc. Among these materials, metallic materials are of great importance in the biomedical field. The metallic materials used in AM technology must adhere to two crucial requirements: First, they must have good weldability to prevent crack formation during solidification; second, the raw metallic material should be prepared in the form of spherical powder with a size of tens micrometers range to satisfy the acceptable packing density and homogeneity requirements of the AM manufactured part. About 50 metallic alloys can be used in AM manufacturing, and they are mostly Ti-, Ni-, Al-, and Cu-based alloys, tool steels, stainless steels, Co-Cr alloys, and some precious and refractory metals[14]. More than 80% of all used implants in medicine are metallic ones and they are categorized into two different groups: Bio-degradable and non-degradable metallic implants[1]. Biodegradable metals include iron, magnesium, zinc, and calcium. Considering the excellent advantages of 3DP, this technology will have a great impact and an increase of its applications, especially in the biomedical field, is expected in near future. Therefore, a comprehensive understanding of the recent methods and techniques opens up a new horizon for optimum design and fabrication of more advanced materials for implant applications. This thematic review provides some insights into the realization of this purpose.

## 2. 3DP process techniques

ASTM Committees grouped different types of AM into seven main categories based depending on the material addition method and working procedure (**Figure 3**). In fact, each of these seven main methods has its pros and cons according to the main objective of fabricating a 3D printed specimen. A right method is essential and it is generally selected according to the following parameters: Material type (plastic, metal alloys, ceramics, sand, and wax), material state (liquid, powder, wire, etc.), material compatibility, and its availability, consolidation type (polymerizing, laser melting or sintering, fusing, UV curing, etc.), desired feature size, resolution, throughput, and speed[13]. In biomedical 3DP extrusion[15], thermal inkjet and laser-assisted techniques are commonly used. The most common techniques for metal 3DP are powder bed fusion or melting methods, among which the selective laser melting (SLM) and electron beam melting (EBM) are very popular and they are the most widely used 3DP methods in the world. Direct energy deposition uses metal feedstock and a laser to fabricate parts. Vat photopolymerization selectively cures a vat of liquid photopolymer through targeted light-activated polymerization to produce 3D printed components. All the various methods are well-classified and represented in **Figure 3** and the detailed information about each of the methods is included in following sections.

### 2.1. Vat photopolymerization

SLA is the first patented and commercialized AM process which uses a vat photopolymerization technique, and the 3D objects are generated in this process by selectively curing a vat of liquid photopolymer through targeted light-activated polymerization. The SLA, digital light processing (DLP), continuous, direct light processing

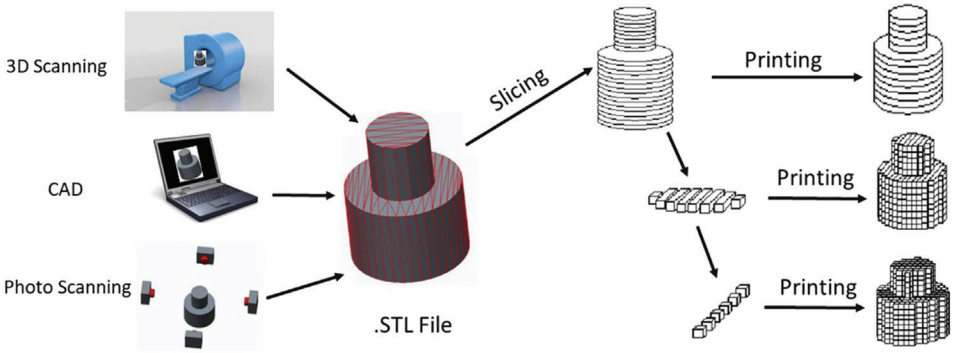


**Figure 2.** Schematic representation of the 3D printing process (Reprinted from 3D *Printing Technology* in *Nanomedicine*, 1st edition, Ashish, Ahmad N, Gopinath P, *et al*, 3D *Printing* in Medicine: Current Challenges and Potential Applications, pp 1-22, Copyright (2019), with permission from Elsevier)[13].

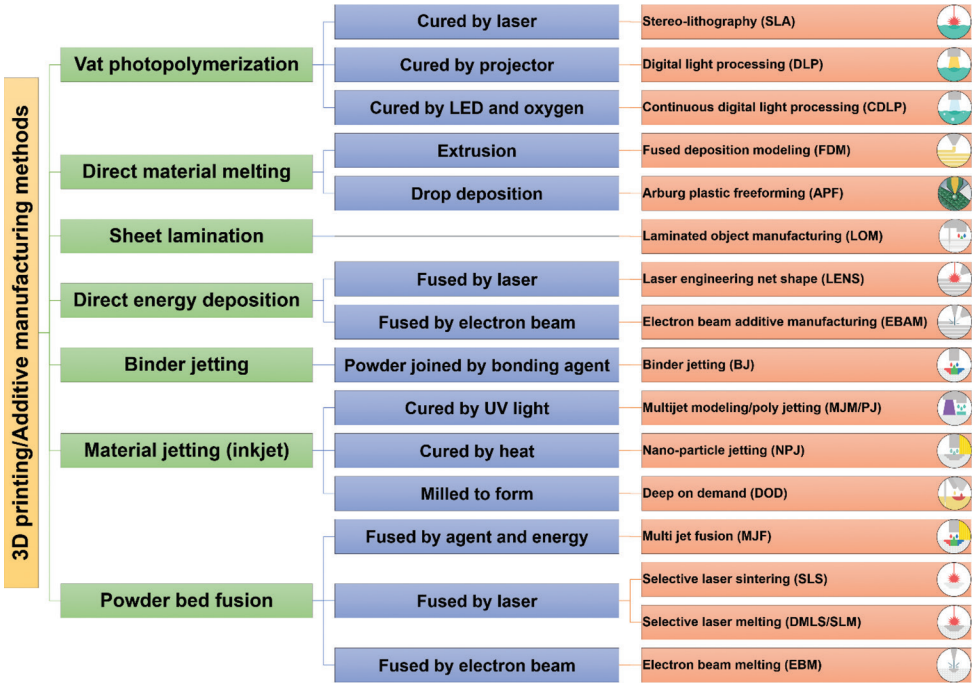


**Figure 3.** An overview of the most important additive manufacturing technologies.

(CDLP), and bio-plotters use vat photopolymerization technology[13]. In the photopolymerization technology, the primarily used materials are liquid, radiation-curable resins, or photopolymers such as polyimides, elastomers, pure polymer resin, composite resins, supramolecular polymers, graphene, and ceramic slurry + resins. Mostly, UV wavelength and some light systems can be used for radiation of photopolymers. Radiation on photopolymer materials leads to a chemical reaction, known as photopolymerization, that solidifies the materials. Photopolymers were first used in 1960s and later applied in glossy coatings of papers and cardboards, dentistry, etc. In the middle of the 1980s, Charles Hull fabricated a 3D solid part by laser scanning over a UV-curable material and cured one layer over a previous layer, representing the very first step toward SLA technology[16]. In this regard, **Figure 4** shows a schematic of the SLA vat-based method. Vat-based AM methods have numerous advantages, including excellent print resolution, good surface finishing, high efficiency, versatility, and superior printing accuracy.

In SLA technique, the production process starts with the deposition of photopolymer material as a first layer on the build platform by utilizing a recoating mechanism. The desired pattern produced by a UV laser raster on the resin surface and leads to the cross-linking of the liquid photopolymer into solid form. The subsequent layers are built by recoating a new layer and its patterning with a UV beam. The controlling parameters in this technique are scanning speed, exposure time, laser power, material composition, and photoinitiator[17]. Three different

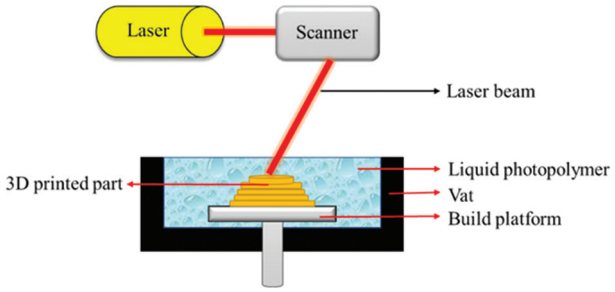


**Figure 4.** A schematic diagram of the stereolithography vat-based technique.

mechanisms are used in vat-based photopolymerization methods, including vector scan SL, mask projection, and two-photon approach (**Figure 5**). Among different influencing parameters, laser wavelength has a key role in regulating laser power. Each laser type uses a specific wavelength; for example, in the SLA-250 device, a helium-cadmium (He-Cd) laser type with 325 nm wavelength is used; other SLA devices from 3D Systems have Nd-YVO4 lasers with 1062 nm wavelengths (near-infrared); a high power titanium-sapphire laser with 790 nm wavelength is used in a 2p-VP two-photon vat-based device[16].

Another popular vat-based method is mask-projection vat photopolymerization (MPVP), also known as DLP, that can achieve resolutions in the range of 30 μm. In DLP method instead of laser beam utilization in the two-photon and vector scan systems, a large radiation beam is patterned by the utilization of another device such as Digital Micromirror Device™ (DMD) a large radiation

beam is patterned by the utilization of another device such as Digital Micromirror Device™. In the two-photon approach, the photopolymerization process is implemented at the intersecting point of two laser beams[16].

## 2.2. Powder-bed fusion

In powder-bed 3DP techniques, a thermal source is utilized to selectively melt or fuse the substances (wax, metal, nylon, polymer, plastic, ceramic, composite) which are held in a tray and the melt or fused materials are then sequentially printed in a layer-by-layer manner. Several examples of the printing methods following the power-bed 3D printing include EBM, SLS, polymer laser sintering, direct metal laser sintering and SLM[18].

The basic of laser powder-bed fusion is shown in **Figure 6A**. A laser beam scans the target location of the powder bed with specified speed and energy to convert the powder fusion into solid form, under full melting SLS (SLM) or partial melting SLS condition. According to the defined layer thickness, the powder bed is lowered, and the fresh layer of powder is prepared after the completion of previous layers. This method was repeated several times to complete the fabrication[19,20].

### *(1) SLM method*

Being one of the most popular prototyping methods, the SLM method uses high power-density laser to fuse metal or metallic alloy powders to produce AlSi10Mg parts[22], martensitic high strength steel[23], and Al–Scalloy[24]. The production of 3D part by SLM involves a series of steps from digital design data preparation to the removal of the completed part from the building platform. First, to generate the slice data of each layer for laser scanning, SLA (STL) files must be produced by software such as Materialise Magics. Then, the CAD data are uploaded to the SLM machine. The building procedure starts with laying the first thin layer of metal powder on a tray. Soon after the powder is laid, a laser beam with a high energy-

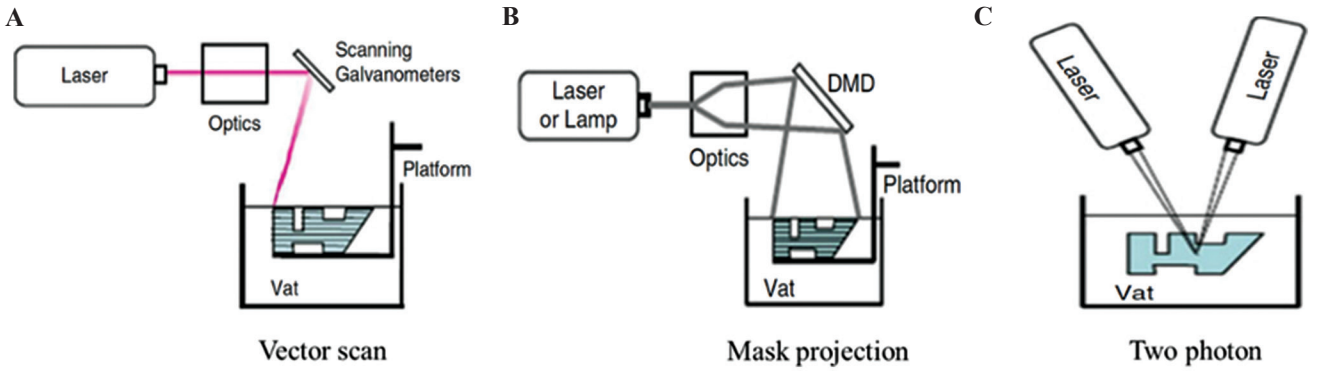


**Figure 5.** Various photopolymerization mechanisms in vat-based methods. (A) Vector scan SL. (B) Mask projection. (C) Two-photon approaches.

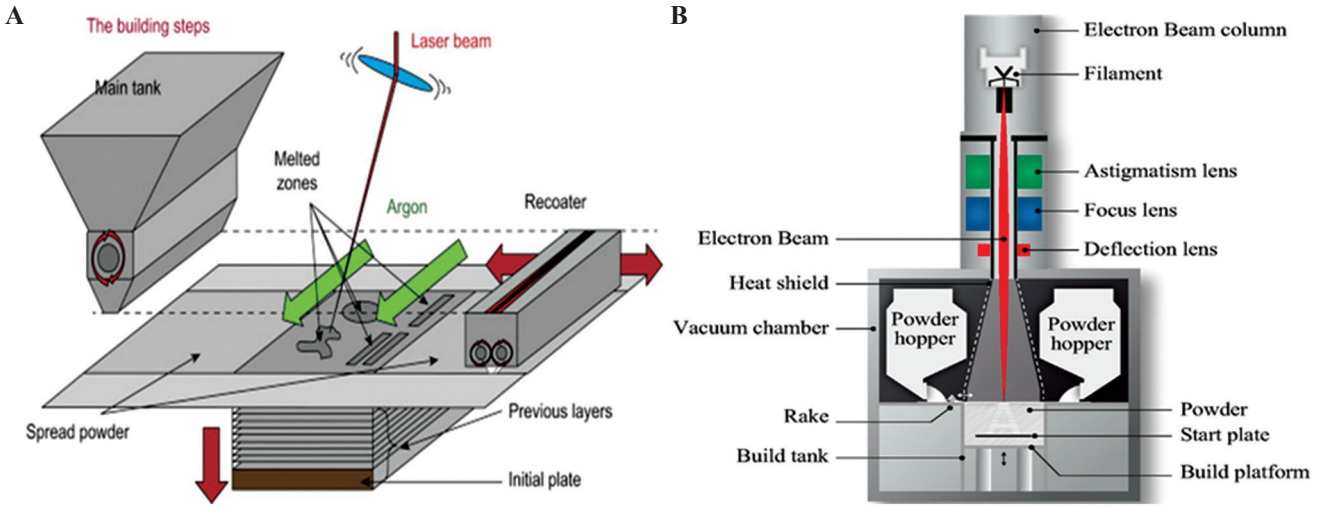


**Figure 6.** (A) Schematic presentation of the laser-based powder-bed fusion process. (B) Main components of an electron beam melting technique (Reprinted from *Additive Manufacturing*, Volume 19, Galati M and Luliano L, A literature review of powder-based electron beam melting focusing on numerical simulations, pp 1-20, Copyright (2018), with permission from Elsevier)[21].

density beam is utilized to melt and fuse the preferred regions according to CAD data. After the completion of the first layer, the building platform is lowered, and the subsequent layer of powder is deposited on the previous layer before the laser beam begins to scan a new layer. This procedure is repeated several times until the entire 3D part is fabricated. The completed 3D part is then removed from the platform manually or by electrical discharge machining (EDM) and the loose powders removed from the surface[25]. **Figure 7** shows the schematic presentation of the processing steps in the SLM technique.

The key process variables of the SLM technique, such as scanning speed, laser power, hatch spacing, and layer thickness, must be accurately regulated. Furthermore, some important physical aspects should be considered, including thermal fluctuation in the material that will lead to crack initiation and failure, the balling issue that intervenes in continuous melt formation, and the absorptivity of material toward laser irradiation[25].

### *(2) EBM method*

The EBM method, as one of the layer-by-layer techniques, is among the most used AM techniques. It can be used to produce high-quality metal and metallic alloys parts[27-29] and the near net shape metallic samples with complex geometries[30]. In this method, the structures are made by selective melting of discrete powder layers through electron-beam gun under the vacuum condition. The melting process is engendered by the energy emission from the electron beam of a tungsten filament which consists of two magnetic coils for controlling the beam position and diameter and the adjustment of focusing and defocusing conditions[31]; **Figure 6B** demonstrates a schematic presentation of the EMB device. Furthermore, **Figure 8** represents the EBM chamber (**Figure 8A**) and the EBM process steps (**Figure 8B**). In the EBM technique, each slice is categorized in two distinct regions named contours and squares. First, the contour region which acts as an interface between the part and the surrounding powders is produced. Then, the square parts of the inner region of these boundary and contour zones are fabricated by EBM. Performing the EBM process in the vacuum condition prevents impurity and contamination that leads to the formation of high-quality parts with good mechanical properties[32,33]. After the complete fabrication of a 3D printed object, the part is kept inside the chamber for cooling. Then, excess powders are removed from the part, and because of the relatively rough surface of the EBM parts[34,35], they are subject to final surface treatments through milling, turning, polishing, and grinding devices[36].

## 2.3. Binder jetting

The binder jetting-based techniques, also known as the direct 3DP, use the inkjet printing system. Specifically, the printer head in this system not only moves in the x-y plane as the conventional state but also runs in the

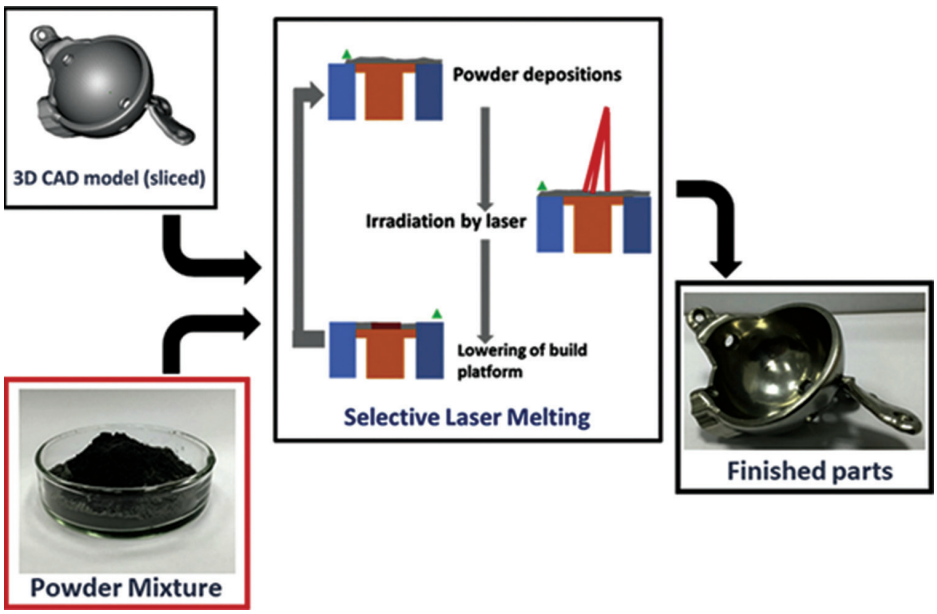


**Figure 7.** Schematic representation of the processing steps in the selective laser melting (Reprinted from International Journal of Refractory Metals and Hard Materials, Volume 77, Sing SL, Wiria F E and Yeong WY, Selective laser melting of titanium alloy with 50 wt% tantalum: Effect of laser process parameters on part quality, pp 120-127, Copyright (2018), with permission from Elsevier)[26]. The powder mixture is added into chamber and then the laser scanned and fused the powders according to the sliced computer-aided design data. Subsequently, the cycle of powder deposition, laser irradiation, and lowering the tray is repeated until the entire 3D part is produced.

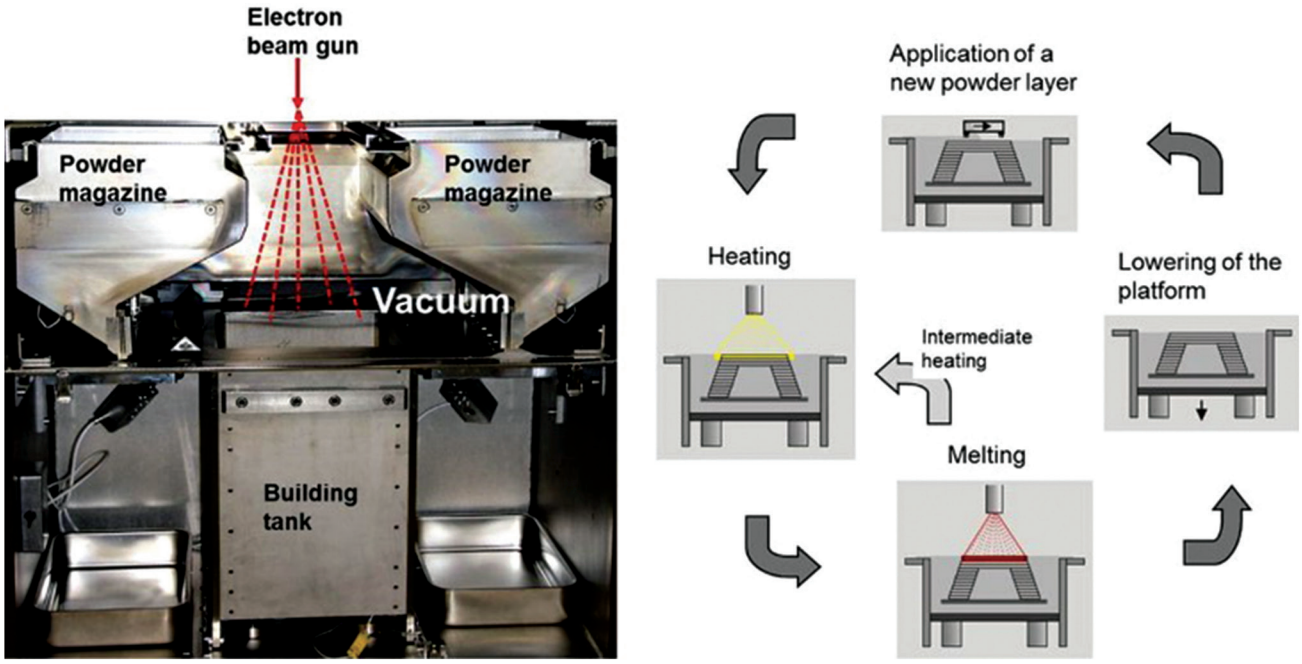


**Figure 8.** Selective electron beam melting technique. (A) Process chamber. (B) Four-step cyclic process for building layer-by-layer final 3D part[37]

z-direction using the height-adjustable platform. This type of movement in the coordinate system is suitable for simultaneous printing of the objects in all directions[38]. This system is similar to that of the powder-bed fusion, in which a substance layer is deposited over the bed and then leveled with the roller. Then, the multichannel print head, according to the coordinate system and parameters of the CAD file, dispenses the droplets of binder material onto the powder bed before the ultimate binding of powder particles. After finishing the first layer, the device piston lowered the powder bed and the deposition of the next layer began[39]. **Figure 9** shows the schematic presentation of binder jetting technology in 3DP.

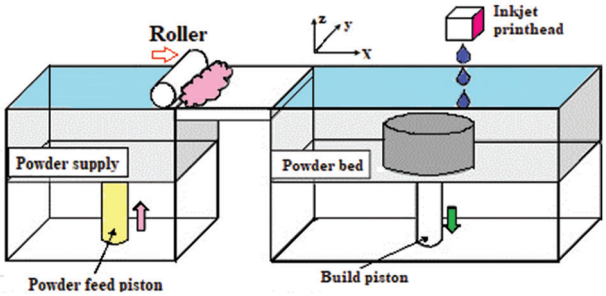


**Figure 9.** The binder jetting technology (Reprinted from *Additive Manufacturing*, Zhang Y, Jarosinski W, Jung YG, *et al*, Additive manufacturing processes and equipment, pp. 39 –51, Copyright (2018), with permission from Elsevier)[40].

## 2.4. Material jetting

Material jetting or multijet modeling (MJM) is one of the photopolymer-based injecting systems which build the whole 3D object layer-by-layer through multiple nozzles. The chemical basis that is similar with vat photopolymerization is also utilized in material jetting technique, but the liquid material is not kept inside the vat container. Furthermore, similar to the inkjet printing technology, the printer head of this method distributes the polymeric substance over the substrate which is subsequently cured with UV light. Afterward, the finished layer of the object is gradually lowered to let the upper layers to be built[41]. Along with the photopolymeric substance, some kind of jelly or wax material was added to support the printing procedure[42]. The impressive characteristic of these MJM methods is their ability to simultaneously deliver up to fourteen types of materials; therefore, this kind of method can build a 3D object with multiple properties such as various colors, hard and soft type of plastics for different regions of an object, and different morphological and elastomeric conditions[43]. **Figure 10** represents the schematic illustration of this method.

## 2.5. Material extrusion

Material extrusion method utilizes special heating nozzles and pneumatic or mechanical facilities and through them the collected 3D printing material in the chamber is dispensed. These extrusion-based methods are favorites of both industrial manufacturers and researchers since they are easy to use and economical. This method can

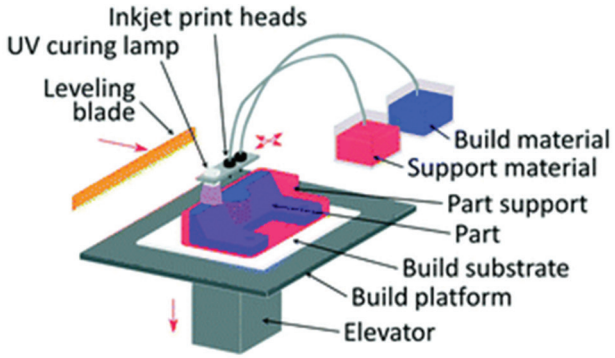


**Figure 10.** Schematic illustration of material jetting or multijet modelling (Reproduced by permission of The Royal Society of Chemistry)[44].

be used in two distinctive ways along with material melting (precise extrusion deposition[45], precise extrusion manufacturing[46], multiphase jet solidification[47], and fused deposition modeling[48]) and without material melting (direct-write assembly[49], solvent-based extrusion free-forming[50], 3D bioplotting, robocasting[51], pressure-assisted microsyringe[52], and low temperature deposition manufacturing)[53]. FDM is the most well-known among these versatile material extrusion techniques. In FDM, the material (usually a thermoplastic or composite) is extruded by special nozzle systems which consist of, for instance, heated and digitally controllable nozzles that can move in all three directions. After the heating or melting procedure, the material or substance that flows through the nozzle equipped with a temperature control system will rapidly solidify upon its first contact with the air. After the deposition of the first layer, the stage is lowered to continue and complete the layer-by-layer formation of the 3D object[39,44].

## 2.6. Sheet lamination

The 3DP methods, similar to laminated object manufacturing (LOM), are categorized in sheet lamination group. This type of method fabricates a 3D object that involves a layer-by-layer lamination of a sheet material such as metal, plastic, and paper. Initially, the sheet material which is coated with an adhesive substance is located on the stage; subsequently, the sheet is traced using a beam of laser or a razor, and its cross-section is cut based on the 3D CAD model[54,55]. Second, the excess material that is not needed anymore is removed by the laser. Following this procedure, the stage is lowered to deposit the next layers on the previous ones. Finally, these steps are repeated until a 3D object is made. **Figure 11** shows the schematic illustration of the LOM process. The LOM-fabricated objects have several benefits compared to other AM-produced objects, including (i) higher resistance to deformation and distortions due to their low internal tensions, (ii) lower

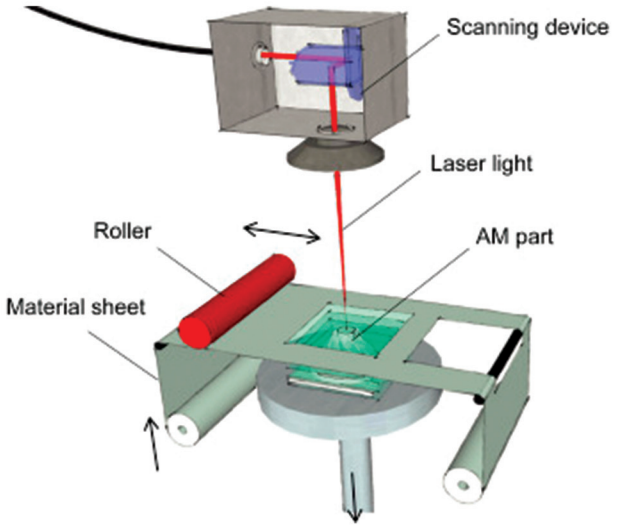


**Figure 11.** Schematic representation of laminated object manufacturing (Reprinted from Laser Additive Manufacturing, Hagedorn Y, *Laser additive manufacturing* of ceramic components: Materials, processes and mechanisms, pp. 163-180, Copyright (2017), with permission from Elsevier)[57].

production price, (iii) lower fragility or higher durability, (iv) a wide range of materials with versatile mechanical and chemical properties can be used in LOM, and (v) no post-processing is required. Unfortunately, the z-direction accuracy of LOM products is low.

## 2.7. Directed energy deposition (DED)

In DED methods, a focused energy source like laser and electron beam and plasma arc is utilized to melt the material, and the melted substance is deposited in the wire or in powder form through a nozzle. This method uses both features of material extrusion and power bed fusion AM processes. Unlike DED, the powder-bed fusion method melts the material during the deposition procedure[57]. In DED technique, the nozzle head can shift in multiple directions and around the fixed object according to the 3D CAD model. The high-energy beam is directed to the desired location to melt the material which immediately solidifies on the platform[58]. After the deposition of the initial layer, both nozzle and energy source shift upward to enable the deposition of the next layers on the previous ones, and this procedure is continued and repeated until the final 3D object is fabricated. The DED-based technique includes electron beam direct manufacturing, direct metal deposition (DMD), direct laser deposition, directed light fabrication, and laser engineered net shaping (LENS)[58]. These methods have the same processing steps but do not use the same energy source (type, power, and resolution), motion-control and powder delivery system, etc. **Figure 12** shows a schematic of the laser powder DED process.

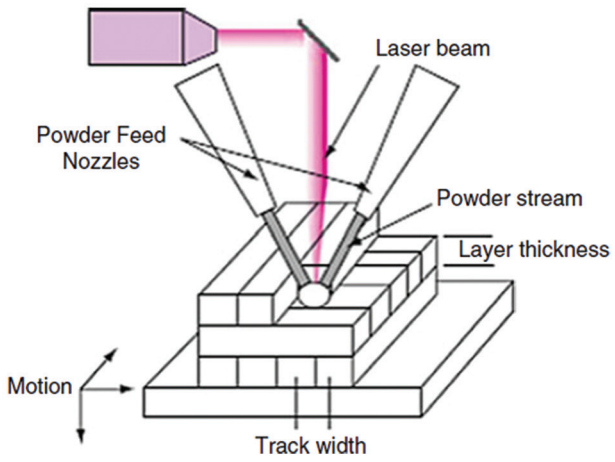


**Figure 12.** Schematic presentation of simple laser powder directed energy deposition technique (Reprinted from *Additive Manufacturing Technologies*, Directed energy deposition processes, 2015, pp. 245-168, Gibson I, Rosen D and Stucker B (original copyright notice as given in the publication in which the material was originally published) "With permission of Springer"[59].

## 3. AM in bioimplant applications

Until 2019, roughly 13% of annual 3DP revenues come directly from the medical industry. Medical experts can make use of AM technology to design patient-specific devices at an affordable cost. There are several reasons for the growing utilization of AM products in medicine: (i) Complex patient-specific implants and other specimens can be created by AM without any additional costs; (ii) 3D printed parts can be designed with high resolution (even nanometric ranges) to fit perfectly with a patient's anatomy; (iii) it is very easy to conduct sterilization during production and post-production stages on 3D printed samples; (iv) being a high-speed technology, AM can produce the implants at a rapid rate, thereby delivering therapies quickly; and (v) the flexible nature of AM technology significantly reduces the cost of custom medical devices. Considering these benefits, AM is utilized in many medical aspects, ranging from hearing aids, artificial limbs, surgical implants, bones, and blood cells to synthesized human organs[60]. Common applications of AM manufactured for biomedical applications are listed in **Table 1**[61].

### 3.1. Influencing parameters in biological response of 3D printed metals

#### *(1) Pore size*

In 3D printed metallic parts, two types of pores can be found; the first one is inter-particle pores and the second one is pre-designed pores. These pores can be arranged in an interconnected or non-interconnected manner that allows the formation of open or close porosity. Inter-particle pores are usually produced due to insufficient melting of metal powders, and afterward incomplete bonding but the fabrication of these inter-particle pores is totally undesirable. On the other hand, the pre-designed pores are in a regular arrangement and are particularly used for triggering osteoinduction, reduction of elastic modulus, and weight of implant[79-82]. The word "pore" in this review refers to the pre-designed version.

Pore size is among the crucial parameters which control the osteogenesis, migration of various cells, and supplement of nutrients and thus, the optimal pore size should be used in implant applications[83,84]. The favorable pore size for cell seeding should be in the range from 100 to 400 μm. It was reported that above this size range, cell seeding would become extremely difficult, the increased cell sizes are suitable for nutrients, waste, and blood transfer[85]. Cheng *et al*. produced porous Ti6Al4V constructs with different porosity and pore sizes through laser sintering and discussed the effects of 177-μm, 383-μm, and 653-μm pore sizes on biological behavior[86]. By increasing the pore size, the level of osteocalcin was increased and the alkaline phosphatase activity was reduced since it is more beneficial to maturation rather than proliferation. Another study confirmed that 500-μm pore sizes are better than 700- and 1000-μm ones from the osteogenic activity aspect since it seems that the optimum pore size range is about 300 – 600 μm[87].

It has been demonstrated that the heterogeneous pore size designs are very beneficial both from the mechanical property and biomedical reaction points of view[85,88]. The upgraded heterogenous gyroid structures with both coarse and fine pore sizes were produced by EBM through the control of cell wall spacing and the contribution of patterned extrude cuts onto the gyroid walls; hence, a dual bio-structural functionalization was achieved. Nutrient transportation can be improved by the smooth curvature of the gyroid walls. Moreover, the introduction of the micro-pores led to efficient bone cell seeding. This design has acceptable values of Young's modulus and compressive strength that are similar to those of the natural human bone[88]. In addition, Wang *et al*. produced a FEM-optimized heterogeneous porous lattice structure mimicking the human bone mechanical properties[85]. The produced structure includes a combination of micro-scaled pores for nutrients transfer and milli-scaled pores for cell seeding. The obtained results show the successful anisotropic design with mechanical properties similar to those of the human bone with the compressive strengths between 169 and 250 MPa, Young's modulus of 14 and 25 GPa, and densities of about 1.57 and 1.85 g/cm$^3$.

#### *(2) Porosity*

Porosity simply shows the volume percentage of voids in a solid material which is measured in comparison

**Table 1.** Various AM technologies in medical applications and their advantages and disadvantages reproduced (Reprinted from 3D and 4D Printing of *Polymer Nanocomposite Materials,* Sinha SK, Additive manufacturing (AM) of medical devices and scaffolds for tissue engineering based on 3D and 4D printing, pp 119-160, Copyright (2020), with permission from Elsevier)[61]

| Technique | Pros | Cons | References |
|---|---|---|---|
| Vat photopolymerization and Selective laser sintering | • High resolution<br>• Enhanced mechanical property<br>• Able to print high-density cells<br>• Suitable for many photocurable polymers<br>• The raw material base is a fluid<br>• Complex structure formation through power bed<br>• Biomaterial deposition in the solid or liquid phase<br>• Able to use ceramic materials | • Shrinkage and heat effects<br>• Material limitation<br>• Require a UV source<br>• Toxicity due to near UV blue light<br>• Cell damage<br>• Limitations in multicomponent cells<br>• Thermal damage during the procedure | [62-68] |
| Stereolithography | • Great resolution and fast production<br>• Independency of printing time to complexity<br>• Nozzle-free technique | • Common for photopolymers<br>• UV blue light is toxic to cells<br>• Multicell printing is not possible | [69] |
| Powder fusion printing (PFP) | • High range of materials (metals, polymers, etc.)<br>• Excellent mechanical strength<br>• Complex geometries<br>• Powder recycling | • Microfractures and voids<br>• Crack generation<br>• Hard to produce horizontal gradients<br>• Need post processing<br>• High power usage<br>• Thermal distortion | [61,63] |
| Extrusion printing | • High simplicity<br>• Excellent controlling<br>• Capability to print both physical and compositional gradients<br>• Capability to print cells and bioactive factors<br>• Able to print polymers, metals, and ceramic parts | • Low speed<br>• Only applicable for viscous liquids<br>• Should control the material usage and other factors<br>• Require binder/polymer removal at high temperature followed by sintering | [66,70,71] |
| Directed energy deposition | • The raw material platform is solid polymers<br>• High resolution<br>• No need to powder bed<br>• Able to easily print multi-material structures along with compositional gradient | • Expensive procedure<br>• Possibility of thermal damages<br>• Poor part resolution and tolerances | [64-67,72] |
| Sheet lamination | • Speed, low cost, ease of material handling<br>• Formation of layered laminate structure<br>• Possibility to print hydroxyapatite, zirconia, various cells | • Just for layered laminates<br>• Post-processing is needed<br>• The strength and integrity of models are reliant on the adhesive used<br>• May require post-processing<br>• Limited material use | [64-67,73] |
| Indirect 3D printing | • Suitable for prototyping/preproduction<br>• Applicable for various materials | • Low resolution<br>• Time-consuming<br>• Requirement for dedicated waxes for biocompatibility and molds for casting | [74] |
| Inkjet printing | • Applicable for wide range of biomaterials<br>• Without any need to support structural complexities<br>• High-speed<br>• Coprinting the multiple solution compositions<br>• It can simultaneously print bioactive composites<br>• Materials with low viscosity can be printed | • Toxic nature<br>• Compared to SLS, low mechanical strength<br>• Expensive setup<br>• Low applicable material range<br>• Continuous procedures are not possible<br>• Low cell density<br>• Clogging of the head issues | [74,75] |

(*Contd...*)

**Table 1.** (*Continued*)

| Technique | Pros | Cons | References |
|---|---|---|---|
| Direct ink writing (DIW) | • Easy to use with hydrogels<br>• Simple nature<br>• Possibility to use multiple inks<br>• Cost-effectiveness<br>• Environmental friendliness | • It is not a good choice for complex parts and processes<br>• Crucial to carefully control the thickening and thinning agents in bio-ink<br>• Hard to attain the desired microstructure<br>• Hard to extrude liquids | [76,77] |
| Fused deposition modeling (FDM) | • Lower toxicity compared to 3D printing with photopolymers<br>• Cheap procedure | • Need to use additional support structure<br>• Need to do post-processing<br>• Low resolution | [78] |
| Bioplotting | • Possibility to print viable cells<br>• Suitable for soft tissue | • Limited size ranges for nozzle<br>• Need to use additional support structure | [74] |
| Laser-assisted bioprinting (LAB) | • Excellent precision printing<br>• Single-cell patterns<br>• It can use various bioactive materials<br>• It can print different solutions at a time<br>• Easy automation<br>• High throughput | • Expensive<br>• Scaffolds have limited heights | [74,77] |

with materials without any pores. This parameter can be influenced by pore size, strut thickness, and pore shape. It is believed that higher porosities lead to better growth of osteon cells, increase the surface area which causes more cellular interactions, and provide proper interface-locking in laser-processed porous titanium[89]. Moreover, it has been shown that pore shape can affect osteogenic differentiation[90]. The improved osteogenic differentiation was observed on scaffolds with high porosities compared to low-density ones[91]. In fact, the porosity of human trabecular bone is within in the range of 70 – 90%, so this range seems to be suitable for a 3D printed implant. In a previous study by Cheng *et al*., different porosities (70%, 37.9%, and 15%) were designed in EBM-produced Ti6Al4V samples, and the sample with the highest porosity has a higher potential for stimulating osteoblast differentiation than the other samples[92]. Other studies also confirmed this observation and asserted that implants with porosities similar to human bone's (70 – 90%) had the best bone ingrowth and greatly improved cell viability, but there would be some differences about the results of other biological responses toward porosity, like cell proliferation and differentiation[87,93].

### *(3) Interconnectivity of pores*

The interconnectivity of pores determines whether the pores are connected or isolated. Formation of tissues in the interconnective structures can be progressively continued from the openings up to the central regions while dead ends due to isolated pore structures impede the growth of the cells and cause poor cellular interactions, such as differentiation, osteogenesis, and angiogenesis. Higher values of the influencing factors, such as detour indexes and pore throats, can sometimes lead to suppression of the proper bone ingrowth and tissue formation[94].

It is difficult to obtain the desired pore size and shape, porosity, and interconnection at the microscale level with traditional ways and evaluate their possible biological effects. However, it is rather simple to obtain well-designed and regular pore structures through AM technology. The CAD-based models can be utilized to predesign and produce any kind of porous structure using 3DP technologies. Two porous structures can be used: The honeycomb-like structure is a CAD-based structure with a diamond lattice, in which each atom is enveloped by four neighboring atoms[95,96], while the cubic structure is formed by scanning powder layers with the use of electron beams in constant intervals and parallel manner, and in every eighth layer, the scanning direction is rotated 90°[97].

### *(4) Lattice structure topologies*

Many studies have focused on improving the lattice designs, especially on from the aspects of weight reduction and customizability, and various lattice structure topologies have therefore been proposed. In this regard, truss lattices with interconnecting struts in a 3D space are among the well-known class of lightweight parts. They have superior strength, stiffness, and energy

absorption capabilities[98]. The high-quality trusses with complex geometry and fine features can only be made by AM methods, specifically the SLM and EBM techniques. Some of the most popular truss lattices include simple cubic (SC), body-centered cubic (BCC), and face-centered cubic (FCC), as shown in **Figure 13**. These structures are made from the unification of vertical and inclined struts; for example, SC lattice includes vertical struts (and some tension in the horizontal struts) under compression; BCC consists of pure bended-inclined structure and FCC is a mixture of inclined struts with both bending and tension[98].

Structures can be categorized according to their geometrical features as shown in **Figure 13** the well-known truss lattices include: SC, BCC, and FCC. The structure with only some solid edges is called an open cell structure, whereas the structure with both solid edges and faces is known as a closed-cell structure. Foams have random connectivity of unit cells, and lattices have regular or periodic connectivity[99]. In this regard, other possible lattice structures and topologies were shown in **Figure 14** and include (a) Kagome, (b) octet truss, (c) MS1 lattice, (d) pillar textile, (e) square collinear/cubic, (f) re-entrant auxetic, (g) octahedron, (h) honeycomb, (i) square, (j) diamond, (k) triple periodic minimal surfaces (TPMS) P-type, (l) TPMS gyroid, (m) TPMS D-type, and (n) TPMS I-WP type[99]. It was found that topological features can affect the mechanical behavior of the material, and the octet truss design demonstrates superior mechanical properties, in addition to its ability to tolerate higher loads compared with other cellular structures. The main advantage of using cellular structure design is its ability in systematic and adroit utilization of material to reduce unnecessary consumption of material, energy, and time and manufacture lightweight parts with favorable mechanical strength[100]. Furthermore, cellular structures have a potential to show excellent thermal energy absorption and acoustic insulation properties[101]. From the aspects of geometry, porosity, and pores size, TPMS can be used as a topology suitable for manufacturing trabecular bone scaffolds[102].

## 3.2. Metallic scaffold parts in medicine

At present, metallic porous scaffolds are becoming one of the popular material choices in medical applications. One of the most important classes of materials in these applications is titanium (Ti) and its alloys due to its numerous mechanical advantages along with biocompatibility with living tissues[103-105]. Compared to stainless steel and other metallic systems, the medical-grade Ti-based alloys show enhanced performance, especially in bone tissue ingrowth capability since Ti has a 50% higher strength to weight ratio and less Young modulus in comparison to stainless steel[106-108]. Moreover, Ti-based materials are free of any toxic effects[109], and

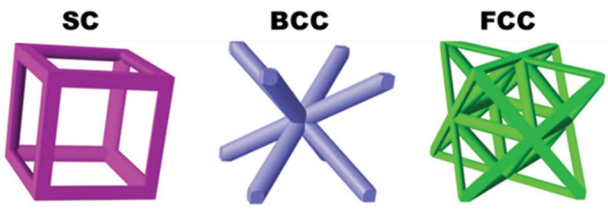


**Figure 13.** The most popular truss lattices: Simple cubic, body-centered cubic, and face-center-cubic (FCC) ((Reprinted from *Composites Part A: Applied Science and Manufacturing*, Volume 135, Li X, Tan YH, Wang P, *et al*, Metallic microlattice and epoxy interpenetrating phase composites: Experimental and simulation studies on superior mechanical properties and their mechanisms, Copyright (2020), with permission from Elsevier)[98].

they have acceptable mechanical properties (strength, elastic modulus, and hardness). In fact, the Young elastic modulus is of great importance in bone applications since a higher elastic modulus can lead to stress-shielding effect that could lead to implant failure; hence, the porous designs are preferred since they have a potential to control the stress-shielding effect[110]. Furthermore, Ti-based alloys exhibit excellent corrosion resistance in simulated body fluids[111,112]. Considering the above-mentioned superior features of Ti-based materials, 3DP of Ti is growing in importance for its application and bound to attract much attention. Recently, a successful case of 3DP of titanium was reported in a cancer patient; a 15-year-old boy received a Ti implant fabricated by the EOS Technology in a process that takes only about 6 weeks, starting from the CAD model designing model to the final implanting[61].

### *(1) Titanium-based porous structures*

Recently, the AM manufactured porous structures attract much attention. Trabecular bone structure is one of the examples that can be designed by 3DP, and the obtained Ti porous structures can improve the bioactivity of implant, enhance cell adhesion, proliferation, and differentiation of osteoblasts[113]. Li *et al*. performed a systematic investigation about different aspects of 3D printed porous Ti-based materials that were produced by the EBM technique[114]. The highly porous and well-interconnected pore architecture shows good mechanical properties with enhancements in biological activity, osteoblast adhesion, cell morphology, proliferation, and alkaline phosphatase (ALP) activity. Moreover, to produce a Ti-based porous structure by the EBM technique, Zhang *et al*. designed a repeating array of titanium alloy unit-cells to mimic trabecular or cancellous bone structure[115]. Toward this end, various kinds of unit cells mimicking the trabecular bone structure with different pore sizes and porosity were produced. The result shows that the capacity of load-bearing is dependent on the porosity; a higher porosity value leads to a reduction of

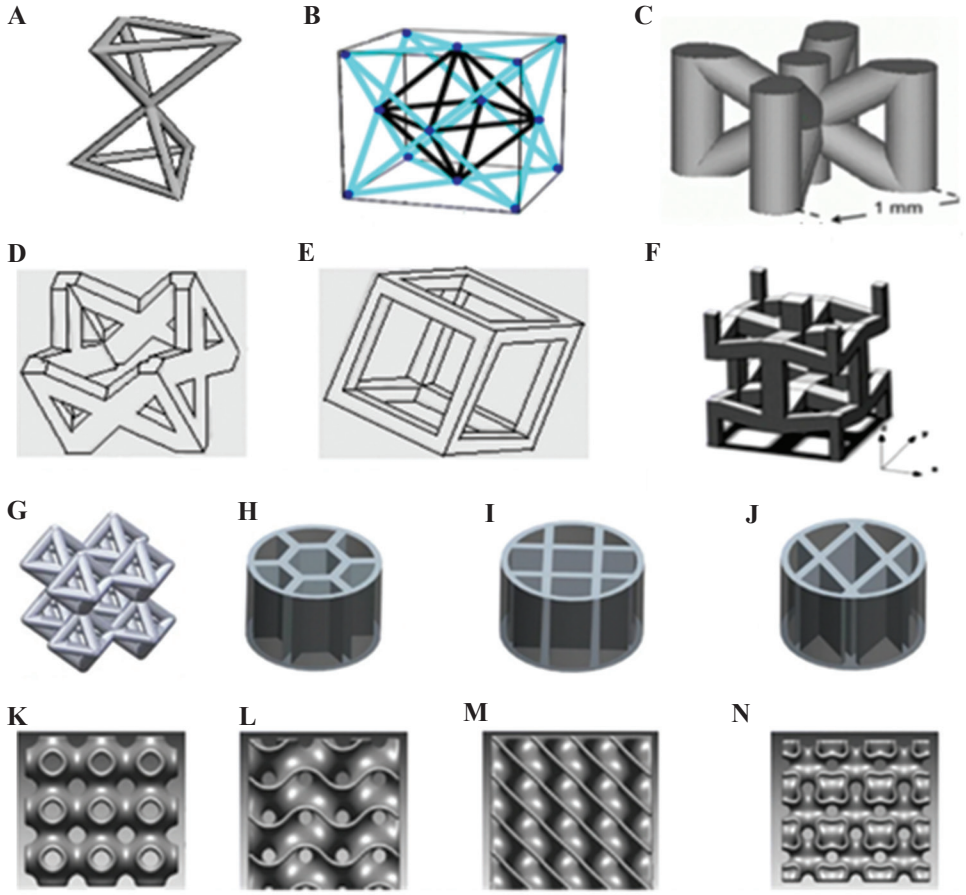


**Figure 14.** Various lattice structure topologies (*International Journal of Advanced Manufacturing Technology*, A state-of-the-art review on types, design, optimization, and additive manufacturing of cellular structures, Volume 104, 2019, pp. 3489–3510, Nazir A, Abate KM, Kumar A, *et al* (original copyright notice as given in the publication in which the material was originally published) "With permission of Springer")[99]. (A) Kagome, (B) octet truss, (C) MS1 lattice, (D) pillar textile, (E) square collinear/cubic, (F) re-entrant auxetic, (G) octahedron, (H) honeycomb, (I) square, (J) diamond, (K) triple periodic minimal surfaces (TPMS) P-type, (L) TPMS gyroid, (M) TPMS D-type, and (N) TPMS I-WP type.

stiffness and load capacity; compared to dense Ti material, the 3D printed porous structure manifested a 96% decrease in elastic modulus and strength values.

AM manufactured porous titanium interbody cages are very useful in spine treatment, and they have desirable levels of biocompatibility that is beneficial for better bone ingrowth and fixation. A comparative *in vivo* study that utilized 3D printed titanium porous implants produced by Stryker on several mature sheep found that bone ingrowth on porous titanium alloy was superior to both PEEK and plasma spray-coated implants and the histomorphometric results showed better osteoblastic deposition on these implants[116]. Furthermore, peri-implant osteogenesis and increased stability were observed in 3D printed titanium samples. The titanium porous materials can be further improved in different strategies. For instance, Song *et al*. capitalized upon the varying macro architectures and surface topological morphology on SLM produced porous titanium for modulation[117]. This dual modulation was initially carried out together with the utilization of a wide range of compressive strengths and subsequently by alkali treatment, heat treatment, and hydroxyapatite coating formation through electrochemical deposition. The *in vitro* results indicated good cytocompatibility, improved osteon cell adhesion, and proliferation, while *in vivo* experiments indicated superior tissue-materials interfaces in dual modulated samples. **Figure 15** shows the fabrication method of dual modulation on 3D printed titanium material.

Coating with biologically beneficial substances is one of the methods for improving AM manufactured porous materials. Bose *et al*.[118] manufactured titanium porous structures with about 25% volume porosity through LENS method, produced $TiO_2$ nanotubes on the structure surface and a coating functionalized by $Sr^{2+}$ and $Si^{4+}$ ions, doped bioactive calcium phosphate (CaP) ceramic in simulated body fluid and implanted the samples in the rat model. These doped CaP-coated 3D printed Ti implants

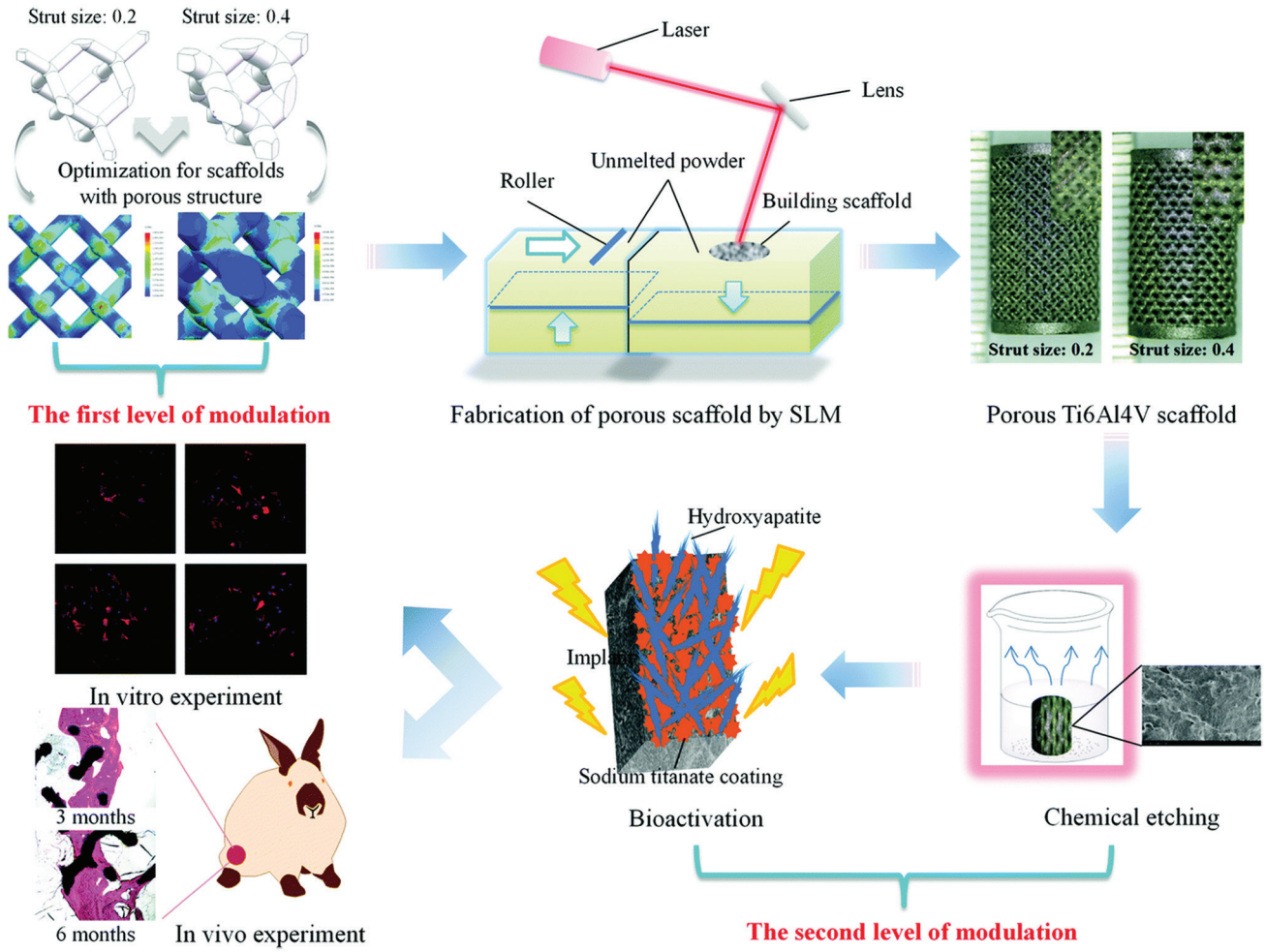


**Figure 15.** Schematic presentation of the dual modulation procedure (Adapted from Ref [117] with permission from The Royal Society of Chemistry).

resulted in early bone tissue integration and proper tissue ingrowth. Furthermore, a good bonding in the interfacial regions between the bone tissue and the implant surface was observed. Moreover, it enhanced new bone formation and accelerated mineralization were seen in the periphery of the implant material. Overall, porous materials have better biological performance than the dense type. Furthermore, CaP plays a crucial role in early bone tissue integration with the implant. **Figure 16** shows a brief explanation about doping and coating procedure.

Among the titanium-based biomaterials, Ti6Al4V is known for its improved mechanical properties relative to the pure Ti. Unfortunately, the toxic effects of Al and V restrict its application in clinical settings. Nevertheless, since the release of Al and V is in low amounts, Ti6Al4V can still be used in medical devices and implants. Many studies have been performed to examine the design parameters, such as porosity and pore size, in relation to this subject. **Table 2** presents a brief review of these studies.

The production of 3D printed titanium porous structure is progressing toward the commercial stage; for instance, U.S. Food and Drug Administration (FDA) has approved the 3D printed titanium implants, which are known as Emerging Implant Technologies (EIT) Cellular Titanium® (**Figure 17**) produced by a German medical device manufacturer, for spinal applications. This new product was designed based on the ideal pore shape and size, with the goal to achieve improved cell proliferation and bone ingrowth conditions. In fact, the EIT cervical cage's anatomical architecture can potentially overcome the surgical and biomechanical issues related to the cervical multi-level fusion by modifying the vertebral endplate contact and sagittal balance restoration[126]. Another example approved by FDA is the MATRIXX® stand-alone cervical system for patients suffering from degenerative disc treatment will be assisted by it. Furthermore, a number of companies that utilize direct metal printing technology, such as IMR, nuVasive, and Stryker, are working on production AM manufactured titanium implants[127].

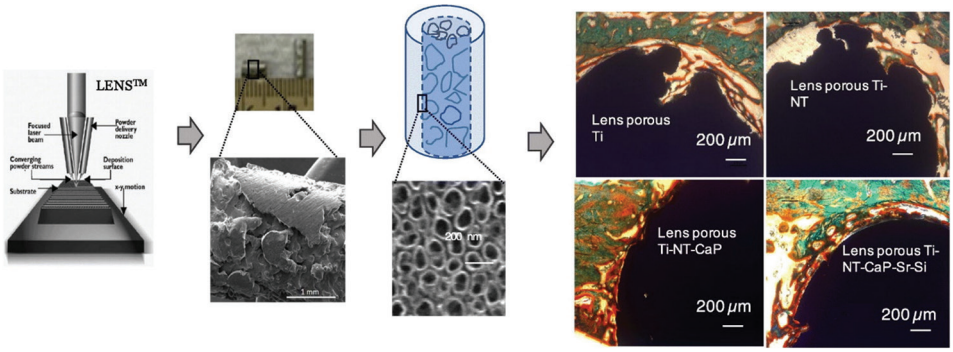


**Figure 16.** Schematic presentation of $Sr^{+2}$ and $Si^{+4}$ doped CaP coating on 3D printed porous titanium with nanoscale surface modification (Reprinted from *Materials & Design*, Volume 151, Bose S, Banerjee D, Shivaram A, *et al*, Calcium phosphate coated 3D printed porous titanium with nanoscale surface modification for orthopedic and dental applications, pp 102-112, Copyright (2018), with permission from Elsevier)[119].

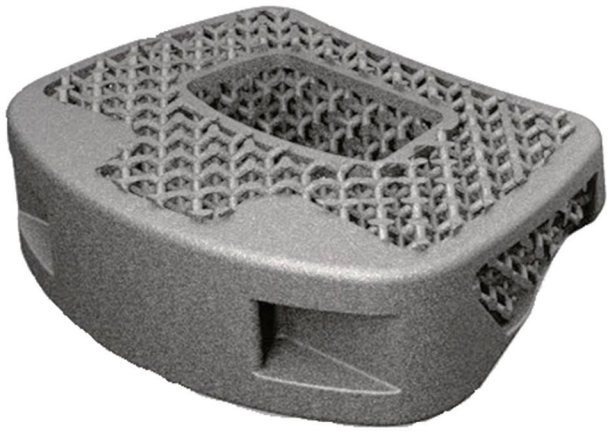

**Figure 17.** Emerging Implant Technologies (EIT) cervical cage or the EIT Cellular Titanium® approved by the U.S. Food and Drug Administration[126].

### *(2) 3D printed cobalt chromium (CoCr) alloys*

In orthopedic surgery, CoCr-based alloys are of significant importance and utilized extensively in high loaded areas. Nonetheless, the stress shielding effect and bone resorption are the major concerns when it comes to applications due to the high stiffness level of CoCr alloys[128]. Smart design and structural modifications can help overcome these issues; one of the best options to reduce the stiffness mismatch in metal-alloy implants' interface and the periphery natural bone tissue is designing the porous structures. In this regard, additively manufactured CoCr alloys have attracted much attention. Shah *et al*. produced a 3D printed CoCr alloy specimen with interconnected open-pore architecture and macro-geometry with EBM technology[129]. The produced samples were implanted in adult sheep femora and the outcomes after 26 weeks revealed that the density of osteocyte was higher in the CoCr sample compared to that in Ti6Al4V, but the total bone-implant contact of Ti6Al4V was higher. Furthermore, the CoCr alloy does not significantly change the mineralized interfacial tissue composition compared to Ti6Al4V alloy. Overall, the results indicated the possibility of bone in growth in the interconnected porous structure of CoCr samples. In a different study, Limmahakhun *et al*. studied the micro-pore structure, biological response, and mechanical properties of CoCr alloy scaffolds that were produced by SLM and reported that the SLM techniques are capable of fabricating the CoCr cellular structures with graded beam thickness and the unit cells with pillar-octahedral shape and human bones share the similar mechanical properties and morphology[130].

### *(3) 3D printed tantalum*

Tantalum is an inert material both in *in vivo* and *in vitro* condition and has low solubility and very low toxicity in its pure and oxide forms. Tantalum behavior in hard tissues is similar to titanium with osteointegration properties. This material has been clinically utilized since 1940 and its applications in implantation and diagnosis are growing[131]. The characteristics of tantalum, which are similar to that of cancellous bone, enable its applications in orthopedic surgeries in the spine and hip, knee arthroplasty, and as bone graft substitutes. Levine *et al*.[132] studied the porous tantalum structure which was produced through carbon vapor deposition/infiltration onto vitreous carbon scaffolding. This open-cell design with continuous dodecahedrons unit cells indicated enhanced volumetric porosity (70 – 80%), low Young's modulus (~3 MPa), and improved frictional properties. Furthermore, it has good biocompatibility and can produce a self-passivating surface oxide layer which is beneficial for biological applications. Therefore, tantalum is an appropriate option for biomedical applications, and 3DP of tantalum would be a good way to further improve its features. In 2017, a Chinese research group performed

**Table 2.** Brief information about the characteristics and outcomes of 3D printed Ti-based porous scaffolds

| AM method | Characteristics | Results | References |
|---|---|---|---|
| SLM |  Diamond lattice pore structure, porosity 66.1 – 79.5%, pore size 0.65 mm, strut diameter 0.2 – 0.4 mm | Dimensional accuracy is dependent on printing parameters, such as laser power, scanning speed, and power layer thickness. The 10% porosity reduction results in a 100-MPa increase in compression strength. New inward bone tissue growth was observed in both cancellous and compact bone within 0.4 mm strut diameter and 66.1% porosity | [4] |
| SLM |  Interconnecting channels with various diameters (500, 700, and 900 μm) | Well-defined pore distribution with proper interconnectivity, the small pores are helpful for cell adhesion, the large pores improve cell proliferation. Pores with about 600-μm size are beneficial for bone ingrowth, maturation, and bone-implant fixation stability | [119] |
| SLM |   Three gradient patterns (cell size, density, heterostructure), gyroid and diamond unit cells with triply periodic minimal surfaces (TPMS) | The TPMS method is suitable for obtaining functional graded structures that mimic natural bone. Gyroid and diamond unit cells possess a suitable strength (152.6 MPa and 145.7 MPa) and comparable elastic modulus (3.8 GPa) with compact bone. The pore size gradient does not lead to considerable density alterations | [120] |
| SLM | 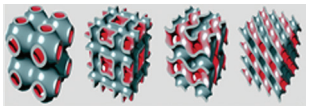 TPMS porous structures, from left to right: primitive, I-WP, gyroid, and diamond | TMPS structures well resembled the topological properties of trabecular bone, high fatigue resistance, and endurance limit as high as 60% of their yield stress. It has comparable morphology and permeability values with trabecular bone. Excellent mechanical properties such as low elastic modulus and high yield strength | [121] |
| SLM | 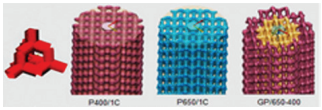 Dense center and graded periphery structure, porosity in the range of 50 – 80% | Other favorable properties are high compressive strength, improvement of bone integration, enhanced cell growth, maximum calcium deposition in 400 um pore size, and better osteointegration. Spider web structures show higher Young's modulus values. Web structures (70% porosity) and diamond unit structures (porosity 50%) share almost similar mechanical properties | [122] |
| EBM | 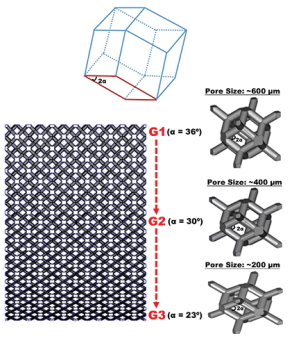  Dodecahedron unit cells with various pore sizes (600, 400, and 200 μm). Porosity 65%, with 500 μm strut sizes | Porous structure minimizes the stress-shielding effect. Other beneficial effects are increased osteoblasts function, cell adhesion, proliferation, proteins' function, and calcium deposition. Smaller pore sizes have better biological performance than larger ones | [123] |

(*Contd...*)

**Table 2.** (*Continued*)

| AM method | Characteristics | Results | References |
|---|---|---|---|
| SLM | 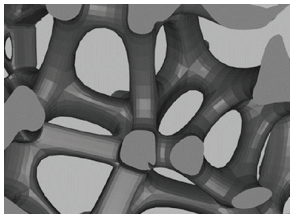 Trabecular like scaffolds based on the Voronoi Tessellation principle with a porosity range of 48.83 – 74.28% and varying irregularities (0.05 – 0.5) | This scaffold has the elastic modulus in the range of 1.93-5.24GPa and an ultimate strength ranging within 44.9- 237.5 MPa, enhanced osteoblasts adhesion and migration, improved cell proliferation, and early osteoblast differentiation | [124] |
| SLM | 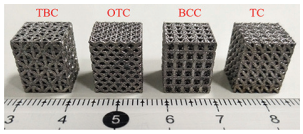  Exterior with octet truss cell (75% porosity and pore size of 1042 μm) and internal structure with tetrahedron cell (80% porosity and pore size of 700 μm) | SLM has high accuracy in printing CAD modeled scaffolds associated with cell proliferation of about 140% which is superior to that of about 90% in other uniform structures. Hence, these porous functional graded structures are a better option for bone implant applications. | [125] |
| EBM | 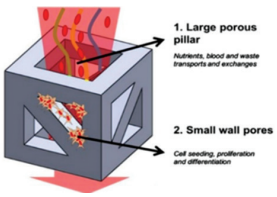  Heterogeneous porous micro lattices with the coarse central porous pillar and fine pores within walls. Nutrients exchange through micro-scaled pores and milli-scaled pores are responsible for cell seeding, porosities up to ~ 60% | The mechanical properties of microlattices are in the range of the same parameters of human cortical bone. In addition, their compressive strengths and Young's modulus are in the range of 169.5 – 250.9 MPa and 14.7 – 25.3 GPa, respectively. The existence of edges to close up the lattice boundaries enhances the mechanical properties. The anisotropic design could improve structural efficiency in a specific loading direction | [85] |
| EBM | 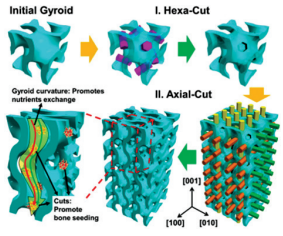  Upgraded gyroid lattices, gyroid wall spacings in millimeter range and additional micrometer-scaled pores on the walls | The wide wall spacing facilitates nutrients transports into the implant, and the micro-pores are responsible for seeding the bone cells. The stress-shield effect is inhibited by maintaining the Young's modulus values between 8 and 15 GPa. The compressive strength was in the range of 150 – 250 MPa. The mechanical properties fall within the natural range of the human bone | [88] |

SLM, selective laser melting; EBM, electron beam melting.

a total knee replacement using the 3D printed tantalum on an 84-year-old man who was able to do some basic movements only a day after the surgery[133]. Despite the challenges in the 3DP of tantalum due to the high melting temperature (~3000°C), the produced samples are still praiseworthy for being very compact and having fewer defects.

### *(4) Shape memory alloys (SMA)*

The shape memory effect is a unique phenomenon in which the deformed material has the ability to recover to its original shape and size when heated in a special characteristic temperature range or as a response to mechanical stresses by a reversible martensitic transformation. This impressive feature bequeaths the

SMA many applications, especially in medical and spine surgeries[134-136]. Moreover, the SMAs also have other stimulating uses in actuators, sensors, the aerospace industry, and even fashion products[137].

One of the most imperative classes of SMAs in medical applications is NiTi alloys. In addition to its very interesting shape memory effect, NiTi has good ductility, outstanding corrosion and wear resistance, and terrific biocompatibility[137]. This section focuses only on NiTi or nitinol since they are the most utilized SMAs. Manufacturing parameters can largely influence the functionality of SMAs, texture, microstructure, surface quality, precipitates, and several defects[138,139]; hence, the production process needs to be precisely controlled. LAM methods, including LSM, are highly utilized in the production of 3D printed SMAs since these methods ensure proper homogeneity, especially in complex and dense structures. Furthermore, these methods are applied in the production of various-shaped SMAs because they can produce graded porous structures accurately. Usually, SLM method and laser metal deposition (LMD) are commonly used in the production of 3D printed SMAs (**Figure 18**). Both methods utilize metal powders and the sample is produced by cross-sectional slicing of the CAD model and layer by layer deposition. In SLM, special regions in a metal powder bed are melted and solidified, while in LMD, several nozzles are used to feed successive layers of powders onto the building substrate on which the powder is melted by laser exposure. Several key parameters that influence the final quality of 3D printed part should be considered while using either one of both methods. These parameters include material condition (powder size, morphology, and composition), machine parameters (laser type, atmosphere), processing variables (laser power, track spacing, scanning rate and pattern, powder layer thickness, and beam spot diameter), and power feed rate in LDM method.

Achieving the highest material density is of high importance in 3DP. In SLM, increasing the density of laser-energy leads to enhancement of component density up to the maximum value. After this peak, density reduction is possible, especially in materials which are vulnerable to oxidation and evaporation materials. This issue is very crucial in NiTi alloys since slight changes in composition can alter the shape memory effect of the material. Powder re-melting can potentially homogenize and eliminate the local compositional variations and enhance the overall SMA effect. Reducing the SLM scan speed and increasing SLM energy density can increment the transformation temperature and leads to a better temperature SMA temperature range[140,141].

NiTi SMA has excellent corrosion and wears resistance along with desirable biocompatibility which is attributed to the formation of the titanium oxide layer on its surface. This layer has a protective nature and even prevents the possible toxic and allergic effects of Ni release; therefore, the thicker $TiO_2$ layers are preferred[142,143]. Laser irradiation can influence the $TiO_2$ formation and thickness which affects its biocompatibility. For instance, Nd-YAG laser irradiation has very beneficial effect on corrosion improvement and prevention of Ni ion release. This Nd-YAG laser irradiation can produce a thick oxide layer inhibiting the corrosion while retaining other properties[144]. Moreover, to enhance the biological response of the material and mesenchymal stem cells, the metal AM fiber lasers (optical fibers that doped with rare-earth elements) can be a good option since they are associated with desirable surface parameters, such as increased roughness and wettability, and improved surface chemistry[145].

A review of research literature shows that 3D printed NiTi alloys are potential candidates for implantation as they act as a good host for living cells and tissues. Habijan *et al*.[146] showed that the surface of SLM-produced porous NiTi scaffolds was entirely covered with live cells with a very insignificant number of dead cells after 8 days of cell culture. Other similar studies on SLM-produced porous

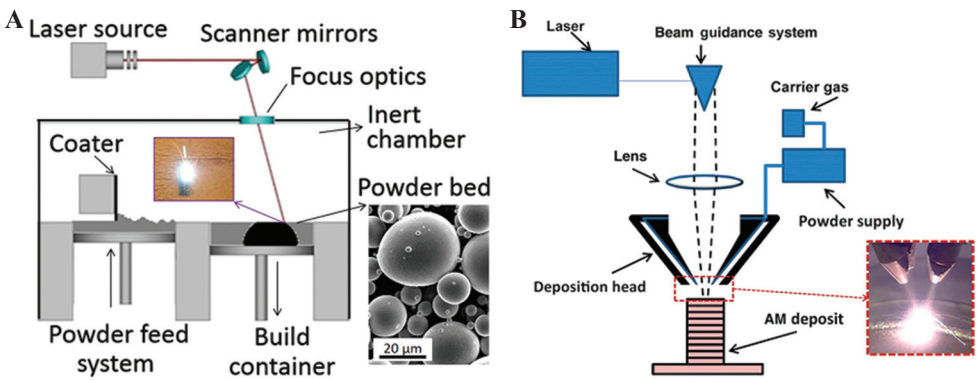


**Figure 18.** Schematic presentation of (A) selective laser melting method with a scanning electron microscope image of powder and (B) laser metal deposition process with a metal deposition condition (Reproduced from Ref. [137] with permission from Cambridge University Press, https://doi.org/10.1557/mrs.2016.209, Copyright 2016 Materials Research Society 2016).

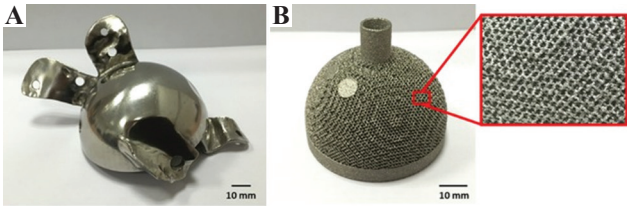


**Figure 19.** The 3D printed NiTi samples. (A) Selective laser melting-produced hip joint after polishing. (B) Electron beam melting-produced acetabular cup and the magnified view of the porous lattice structure (Reproduced from Ref [152] with permission from Wiley Periodicals, Inc., https://doi.org/10.1002/jor.23075, Copyright 2015 Orthopaedic Research Society

NiTi scaffolds through osteogenic cell culture confirms the good mechanical properties and successful activity of osteogenic stem cells in a salty medium or even under-controlled compression stresses[147-149]. Furthermore, it was found that Ni ion release was below the cytotoxic level in both dense and AM produced porous NiTi scaffolds and reduced laser-beam diameter can decline the Ni ion release in SLM-produced NiTi scaffolds[146,150]. **Figure 19** shows examples of 3D printed NiTi components that have medical applications.

## 4. Conclusions

The 3D printed implants have attracted much attention in recent years since they are amenable to rapid production, custom-built design, and precise control over the dimension and porosity. In this regard, the present review focuses on the history of various AM methods that are utilized in the production of metallic implants. Different technologies and effective parameters are discussed. Furthermore, the porous 3D printed metallic scaffolds that are lighter in weight, osteoconductive, can prevent stress-shield effect, and form interconnected structures to facilitate the nutrients transformation and cell growth is a subject of discussion in this review. Moreover, the 3DP of various imperative metallic systems for titanium, Ti6Al4V alloy, CoCr alloy, tantalum, and SMA are introduced. Considering the growing attention and utilization of AM manufactured products in medicine, it is necessary to develop more sophisticated technologies that have more precise control over the effective parameters in biological environments. These new technologies need to fulfill some key requirements, such as fast production, higher resolution of products, economical and environmentally friendly methods, less defective procedures, proper custom-built designs, biocompatibility, resistance to corrosion, wear, and compressive loads, inhibition of stress-shielding effects, proper surface conditions (roughness, wettability), and antibacterial designs. Recently, the emergence of smart and novel methods, including 4D printing, seems to represent a revolutionary step in AM technology. This review briefly summarizes the current knowledge in 3DP of implants with a special emphasis on the technologies and procedures which are instrumental in the conception and development of de novo technologies.

## Acknowledgments

This research was funded by the National Natural Science Foundation of China (no. 31971246 and no. 51831011) and Medical Engineering Cross Research Foundation of Shanghai Jiao Tong University (no. YG2019QNA46).

## Conflicts of interest

The authors declare no conflicts of interest.

## Data availability

All data generated or analyzed during this study are included in this published article.

## References

1. Ni J, Ling H, Zhang S, *et al*., 2019, Three-dimensional Printing of Metals for Biomedical Applications. *Mater Today Bio*, 3:100024. https://doi.org/10.1016/j.mtbio.2019.100024.
2. Attaran M, 2017, The Rise of 3-D Printing: The Advantages of Additive Manufacturing Over Traditional Manufacturing. *Bus Horiz*, 60:677–88. https://doi.org/10.1016/j.bushor.2017.05.011.
3. Skylar-Scott MA, Uzel SG, Nam LL, *et al*., 2019, Biomanufacturing of Organ-specific Tissues with High Cellular Density and Embedded Vascular Channels. *Sci Adv*, 5:eaaw2459. https://doi.org/10.1126/sciadv.aaw2459.
4. Zhang B, Pei X, Zhou C, *et al*., 2018, The Biomimetic Design and 3D Printing of Customized Mechanical Properties Porous Ti6Al4V Scaffold for Load-bearing Bone Reconstruction. *Mater Des*, 152:30–9. https://doi.org/10.1016/j.matdes.2018.04.065.
5. Söhling N, Neijhoft J, Nienhaus V, *et al*., 2020, 3D-Printing of Hierarchically Designed and Osteoconductive Bone Tissue Engineering Scaffolds. *Materials* (*Basel*), 13:1836. https://doi.org/10.3390/ma13081836.
6. Pei X, Ma L, Zhang B, *et al*., 2017, Creating Hierarchical Porosity Hydroxyapatite Scaffolds with Osteoinduction by Three-dimensional Printing and Microwave Sintering. *Biofabrication*, 9:45008. https://doi.org/10.1088/1758-5090/aa90ed.
7. Stepniak K, Ursani A, Paul N, *et al*., 2020, Novel 3D Printing

Technology for CT Phantom Coronary Arteries with High Geometrical Accuracy for Biomedical Imaging Applications. *Bioprinting*, 18:e00074. https://doi.org/10.1016/j.bprint.2020.e00074.

8. Jardini AL, Larosa MA, Filho RM, *et al*., 2014, Cranial Reconstruction: 3D Biomodel and Custom-built Implant Created Using Additive Manufacturing. *J Craniomaxillofac Surg*, 42:1877–84. https://doi.org/10.1016/j.jcms.2014.07.006.
9. Mobbs RJ, Coughlan M, Thompson R, *et al*., 2017, The Utility of 3D Printing for Surgical Planning and Patient-specific Implant Design for Complex Spinal Pathologies: Case Report. *J Neurosurg Spine*, 26:513–8. https://doi.org/10.3171/2016.9.SPINE16371.
10. Kodama H, 1981, A Scheme for Three-Dimensional Display by Automatic Fabrication of Three-Dimensional Model. *IEICE Trans Electron* (*Japanese Ed*), 64:237–41.
11. Hull CW, Spence ST, Albert DJ, *et al*., 1988, Methods and Apparatus for Production of Three-dimensional Objects by Stereolithography, Patents No. 5059359.
12. Noor N, Shapira A, Edri R, *et al*., 2019, 3D Printing of Personalized Thick and Perfusable Cardiac Patches and Hearts. *Adv Sci*, 2019:1900344. https://doi.org/10.1002/advs.201900344.
13. Ahmad AN, Gopinath P, Vinogradov A, 2019, 3D Printing in Medicine. In: 3D Printing Technology, Nanomedicine. Elsevier, Amsterdam, Netherlands, pp. 1–22. https://doi.org/10.1016/B978-0-12-815890-6.00001-3.
14. Gorsse S, Hutchinson C, Gouné M, *et al*., 2017, Additive Manufacturing of Metals: A Brief Review of the Characteristic Microstructures and Properties of Steels, Ti-6Al-4V and High-entropy Alloys. *Sci Technol Adv Mater*, 18:584–610. https://doi.org/10.1080/14686996.2017.1361305.
15. Boularaoui S, Al Hussein G, Khan KA, *et al*., 2020, An Overview of Extrusion-based Bioprinting with a Focus on Induced Shear Stress and its Effect on Cell Viability. *Bioprinting*, 20:e00093. https://doi.org/10.1016/j.bprint.2020.e00093.
16. Gibson I, Rosen D, Stucker B, 2015, Vat Photopolymerization Processes. In: Addition Manufacturing Technologies. Springer, New York, pp. 63–106. https://doi.org/10.1007/978-1-4939-2113-3_4.
17. Appuhamillage GA, Chartrain N, Meenakshisundaram V, *et al*., 2019, 110th Anniversary : Vat Photopolymerization-Based Additive Manufacturing: Current Trends and Future Directions in Materials Design. *Ind Eng Chem Res*, 58:15109–18. https://doi.org/10.1021/acs.iecr.9b02679.
18. Shirazi SF, Gharehkhani S, Mehrali M, *et al*., 2015, A Review on Powder-based Additive Manufacturing for Tissue Engineering: Selective Laser Sintering and Inkjet 3D Printing. *Sci Technol Adv Mater*, 16:033502. https://doi.org/10.1088/1468-6996/16/3/033502.
19. Sun S, Brandt M, Easton M, 2017, 2-Powder Bed Fusion Processes: An Overview. In: Brandt MB, editor. Woodhead Publishing Series in Electronic and Optical Materials. Woodhead Publishing, Sawston, United Kingdom, pp. 55–77. https://doi.org/https://doi.org/10.1016/B978-0-08-100433-3.00002-6.
20. Sing SL, Huang S, Yeong WY, 2020, Effect of Solution Heat Treatment on Microstructure and Mechanical Properties of Laser Powder Bed Fusion Produced Cobalt-28chromium-6molybdenum. *Mater Sci Eng A*, 769:138511. https://doi.org/10.1016/j.msea.2019.138511.
21. Galati M, Iuliano L, 2018, A Literature Review of Powder-based Electron Beam Melting Focusing on Numerical Simulations. *Addit Manuf*, 19:1–20. https://doi.org/https://doi.org/10.1016/j.addma.2017.11.001.
22. Yu W, Sing SL, Chua CK, *et al*., 2019, Influence of Re-melting on Surface Roughness and Porosity of AlSi10Mg Parts Fabricated by Selective Laser Melting. *J Alloys Compd*, 792:574–81. https://doi.org/10.1016/j.jallcom.2019.04.017.
23. Li X, Tan YH, Willy HJ, *et al*., 2019, Heterogeneously Tempered Martensitic High Strength Steel by Selective Laser Melting and its Micro-lattice: Processing, Microstructure, Superior Performance and Mechanisms. *Mater Des*, 178:107881. https://doi.org/10.1016/j.matdes.2019.107881.
24. Kuo CN, Chua CK, Peng PC, *et al*., 2020, Microstructure Evolution and Mechanical Property Response via 3D Printing Parameter Development of Al-Sc alloy. *Virtual Phys Prototyp*, 15:120–9. https://doi.org/10.1080/17452759.2019.1698967.
25. Yap CY, Chua CK, Dong ZL, *et al*., 2015, Review of Selective Laser Melting: Materials and Applications. *Appl Phys Rev*, 2:041101. https://doi.org/10.1063/1.4935926.
26. Sing SL, Wiria FE, Yeong WY, 2018, Selective Laser Melting of Titanium Alloy with 50 wt% Tantalum: Effect of Laser Process Parameters on Part Quality. *Int J Refract Met Hard Mater*, 77:120–7. https://doi.org/10.1016/j.ijrmhm.2018.08.006.
27. Wang P, Nai ML, Tan X, *et al*., 2016, Recent Progress

of Additive Manufactured Ti-6Al-4V by Electron Beam Melting. In: Solid Free from fabrication. 2016 Proceeding 27th Annual International Solid Freeform Fabrication Symposium Additive Manufacturing. Conference, pp. 691–704.

28. Nandwana P, Lee Y, 2020, Influence of Scan Strategy on Porosity and Microstructure of Ti-6Al-4V Fabricated by Electron Beam Powder Bed Fusion. *Mater Today Commun*, 24:100962. https://doi.org/10.1016/j.mtcomm.2020.100962.
29. Tan JH, Sing SL, Yeong WY, 2020, Microstructure Modelling for Metallic Additive Manufacturing: A Review. *Virtual Phys Prototyp*, 15:87–105. https://doi.org/10.1080/17452759.2019.1677345.
30. Wang P, Tan X, Nai ML, *et al*., 2016, Spatial and Geometrical-based Characterization of Microstructure and Microhardness for an Electron Beam Melted Ti-6Al-4V Component. *Mater Des*, 95:287–95. https://doi.org/10.1016/j.matdes.2016.01.093.
31. Galarraga H, Lados DA, Dehoff RR, *et al*., 2016, Effects of the Microstructure and Porosity on Properties of Ti-6Al-4V ELI Alloy Fabricated by Electron Beam Melting (EBM). *Addit Manuf*, 10:47–57. https://doi.org/10.1016/j.addma.2016.02.003.
32. Wang P, Nai ML, Sin WJ, *et al*., 2018, Realizing a Full Volume Component by *In-Situ* Welding during Electron Beam Melting Process. *Addit Manuf*, 22:375–80. https://doi.org/10.1016/j.addma.2018.05.022.
33. Wang P, Goh MH, Li Q, *et al*., 2020, Effect of Defects and Specimen Size with Rectangular Cross-section on the Tensile Properties of Additively Manufactured Components. *Virtual Phys Prototyp*, 15:251–64. https://doi.org/10.1080/17452759.2020.1733430.
34. Pan Wang JW, Sin WJ, Nai ML, 2017, Effects of Processing Parameters on Surface Roughness of Additive Manufactured Ti-6Al-4V via Electron Beam Melting. *Materials* (*Basel*), 10:1121. https://doi.org/10.3390/ma10101121.
35. Zhang LC, Chen LY, Wang L, 2020, Surface Modification of Titanium and Titanium Alloys: Technologies, Developments, and Future Interests. *Adv Eng Mater*, 22: 1901258. https://doi.org/10.1002/adem.201901258.
36. Singh R, Singh S, Hashmi MS, 2016, Implant Materials and Their Processing Technologies. In: The Reference Module in Materials Science and Materials Engineering. Elsevier, Amsterdam, Netherlands. https://doi.org/10.1016/B978-0-12-803581-8.04156-4.
37. Körner C, 2016, Additive Manufacturing of Metallic Components by Selective Electron Beam Melting a Review. *Int Mater Rev*, 61:361–77. https://doi.org/10.1080/09506608.2016.1176289.
38. Chia HN, Wu BM, 2015, Recent Advances in 3D Printing of Biomaterials. *J Biol Eng*, 9:4. https://doi.org/10.1186/s13036-015-0001-4.
39. Waheed S, Cabot JM, Macdonald NP, *et al*., 2016, 3D Printed Microfluidic Devices: Enablers and Barriers. *Lab Chip*, 16:1993–2013. https://doi.org/10.1039/C6LC00284F.
40. Zhang Y, Jarosinski W, Jung YG, *et al*., 2018, Additive Manufacturing Processes and Equipment. In: Additive Manufacturing. Elsevier, Amsterdam, Netherlands, pp. 39–51. https://doi.org/10.1016/B978-0-12-812155-9.00002-5.
41. Upcraft S, Fletcher R, 2003, The Rapid Prototyping Technologies. *Assem Autom*, 23:318–30. https://doi.org/10.1108/01445150310698634.
42. Hwang HH, Zhu W, Victorine G, *et al*., 2018, 3D-Printing of Functional Biomedical Microdevices via Light and Extrusion-Based Approaches. *Small Methods*, 2:1700277. https://doi.org/10.1002/smtd.201700277.
43. Pilipović A, RaosP, Šercer M, 2009, Experimental Analysis of Properties of Materials for Rapid Prototyping. *Int J Adv Manuf Technol*, 40:105–15. https://doi.org/10.1007/s00170-007-1310-7.
44. Bhattacharjee N, Urrios A, Kang S, *et al*., 2016, The Upcoming 3D-Printing Revolution in Microfluidics. *Lab Chip*, 16:1720–42. https://doi.org/10.1039/C6LC00163G.
45. Hamid Q, Snyder J, Wang C, *et al*., 2011, Fabrication of Three-dimensional Scaffolds Using Precision Extrusion Deposition with an Assisted Cooling Device. *Biofabrication*, 3:034109. https://doi.org/10.1088/1758-5082/3/3/034109.
46. Vaezi M, Zhong G, Kalami H, *et al*., 2018, Extrusion-based 3D Printing Technologies for 3D Scaffold Engineering. In: Functional 3D Tissue Engineering Scaffolds: Materials, Technologies, and Applications. Elsevier, Amsterdam, Netherlands, pp. 235–54. https://doi.org/10.1016/B978-0-08-100979-6.00010-0.
47. Greulich M, Greul M, Pintat T, 1995, Fast, Functional Prototypes via Multiphase Jet Solidification. *Rapid Prototyp J*, 1:20-5. https://doi.org/10.1108/13552549510146649.
48. Carneiro OS, Silva AF, Gomes R, 2015, Fused Deposition Modeling with Polypropylene. *Mater Des*, 83:768–76. https://doi.org/10.1016/j.matdes.2015.06.053.

49. Sun L, Parker ST, Syoji D, *et al*., 2012, Direct-Write Assembly of 3D Silk/Hydroxyapatite Scaffolds for Bone Co-Cultures. *Adv Healthc Mater*, 1:729–35. https://doi.org/10.1002/adhm.201200057.
50. Rane K, Strano M, 2019, A Comprehensive Review of Extrusion-based Additive Manufacturing Processes for Rapid Production of Metallic and Ceramic Parts. *Adv Manuf*, 7:155–73. https://doi.org/10.1007/s40436-019-00253-6.
51. Highley CB, 2019, 3D Bioprinting Technologies. In: 3D Bioprinting Medicine. Springer International Publishing, Cham, Switzerland, pp. C1–2. https://doi.org/10.1007/978-3-030-23906-0_8.
52. El Aita I, Breitkreutz J, Quodbach J, 2019, On-demand Manufacturing of Immediate Release Levetiracetam Tablets Using Pressure-assisted Microsyringe Printing. *Eur J Pharm Biopharm*, 134:29–36. https://doi.org/10.1016/j.ejpb.2018.11.008.
53. Vaezi M, Seitz H, Yang S, 2013, A Review on 3D Micro-additive Manufacturing Technologies. *Int J Adv Manuf Technol*, 67:1957–7. https://doi.org/10.1007/s00170-013-4962-5.
54. Mekonnen BG, Bright G, Walker A, 2016, A Study on State of the Art Technology of Laminated Object Manufacturing (LOM). Springer, Berlin, Germany, pp. 207–16. https://doi.org/10.1007/978-81-322-2740-3_21.
55. Dermeik B, Travitzky N, 2020, Laminated Object Manufacturing of Ceramic-Based Materials. *Adv Eng Mater*, 2020:2000256. https://doi.org/10.1002/adem.202000256.
56. Hagedorn Y, 2017, Laser Additive Manufacturing of Ceramic Components. In: Laser Additive Manufacturing. Elsevier, Amsterdam, Netherlands, pp. 163–80. https://doi.org/10.1016/B978-0-08-100433-3.00006-3.
57. Horn TJ, Harrysson OL, 2012, Overview of Current Additive Manufacturing Technologies and Selected Applications. *Sci Prog*, 95:255–82. https://doi.org/10.3184/003685012X13420984463047.
58. Gibson I, Rosen DW, Stucker B, 2009, Additive Manufacturing Technologies: Rapid Prototyping to Direct Digital Manufacturing. Springer US, Berlin, Germany. https://doi.org/10.1007/978-1-4419-1120-9.
59. Gibson I, Rosen D, Stucker B, 2015, Directed Energy Deposition Processes. In: Addition Manufacturing Technologies. Springer, New York, pp. 245–68. https://doi.org/10.1007/978-1-4939-2113-3_10.
60. Ventola CL, 2014, Medical Applications for 3D Printing: Current and Projected Uses. *P T*, 39:704–11.
61. Sinha SK, 2020, Additive Manufacturing (AM) of Medical Devices and Scaffolds for Tissue Engineering Based on 3D and 4D Printing. In: 3D 4D Printing of Polymer Nanocomposite Materials. Elsevier, Amsterdam, Netherlands, pp. 119–60. https://doi.org/10.1016/B978-0-12-816805-9.00005-3.
62. Wang D, Wang Y, Wu S, *et al*., 2017, Customized a Ti6Al4V Bone Plate for Complex Pelvic Fracture by Selective Laser Melting. *Materials* (*Basel*), 10:35. https://doi.org/10.3390/ma10010035.
63. Turnbull G, Clarke J, Picard F, *et al*., 2018, 3D Bioactive Composite Scaffolds for Bone Tissue Engineering. *Bioact Mater*, 3:278–314. https://doi.org/10.1016/j.bioactmat.2017.10.001.
64. Roopavath UK, Kalaskar DM, 2017, Introduction to 3D Printing in Medicine. In: 3D Printing in Medicine. Elsevier, Amsterdam, Netherlands, pp. 1–20. https://doi.org/10.1016/B978-0-08-100717-4.00001-6.
65. Wang X, Ao Q, Tian X, *et al*., 2016, 3D Bioprinting Technologies for Hard Tissue and Organ Engineering. *Materials* (*Basel*). 9:802. https://doi.org/10.3390/ma9100802.
66. Derakhshanfar S, Mbeleck R, Xu K, *et al*., 2018, 3D Bioprinting for Biomedical Devices and Tissue Engineering: A Review of Recent Trends and Advances. *Bioact Mater*, 3:144–56. https://doi.org/10.1016/j.bioactmat.2017.11.008.
67. Nagarajan N, Dupret-Bories A, Karabulut E, *et al*., 2018, Enabling Personalized Implant and Controllable Biosystem Development through 3D Printing. *Biotechnol Adv*, 36, 521–33. https://doi.org/10.1016/j.biotechadv.2018.02.004.
68. Bandyopadhyay A, Mitra I, Bose A, 2020, 3D Printing for Bone Regeneration. *Curr Osteoporos Rep*, 18:505–14. https://doi.org/10.1007/s11914-020-00606-2.
69. Bittner SM, Guo JL, Melchiorri A, *et al*., 2018, Three-dimensional Printing of Multilayered Tissue Engineering Scaffolds. *Mater Today*, 21:861–74. https://doi.org/10.1016/j.mattod.2018.02.006.
70. Chang J, He J, Mao M, *et al*., 2018, Advanced Material Strategies for Next-Generation Additive Manufacturing. *Materials* (*Basel*), 11:166. https://doi.org/10.3390/ma11010166.
71. Peng F, Vogt BD, Cakmak M, 2018, Complex Flow and Temperature History during Melt Extrusion in Material Extrusion Additive Manufacturing. *Addit Manuf*, 22:197–206. https://doi.org/10.1016/j.addma.2018.05.015.
72. Bandyopadhyay A, Traxel KD, 2018, Invited Review Article:

Metal-additive Manufacturing Modeling Strategies for Application-optimized Designs. *Addit Manuf*, 22:758–74. https://doi.org/10.1016/j.addma.2018.06.024.

73. Thakar CM, Deshmukh SP, Mulla TA, 2020, A Review on Selective Deposition Lamination 3D Printing Technique. *Int J Adv Sci Res Eng Trends*, 4:7–11.
74. Do AV, Smith R, Acri TM, Geary SM, *et al*., 2018, 3D Printing Technologies for 3D Scaffold Engineering. In: Functional 3D Tissue Engineering Scaffolds: Materials, Technologies, and Applications. Elsevier, Amsterdam, Netherlands, pp. 203–34. https://doi.org/10.1016/B978-0-08-100979-6.00009-4.
75. Devillard R, Pagès E, Correa MM, *et al*., 2014, Cell Patterning by Laser-Assisted Bioprinting. *Methods Cell Biol*, 119:159-74. https://doi.org/10.1016/B978-0-12-416742-1.00009-3.
76. Akbari S, Zhang YF, Wang D, *et al*., 2018, 4D Printing and its Biomedical Applications. In: 3D 4D Printing in Biomedical Applications. Wiley-VCH Verlag GmbH and Co., KGaA, Weinheim, Germany, pp. 343–72. https://doi.org/10.1002/9783527813704.ch14.
77. Hao L, Tang D, Sun T, *et al*., 2020, Direct Ink Writing of Mineral Materials: A review. *Int J Precis Eng Manuf Technol*, 1:266. https://doi.org/10.1007/s40684-020-00222-6.
78. An J, Teoh JE, Suntornnond R, *et al*., 2015, Design and 3D Printing of Scaffolds and Tissues. *Engineering*, 1:261–8. https://doi.org/10.15302/J-ENG-2015061.
79. Krishna BV, Xue W, Bose S, *et al*., 2008, Engineered Porous Metals for Implants. *JOM*, 60: 45–8. https://doi.org/10.1007/s11837-008-0059-2.
80. Yang J, Gu D, Lin K, *et al*., 2020, Laser 3D Printed Bio-inspired Impact Resistant Structure: Failure Mechanism under Compressive Loading. *Virtual Phys Prototyp*, 15:75–86. https://doi.org/10.1080/17452759.2019.1677124.
81. du Plessis A, Razavi SM, Berto F, 2020, The Effects of Microporosity in Struts of Gyroid Lattice Structures Produced by Laser Powder Bed Fusion. *Mater Des*, 194:108899. https://doi.org/10.1016/j.matdes.2020.108899.
82. Meng L, Zhao J, Lan X, *et al*., 2020, Multi-objective Optimisation of Bio-inspired Lightweight Sandwich Structures Based on Selective Laser Melting. *Virtual Phys Prototyp*, 15:106–19. https://doi.org/10.1080/17452759.2019.1692673.
83. Matena J, Petersen S, Gieseke M, *et al*., 2015, SLM Produced Porous Titanium Implant Improvements for Enhanced Vascularization and Osteoblast Seeding. *Int J Mol Sci*, 16:7478–92. https://doi.org/10.3390/ijms16047478.
84. Van Cleynenbreugel T, Schrooten J, Van Oosterwyck H, *et al*., 2006, Micro-CT-based Screening of Biomechanical and Structural Properties of Bone Tissue Engineering Scaffolds. *Med Biol Eng Comput*, 44:517–25. https://doi.org/10.1007/s11517-006-0071-z.
85. Wang P, Li X, Jiang Y, *et al*., 2020, Electron Beam Melted Heterogeneously Porous Microlattices for Metallic Bone Applications: Design and Investigations of Boundary and Edge Effects. *Addit Manuf*, 36:101566. https://doi.org/10.1016/j.addma.2020.101566.
86. Cheng A, Humayun A, Cohen DJ, *et al*., 2014, Additively Manufactured 3D Porous Ti-6Al-4V Constructs Mimic Trabecular Bone Structure and Regulate Osteoblast Proliferation, Differentiation and Local Factor Production in a Porosity and Surface Roughness Dependent Manner. *Biofabrication*, 6:045007. https://doi.org/10.1088/1758-5082/6/4/045007.
87. Markhoff J, Wieding J, Weissmann V, *et al*., 2015, Influence of Different Three-Dimensional Open Porous Titanium Scaffold Designs on Human Osteoblasts Behavior in Static and Dynamic Cell Investigations. *Materials* (*Basel*), 8:5490–507. https://doi.org/10.3390/ma8085259.
88. Wang P, Li X, Luo S, *et al*., 2021, Additively Manufactured Heterogeneously Porous Metallic Bone with Biostructural Functions and Bone-like Mechanical Properties. *J Mater Sci Technol*, 62:173–9. https://doi.org/10.1016/j.jmst.2020.05.056.
89. Xue W, Krishna BV, Bandyopadhyay A, *et al*., 2007, Processing and Biocompatibility Evaluation of Laser Processed Porous Titanium. *Acta Biomater*, 3:1007–18. https://doi.org/10.1016/j.actbio.2007.05.009.
90. Balla VK, Bodhak S, Bose S, *et al*., 2010, Porous Tantalum Structures for Bone Implants: Fabrication, Mechanical and *In Vitro* Biological Properties. *Acta Biomater*, 6:3349–59. https://doi.org/10.1016/j.actbio.2010.01.046.
91. Jeon H, Lee H, Kim G, 2014, A Surface-Modified Poly(ε-caprolactone) Scaffold Comprising Variable Nanosized Surface-Roughness Using a Plasma Treatment. *Tissue Eng Part C Methods*, 20:951–63. https://doi.org/10.1089/ten.tec.2013.0701.
92. Lv J, Jia Z, Li J, *et al*., 2015, Electron Beam Melting Fabrication of Porous Ti6Al4V Scaffolds: Cytocompatibility and Osteogenesis. *Adv Eng Mater*, 17:1391–8. https://doi.org/10.1002/adem.201400508.
93. Biemond JE, Aquarius R, Verdonschot N, *et al*., 2011, Frictional and Bone Ingrowth Properties of Engineered Surface Topographies Produced by Electron Beam

Technology. *Arch Orthop Trauma Surg*, 131:711–8. https://doi.org/10.1007/s00402-010-1218-9.

94. Otsuki B, Takemoto M, Fujibayashi S, *et al*., 2006, Pore Throat Size and Connectivity Determine Bone and Tissue Ingrowth into Porous Implants: Three-dimensional Micro-CT Based Structural Analyses of Porous Bioactive Titanium Implants. *Biomaterials*, 27:5892–900. https://doi.org/10.1016/j.biomaterials.2006.08.013.
95. Rumpler M, Woesz A, Dunlop JW, *et al*., 2008, The Effect of Geometry on Three-dimensional Tissue Growth. *J R Soc Interface*, 5:1173–80. https://doi.org/10.1098/rsif.2008.0064.
96. Marin E, Fusi S, Pressacco M, *et al*., 2010, Characterization of Cellular Solids in Ti6Al4V for Orthopaedic Implant Applications: Trabecular Titanium. *J Mech Behav Biomed Mater*, 3:373–81. https://doi.org/10.1016/j.jmbbm.2010.02.001.
97. Parthasarathy J, Starly B, Raman S, *et al*., 2010, Mechanical Evaluation of Porous Titanium (Ti6Al4V) Structures with Electron Beam Melting (EBM). *J Mech Behav Biomed Mater*, 3:249–59. https://doi.org/10.1016/j.jmbbm.2009.10.006.
98. Li X, Tan YH, Wang P, *et al*., 2020, Metallic Microlattice and Epoxy Interpenetrating Phase Composites: Experimental and Simulation Studies on Superior Mechanical Properties and their Mechanisms. *Compos Part A Appl Sci Manuf*, 135:105934. https://doi.org/10.1016/j.compositesa.2020.105934.
99. Nazir A, Abate KM, Kumar A, *et al*., 2019, A State-of-the-art Review on Types, Design, Optimization, and Additive Manufacturing of Cellular Structures. *Int J Adv Manuf Technol*, 104:3489–510. https://doi.org/10.1007/s00170-019-04085-3.
100. Parthasarathy J, Starly B, Raman S, 2011, A Design for the Additive Manufacture of Functionally Graded Porous Structures with Tailored Mechanical Properties for Biomedical Applications. *J Manuf Process*, 13:160–70. https://doi.org/10.1016/j.jmapro.2011.01.004.
101. Gibson LJ, Ashby MF, 1999, Cellular Solids: Structure and Properties. Cambridge University Press, Cambridge, United Kingdom. https://doi.org/10.1017/CBO9781139878326.
102. Fantini M, Curto M, De Crescenzio F, 2017, TPMS for Interactive Modelling of Trabecular Scaffolds for Bone Tissue Engineering BT Advances on Mechanics, Design Engineering and Manufacturing : Proceedings of the International Joint Conference on Mechanics, Design Engineering and Advanced Manufactur. In: Eynard B, Nigrelli V, Oliveri SM, Peris-Fajarnes G, Rizzuti S, editors. Springer International Publishing, Cham, Switzerland, pp. 425–35. https://doi.org/10.1007/978-3-319-45781-9_43.
103. Attarilar S, Salehi MT, Al-Fadhalah KJ, *et al*., 2019, Functionally Graded Titanium Implants: Characteristic Enhancement Induced by Combined Severe Plastic Deformation. *PLoS One*, 14:1–18. https://doi.org/10.1371/journal.pone.0221491.
104. Roach P, Eglin D, Rohde K, *et al*., 2007, Modern Biomaterials: A Review Bulk Properties and Implications of Surface Modifications. *J Mater Sci Mater Med*, 18:1263–77. https://doi.org/10.1007/s10856-006-0064-3.
105. Triyono J, Alfiansyah R, Sukanto H, *et al*., 2020, Fabrication and Characterization of Porous Bone Scaffold of Bovine Hydroxyapatite-glycerin by 3D Printing Technology. *Bioprinting*, 18:e00078. https://doi.org/10.1016/j.bprint.2020.e00078.
106. Wang Q, Zhou P, Liu S, *et al*., 2020, Multi-Scale Surface Treatments of Titanium Implants for Rapid Osseointegration: A Review. *Nanomaterials*, 10:1244. https://doi.org/10.3390/nano10061244.
107. Wang P, Todai M, Nakano T, 2019, Beta titanium Single Crystal with Bone-like Elastic Modulus and Large Crystallographic Elastic Anisotropy. *J Alloys Compd*, 782:667–71. https://doi.org/10.1016/j.jallcom.2018.12.236.
108. Wang P, Wu L, Feng Y, *et al*., 2017, Microstructure and Mechanical Properties of a Newly Developed Low Young's Modulus Ti-15Zr-5Cr-2Al Biomedical Alloy. *Mater Sci Eng C*, 72:536–42. https://doi.org/10.1016/j.msec.2016.11.101.
109. Attarilar S, Yang J, Ebrahimi M, *et al*., 2020, The Toxicity Phenomenon and the Related Occurrence in Metal and Metal Oxide Nanoparticles: A Brief Review From the Biomedical Perspective. *Front Bioeng Biotechnol*, 8:822. https://doi.org/10.3389/fbioe.2020.00822.
110. Niinomi M, Nakai M, 2011, Titanium-Based Biomaterials for Preventing Stress Shielding between Implant Devices and Bone. *Int J Biomater*, 2011:836587. https://doi.org/10.1155/2011/836587.
111. Gode C, Attarilar S, Eghbali B, *et al*., 2015, Electrochemical Behavior of Equal Channel Angular Pressed Titanium for Biomedical Application. AIP Conference Proceedings, United States. https://doi.org/10.1063/1.4914232.
112. Attarilar S, Djavanroodi F, Irfan OM, *et al*., 2020, Strain Uniformity Footprint on Mechanical Performance and

Erosion-corrosion Behavior of Equal Channel Angular Pressed Pure Titanium. *Results Phys*, 17:103141. https://doi.org/10.1016/j.rinp.2020.103141.

113. Taniguchi N, Fujibayashi S, Takemoto M, *et al*., 2016, Effect of Pore Size on Bone Ingrowth into Porous Titanium Implants Fabricated by Additive Manufacturing: An *In Vivo* Experiment. *Mater Sci Eng C*, 59:690–701. https://doi.org/10.1016/j.msec.2015.10.069.
114. Li X, Ma XY, Feng YF, *et al*., 2015, A Novel Composite Scaffold Consisted of Porous Titanium and Chitosan Sponge for Load-bearing Applications: Fabrication, Characterization and Cellular Activity. *Compos Sci Technol*, 117:78–84. https://doi.org/10.1016/j.compscitech.2015.05.019.
115. Zhang C, Zhang L, Liu L, *et al*., 2020, Mechanical Behavior of a Titanium Alloy Scaffold Mimicking Trabecular Structure. *J Orthop Surg Res*, 15:40. https://doi.org/10.1186/s13018-019-1489-y.
116. McGilvray KC, Easley J, Seim HB, *et al*., 2018, Bony Ingrowth Potential of 3D-Printed Porous Titanium Alloy: A Direct Comparison of Interbody Cage Materials in an *In Vivo* Ovine Lumbar Fusion Model. *Spine J*, 18:1250–60. https://doi.org/10.1016/j.spinee.2018.02.018.
117. Song P, Hu C, Pei X, *et al*., 2019, Dual Modulation of Crystallinity and Macro-/Microstructures of 3D Printed Porous Titanium Implants to Enhance Stability and Osseointegration. *J Mater Chem B*, 7:2865–77. https://doi.org/10.1039/C9TB00093C.
118. Bose S, Banerjee D, Shivaram A, *et al*., 2018, Calcium Phosphate Coated 3D Printed Porous Titanium with Nanoscale Surface Modification for Orthopedic and Dental Applications. *Mater Des*, 2018:S0264127518303198. https://doi.org/10.1016/j.matdes.2018.04.049.
119. Ran Q, Yang W, Hu Y, *et al*., 2018, Osteogenesis of 3D Printed Porous Ti6Al4V Implants with Different Pore Sizes. *J Mech Behav Biomed Mater*, 84:1–11. https://doi.org/10.1016/j.jmbbm.2018.04.010.
120. Liu F, Mao Z, Zhang P, *et al*., 2018, Functionally Graded Porous Scaffolds in Multiple Patterns: New Design Method, Physical and Mechanical Properties. *Mater Des*, 160:849–60. https://doi.org/10.1016/j.matdes.2018.09.053.
121. Bobbert FS, Lietaert K, Eftekhari AA, *et al*., 2017, Additively Manufactured Metallic Porous Biomaterials Based on Minimal Surfaces: A Unique Combination of Topological, Mechanical, and Mass Transport Properties. *Acta Biomater*, 53:572–84. https://doi.org/10.1016/j.actbio.2017.02.024.
122. Wally ZJ, Haque AM, Feteira A, *et al*., 2019, Selective Laser Melting Processed Ti6Al4V Lattices with Graded Porosities for Dental Applications. *J Mech Behav Biomed Mater*, 90:20–9. https://doi.org/10.1016/j.jmbbm.2018.08.047.
123. Nune KC, Kumar A, Misra RD, *et al*., 2017, Functional Response of Osteoblasts in Functionally Gradient Titanium Alloy Mesh Arrays Processed by 3D Additive Manufacturing. *Colloids Surf B Biointerfaces*, 150:78–88. https://doi.org/10.1016/j.colsurfb.2016.09.050.
124. Liang H, Yang Y, Xie D, *et al*., 2019, Trabecular-like Ti-6Al-4V Scaffolds for Orthopedic: Fabrication by Selective Laser Melting and *In Vitro* Biocompatibility. *J Mater Sci Technol*, 35:1284–97. https://doi.org/10.1016/j.jmst.2019.01.012.
125. Wang S, Liu L, Li K, *et al*., 2019, Pore Functionally Graded Ti6Al4V Scaffolds for Bone Tissue Engineering Application. *Mater Des*, 168:107643. https://doi.org/10.1016/j.matdes.2019.107643.
126. Yosra K, 2018, EIT Emerging Implant Technology Granted FDA Multilevel Approval for their 3D Printed Cervical Cage, SPINEMarketGroup. Available from: https://3dadept.com/eit-emerging-implant-technology-granted-fda-multilevel-approval-for-their-3d-printed-cervical-cage/. [Last accessed on 2020 Nov 30].
127. Martial Y, 2019, Nexxt Spine creates 3D Printed Porous Titanium Interbodies Using GE Additive's Mlab Printer. Available from: https://3dadept.com/nexxt-spine-creates-3d-printed-porous-titanium-interbodies-using-ge-additives-mlab-printer/. [Last accessed on 2020 Nov 30].
128. Semba JA, Mieloch AA, Rybka JD, 2020, Introduction to the State-of-the-art 3D Bioprinting Methods, Design, and Applications in Orthopedics. *Bioprinting*, 18:e00070. https://doi.org/10.1016/j.bprint.2019.e00070.
129. Shah FA, Omar O, Suska F, *et al*., 2016, Long-term Osseointegration of 3D Printed CoCr Constructs with an Interconnected Open-pore Architecture Prepared by Electron Beam Melting. *Acta Biomater*, 36:296–309. https://doi.org/10.1016/j.actbio.2016.03.033.
130. Limmahakhun S, Oloyede A, Sitthiseripratip K, *et al*., 2017, Stiffness and Strength Tailoring of Cobalt Chromium Graded Cellular Structures for Stress-shielding Reduction. *Mater Des*, 114:633–41. https://doi.org/10.1016/j.matdes.2016.11.090.
131. Black J, 1994, Biologic Performance of Tantalum. *Clin Mater*, 16:167–73. https://doi.org/10.1016/0267-6605(94)90113-9.
132. Levine BR, Sporer S, Poggie RA, *et al*., 2006, Experimental and Clinical Performance of Porous Tantalum in Orthopedic

Surgery. *Biomaterials*, 27:4671–81. https://doi.org/10.1016/j.biomaterials.2006.04.041.

133. Saunders S, 2017, Chinese Hospital Uses 3D Printed Tantalum Implant in Successful Knee Replacement Surgery. Available from: https://3dprint.com/195286/3d-printed-tantalum-knee-implant/. [Last accessed on 2020 Nov 30].
134. Wever D, Elstrodt J, Veldhuizen A, *et al*., 2002, Scoliosis Correction with Shape-memory Metal: Results of an Experimental Study. *Eur Spine J*, 11:100–6. https://doi.org/10.1007/s005860100347.
135. Wang Y, Zheng G, Zhang X, *et al*., 2011, Temporary Use of Shape Memory Spinal Rod in the Treatment of Scoliosis. *Eur Spine J*, 20:118–22. https://doi.org/10.1007/s00586-010-1514-7.
136. Márquez JM, Pérez-Grueso, Fernández-Baíllo N, *et al*., 2012, Gradual Scoliosis Correction Over Time with Shape-memory Metal: A Preliminary Report of an Experimental Study. *Scoliosis*, 7:20. https://doi.org/10.1186/1748-7161-7-20.
137. Dadbakhsh S, Speirs M, Van Humbeeck J, *et al*., 2016, Laser Additive Manufacturing of Bulk and Porous Shape-memory NiTi Alloys: From Processes to Potential Biomedical Applications. *MRS Bull*, 41:765–74. https://doi.org/10.1557/mrs.2016.209.
138. Liu Y, Xie ZL, Van Humbeec J, *et al*., 1999, Effect of Texture Orientation on the Martensite Deformation of NiTi Shape Memory Alloy Sheet. *Acta Mater*, 47:645–60.
139. Motemani Y, Nili-Ahmadabadi M, Tan MJ, *et al*., 2009, Effect of Cooling Rate on the Phase Transformation Behavior and Mechanical Properties of Ni-rich NiTi Shape Memory Alloy. *J Alloys Compd*, 469:164–8. https://doi.org/10.1016/j.jallcom.2008.01.153.
140. Dadbakhsh S, Speirs M, Kruth JP, *et al*., 2014, Effect of SLM Parameters on Transformation Temperatures of Shape Memory Nickel Titanium Parts. *Adv Eng Mater*, 16:1140–6. https://doi.org/10.1002/adem.201300558.
141. Bormann T, Schumacher R, Müller B, *et al*., 2012. Tailoring Selective Laser Melting Process Parameters for NiTi Implants. *J Mater Eng Perform*, 21:2519–24. https://doi.org/10.1007/s11665-012-0318-9.
142. Figueira N, Silva TM, Carmezim MJ, *et al*., 2009, Corrosion Behaviour of NiTi Alloy. *Electrochim Acta*, 54:921–6. https://doi.org/10.1016/j.electacta.2008.08.001.
143. Muhonen V, Heikkinen R, Danilov A, *et al*., 2007, The Effect of Oxide Thickness on Osteoblast Attachment and Survival on NiTi Alloy. *J Mater Sci Mater Med*, 18:959–67. https://doi.org/10.1007/s10856-006-0082-1.
144. Cui ZD, Man HC, Yang XJ, 2005, The Corrosion and Nickel Release Behavior of Laser Surface-melted NiTi Shape Memory Alloy in Hanks' Solution. *Surf Coatings Technol*, 192:347–53. https://doi.org/10.1016/j.surfcoat.2004.06.033.
145. Chan CW, Hussain I, Waugh DG, *et al*., 2014, Effect of Laser Treatment on the Attachment and Viability of Mesenchymal Stem Cell Responses on Shape Memory NiTi Alloy. *Mater Sci Eng C*, 42:254–63. https://doi.org/10.1016/j.msec.2014.05.022.
146. Habijan T, Haberland C, Meier H, *et al*., 2013, The Biocompatibility of Dense and Porous Nickel-Titanium Produced by Selective Laser Melting. *Mater Sci Eng C*, 33:419–26. https://doi.org/10.1016/j.msec.2012.09.008.
147. Strauß S, Dudziak S, Hagemann R, *et al*., 2012, Induction of Osteogenic Differentiation of Adipose Derived Stem Cells by Microstructured Nitinol Actuator-Mediated Mechanical Stress. *PLoS One*, 7:e51264. https://doi.org/10.1371/journal.pone.0051264.
148. Liu S, Liu J, Wang L, *et al*., 2020, Superelastic Behavior of *In-Situ* Eutectic-Reaction Manufactured High Strength 3D Porous NiTi-Nb Scaffold. *Sci Mater*, 181:121–6. https://doi.org/10.1016/j.scriptamat.2020.02.025.
149. Hafeez N, Liu J, Wang L, *et al*., 2020, Superelastic Response of Low-modulus Porous Beta-type Ti-35Nb-2Ta-3Zr Alloy Fabricated by Laser Powder Bed Fusion. *Addit Manuf*, 34:101264. https://doi.org/10.1016/j.addma.2020.101264.
150. Putters JL, Sukul K, de Zeeuw GR, *et al*., 1992, Comparative Cell Culture Effects of Shape Memory Metal (Nitinol), Nickel and Titanium: A Biocompatibility Estimation. *Eur Surg Res*, 24:378–82. https://doi.org/10.1159/000129231.
151. Sing SL, An J, Yeong WY, *et al*., 2016, Laser and Electron-beam Powder-bed Additive Manufacturing of Metallic Implants: A Review on Processes, Materials and Designs. *J Orthop Res*, 34:369–85. https://doi.org/10.1002/jor.23075.

RESEARCH ARTICLE

# Considerations Using Additive Manufacture of Emulsion Inks to Produce Respiratory Protective Filters Against Viral Respiratory Tract Infections Such as the COVID-19 Virus

**Colin Sherborne, Frederik Claeyssens***

The Kroto Research Institute, North Campus, University of Sheffield, Broad Lane, Sheffield, S3 7HQ, UK

**Abstract:** This review paper explores the potential of combining emulsion-based inks with additive manufacturing (AM) to produce filters for respiratory protective equipment (RPE) in the fight against viral and bacterial infections of the respiratory tract. The value of these filters has been highlighted by the current severe acute respiratory syndrome coronavirus-2 crisis where the importance of protective equipment for health care workers cannot be overstated. Three-dimensional (3D) printing of emulsions is an emerging technology built on a well-established field of emulsion templating to produce porous materials such as polymerized high internal phase emulsions (polyHIPEs). PolyHIPE-based porous polymers have tailorable porosity from the submicron to 100 s of μm. Advances in 3D printing technology enables the control of the bulk shape while a micron porosity is controlled independently by the emulsion-based ink. Herein, we present an overview of the current polyHIPE-based filter applications. Then, we discuss the current use of emulsion templating combined with stereolithography and extrusion-based AM technologies. The benefits and limitation of various AM techniques are discussed, as well as considerations for a scalable manufacture of a polyHIPE-based RPE.

**Keywords:** Polymerized high internal phase emulsions; Emulsion templating; COVID-19; Additive manufacturing; Respirator protective equipment

***Correspondence to:** Frederik Claeyssens, The Kroto Research Institute, North Campus, University of Sheffield, Broad Lane, Sheffield, S3 7HQ, UK; F.Claeyssens@sheffield.ac.uk

**Received:** October 20, 2020; **Accepted:** November 18, 2020; **Published Online:** January 13, 2021

**Citation:** Sherborne C, Claeyssens F, 2021, Considerations Using Additive Manufacture of Emulsion Inks to Produce Respiratory Protective Filters Against Viral Respiratory Tract Infections Such as the COVID-19 Virus. *Int J Bioprint,* 7(1): 316.http://doi.org/10.18063/ijb.v7i1.316

## 1. Introduction

Personal protective equipment (PPE) and respiratory protective equipment (RPE) are vital for frontline health workers that work with patients infected with contagious respiratory tract infections, such as the coronavirus disease 2019 (COVID-19). During the early pandemic, there was an exceptionally high global demand for RPE but supply chains were under severe strain and supply continuality remained uncertain. There is a constant demand for RPE masks as they are disposable items or have a short lifetime as the filters need to be replaced or decontaminated after prolonged use, which could damage the integrity of the fibers and remove their electrostatic charge. Additive manufacturing (AM) has been widely utilized for various applications, such as in the fields of aerospace[1], automobiles[2], and tissue engineering[3], and now, the AM community has developed three-dimensional (3D) printing initiatives to support health care and frontline workers[4]. This includes rapid printable face shields for health care workers that can reduce direct exposure from large airborne respiratory droplets[5]. However, these initiatives are limited by the material choice and technology that produces masks for respiratory protection. A key component of RPE is the filtering mechanism. The filter traps and retains airborne

contaminants, such as virus-laden aerosol particles, while letting air pass through.

This review presents the feasibility of a polymerized high internal phase emulsion (polyHIPE)-based filter, and whether current emulsion-based AM techniques can be used to produce RPE against COVID-19. The motivation behind AM to make a porous foam is that it can produce complex geometries. The advantages include a multimaterial filter, localized and functionalized surface, or tunable porosity gradients to control the airflow within the filter itself. This approach could facilitate new filter designs that capitalize on new material processing and manufacturing techniques that may overcome some limitations of fibrous filters. Furthermore, the new filter designs may potentially filter the most penetrating particle size of 0.3 μm, which is the most difficult to filter because this size is at the transition point between particles that predominantly move by Brownian motion and larger particles that move by straight trajectory. This review provides an overview of the current filter-based applications of emulsion templating, including the current state of emulsion ink-based AM and the European Standard (EN) guidelines regarding the requirements of a RPE filter.

In this review, the following considerations are covered:

- RPE requirements including ISO standards and regulations that a new filter material will need to comply with;
- An overview of the polyHIPE material, current filter, and separation-based applications;
- AM of polyHIPE foams, their advantages, limitations, and the current progress in the literature to 3D printing using emulsions.

## 2. Respiratory filter requirements for COVID-19 prevention

RPE is a broad term covering respirators or breathing apparatus that filter or remove harmful substances from the air we breathe. For health care workers, different RPE types are recommended depending on the exposure risk from the COVID-19 patients[6]. Furthermore, government guidelines are in place for infection prevention[7]. The size of severe acute respiratory syndrome coronavirus-2 that causes COVID-19 is between 50 and 200 nm wide[8]. COVID-19 is thought to transmit through close contact and contaminated droplets over short distances[9]. When an infected patient coughs or sneezes, large airborne respiratory droplets laden with the virus are produced, contaminating surfaces and potentially transmitting the virus to others nearby. Hence, wearing a face mask is able to protect the surrounding people from respiratory droplets. Two-meter social distancing, frequent hand washing, and usage of mouth coverings/face mask are approaches to prevent the transmission. It is widely accepted that mask wearing could reduce COVID-19 transmission as it provides continuous protection from the contamination from the respiratory droplets and acts as a barrier to stop direct contacts of hands to mouth, nose, or eyes[10]. There is high certainty that the inhalation of the virus-containing aerosols is one of the infection modes, as determined by computer modeling of speech and cough generated droplets from infected individuals[11]. Nevertheless, this is largely dependent on the respiratory droplets that suspend in the air for a certain period of time.

The health care workers are at a great risk of infection when using aerosol-generating procedures on COVID-19 patients[6] as these airway-based procedures can create fine particles of <5 μm which can remain suspended in the air. For example, procedures such as tracheal intubation and non-invasive ventilation can produce virus-laden particles of smaller than 10 μm, which are very likely to bypass the respiratory mucosa in the upper airways and penetrate deep into the lung, thereby increasing the infection risk[12]. The World Health Organization recommends having adequate supply of PPE, such as N95 respirators, filtering facepieces (FFP3 or FFP2), or their equivalents, as part of the RPE[9].

Several ways the airborne particles can deposit onto the fibers include impaction, interception, and electrostatic forces. To improve breathability, the respirators must be permeable to air while maintaining their particle filtering function. To achieve this, the fibers have electrostatic charge to attract and trap airborne particles that attach onto the fiber[13]. Sterilizing these filters using ethanol[14] or isopropanol[15] removes the electric charge from the fibers which reduces their effectiveness.

According to the US National Institute for Occupational Safety and Health, N95 masks that can filter at least 95% of the airborne particles use an electrostatically charged non-woven polypropylene (PP) fiber to filter out airborne particles. The protective feature of these masks is comparable to that of the European FFP2 filters. In future, the masks should be designed in a way to include a seal around the face to prevent the bypass of submicron particles through the filter mechanism, which can occur during head movements[16]. 3D printing is a potential solution as it can be combined with detailed face scans to produce a customized face seal for improved wearer comfort and fit[17]. A customized 3D-printed reusable facemask with a replaceable filter membrane has been proposed[18]. FFP2/3 filter membranes can be used as a replaceable part of the mask.

## 3. RPE regulations

There are three classes of respiratory filters: FFP1, FFP2, and FFP3. A higher grade indicates a better filter efficiency; FFP3 can filter out at least 99% of airborne

particulates. During classification, the respirators are tested to certify whether they conform to the British or European standard (BS) EN 149:2001+A1:2009[19]. The "Conformité Européen" (CE) marking affixed to the PPE is an evidence of compliance to this legislation and an indication of the effectiveness of the respirator. A selection of these requirements is summarized in **Table 1**. In the United Kingdom, the HSG53 (2013) is a guideline recommending the best industry practice for the usage of RPE and its standard requirement. FFP3 is recommended in clinical use for protection against biological agents, including pandemic flu. Comparison tests between FFP3, FFP2, FFP1, and surgical masks show that there is a gradual decrease in the protection level with surgical masks offering the lowest level as they do not seal around the face[20]. Performance testing showed that the FFP2 and FFP3 masks achieved <1% and <0.03% for the penetration of polydisperse sodium chloride (NaCl) aerosols with a MMD (mass median diameter) of 238 nm, respectively[15]. Surgical masks offer some protection against the large droplets and contact transmission so symptomatic patients should wear it to minimize the spread of respiratory secretions that could transmit the infection to the surrounding. Respirators with a tight face seal are recommended over masks for enhanced protection. In regard to 3D-printed PPE-related devices from the 3D printing community, care should be taken when using them, as the devices are not approved by the relevant regulatory bodies for clinical use and their effectiveness is not guaranteed. Therefore, these devices should be used at the user's discretion.

The assigned protection factor indicates the level of protection that could be provided by the respirator (**Table 1**). A protection factor of 10 means that the user particle exposure level is reduced by a factor of 10, so one-tenth of the air contaminants will be breathed in. FFP3 is considered to be twice as effective as FFP2. All respirators require a tight-fitting face seal otherwise particles can bypass the filter through the open gaps. The total permitted inward leakage accounts for all potential leakage paths around the filter when the face seal leaks[21].

Furthermore, any PPE or RPE for the European market has to meet the required health and safety requirements of the European Directive on PPE Regulation (EU) 2016/425. This covers the legal obligations to ensure that the manufacture of PPE meets the required standards relating to the design, manufacture, and marketing of PPE. Furthermore, commission recommendation (EU) 2020/403 was introduced recently during the COVID-19 crisis to speed up the delivery of PPE to the market, specifically for the medical professionals.

## 4. Overview of the polyHIPE

PolyHIPE is a porous polymer that is created by polymerizing the continuous phase of an emulsion where the droplet phase exceeds over 74% of the total liquid volume; this type of emulsion is called a high internal phase emulsion (HIPE). The two liquids have to be immiscible with each other; therefore, when they are mixed together with either a surfactant or a small pickering particle, one of the liquids is broken into droplets (droplet phase) that disperses within the other (continuous phase). A polymeric material known as a polyHIPE is created when the emulsion's continuous phase is set into a solid. This can be done using either a light[22], heat[23], or a redox-based polymerization reaction[24]. During the crosslinking, the 3D architecture of the emulsion's continuous phase is fixed as a solid polymer, and subsequently, the draining of the droplet phase leaves behind a porous polymer. A unique property of the polyHIPE is that the porosity parameters can be independently tuned through the initial emulsion mixing conditions and ingredients. These include physical parameters, such as temperature[23], speed of mixing[25-27], and the rate the droplet phase is added[28]. The emulsion constituents can be varied from different aspects, such as water volume ratio[29], monomer type[30,31], solvent used in the emulsion[32,33], amount of surfactant[34], surfactant-free pickering emulsion[35], solubility of the initiator[36], and addition of electrolytes to the droplet phase[31]. These variables affect the stability of emulsion, the droplet size, and the way the monomer polymerizes around the droplets. A representative scanning electron microscope image of the polyHIPE structure is shown in **Figure 1**.

During the polymerization, the monomers cross-link to form a polymer chain. This process coincides with a significant volume reduction or contraction.

**Table 1.** Classification requirements of FFP1, FFP2, and FFP3 respirators

| Classification | Protection factor | Max. penetration of test aerosol: 95 l/min max % | | Max. permitted resistance (mbar) | | Total permitted inward leakage (%) |
|---|---|---|---|---|---|---|
| | | Sodium chloride | Paraffin oil | Inhalation 30/l min | Exhalation 160 l/min | |
| FFP1 | 4 | 20 | 20 | 0.6 | 3 | 25 |
| FFP2 | 10 | 6 | 6 | 0.7 | 3 | 11 |
| FFP3 | 20 | 1 | 1 | 1 | 3 | 5 |

Information adapted from the British standard: BS EN 149:2001+A1:2009[19]. FFP, filtering facepieces.

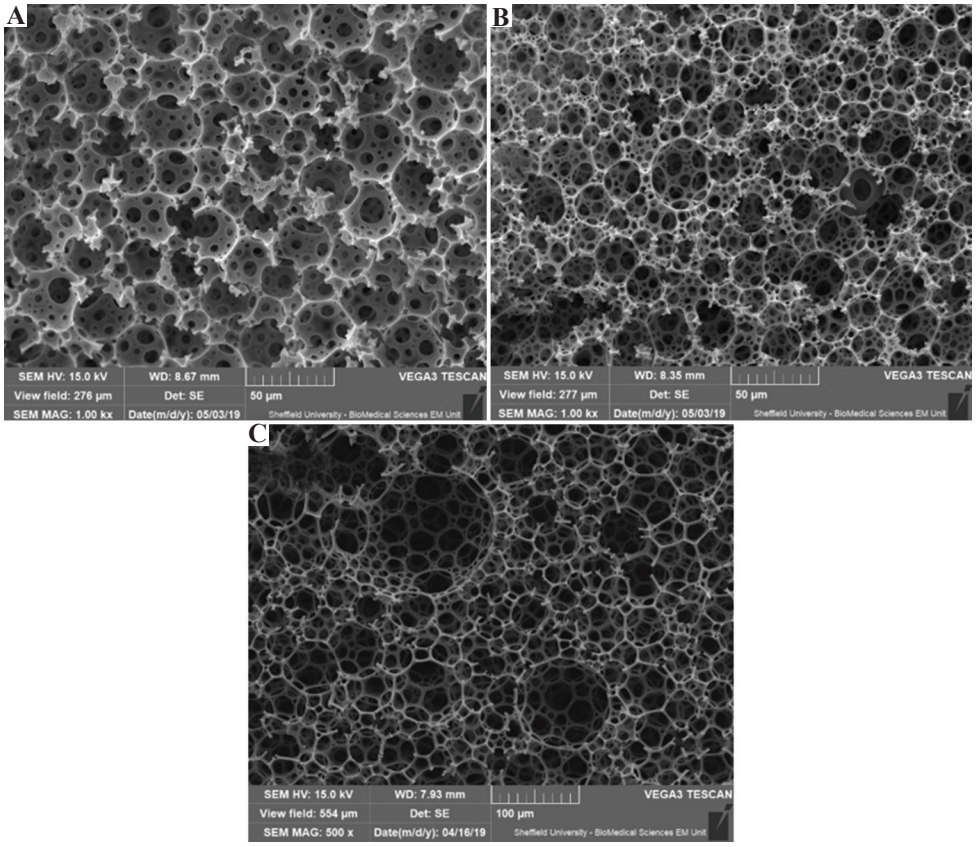


**Figure 1.** Scanning electron microscope pictures showing an example of the polymerized high internal phase emulsions structure made with different water ratios. The monomer-to-water ratios are (A) 1:9, (B) 1:20, and (C) 1:40. All samples contain 10 wt% surfactant relative to the monomer and were mixed at 350 rpm.

This is because the distance between the monomers reduces from a typical van der Waals distance (~3 Å) to a covalent bond distance (~1.54 Å) during polymerization. This contraction creates interconnecting windows (holes) between adjacent water droplets[37]. In the HIPE emulsion, tightly packed water droplets deform into polyhedral shapes[38]. A thin coating of monomer and surfactant prevents them from merging together. This barrier ruptures and breaks apart during the polymerization reaction to create the connecting windows. Monomers such as methyl acrylate have a high contraction level during polymerization, and varying its amount in the emulsion can modify the interconnectivity[30]. Furthermore, increasing the water volume ratio in the initial emulsion increases porosity and openness by creating a thinner monomer film surrounding water droplets[39].

The surfactant has a profound effect on emulsion stability and directly affects the polyHIPE interconnectivity, permeability, and size of the pores in the polymer structure[40]. A surfactant with a concentration below 5 wt% relative to the monomer in the initial emulsion creates a polyHIPE with closed porosity, up to 10 wt% creates small connecting windows which increase until around 45 wt%; an amount higher than this will cause a gradual decline in the physical properties and structural collapse[34]. The surfactant is an amphiphilic compound which stabilizes the emulsion by orientating itself at the interface between the two emulsion phases with the hydrophobic part pointed toward the oil phase and the hydrophilic head group toward the aqueous phase[41]. Surfactants are classified by their hydrophilic-lipophilic balance (HLB) number which relates to the ratio between the hydrophilic and the lipophilic parts of the surfactant; low HLB (3–6) is oil soluble and used for water droplets in oil (W/O) emulsions, whereas high HLB (8–18) is water soluble for O/W emulsions[41]. A stable emulsion can accommodate a thin barrier film between adjacent water droplets, which is more prone to rupture during polymerization.

Filter-based applications may require small pore sizes and high surface area. This can be achieved by either an increase in the surfactant or addition of a salt to the emulsions droplet phase, as shown comprehensively by Williams *et al.*[31] Typical polyHIPEs have a surface area around 3–20 $m^2g^{-1}$, but replacing some monomeric continuous phase with a solvent can increase the area to 829 $m^2g^{-1}$ depending on the solvent used[33]. Solvents in

the continuous phase can act as a cosurfactant that results in smaller pores and an increased interconnectivity between the pores[32].

There is a range of research interest in emulsion templating to create porous polyHIPE structures[42-46]. The research interest also extends to their potential for a range of fluid separation applications, including filters, membranes, and chromatography[47]. There are detailed reviews on emulsion templating applications[48-51] as well as the range of materials and uses of a porous foam manufactured using both liquid- and bubble-based templating[52]. Some specific reviews also detailed the porous materials and uses of HIPE-based emulsions and foam templating[53] as well as the potential of 3D printing as a method to produce tissue engineering scaffolds[54].

## 5. Considerations for a polyHIPE-based RPE filter against viruses

The perspective polyHIPE filters need to be tested to determine its effectiveness as a RPE filter in relation to different porosities, thicknesses, and surface functionalization. The average inhalation under moderate and strenuous workload 30 L/min and 85 L/min, respectively[14]. To test the filter efficiency under these flow rates, typically NaCl particles are aerosolized using a particle generator and the particle concentration is tested up- and downstream of the filter. This testing can also represent aerosolized single viruses using small, 0.037–3.2 μm, sized particles[14].

The porosity, chemical functionality, and mechanical strength of the polyHIPE can be independently tuned based on the emulsion constituents or conditions. This adjustment has led to a variety of separation-based applications, including filter, metal ion separation, and chromatography[55]. PolyHIPEs have a huge separation potential with a tunable permeability, an ability to alter surface chemistry, different material choices, and interconnected pores; their uses as a filter for small molecule separation have been reviewed[56].

The requirements of polyHIPE specifically for the production of a respirator filter that can prevent the transmission of aerosolized virus-laden particles have yet to be defined. In the aspect of virus filtration, there is a difference between mechanical filtration (pore size/interconnectivity) and the use of an optimally functionalized surface for immobilizing the virus onto the polymer. Despite lacking the information regarding the pore size, an example of virus filtration elaborated in the withdrawn 2008 patent EP 1 889 811 A1 highlights the importance of a functionalized surface (aminated, sulfonated, or betainated) to improve the filtration of poliovirus type 1 from water. The presented data showed the removal of 99.99% poliovirus through a functionalized surface against the 99% reduction in a non-functionalized one. The filter could also be regenerated using either a concentrated electrolyte/acidic or alkaline solution depending on the surface functionalization. A heparin-coated polyHIPE-based chromatographic column has also been used to selectively bind *Enterovirus* 71 and purify it from solutions, and the polyHIPE has a porosity of 0.2–0.5 μm and interconnected pore sizes in the range of 0.5–2 μm for the isolation of virus particles[57]. The virus can be eluted from the column afterward.

Infection by airborne transmission occurs after the inhalation of the contaminated droplets. Aerosol transmission of virus-laden droplets is still not fully understood in terms of the effects of the exhaled particle size distribution and the number of infectious viruses in each particle[11]. The virus itself is between 50 and 200 nm in radius. Typical speech and coughing can produce aerosolized liquid droplets with an average size of <20 μm which could linger in the air between 20 min and 1 h depending on the environmental conditions; 50 and 100 μm sized particles can stay in the air for approximately 20 s and 3 min while smaller particles can potentially remain airborne for a longer period of time. Nevertheless, all particles pose a potential risk of being inhaled while they remain airborne. It is important to note that the chances of inhalation increase as the particle size reduces[11].

The principal function of a majority of the polyHIPE-based air filters is to remove particulates from the air. Vehicle exhaust fumes represent a major source of air pollution, for example, the hydrocarbon fragments produced from the partial combustion of fuel[58]. In particular, there is a need to filter out airborne particulate matter of <2.5 μm ($PM_{2.5}$) as these particles in this size range can damage the respiratory system[59]. According to the ISO standardized vocabulary for ultrafine particulate matter (PM), PM0.1 refers to the particulates with aerodynamic diameters of 100 nm or less, PM2.5 with 2.5 μm, and PM10 with 10 μm[60]. Small pollutants of <2.5 μm are small enough to penetrate deep into the lungs and cause damage to the alveolar walls.

A polyHIPE-based aerosol filter for automobile exhaust achieved an increase in the capture efficiency of particles (<2.5 μm) from 1.2% to 72.2% after surface functionalisation of an amino ($–NH_2$) end group[61]. The polyHIPE filter captured these particles both on the outer surface and within the pores (pore sizes were between 3.0 and 7.4 μm, interconnects of 1.1 and 2.4 μm), and its effectiveness was attributed to the surface coating as well as the coating thickness physically reducing the interconnect and pore size. The filtering efficiency of a sample with a thickness between 1 and 14 mm rose from 65 to 80% in filtering particulates of <2.5 μm.

This highlights that in addition to sample thickness, other factors, such as porosity and interconnectivity of the polyHIPE, are also required for improving filtering efficiency.

There is trade-off between the polyHIPE pore size/interconnectivity and the air flow resistance through the material. Smaller pores not only increase the strength of filtration but also the air flow resistance, which is recorded as an increased pressure drop[62]. A more permeable filter will have a lower pressure drop, but at a cost of filtration efficiency. This is the same for fibrous masks in which the air flow is typically perpendicular to the packed fibres. Increasing the amount of fibrous material improves particle capture, but causes more air flow resistance[63]. Ideally, the filter should have a low pressure drop and high collection efficiency[13]. Typical filters are porous materials that allow air transfer while trapping airborne particles; there are several types of trapping mechanisms[13]. A typical filter example is Nylon6 (N6)-based non-woven fibrous mesh made by electrospinning[63].

## 6. PolyHIPE filter applications

To create micron-sized pores within the polyHIPE, the initial emulsion can be mixed using a high-speed homogenizer (25,000 rpm), resulting in average pore diameters between 0.6 and 4.5 μm, an increase in interconnectivity was observed when increasing the surfactant from 5 to 15wt%, and the porosity from 75 to 90%[27]. A styrene/divinylbenzene (St-DVB)-based fibrous polyHIPE with pore sizes ranging from 2 to 7 μm and interconnect windows down to 1 μm was produced by tuning both the surfactant and mixing methods[29].

The polyHIPE structure has been used for the chromatographic separation of proteins because of its tunable porosity and flexible polymer choice. Glycidyl methacrylate (GMA) is a popular monomer for this application because it can be chemically functionalized through the epoxy groups[64]. A list can be found in **Table 2**. When used with the cross-linker ethylene glycol dimethacrylate (EGDMA), polyHIPEs created from these monomers are more hydrophilic compared to their styrene/DVB counterparts. Poly(GMA-co-EGDMA)-based polyHIPEs have been reported to have 1–10 μm pores with submicron interconnects for protein separation[64]. They can be blended with an elastomer chemically modified with diethylamine to get weak anion exchange supports in the flexible membrane for protein purification by ion exchange chromatography with 3–10 μm porosity and 1–3 μm interconnects[65]. A similar polyHIPE polymer blend has been continuously reused over 300 times[66], and grafted GMA brushes have been used for chromatographic separation of proteins in an epoxy-based monoliths[67].

A redox-initiated polymerization of a poly(methyl methacrylate)-based polyHIPE filter can be cured *in situ* within a tubular mold and used within 20 min. This is useful if the housing material is opaque to light or heat sensitive as the reaction can occur at room temperature[24]. A similar polymerization method has been used for the polyHIPE-based chromatography protein purification[65]. Low porosity emulsion templated foams still retain some permeability[40], but it lacks the interconnectivity level obtained using high volumes of water in the initial emulsion.

PolyHIPEs created from a W/O emulsion are hydrophobic because a water immiscible monomer is used in the initial emulsion. This hydrophobicity has led to applications such as oil or organic solvent removal from water where recycled polystyrene is one of the monomers[68]. Hydrophobicity can be increased by adding $Fe_3O_4$ to the initial monomer to create superhydrophobic foams (contact angle over 150°) to remove oil or organic solvent pollutants from water[69]. A poly(dicyclopentadiene)-based polyHIPE oxidizes in air to produce reactive peroxy species that can be used to either decontaminate nerve agents[70] or produce a self-decontaminating air filter[71].

A poly(styrene-co-DVB) polyHIPE column with mean interconnects 0.57–0.59 μm can separate 52 nm particles from 155 nm ones through a difference in retention time[72]. For other aqueous-based filter applications, the surface of the polyHIPE can be sulfonated to create a more hydrophilic surface and subsequently used to filter 1–11 μm particles of calcium carbonate (aragonite) dispersed in water[73]. For microfiltration applications, the outer surface of polyHIPEs can also be functionalized *in situ* by adding a hydrophilic monomer, such as sodium acrylate, to the emulsion droplet phase to filter out microalgae[74]. PolyHIPE scaffolds coated with iron hydroxides can remove arsenic from contaminated water[75]. The use of pickering based polyHIPEs for the decontamination of pollutants water has been reviewed in detail elsewhere[76].

To create a simple polyHIPE sheet, an open pored surface is critical and care is needed to maintain the surface porosity when curing the HIPE into a mold to create a porous membrane. The use of either a hydrophilic or hydrophobic mold material affects the surface porosity of the polyHIPE at the HIPE/mold interface[43,73,77-80]. An open or closed pored surface is created by preferential wetting of the mold surface with either the aqueous or monomeric (oil) phase of the HIPE and is postulated to relate to the surfactant orientation at the mold surface[73]. When polymerizing a W/O emulsions such as St-DVB in water, the emulsion can destabilize against a PVC mold, have a closed pored surface skin against a PP mold and an open porosity against a PTFE one[43]. The amount of open surface porosity can be fine-tuned by varying the

**Table 2.** PolyHIPE filter-based applications

| Material | Application | Pore size (μm) | Interconnect (μm) | Surface functionalization | Characteristics | Ref |
|---|---|---|---|---|---|---|
| Poly(St-MMA-DVB) | Air filter | 3.0–7.4 | 1.1–2.4 | Amino (–NH2) functionalized | High thermal resistance | [61] |
| Poly(St-GMA-DVB) | Column to purify virus for vaccine production | 0.5–2 | 0.2–0.5 | Heparin | Heparin functionalized to purify *Enterovirus* 71 (EV71) | [57] |
| PEGMA-SA-PEGDA | 3D-printed hemostatic and absorbent polyHIPE wound dressing | ≈3 | ≈0.75 | - | Kaolin-loaded, 3D-printed cure on dispense 3D printed | [87] |
| Poly(GMA -EGDMA) | Protein separation through chromatography | 1–10 | 0.1–0.5 | Modified to bear weak anion exchange groups | Surface epoxy groups can be chemically modified | [64] |
| Poly(GMA -EGDMA-EHA) | Protein purification by chromatography | 3 – 10 | 1 – 3 | Surface functionalized to create weak anion exchange supports | Flexible polyHIPE membranes that can be rolled into a module | [65] |
| Epoxy resin-based monolith with GMA brushes | Ion exchange chromatography | - | - | Anion exchange functionality using iodomethane | Proteins recovery with no obvious sign of unfolding | [67] |
| Poly(GMA -co-EGDMA) | Protein separation by chromatography | 0.6–0.1 | - | Surface modified by diethylamine | High column efficiency and protein-binding capacity | [66] |
| Poly(MMA-co-EGDMA) and poly(BeMa-co-EGDMA) | *In situ* cured open pored filter | 16–29 | 2.4–6.4 | - | Redox-initiated polymerization for *in situ* polymerization of a filter | [24] |
| Sulfonated polystyrene, EGDMA, TEOS, and butyl acrylate | Oil recovery | 82.3–145.6 | 7.8–13.5 | - | Made using recycled polystyrene | [68] |
| Poly(St-DVB) | Oil spill recovery | - | - | - | $Fe_3O_4$ increased hydrophobicity | [69] |
| Poly(DCPD) | Decontamination of chemical warfare agent and self-decontaminating air filter | 1–4<br>23.9±16.4 | - | Air oxidation produces hydroperoxide species | Rapidly oxidizes at 85°C; decontaminates chemical warfare agents | [70,71] |
| Poly(St-DVB) with EHA or ethyl vinyl benzene | Microfiltration | - | - | Sulfonated to produce hydrophilic surface | Filtration of 1–11 μm particles of calcium carbonate in water | [73] |
| Poly(St-DVB) and poly(EGDMA) | Chromatographic separation of nanoparticles | 1.08–1.12 | 0.19–0.59 | - | Separation of engineered nanoparticles (52 nm, 155 nm) | [72] |
| Poly(butyl acrylate- EGDMA) | Ultrafiltration of microalgae | 1–80 | 0.1–3 | *In situ* functionalization using sodium acrylate | Hydrophilic surface through *in situ* functionalization | [74] |
| Poly(St-b -P4VP) | Bacteria filter and its inactivation using NIR sterilization | 5–50 | 1–5 | Stabilized with amphiphilic block copolymers for potential surface functionalization | Coating with polypyrrole nanoparticles and NIR-induced heat to sterilize (20–180°C) within 10 s | [82] |
| Poly(MMA-EGDMA) | Improved mechanical properties of polyHIPE | 0.8–25 and 0.6–4.5 | 0.2–5.9 | - | High E-moduli up to 211 MPa | [27] |
| Poly(St-DVB) | Ultra-low-density polyHIPE | 1.6–9.3 | - | - | Ultra-low-density achieved 0.0126 g/cm$^3$ | [29] |

The monomer abbreviations used are: MMA, methyl methacrylate; EGDMA, ethylene glycol dimethacrylate, DVB, divinylbenzene; GMA, glycidyl methacrylate; EHA, ethylhexyl acrylate; BeMA, benzyl methacrylate, TEOS, tetraethyl orthosilicate; St, styrene; DCPD, dicyclopentadiene, P4VP, polyvinylpyridine; PEG, polyethylene glycol; SA, sodium acrylate; PEGDA, polyethylene glycol diacrylate; PEGMA, polyethylene glycol methacrylate.

surfactant amount and droplet volume ratio of the initial emulsion[77]. A hydrophilic material is required to create an open surface with W/O emulsions. This can include hydrophilic glass surface[78-80] or alginate[81].

PolyHIPE-based bacteria filters can be surface-coated with polypyrrole nanoparticles. These particles act as nanoheater that can be heated to 180°C within 10 s using near-infrared irradiation to kill trapped bacteria[82]. An approach like this could be beneficial for sterilizing a polyHIPE-based filter as the inner surface of current N95 filters can have a warm, wet microclimate which can contribute to bacterial growth (a strategy that could also work for viral infections)[83]. Silver is an effective antibacterial agent and can be coated on the surface of a polystyrene sulfonate-based polyHIPE[84] or a polystyrene-based polyHIPE[85]. Alternatively, broad-spectrum antimicrobial activity can be obtained by iodine-releasing polyHIPEs made from kaolin-containing cross-linked PEG-NaAA-PEG polyHIPEs[86]. These can be 3D printed into a mesh for wound dressing[87] as iodine is both antimicrobial and virucidal[88]. Alternatively, antibacterial properties of the polyHIPE surface can be acquired by dipping the polymer in antibiotics, such as ciprofloxacin or tetracycline HCL, although freezing and lyophilizing are required afterward as reported in this case[89]. However, antibiotics do not work against viral infections.

Electrospinning has also been combined with emulsion templating to prevent cell migration in a tissue engineered scaffold[90]. This hybrid manufacture approach has the potential to combine the strengths of fibrous and emulsion templated porous structures. Nanofibrous-based emulsion templated foams are fragile and can be difficult to scale. Nanofibrous porous syndiotactic polystyrene-based polyHIPE (average fibrous diameter of about 24 nm) can be used to remove airborne volatile organic compounds; however, the reported manufacture method required extensive extraction through boiling in acetone and freeze-drying to produce the structures according to the choice of material[91].

## 7. AM of emulsions

Emulsions, in particular, HIPEs that contain photocurable monomer can be used as an ink for AM techniques. Stereolithography and extrusion-based printing are 3D printing techniques that can be used to print with these emulsions. The conditions of the emulsion used in these techniques can control the porosity, while the print design determines the bulk shape. The HIPE viscosity can be tailored for each technique: low speed mixing (350rpm) creates a liquid suitable for stereolithography[92]. While, a highly viscous emulsion is advantageous for its shape retention during extrusion-based 3D printing. This can be achieved either through additives[93], high-speed mixing (2500 rpm)[94], or other methods to change the viscosity[95]. Since the emulsion is a liquid, its benefits and constraints are similar to those of the liquid-based 3D printing[96]. A review of the current progress of AM coupled with emulsion templating is discussed below.

## 8. Stereolithography of HIPE

Raster scanning UV laser light across the top surface of a vat of HIPE can be used to polymerize both simple porous polyHIPE shapes on top of a glass surface using an in-house built microstereolithography (μSL) rig[92]. Later, the group produced a woodpile structure of alternative polyHIPE lines of 350 μm and used it as a porous scaffold for tissue culture support[39,97,98] (**Figure 2**). The size of the polymerized regions varied with write speed and UV light power, and the droplet size determines the achievable minimum feature size. The internal microporosity of the 3D-printed polyHIPE was preserved and comparable to a bulk cured emulsion.

Light-based raster scanning of HIPEs requires careful control over light scattering to reduce both the overcuring and formation of a surface skin on the polyHIPE[99]. The refractive index mismatches between the water and oil phase scatters light, and this results in the characteristic whiteness of the emulsion. This effect is problematic during stereolithography as the emulsion also scatters the polymerizing light outward from the point of exposure, creating a gradually reduced cross-linked monomer gradient that decreases outward from polymerized polymer to liquid monomer. On washing, this partially polymerized polymer collapses on itself, covering the polyHIPE with a surface skin. Overlapping of two partially polymerized regions fully polymerizes the polymer causing overcuring and connecting polymer bridges[99]. To reduce the surface skin and increase printable resolution, a light absorber can be used to control the light scattering[99]. A surface skin is also found when the HIPE is polymerized against certain mold materials.[43,73,77-80]. Although a closed, pored outer surface can act as a barrier to slow down drug release from a 3D-printed emulsion-based hydrogel[100], it is detrimental for filter-based applications.

A dynamic mask projection-based stereolithography approach can be used to 3D print the HIPE ink using a digital micromirror device (DMD) to produce complex 3D shapes in a layer-by-layer fashion[101]. A light absorber is still required to improve resolution, and the authors did not mention whether there was an outer surface skin. The authors reported that this layer-by-layer-based printing is sensitive to viscosity of the emulsion, which can be lowered using a solvent such as toluene. Furthermore, DMD projection can be used to 3D print porous polyHIPE tubes in a continuous process[92]. A functional polymer-based polyHIPE made of GMA was 3D printed using a digital light processing (DLP) printer to create

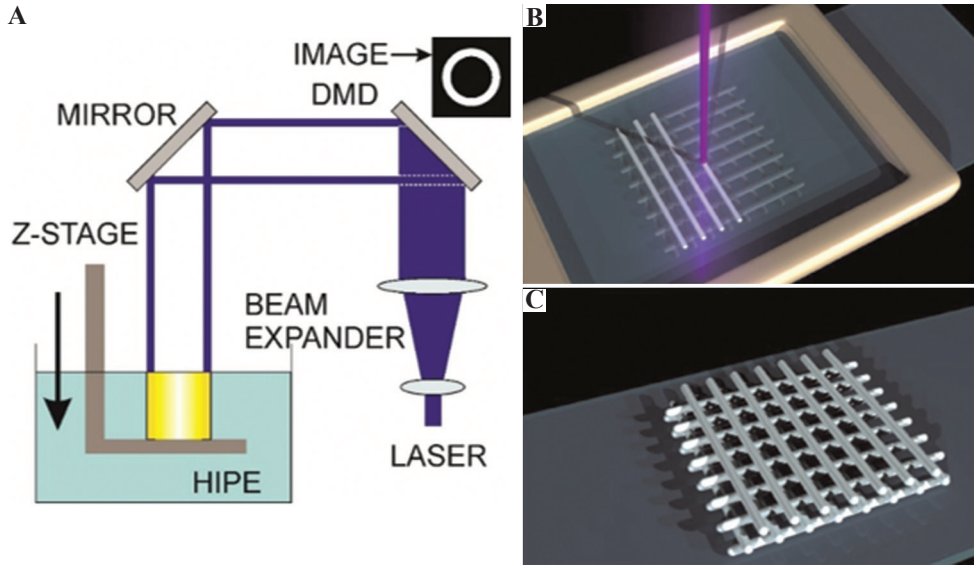


**Figure 2.** Schematic (A) and 3D rendering (B and C) showing a projection and raster scanning-based 3D printing. (A) reproduced from Ref.[92] with permission from John Wiley and Sons, Licensed under Creative Common License. (B) and (C) modified from Journal of the Mechanical Behavior of Biomedical Materials, Volume 54, Owen R, Sherbone C, Paterson T, *et al*. Emulsion templated scaffolds with tunable mechanical properties for bone tissue engineering, pp 159-172, Copyright (2016), with permission from Elsevier[39].

a chromatography column[102]. Other DLP-based 3D printing techniques have used an oil-in-water emulsion-based ink consisting of droplets of photocurable ink within an aqueous suspension[103].

The 3D print speeds vary depending on the method used. The single line writing speeds of direct laser writing for printing polyHIPE are 1 – 5 mm/s, which is dependent on the laser power[92]. With these speeds the authors created a circular 13mm, 4 layered woodpile structure in 13 minutes[39]. Alternatively, the projection-based stereolithography can print a 17.25 $mm^2$ surface area and complex geometries simultaneously at a printing speed of 2 vertical $mm/h^{-1}$ for a layer thickness of 25 μm[101]. Stereolithography-based 3D printing setups are becoming quite cost effective, after the major patent protecting the technique (US5762856A, Hull) expired in 2015 and start-up companies started to produce low-cost setups.

## 9. Extrusion-based 3D printing

Through a manufacturing process known as material extrusion (also called fused deposition modeling or robocasting), a HIPE ink can be extruded through a syringe and polymerized using UV light to create a porous polyHIPE-based structure (**Figure 3**). High emulsion viscosity is suitable for this 3D printing method as the emulsion ink can maintain its structure post-extrusion without unwanted spreading before polymerization, and the emulsion viscosity is tunable by altering the respective component amounts in the emulsion[93]. No surface skin is observed on the outer surface of extrusion-based 3D-printed polyHIPEs[93]. This is expected as the emulsion is curing against air; therefore, there is no surface contact with a material that can adversely affect the surface porosity by surface destabilization. This technique has also been used to create a composite polyHIPE for use as a biocatalytic flow reactor using an enzyme-laden hydrogel as the emulsion droplet phase[104]. Alternatively, an emulsion can simply be injected directly into a void before bulk polymerization[25]. Extrusion-based printing of emulsion has been demonstrated to print at a speed of 10 mm $s^{-1}$ with extrusion width of 0.6 mm using a modified RepRap style 3D printer[93]. Modified extrusion-based 3D printers have been used to print emulsions that are cured on demand, with print speeds tested up to 9 mm/s and layer heights of 100–300 μm[104].

To create hydrophilic porous foams through material extrusion, an oil-in-water emulsion can be used with a UV cure during extrusion. Some of the materials include poly(ethylene glycol) diacrylate (PEGDA), alginate, and hyaluronic acid with mineral oil as the dispersed phase to increase emulsion viscosity[105]. However, the droplet size was reported to increase overtime and the samples are required to wash in DCM to remove the oil and subsequently lyophilized at −80°C for 24 h to solidify and dry.

Extrusion-based 3D printing combined with emulsion templating can be used to create a porous ceramic that will be sintered at 1600°C for 2 h to form a solid[106]. Nanoscale porosity of 100-900 nm can be achieved using a nanodroplet-stabilized pickering emulsions which are 3D printed through direct ink writing. It shows that 3D extrusion-based printing using nanoporosity emulsions is achievable[107]. Furthermore, large 100 μm pores

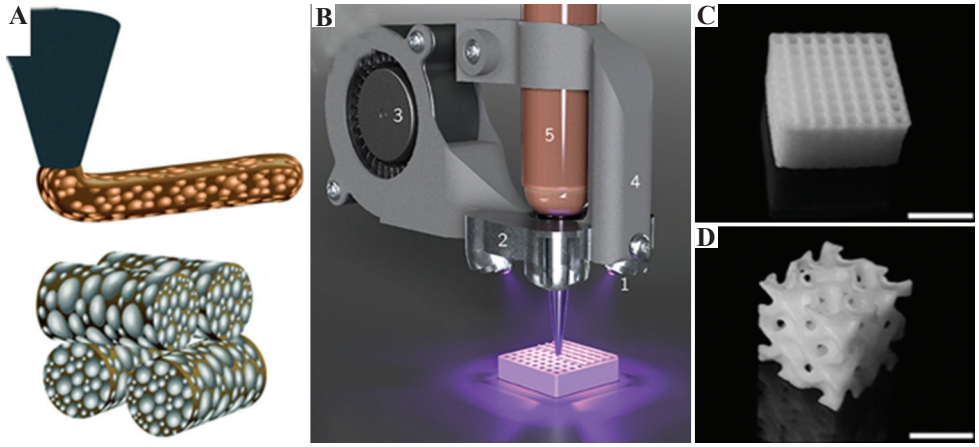


**Figure 3.** (A) 3D schematic showing an extruded silica-chitosan-based emulsion and the theoretical pore distribution within the extruded part and subsequent polymerized structure. Adapted from ref.[105] with permission from The Royal Society of Chemistry. (B) 3D model showing a cure-on-dispense 3D printing of a photocurable monomeric-based emulsion, (C and D) two pictures of polymerized high internal phase emulsions based structures created using this device. (B-D) Images adapted from ref.[104] licensed under Creative Commons Attribution License.

were also created using sacrificial polymer beads in the emulsion, highlighting the versatility of this method to use porogens other than water for additional level of porosity control. Emulsions stabilized with submicron pickering particles can be used with a range of liquids and applied to create both micro- and nano-sized emulsion droplets[108]. $SiO_2$ nanoparticles can stabilize a styrene-based W/O emulsion which holds its shape before being thermally polymerized in an oil bath[109]. Pickering emulsions using hydrophobized silica particle can create a 140–450 nm droplet size distribution[110]. However, when particle-stabilized emulsions are used for foam templating, they typically have low interconnectivity as the particles hinder interconnecting window formation. Nevertheless, adding a small amount of surfactant fixes this by orientating itself at the contact point between adjacent droplets, creating interconnectivity windows during polymerization[111].

Extrusion-based emulsion templating, including a variety of AM techniques, has numerous applications in tissue engineering as the inherent interconnectivity facilitates cell ingrowth[54]. These include a 3D-printed cure-on-dispense kaolin clay-loaded poly(ethylene glycol) diacrylate and methacrylate-based O/W HIPE (3 μm average porosity with 0.75 μm interconnects) with an ability to swell up to 11 times its size in buffer solution[87]. A chitosan-modified silica nanoparticle for potential drug release of 3D-printed materials has been reported, although the post-cross-linking with glutaraldehyde took up to 48 h[112]. Extrusion-based printing also lends itself useful for printing multiple materials together, such as a degradable UV curable HIPE combined with an outer thermoplastic extruded poly(ε-caprolactone) (PCL) or poly(lactic acid) (PLA) polymer[94].

Extrusion-based 3D printing can be applied with non-polymerizable polymers dissolved in a solvent. Here, the solvent acts as a porogen through polymer precipitation-based 3D printing. This technique uses the difference in polymer solubility between two mutually miscible solvents to inject a solvent dissolved polymer into a vat of a non-solvent to evoke rapid polymer solidification *in situ*[113]. By varying the solvent/polymer ratio within this immersion precipitation 3D printing *(ip3DP),* tunable porous structures can be created from a range of dissolvable polymers[114]. Air-based drying using a similar solvent for dissolving has been reported using a pickering polyHIPE made from degradable polymers, such as poly(l-lactic acid) (PLLA) and PCL with hydrophobically modified silica nanoparticles (h-$SiO_2$) to both stabilize the initial emulsion and increase its viscosity. The polymers were dissolved in dichloromethane, and after printing, the solvent was evaporated to leave behind solid scaffolds, although the samples were deformed during solvent evaporation[115]. The authors reported in a follow-up study that this deformation can be avoided using hydrophobically modified hydroxyapatite (HAp) nanoparticles in the initial PCL-based pickering emulsion[116].

There are alternative routes, other than emulsion templating, for producing porous structures. Air bubbles can be used as a porogen, either by directly printing a UV curable foamed monomer[117] or using a foam that sets by thermogelation after it has been printed[118]. Alternatively, a blowing agent can be used within the 3D-printed part, which is decomposed post-processing to expand it into a porous material[119]. Furthermore, particles such as sieved salt can be used as a sacrificial template for a monomer to cross-link around, 75 μm extra

fine salt crystals can be combined with a DLP printer and photocurable ink, although the samples had limited interconnectivity[120]. Similarly, monodisperse particles of wax or polycaprolactone can be used within a 3D-printed silk to create porosity[121].

## 10. Emulsion reproducibility and scalability

Commercial virus filtration membranes that use size exclusion as the primary filtering mechanism require a high degree of control over the pore size distribution; where a larger pore sizes reduces the filters ability to retain the virus[122]. To create a reproducible filter using emulsion templating, every mixing aspect of the initial emulsion has to be controlled. The same mixing speed can be used; however, using mechanical mixing to break up the droplet phase creates a broad distribution of pore sizes. These include overhead stirrers (320–1260 rpm)[26] and high-speed homogenizers (25,000 rpm)[27]. A syringe pump can be used to add the droplet phase during mixing to create a more uniform droplet breakup to increase reproducibility between emulsions[28]. However, this will still produce a polydisperse droplet size distribution. Depending on the difference between the smallest and largest pores, this may be sufficient for an antiviral filter. Many large-scale emulsification techniques that are used in industries, such as the pharmaceuticals and cosmetics, could potentially be adapted[123].

Emulsification techniques using membrane, microchannel or microfluidic-based devices can create an unprecedented level of control over emulsion droplets as well as particle synthesis[124]. A microfluidic device can create droplets one by one to produce a highly ordered monodisperse polyHIPE with precise control over pore size and interconnectivity throughout the structure[125,126] (**Figure 4**), especially when combined with the control of the locus of initiation[127]. Microfluidic-based devices can be adapted to produce bubbles of air as the dispersed phase template that produces a foamed styrene-in-water emulsion for creating a porous material[128]. In addition, when using a valve-based flow-focusing junction (vFF) within a microfluidic device, the air bubble size can be adjusted in real time to produce a porous gradient ranging from 80 to 800 μm pores, and this method has been used to produce nanohydroxyapatite particle-loaded gelatin-based foams that were 3D printed and then sintered to produce a porous ceramic[129]. This valve-based approach can also be used for W/O emulsions[130].

The logistics, potential benefits, and limitations regarding the upscaling of both emulsion- and foam-based templating methods to produce porous polymers have been reviewed in detail by Stubenrauch *et al*.[131]. The limitation of microfluidic setups is that droplets are made one by one. Scaled-up production of monodisperse droplets is achievable using a circularly arranged microfluidic channels with 128 cross-junctions[132] which can be adapted to a parallelized network of channels within a coaxial annular world-to-chip interface[133].

Membrane-based emulsification is one such way to create a scalable emulsion templating process. A monodisperse foam can potentially be continuously made using a dispersion cell, and this has recently been used for emulsion templating where the air is the dispersed phase[134]. Furthermore, other studies about membrane-based emulsions demonstrated the creation of a range of micro- and nanoemulsions with tunable droplet sizes[135] and these techniques were used to produce porous particles and materials[136].

## 11. Challenges and future perspectives

In this review, the current research on the AM of emulsion-based inks that produce porous foams of various materials and sizes is discussed. The versatility of emulsion templating in the manufacture of porous materials and its use in 3D printing indicate that there are many potential crossovers that could adapt this technology to new applications, such as a respirator filter against bacterial and viral infections of the respiratory tract. Nevertheless, the AM aspects of this technique are still in its infancy. Therefore, precautions should be taken when choosing a specific emulsion-based AM technique. Specifically, an aerosol filter is part of the RPE that is used prevent the transmission of COVID-19.

Emulsion templating is a versatile manufacturing technique. The porosity, interconnectivity, surface chemistry, and material choice are all independent variables that can be varied depending on the desired filter requirements. A 3D-printed polyHIPE-based respirator needs to adhere to the strict strict classification requirements before being categorized as FFP1, FFP2, or FFP3. These requirements include being permeable to air while adhering to the required standards of air flow resistance and retaining high filter efficiency. The European standards EN 149:2001 + A1:2009 set specific criteria for this, including particle penetration determined using a NaCl aerosol generator.

PolyHIPE-based filters can be used to remove airborne particulates, such as 2.5 μm hydrocarbon fragments from the exhaust fumes, and as a water filter which can remove 1–11 μm suspended particulates. PolyHIPE publications relating to specific virus binding and antibacterial feature are limited but they highlight the importance of surface functionalization that leads to efficient trapping of virus-laden particles by the polymer surface. We foresee the inherent hydrophobicity of the polyHIPE created from water-in-oil emulsions being advantageous in preventing virus-containing airborne water droplets from penetrating the material. Furthermore, the tunable mechanical properties, manufacture flexibility,

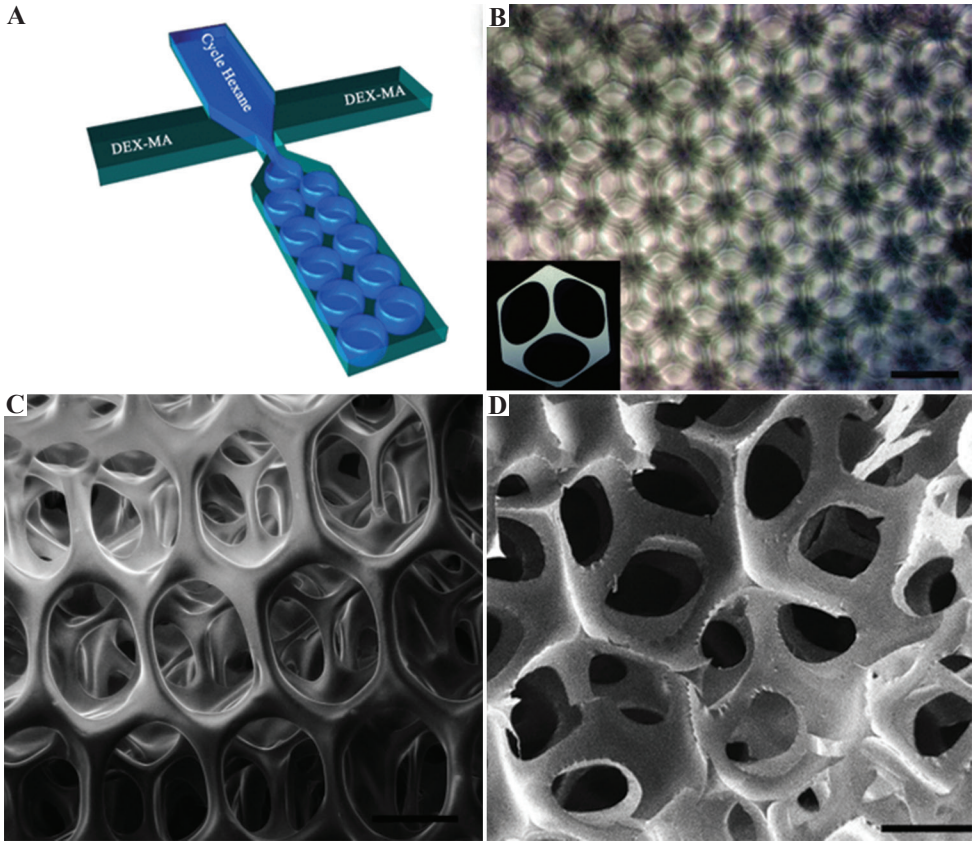


**Figure 4.** (A). A computer-generated schematic representation of the microfluidic monodisperse droplet formation. (B) Optical microscope picture of the closely packed droplets in the emulsion (scale bar 200 μm). (C and D) Scanning electron microscope image of the polymerized high internal phase emulsions created using this microfluidic system showing the surface and a fractured section (scale bar 100 μm). Images were adapted from Costantini *et al.*[125], respectively, under the Creative Commons License.

increased temperature resistance, and potential reusability are some of its strengths.

A scalable emulsification process is required to produce reproducible emulsions with high control over porosity and interconnectivity between batches. There are many industrial emulsification tools that can meet this need. Emulsion stability needs to be considered if the printable emulsion is to be stored for an extended period. Emulsion destabilization can cause larger droplets to form at the expense of smaller ones. 3D printing of the emulsion will need to preserve the initial droplet size, not cause destabilization, and minimize the time between the creation of emulsion and its subsequent polymerization into the filter material.

From an AM perspective, an extrusion-based 3D printing is recommended as a viable printing technique for filter applications because it maintains an open outer porosity. A micro- or nanoemulsion with tightly packed water droplets has high viscosity so this type of emulsion is not suitable for stereolithography-based 3D printing as the emulsion cannot spread over the surface for layering. Furthermore, this technique has the capability to extrude multiple emulsions on the same print, giving user control over multiple materials, surface functionalities, and a porosity gradient within the filter. All of which could be used to create a complex internal geometry that controls the air movement through the filter. Nevertheless, this is only viable for niche applications currently because 3D printing emulsion inks are a time-consuming process. Its strength lies in its customizability or complex bespoke applications that cannot be made by the traditional manufacturing techniques.

For an aerosol-based filter application that only requires a porous membrane or column, bulk polymerization is preferable over AM. Pouring the emulsion into a membrane or mold should suffice, and specific mold materials can be chosen to prevent the formation of a surface skin on the polyHIPE surface. This would also be the simplest method for producing a filter that can be brought to the market and can be incorporated into the current RPE production using 3D printing. UV or redox based cured emulsions could be the most suitable for the industrial sector because of their fast curing times.

## Acknowledgements

We would like to acknowledge funding from the Engineering and Physical Sciences Research Council (Grant no. EP/R511754/1 and EP/L505055/1).

## Conflicts of interest

No conflicts of interest were reported by all authors.

## References


1. Joshi SC, Sheikh AA, 2015, 3D printing in aerospace and its long-term sustainability. *Virtual Phys Prototyping*, 10:175–85. https://doi.org/10.1080/17452759.2015.1111519
2. Conner BP, Manogharan GP, Martof AN, *et al.*, 2014, Making Sense of 3-D Printing: Creating a Map of Additive Manufacturing Products and Services. *Addit Manuf*, 1:64–76. https://doi.org/10.1016/j.addma.2014.08.005
3. Ng WL, Chua CK, Shen YF, 2019, Print me an organ? Why we are not there yet. *Progress Polymer Sci*, 97:101145. https://doi.org/10.1016/j.progpolymsci.2019.101145
4. Tino R, Moore R, Antoline S, *et al.*, 2020, COVID-19 and the Role of 3D Printing in Medicine. Springer, Berlin, Germany.
5. Celik HK, Kose O, Ulmeanu ME, *et al.*, 2020, Design and Additive Manufacturing of a Medical Face Shield for Healthcare Workers Battling Coronavirus (COVID-19). *Int J Bioprint*, 6:286. https://doi.org/10.18063/ijb.v6i4.286
6. Cook TM, 2020, Personal protective equipment during the coronavirus disease (COVID) 2019 pandemic-a narrative review. *Anaesthesia*, 75:920–7. https://doi.org/10.1111/anae.15071
7. Public Health England, 2020, COVID-19: Infection Prevention and Control Guidance. Public Health England, United Kingdom, England.
8. Chen N, Zhou M, Dong X, *et al.*, 2020, Epidemiological and Clinical Characteristics of 99 Cases of 2019 Novel Coronavirus Pneumonia in Wuhan, China: A Descriptive Study. *Lancet*, 395:507–13. https://doi.org/10.1016/s0140-6736(20)30211-7
9. World Health Organization, 2020, Rational Use of Personal Protective Equipment (PPE) for Coronavirus Disease (COVID-19): Interim Guidance. World Health Organization, Geneva, Switzerland.
10. Cheng VC, Wong SC, Chuang VW, *et al.*, 2020, The Role of Community-wide Wearing of Face Mask for Control of Coronavirus Disease 2019 (COVID-19) Epidemic Due to SARS-CoV-2. *J Infect*, 81:107–14. https://doi.org/10.1016/j.jinf.2020.04.024
11. Vuorinen V, Aarnio M, Alava M, *et al.*, 2020, Modelling Aerosol Transport and Virus Exposure with Numerical Simulations in Relation to SARS-CoV-2 Transmission by Inhalation Indoors. *Saf Sci*, 130:104866. https://doi.org/10.1016/j.ssci.2020.104866
12. Gralton J, Tovey E, McLaws ML, *et al.*, 2011, The Role of Particle Size in Aerosolised Pathogen Transmission: A Review. *J Infect*, 62:1–13. https://doi.org/10.1016/j.jinf.2010.11.010
13. Wang CS, Otani Y, 2013, Removal of Nanoparticles from Gas Streams by Fibrous Filters: A Review. *Ind Eng Chem Res*, 52:5–17. https://doi.org/10.1021/ie300574m
14. Grinshpun SA, Yermakov M, Khodoun M, 2020, Autoclave Sterilization and Ethanol Treatment of Re-used Surgical Masks and N95 Respirators During COVID-19: Impact on Their Performance and Integrity. *J Hosp Infect*, 105:608–14. https://doi.org/10.1016/j.jhin.2020.06.030
15. Rengasamy S, Eimer BC, Shaffer RE, 2009, Comparison of Nanoparticle Filtration Performance of NIOSH-approved and CE-marked Particulate Filtering Facepiece Respirators. *Ann Occup Hyg*, 53:117–28. https://doi.org/10.1093/annhyg/men086
16. Grinshpun SA, Haruta H, Eninger RM, *et al.*, 2009, Performance of an N95 Filtering Facepiece Particulate Respirator and a Surgical Mask During Human Breathing: Two Pathways for Particle Penetration. *J Occup Environ Hyg*, 6:593–603. https://doi.org/10.1080/15459620903120086
17. Cai M, Li H, Shen S, *et al.*, 2018, Customized Design and 3D Printing of Face Seal for an N95 Filtering Facepiece Respirator. *J Occup Environ Hyg*, 15:226–34. https://doi.org/10.1080/15459624.2017.1411598
18. Swennen GR, Pottel L, Haers PE, 2020, Custom-made 3D-printed Face Masks in Case of Pandemic Crisis Situations with a Lack of Commercially Available FFP2/3 Masks. *Int J Oral Maxillofac Surg*, 49:673-7. https://doi.org/10.1016/j.ijom.2020.03.015
19. British Standards Institution, 2011, 149: 2001+ A1: 2009 Respiratory Protective Devices. Filtering Half Masks to Protect against Particles. Requirements, Testing, Marking. British Standards Institution, London, UK. https://doi.org/10.3403/02279488
20. Gawn J, Clayton M, Makison C, *et al.*, 2008, Evaluating the Protection Afforded by Surgical Masks Against Influenza Bioaerosols: Gross Protection of Surgical Masks Compared to Filtering Facepiece Respirators. *Health Safety Exec*,2020. Available from: https://www.hse.gov.uk/research/rrpdf/rr619.pdf. [Last accessed on 2020 Jan 01].
21. Lee SA, Hwang DC, Li HY, *et al.*, 2016, Particle Size-selective Assessment of Protection of European Standard FFP

Respirators and Surgical Masks Against Particles-tested with Human Subjects. *J Healthc Eng*, 2016:8572493. https://doi.org/10.1155/2016/8572493

22. Langford CR, Johnson DW, Cameron NR, 2015, Preparation of Hybrid Thiol-Acrylate Emulsion-templated Porous Polymers by Interfacial Copolymerization of High Internal Phase Emulsions. *Macromol Rapid Commun*, 36:834–9. https://doi.org/10.1002/marc.201400733
23. Carnachan RJ, Bokhari M, Przyborski SA, *et al.*, 2006, Tailoring the Morphology of Emulsion-templated Porous Polymers. *Soft Matter*, 2:608–16. https://doi.org/10.1039/b603211g
24. Althubeiti KM, Horozov TS, 2019, Efficient Preparation of Macroporous Poly (Methyl Methacrylate) Materials from High Internal Phase Emulsion Templates. *React Function Polymers*, 142:207–12. https://doi.org/10.1016/j.reactfunctpolym.2019.06.015
25. Moglia RS, Holm JL, Sears NA, *et al.*, 2011, Injectable polyHIPEs as High-porosity Bone Grafts. *Biomacromolecules*, 12:3621–8. https://doi.org/10.1021/bm2008839
26. Paterson TE, Gigliobianco G, Sherborne C, *et al.*, 2018, Porous Microspheres Support Mesenchymal Progenitor Cell Ingrowth and Stimulate Angiogenesis. *APL Bioeng*, 2:026103. https://doi.org/10.1063/1.5008556
27. Huš S, Krajnc P, 2014, PolyHIPEs from Methyl Methacrylate: Hierarchically Structured Microcellular Polymers with Exceptional Mechanical Properties. *Polymer*, 55:4420–24. https://doi.org/10.1016/j.polymer.2014.07.007
28. Bokhari M, Carnachan RJ, Przyborski SA, *et al.*, 2007, Emulsion-templated Porous Polymers as Scaffolds for Three Dimensional Cell Culture: Effect of Synthesis Parameters on Scaffold Formation and Homogeneity. *J Mater Chem*, 17:4088–94. https://doi.org/10.1039/b707499a
29. Richez A, Deleuze H, Vedrenne P, *et al.*, 2005, Preparation of Ultra-low-density Microcellular Materials. *J Appl Polymer Sci*, 96:2053–63. https://doi.org/10.1002/app.21668
30. Xu H, Zheng X, Huang Y, *et al.*, 2016, Interconnected Porous Polymers with Tunable Pore Throat Size Prepared via Pickering High Internal Phase Emulsions. *Langmuir*, 32:38–45. https://doi.org/10.1021/acs.langmuir.5b03037
31. Williams JM, Gray AJ, Wilkerson MH, 1990, Emulsion Stability and Rigid Foams from Styrene or Divinylbenzene Water-in-oil Emulsions. *Langmuir*, 6:437–44. https://doi.org/10.1021/la00092a026
32. Cameron NR, Barbetta A, 2000, The Influence of Porogen Type on the Porosity, Surface Area and Morphology of Poly (Divinylbenzene) PolyHIPE Foams. *J Mater Chem*, 10:2466–71. https://doi.org/10.1039/b003596n
33. Barbetta A, Cameron NR, 2004, Morphology and Surface Area of Emulsion-Derived (PolyHIPE) Solid Foams Prepared with Oil-phase Soluble Porogenic Solvents: Span 80 as Surfactant. *Macromolecules*, 37:3188–201. https://doi.org/10.1021/ma0359436
34. Williams JM, Wrobleski DA, 1988, Spatial Distribution of the Phases in Water-in-oil Emulsions. Open and Closed Microcellular Foams from Cross-linked Polystyrene. *Langmuir*, 4:656–62. https://doi.org/10.1021/la00081a027
35. Gurevitch I, Silverstein MS, 2010, Polymerized Pickering HIPEs: Effects of Synthesis Parameters on Porous Structure. *J Polymer Sci Part A*, 48:1516–25. https://doi.org/10.1002/pola.23911
36. Robinson JL, Moglia RS, Stuebben MC, *et al.*, 2014, Achieving Interconnected Pore Architecture in Injectable polyHIPEs for Bone Tissue Engineering. *Tissue Eng Part A*, 20:1103–12. https://doi.org/10.1089/ten.tea.2013.0319
37. Cameron NR, Sherrington DC, Albiston L, *et al.*, 1996, Study of the Formation of the Open-cellular Morphology of Poly (Styrene/Divinylbenzene) polyHIPE Materials by Cryo-SEM. *Coll Polymer Sci*, 274:592–5. https://doi.org/10.1007/bf00655236
38. Lissant KJ, 1966, The Geometry of High-internal-phase-ratio Emulsions. *J Coll Int Sci*, 22:462–8. https://doi.org/10.1016/0021-9797(66)90091-9
39. Owen R, Sherborne C, Paterson T, *et al.*, 2016, Emulsion Templated Scaffolds with Tunable Mechanical Properties for Bone Tissue Engineering. *J Mech Behav Biomed Mater*, 54:159–72. https://doi.org/10.1016/j.jmbbm.2015.09.019
40. San Manley S, Graeber N, Grof Z, *et al.*, 2009, New Insights into the Relationship Between Internal Phase Level of Emulsion Templates and Gas-liquid Permeability of Interconnected Macroporous Polymers. *Soft Matter*, 5:4780–7. https://doi.org/10.1039/b900426b
41. Tadros TF, 2013, Emulsion Formation, Stability, and Rheology. *Emulsion Formation Stabil*, 1:1–75. https://doi.org/10.1002/9783527647941.ch1
42. Brun N, Ungureanu S, Deleuze H, *et al.*, 2011, Hybrid Foams, Colloids and Beyond: From Design to Applications. *Chem*

*Soc Rev*, 40:771–88.
https://doi.org/10.1039/b920518g

43. Cameron NR, 2005, High Internal Phase Emulsion Templating as a Route to Well-defined Porous Polymers. *Polymer*, 46:1439–49.
https://doi.org/10.1016/j.polymer.2004.11.097
44. Cameron NR, Sherrington DC, 1996, High Internal Phase Emulsions (HIPEs)-structure, Properties and Use in Polymer Preparation. *Biopolymers Liquid Crystalline Polymers Phase Emulsion*, 126:163–214.
https://doi.org/10.1007/3-540-60484-7_4
45. Kimmins SD, Cameron NR, 2011, Functional Porous Polymers by Emulsion Templating: Recent Advances. *Adv Function Mater*, 21:211–25.
https://doi.org/10.1002/adfm.201001330
46. Pulko I, Krajnc P, 2012, High Internal Phase Emulsion Templating-a Path to Hierarchically Porous Functional Polymers. *Macromol Rapid Commun*, 33:1731–46.
https://doi.org/10.1002/marc.201200393
47. Tebboth M, Menner A, Kogelbauer A, *et al.*, 2014, Polymerised high internal phase emulsions for fluid separation applications. *Curr Opin Chem Eng*, 4:114–20.
https://doi.org/10.1016/j.coche.2014.03.001
48. Silverstein MS, 2014, PolyHIPEs: Recent Advances in Emulsion-templated Porous Polymers. *Prog Polym Sci*, 39:199–234.
https://doi.org/10.1016/j.progpolymsci.2013.07.003
49. Zhang T, Sanguramath RA, Israel S, *et al.*, 2019, Emulsion Templating: Porous Polymers and Beyond. *Macromolecules*, 52:5445–79.
https://doi.org/10.1021/acs.macromol.8b02576
50. Silverstein MS, 2014, Emulsion-templated Porous Polymers: A Retrospective Perspective. *Polymer*, 55:304–20.
https://doi.org/10.1016/j.polymer.2013.08.068
51. Silverstein MS, 2020, The Chemistry of Porous Polymers: The Holey Grail. *Israel J Chem*, 60:140–50.
52. Andrieux S, Quell A, Stubenrauch C, *et al.*, 2018, Liquid Foam Templating-a Route to Tailor-made Polymer Foams. *Adv Coll Int Sci*, 256:276–90.
https://doi.org/10.1016/j.cis.2018.03.010
53. Moon S, Kim JQ, Kim BQ, *et al.*, 2020, Processable Composites with Extreme Material Capacities: Toward Designer High Internal Phase Emulsions and Foams. *Chem Mater*, 32:4838–54.
https://doi.org/10.1021/acs.chemmater.9b04952
54. Dikici BA, Claeyssens F, 2020, Basic Principles of Emulsion Templating and Its Use as an Emerging Manufacturing Method of Tissue Engineering Scaffolds. *Front Bioeng Biotechnol*, 8:875.
https://doi.org/10.3389/fbioe.2020.00875
55. Taylor-Pashow KM, Pribyl JG, 2019, PolyHIPEs for Separations and Chemical Transformations: A Review. *Solvent Extract Ion Exchan*, 37:1–26.
https://doi.org/10.1080/07366299.2019.1592924
56. Choudhury S, Connolly D, White B, 2015, Supermacroporous polyHIPE and Cryogel Monolithic Materials as Stationary Phases in Separation Science: A Review. *Anal Methods*, 7:6967–82.
https://doi.org/10.1039/c5ay01193k
57. Gu H, Liu Y, Yin D, *et al.*, 2018, Heparin-immobilized Polymeric Monolithic Column with Submicron Skeletons and Well-defined Macropores for Highly Efficient Purification of Enterovirus 71. *Macromol Mater Eng*, 303:1800411.
https://doi.org/10.1002/mame.201800411
58. Muralikrishnan R, Swarnalakshmi M, Nakkeeran E, 2014, Nanoparticle-membrane Filtration of Vehicular Exhaust to Reduce air Pollution-a Review. *Int Res J Environ Sci*, 3:82–6.
59. Xing YF, Xu YH, Shi MH, *et al.*, 2016, The Impact of PM2. 5 on the Human Respiratory System. *J Thorac Dis*, 8:E69.
60. ISO, 2015, ISO/TS 80004-2: 2015. Nanotechnologies-Vocabulary-Part 2: Nano-objects. ISO, United Kingdom.
61. Ramachandran S, Rajiv S, 2020, Emulsion Templated Amino Functionalised Polymeric Monolith Filter for Innovative Air Purification Technology. *J Porous Mater*, 27:939–46.
https://doi.org/10.1007/s10934-019-00856-1
62. Walsh DC, Stenhouse JI, Kingsbury LP, *et al.*, 1996, PolyHIPE Foams: Production, Characterisation, and Performance as Aerosol Filtration Materials. *J Aerosol Sci*, 27:S629–30.
https://doi.org/10.1016/0021-8502(96)00387-4
63. Hung CH, Leung WW, 2011, Filtration of Nano-aerosol Using Nanofiber Filter Under Low Peclet Number and Transitional Flow Regime. *Separat Purificat Technol*, 79:34–42.
https://doi.org/10.1016/j.seppur.2011.03.008
64. Krajnc P, Leber N, Štefanec D, *et al.*, 2005, Preparation and Characterisation of Poly (High Internal Phase Emulsion) Methacrylate Monoliths and Their Application as Separation Media. *J Chromatogr A*, 1065:69–73.
https://doi.org/10.1016/j.chroma.2004.10.051
65. Pulko I, Smrekar V, Podgornik A, *et al.*, 2011, Emulsion Templated Open Porous Membranes for Protein Purification. *J Chromatogr A*, 1218:2396–401.
https://doi.org/10.1016/j.chroma.2010.11.069
66. Yao C, Qi L, Yang G, *et al.*, 2010, Preparation of Sub-micron Skeletal Monoliths with High Capacity for Liquid

Chromatography. *J Separat Sci*, 33:475–83. https://doi.org/10.1002/jssc.200900655

67. Dinh NP, Cam QM, Nguyen AM, *et al.*, 2009, Functionalization of Epoxy-based Monoliths for Ion Exchange Chromatography of Proteins. *J Separat Sci*, 32:2556–64. https://doi.org/10.1002/jssc.200900243
68. Zhang T, Guo Q, 2017, Continuous Preparation of polyHIPE Monoliths from Ionomer-stabilized High Internal Phase Emulsions (HIPEs) for Efficient Recovery of Spilled Oils. *Chem Eng J*, 307:812–9. https://doi.org/10.1016/j.cej.2016.09.024
69. Zhang N, Zhong S, Zhou X, *et al.*, 2016, Superhydrophobic P (St-DVB) Foam Prepared by the High Internal Phase Emulsion Technique for Oil Spill Recovery. *Chem Eng J*, 298:117–24. https://doi.org/10.1016/j.cej.2016.03.151
70. Balow RB, Giles SL, McGann CL, *et al.*, 2018, Rapid Decontamination of Chemical Warfare Agent Simulant with Thermally Activated Porous Polymer Foams. *Ind Eng Chem Res*, 57:8630–4. https://doi.org/10.1021/acs.iecr.8b01546
71. McGann CL, Daniels GC, Giles SL, *et al.*, 2018, Air Activated Self-Decontaminating Polydicyclopentadiene PolyHIPE Foams for Rapid Decontamination of Chemical Warfare Agents. *Macromol Rapid Commun*, 39:1800194. https://doi.org/10.1002/marc.201800194
72. Hughes JM, Budd PM, Tiede K, *et al.*, 2015, Polymerized High Internal Phase Emulsion Monoliths for the Chromatographic Separation of Engineered Nanoparticles. *J Appl Polymer Sci*, 132:41229. https://doi.org/10.1002/app.41229
73. Bhumgara Z, 1995, Polyhipe Foam Materials as Filtration Media. *Filtrat Separat*, 32:245–51. https://doi.org/10.1016/s0015-1882(97)84048-7
74. Malakian A, Zhou M, Zowada RT, *et al.*, 2019, Synthesis and *in Situ* Functionalization of Microfiltration Membranes Via High Internal Phase Emulsion Templating. *Polymer Int*, 68:1378–86. https://doi.org/10.1002/pi.5828
75. Katsoyiannis IA, Zouboulis AI, 2002, Removal of Arsenic from Contaminated Water Sources by Sorption Onto Iron-oxide-coated Polymeric Materials. *Water Res*, 36:5141–55. https://doi.org/10.1016/s0043-1354(02)00236-1
76. Zhu Y, Wang W, Yu H, *et al.*, 2020. Preparation of Porous Adsorbent Via Pickering Emulsion Template for Water Treatment: A Review. *J Environ Sci*, 88:217–36. https://doi.org/10.1016/j.jes.2019.09.001
77. Zhao C, Danish E, Cameron NR, *et al.*, 2007, Emulsion-templated Porous Materials (PolyHIPEs) for Selective Ion and Molecular Recognition and Transport: Applications in Electrochemical Sensing. *J Mater Chem*, 17:2446–53. https://doi.org/10.1039/b700929a
78. Pulko I, Krajnc P, 2008, Open Cellular Reactive Porous Membranes from High Internal Phase Emulsions. *Chem Commun*, 37:4481–3. https://doi.org/10.1039/b807095d
79. Sevšek U, Seifried S, Stropnik Č, *et al.*, 2011, Poly (styrene-co-divinylbenzene-co-2-ethylhexyl) Acrilate Membranes with Interconnected Macroporous Structure. *Mater Tehnol*, 45:247–51.
80. Kovačič S, Preishuber-Pflügl F, Slugovc C, 2014, Macroporous Polyolefin Membranes from Dicyclopentadiene High Internal Phase Emulsions: Preparation and Morphology Tuning. *Macromol Mater Eng*, 299:843–50. https://doi.org/10.1002/mame.201300400
81. Owen R, Sherborne C, Evans R, *et al.*, 2020, Combined Porogen Leaching and Emulsion Templating to Produce Bone Tissue Engineering Scaffolds. *Int J Bioprint*, 6:99–113. https://doi.org/10.18063/ijb.v6i2.265
82. Huang X, Yang Y, Shi J, *et al.*, 2015, High-internal-phase Emulsion Tailoring Polymer Amphiphilicity towards an Efficient NIR-sensitive *Bacteria* Filter. *Small*, 11:4876–83. https://doi.org/10.1002/smll.201501396
83. Yang Q, Li H, Shen S, *et al.*, 2018, Study of the Micro-climate and Bacterial Distribution in the Deadspace of N95 Filtering Face Respirators. *Sci Rep*, 8:1–13. https://doi.org/10.1038/s41598-018-35693-w
84. Wang X, Chen X, Peng Y, *et al.*, 2019, Silver-modified Porous Polystyrene Sulfonate Derived from Pickering High Internal Phase Emulsions for Capturing Lithium-ion. *RSC Adv*, 9:7228–37. https://doi.org/10.1039/c8ra09740b
85. Sadeghi S, Moghbeli MR, 2012, Synthesis and Dispersion of Colloidal Silver Nanoparticles on Microcellular Polyhipe Support. *Coll Surf A*, 409:42–51. https://doi.org/10.1016/j.colsurfa.2012.05.037
86. Lundin JG, McGann CL, Weise NK, *et al.*, 2019, Iodine Binding and Release from Antimicrobial Hemostatic Polymer Foams. *React Function Polymers*, 135:44–51. https://doi.org/10.1016/j.reactfunctpolym.2018.12.009
87. Streifel BC, Lundin JG, Sanders AM, *et al.*, 2018, Hemostatic and Absorbent PolyHIPE-Kaolin Composites for 3D Printable Wound Dressing Materials. *Macromol Biosci*, 18:1700414. https://doi.org/10.1002/mabi.201700414

88. McDonnell G, Russell AD, 1999, Antiseptics and Disinfectants: Activity, Action, and Resistance. *Clin Microbiol Rev*, 12:147–79. https://doi.org/10.1128/cmr.12.1.147
89. McGann CL, Streifel BC, Lundin JG, *et al.*, 2017, Multifunctional polyHIPE Wound Dressings for the Treatment of Severe Limb Trauma. *Polymer*, 126:408–18. https://doi.org/10.1016/j.polymer.2017.05.067
90. Dikici BA, Dikici S, Reilly GC, *et al.*, 2019, A Novel Bilayer Polycaprolactone Membrane for Guided Bone Regeneration: Combining Electrospinning and Emulsion Templating. *Materials*, 12:2643. https://doi.org/10.3390/ma12162643
91. Gui H, Zhang T, Ji S, *et al.*, 2020, Nanofibrous, Porous Monoliths Formed from Gelating High Internal Phase Emulsions Using Syndiotactic Polystyrene. *Polymer*, 2020:122708. https://doi.org/10.1016/j.polymer.2020.122708
92. Johnson DW, Sherborne C, Didsbury MP, *et al.*, 2013, Macrostructuring of Emulsion-templated Porous Polymers by 3D Laser Patterning. *Adv Mater*, 25:3178–81. https://doi.org/10.1002/adma.201300552
93. Sears NA, Dhavalikar PS, Cosgriff-Hernandez EM, 2016, Emulsion Inks for 3D Printing of High Porosity Materials. *Macromol Rapid Commun*, 37:1369–74. https://doi.org/10.1002/marc.201600236
94. Sears N, Dhavalikar P, Whitely M, *et al.*, 2017, Fabrication of Biomimetic Bone Grafts with Multi-material 3D Printing. *Biofabrication*, 9:025020. https://doi.org/10.1088/1758-5090/aa7077
95. Welch CF, Rose GD, Malotky D, *et al.*, 2006, Rheology of High Internal Phase Emulsions. *Langmuir*, 22:1544–50. https://doi.org/10.1021/la052207h
96. Stansbury JW, Idacavage MJ, 2016, 3D Printing with Polymers: Challenges Among Expanding Options and Opportunities. *Dent Mater*, 32:54–64. https://doi.org/10.1016/j.dental.2015.09.018
97. Malayeri A, Sherborne C, Paterson T, *et al.*, 2016, Osteosarcoma Growth on Trabecular Bone Mimicking Structures Manufactured Via Laser Direct Write. *Int J Bioprint,* 2:67–77. https://doi.org/10.18063/ijb.2016.02.005
98. Wang AJ, Paterson T, Owen R, *et al.*, 2016, Photocurable High Internal Phase Emulsions (HIPEs) Containing Hydroxyapatite for Additive Manufacture of Tissue Engineering Scaffolds with Multi-scale Porosity. *Mater Sci Eng C*, 67:51–8. https://doi.org/10.1016/j.msec.2016.04.087
99. Sherborne C, Owen R, Reilly GC, *et al.*, 2018, Light-based Additive Manufacturing of PolyHIPEs: Controlling the Surface Porosity for 3D Cell Culture Applications. *Mater Design*, 156:494–503. https://doi.org/10.1016/j.matdes.2018.06.061
100. Huan S, Mattos BD, Ajdary R, *et al.*, 2019, Two-phase Emulgels for Direct Ink Writing of Skin-Bearing Architectures. *Adv Function Mater*, 29:1902990. https://doi.org/10.1002/adfm.201902990
101. Sušec M, Ligon SC, Stampfl J, *et al*., 2013, Hierarchically Porous Materials from Layer-by-layer Photopolymerization of High Internal Phase Emulsions. *Macromol Rapid Commun*, 34:938–43. https://doi.org/10.1002/marc.201300016
102. Rezanavaz R, 2018, 3D Printing of Porous Polymeric Materials for Stationary Phases of Chromatography Columns. UC Library, California.
103. Cooperstein I, Layani M, Magdassi S, 2015, 3D Printing of Porous Structures by UV-Curable O/W Emulsion for Fabrication of Conductive Objects. *J Mater Chem C*, 3:2040–4. https://doi.org/10.1039/c4tc02215g
104. Wenger L, Radtke CP, Göpper J, *et al*., 2020, 3D-printable and Enzymatically Active Composite Materials Based on Hydrogel-filled High Internal Phase Emulsions. *Front Bioeng Biotechnol*, 8:713. https://doi.org/10.3389/fbioe.2020.00713
105. Sears NA, Wilems TS, Gold KA, *et al.*, 2019, Hydrocolloid Inks for 3D Printing of Porous Hydrogels. *Adv Mater Technol*, 4:1800343. https://doi.org/10.1002/admt.201800343
106. Minas C, Carnelli D, Tervoort E, *et al.*, 2016, 3D Printing of Emulsions and Foams into Hierarchical Porous Ceramics. *Adv Mater*, 28:9993–9. https://doi.org/10.1002/adma.201603390
107. Alison L, Menasce S, Bouville F, *et al.*, 2019, 3D Printing of Sacrificial Templates into Hierarchical Porous Materials. *Sci Rep*, 9:1–9. https://doi.org/10.1038/s41598-018-36789-z
108. Jiang H, Sheng Y, Ngai T, 2020, Pickering Emulsions: Versatility of Colloidal Particles and Recent Applications. *Curr Opin Coll Int Sci*, 49:1–15. https://doi.org/10.1016/j.cocis.2020.04.010
109. Liu J, Wang P, He Y, *et al.*, 2019, Polymerizable Nonconventional Gel Emulsions and Their Utilization in the Template Preparation of Low-density, High-strength Polymeric Monoliths and 3D Printing. *Macromolecules*, 52:2456–63.

https://doi.org/10.1021/acs.macromol.8b02610

110. Sihler S, Schrade A, Cao Z, *et al.*, 2015, Inverse Pickering Emulsions with Droplet Sizes Below 500 nm. *Langmuir*, 31:10392–401. https://doi.org/10.1021/acs.langmuir.5b02735
111. Zhu W, Zhu Y, Zhou C, *et al.*, 2019, Pickering Emulsion-templated Polymers: Insights into the Relationship Between Surfactant and Interconnecting Pores. *RSC Adv*, 9:18909–16. https://doi.org/10.1039/c9ra03186c
112. Sommer MR, Alison L, Minas C, *et al*., 2017, 3D Printing of Concentrated Emulsions into Multiphase Biocompatible Soft Materials. *Soft Matter*, 13:1794–803. https://doi.org/10.1039/c6sm02682f
113. Tu R, Sprague E, Sodano HA, 2020, Precipitation Printing Towards Diverse Materials, Mechanical Tailoring and Functional Devices. *Addit Manuf*, 2020:101358. https://doi.org/10.1016/j.addma.2020.101358
114. Karyappa R, Ohno A, Hashimoto M, 2019, Immersion Precipitation 3D Printing (ip 3DP). *Mater Horiz*, 6:1834–44. https://doi.org/10.1039/c9mh00730j
115. Yang T, Hu Y, Wang C, *et al.*, 2017, Fabrication of Hierarchical Macroporous Biocompatible Scaffolds by Combining Pickering High Internal Phase Emulsion Templates with Three-dimensional Printing. *ACS Appl Mater Int*, 9:22950–8. https://doi.org/10.1021/acsami.7b05012.s001
116. Hu Y, Wang J, Li X, *et al.*, 2019, Facile Preparation of Bioactive Nanoparticle/Poly (ε-caprolactone) Hierarchical Porous Scaffolds Via 3D Printing of High Internal Phase Pickering Emulsions. *J Coll Int Sci*, 545:104–15. https://doi.org/10.1016/j.jcis.2019.03.024
117. Visser CW, Amato DN, Mueller J, *et al.*, 2019, Architected Polymer Foams via Direct Bubble Writing. *Adv. Mater*, 31:1904668. https://doi.org/10.1002/adma.201904668
118. Voisin HP, Gordeyeva K, Siqueira G, *et al.*, 2018, 3D Printing of Strong Lightweight Cellular Structures Using Polysaccharide-based Composite Foams. *ACS Sustain Chem Eng*, 6:17160–7. https://doi.org/10.1021/acssuschemeng.8b04549
119. Wirth DM, Jaquez A, Gandarilla S, *et al.*, 2020, Highly Expandable Foam for Lithographic 3D Printing. *ACS Appl Mater Int*, 12:19033–43. https://doi.org/10.1021/acsami.0c02683
120. Mu X, Bertron T, Dunn C, *et al.*, 2017, Porous Polymeric Materials by 3D Printing of Photocurable Resin. *Mater Horiz*, 4:442–9. https://doi.org/10.1039/c7mh00084g
121. Sommer MR, Schaffner M, Carnelli D, *et al.*, 2016, 3D Printing of Hierarchical Silk Fibroin Structures. *ACS Appl Mater Int*, 8:34677–85. https://doi.org/10.1021/acsami.6b11440
122. Giglia S, Bohonak D, Greenhalgh P, *et al.*, 2015. Measurement of Pore Size Distribution and Prediction of Membrane Filter Virus Retention Using Liquid-liquid Porometry. *J Memb Sci*, 476:399–409. https://doi.org/10.1016/j.memsci.2014.11.053
123. Schultz S, Wagner G, Urban K, *et al.*, 2004, High-pressure Homogenization as a Process for Emulsion Formation. *Chem Eng Technol*, 27:361–8. https://doi.org/10.1002/ceat.200406111
124. Vladisavljević GT, 2016, Recent Advances in the Production of Controllable Multiple Emulsions Using Microfabricated Devices. *Particuology*, 24:1–17. https://doi.org/10.1016/j.partic.2015.10.001
125. Costantini M, Colosi C, Guzowski J, *et al.*, 2014, Highly Ordered and Tunable Polyhipes by Using Microfluidics. *J Mater Chem B*, 2:2290–300. https://doi.org/10.1039/c3tb21227k
126. Quell A, Elsing J, Drenckhan W, *et al.*, 2015, Monodisperse Polystyrene Foams Via Microfluidics-a Novel Templating Route. *Adv Eng Mater*, 17:604–9. https://doi.org/10.1002/adem.201500040
127. Quell A, de Bergolis B, Drenckhan W, *et al.*, 2016, How the Locus of Initiation Influences the Morphology and the Pore Connectivity of a Monodisperse Polymer Foam. *Macromolecules*, 49:5059–67. https://doi.org/10.1021/acs.macromol.6b00494
128. Elsing J, Stefanov T, Gilchrist MD, *et al.*, 2017, Monodisperse Polystyrene Foams Via Polymerization of Foamed Emulsions: Structure and Mechanical Properties. *Phys Chem Chem Phys*, 19:5477–5485. https://doi.org/10.1039/c6cp06612g
129. Costantini M, Jaroszewicz J, Kozoń Ł, *et al.*, 2019, 3D-printing of Functionally Graded Porous Materials Using On-demand Reconfigurable Microfluidics. *Ange Chem Int Ed*, 58:7620–7625. https://doi.org/10.1002/anie.201900530
130. Abate AR, Romanowsky MB, Agresti JJ, *et al.*, 2009, Valve-based Flow Focusing for Drop Formation. *Appl Phys Lett*, 94:023503. https://doi.org/10.1063/1.3067862
131. Stubenrauch C, Menner A, Bismarck A, *et al.*, 2018, Emulsion and Foam Templating-promising Routes to Tailor-made Porous Polymers. *Ange Chem Int Ed*, 57:10024-10032. https://doi.org/10.1002/anie.201801466

132. Nisisako T, Torii T, 2008, Microfluidic Large-scale Integration on a Chip for Mass Production of Monodisperse Droplets and Particles. *Lab Chip*, 8:287–293. https://doi.org/10.1039/b713141k

133. Nisisako T, Ando T, Hatsuzawa T, 2012, High-volume Production of Single and Compound Emulsions in a Microfluidic Parallelization Arrangement Coupled with Coaxial Annular World-to-chip Interfaces. *Lab Chip*, 12:3426–3435. https://doi.org/10.1039/c2lc40245a

134. Carballido L, Dabrowski ML, Dehli F, *et al.*, 2020, Monodisperse Liquid Foams Via Membrane Foaming. *J Coll Int Sci*, 568:46–53. https://doi.org/10.1016/j.jcis.2020.02.036

135. Vladisavljević GT, 2019, Preparation of Microemulsions and Nanoemulsions by Membrane Emulsification. *Coll Surf A*, 2019:123709. https://doi.org/10.1016/j.colsurfa.2019.123709

136. Wang B, Prinsen P, Wang H, *et al.*, 2017, Macroporous Materials: Microfluidic Fabrication, Functionalization and Applications. *Chem Soc Rev*, 46:855–914. https://doi.org/10.1039/c5cs00065c

RESEARCH ARTICLE

# Using Plant Proteins to Develop Composite Scaffolds for Cell Culture Applications

**Linzhi Jing[1,2], Jie Sun[3]*, Hang Liu[1,2], Xiang Wang[1,2], Dejian Huang[1,2]***

[1]National University of Singapore (Suzhou) Research Institute, Suzhou, Jiangsu 215123, China
[2]Department of Food Science and Technology, National University of Singapore, Singapore 117543, Singapore
[3]Department of Mechatronics and Robotics, Xi'an Jiaotong-Liverpool University, Suzhou, Jiangsu 215123, China

**Abstract:** Electrohydrodynamic printing (EHDP) is capable of fabricating scaffolds that consist of micro/nano scale orientated fibers for three-dimensional (3D) cell culture models and drug screening applications. One of the major hurdles that limit the widespread application of EHDP is the lack of diverse biomaterial inks with appropriate printability and desired mechanical and biological properties. In this work, we blended plant proteins with synthetic biopolymer poly(ε-caprolactone) (PCL) to develop composite biomaterial inks, such as PCL/gliadin and PCL/zein for scaffold fabrication through EHDP. The tensile test results showed that the composite materials with a relatively small amount of plant protein portions, such as PCL/gliadin-10 and PCL/zein-10, can significantly improve tensile properties of the fabricated scaffolds such as Young's modulus and yield stress. These scaffolds were further evaluated by culturing mouse embryonic fibroblasts (NIH/3T3) cells and proven to enhance cell adhesion and proliferation, apart from temporary inhibition effects for PCL/gliadin-20 scaffold at the initial growth stage. After these plant protein nanoparticles were gradually released into culture medium, the generated nanoporous structures on the scaffold fiber surfaces became favorable for cellular attachment, migration, and proliferation. As competent candidates that regulate cell behaviors in 3D microenvironment, such composite scaffolds manifest a great potential in drug screening and 3D *in vitro* model development.

**Keywords:** Composite biomaterials ink; Electrohydrodynamics; Additive manufacturing

***Correspondence to:** Jie Sun, Mechatronics and Robotics, Xi'an Jiaotong-Liverpool University, Suzhou, Jiangsu 215123, China; jie.sun@xjtlu.edu.cn. Dejian Huang, Department of Food Science and Technology, National University of Singapore, Singapore 117543, Singapore; fsthdj@nus.edu.sg

**Received:** June 16, 2020; **Accepted:** September 11, 2020; **Published Online:** October 30, 2020

**Citation:** Jing L, Sun J, Liu H, *et al*., 2021, Using Plant Proteins to Develop Composite Scaffolds for Cell Culture Applications. *Int J Bioprint,* 7(1):298. http://doi.org/10.18063/ijb.v7i1.298

## 1. Introduction

Three-dimensional (3D) scaffolds have been developed to facilitate cell culture to circulate nutrition and remove metabolic waste[1]. Such scaffolds have drawn an intensive attention in the fields of cell biology, tissue engineering, and drug discovery since the produced 3D *in vitro* models can closely mimic the cellular states in physiological environment and enhance cell migration, proliferation, and functionalities[2]. For example, 3D collagen gel structure can support fibroblasts to elongate themselves to spindle shape, migrate, and invade similar to *in vivo* observation, whereas they developed prominent stress fibers and became immobile in 2D glass substrate[3]. A 3D reconstituted basement membrane can prompt mammary epithelial cells to self-assemble into spherical structures with a central lumen approximating to normal mammary acini[4]. The metabolic rates of human breast cancer grown on the 3D chitosan scaffold approximated to those *in vivo* tumors[5]. In 3D cell culture, scaffolds' physical and chemical properties can significantly influence cell adhesion, migration, and differentiation. These properties can be detected by the adhesion proteins on the cell membrane and transmitted into downstream biochemical signals[6]. Thus, understanding cell-scaffold interaction is crucial for understanding fundamental cellular behaviors and designing new biomaterial inks.

Traditional scaffolding methods such as freeze-drying, gas-forming, and solvent-casting particulate leaching can produce sponge structure scaffolds for cell culture, but they are not capable of controlling scaffolds' microstructure, which is critical for cell-scaffold interactions[7]. Recent advances in 3D printing, also known as additive manufacturing, bring new chances to fabricate scaffolds with customizable microstructures in reproducible features[8]. For instance, extrusion-based 3D printing such as fused deposition modeling has been widely used to fabricate polymer-based fibrous scaffolds for biomedical devices[9]. Droplet-based bioprinting enables precise control on deposition of microdroplets containing biological substances, such as growth factors, cells, modified genes, small molecule drugs, and biomaterials, in a fast and high-resolution manner. Vat polymerization-based bioprinting allows direct fabrication of high-resolution cell-laden tissue constructs[10].

Among these 3D printing methods, electrohydrodynamic printing (EHDP) has drawn great interest for its capability of producing ultrafine fibers with high resolution and reproducibility[11]. Like the working principle of near-field electrospinning, EHDP employs a high electric field to induce fiber ejection from viscous biopolymer solution, ranging from a few hundreds of nanometers to micrometers, from viscous biopolymer solution.[12]. However, very limited polymer materials are available for this technique due to the harsh requirement on biomaterial ink properties.

The scaffold materials should provide temporary support for cells to attach, proliferate, and deliver bioactive components. In general, synthetic biopolymers such as polyethylene glycol, poly(vinyl alcohol), poly(lactide-co-glycolide), and poly-ε-caprolactone (PCL) are usually used as scaffold materials due to their excellent printability, favorable biodegradability, and biocompatibility[13]. They can be applied to common scaffold fabrication methods to produce porous scaffolds with varied pore size, shape, interconnectivity, and porosity[14]. Especially, PCL, a biodegradable polyester with a low melting point, has received extensive attention on accounts of its ideal rheological and viscoelastic properties, excellent solubility, and biocompatibility[15]. However, the *in vivo* degradation period of PCL is up to few years due to its hydrophobicity and semi-crystallinity[16]. A simple way to overcome this bottleneck is to prepare composite materials by mixing PCL with hydrophilic polymers extracted from animals such as collagen and alginate. The properties of these natural derived components may vary from batch to batch and bring in safety concern like transmission of zoonotic diseases.

Compared with animal-derived components, plant proteins, such as zein and gliadin, are favorable choices due to their wide availability, consistent quality, and structural diversity[17]. As alcohol-soluble plant proteins, zein protein contains different subunits including α-zein (75 – 85 wt% of zein), β-zein, γ-zein, and δ-zein with different molecular weight and composition. Similarly, gliadin also consists of various fractions. Both zein and gliadin can be fabricated into various structures such as thin films, nanoparticles, fibers, and porous scaffold. The poor mechanical strength of natural polymers can be improved by mixing with synthetic polymers. As a class of prolamin protein found in corn, zein resists to microbial attacks and has been applied as coating material for encapsulated nutrition and drugs[18]. Zein has been regarded as a potential biopolymer candidate with its hydrophobicity, cytoaffinity, and biodegradability[19]. Porous zein scaffold can support rat mesenchymal stem cells to grow and differentiate into osteoblasts *in vitro*[16]. Because of the amphiphilic and biodegradable nature of zein, researchers mixed zein with synthetic polymers and produced PCL/zein fibers by coaxial electrospinning to release metronidazole in a controlled manner[20]. Thus, blending PCL with zein to prepare composite biomaterial inks may be an effective way to improve scaffolds' cell affinity and biodegradability.

Gliadin, one of the major gluten storage proteins of wheat, has been investigated for its carrier role for controlled release of lipophilic and cationic drugs due to its unique physicochemical properties[21]. It can also deliver sensitive enzymes and avoid their breakdown by stomach acids. Nevertheless, further developments of gliadin are hindered by its low water stability and immunogenic toxicity in patients with celiac disease[22]. An alternative plan is to blend a small amount of gliadin with PCL in the preparation of composite biomaterial inks for scaffold fabrication, with the purpose of improving cell affinity and suppressing gliadin's side effect. In short, both zein and gliadin are abundant and structurally diverse, which may overcome the current limitations of components extracted from animals in terms of their supply and quality. These plant proteins are also easy to blend with other synthetic biopolymers because of their specific solubility and film-forming properties.

In this study, we introduce plant-derived proteins to develop composite biomaterial inks to improve the biocompatibility and mechanical strength of scaffold materials. These proposed composite biomaterial inks are fed into EHDP system for high-precision scaffold fabrication. Two types of composite scaffolds are developed, namely, PCL/zein and PCL/gliadin. With the help of a developed monitoring and identification system, EHDP process parameters and environmental parameters are optimized to fabricate such composite scaffolds. To analyze the scaffolds' performance, mouse embryonic fibroblasts (NIH/3T3) cells were cultured to examine the cellular responses on PCL/zein, PCL/gliadin, and pure

PCL scaffolds. Although the composite inks we discussed are supplied to EHDP system for scaffold building, the application of such inks can also be implemented on several different kinds of 3D printing systems, such as extrusion-based printing and electrospinning.

## 2. Materials and methods

Natural extracellular matrix (ECM) creates complex physical and chemical environment to support cell/tissue functions. To introduce such complexities to ECM-mimicking fibrous scaffolds, EHDP has been implemented to fabricate scaffolds with aligned fibers to create controllable microstructures using single polymer-based material system. To enhance such EHDP scaffolds' performance, our group has developed plant protein-based composite inks which could distinctly improve fiber surface biocompatibility during cell culture studies.

### 2.1. Materials

The gliadin power was purchased from Tokyo Chemical Industrial Ltd. (Japan). 3-(4,5-dimethylthiazol-2-yl)-2,5-diphenyltetrazolium bromide (MTT) cytotoxicity assay and CellTiter 96® AQueous One Solution Cell Proliferation Assay were obtained from Abcam Ltd. (China) and Promega Co. Ltd. (USA), respectively. The rest of the chemicals and reagents are similar to those reported previously[23].

### 2.2. Preparation of PCL/zein and PCL/gliadin biomaterial inks

PCL, PCL/zein, and PCL/gliadin biomaterial inks were prepared for EHDP scaffold fabrication. PCL ink (70 w/v% in glacial acetic acid [AcOH], g/mL) was prepared by dissolving PCL pellets (3.5 g) in acetic acid (5 mL) with stirring for 1 h to allow complete dissolution. Both zein and gliadin are soluble in acetic acid, and we used two weight ratios, that is, 10% w/v and 20% w/v to prepare both PCL/zein and PCL/gliadin inks in this study. Zein or gliadin powder were first dissolved in glacial AcOH to obtain a clear solution. Subsequently, PCL pellets were added to either solution under ultrasonic condition at 50°C and the mixture was stirred 30 min to produce homogenous PCL/gliadin or PCL/zein biomaterial inks.

Two types of PCL/zein biomaterial inks were prepared: PCL/zein-10 (60% w/v PCL, 10% w/v zein in AcOH) and PCL/zein-20 (50% w/v PCL, 20% w/v zein in AcOH). Similarly, two PCL/gliadin biomaterial inks were prepared: PCL/gliadin-10 (60% w/v PCL, 10% w/v gliadin in AcOH) and PCL/gliadin-20 (50% w/v PCL, 20% w/v gliadin in AcOH). The viscosity of zein and gliadin solution (in acetic acid) is low. Thus, the viscosity of such biomaterial inks is mainly determined by the viscosity of PCL solution due to its high concentration, and no significant viscosity difference was observed between these inks.

### 2.3. EHDP system setup and fabrication process monitoring

**Figure 1A** shows a schematic diagram of a solution-based EHDP setup, which includes an ink feeding system, a high voltage power supply (0 – 10 kV, Dongwen Co. Ltd., China) and a three-axis precision motorized stage from Aerotech Company (Pittsburgh, PA, USA). The solution feeding system consists of a micro-syringe pump, a disposable syringe (5 mL), a flexible plastic hose, and a stainless steel needle (G20). The voltage output from the high-power supply was applied between the nozzle and the substrate to trigger and maintain EHDP jetting process. The precision stage has a travel range of 150 mm/s with 3 μm accuracy on x and y axes. A polished silicon wafer placed on x-y stage was used as the substrate for fiber deposition. The stage moving speed along x and y directions is set between 100 mm/s and 300 mm/s. The ejected fiber could continuously deposit on the stage with the mechanical drawing force which was generated with the stage moving along x and y axes. As shown in **Figure 1B**, this deposited fiber stacked up gradually and formed a scaffold by following predesigned moving path.

### 2.4. EHDP fabrication process monitoring

As the EHDP's printing resolution can approach submicron to nanoscale, any slight fluctuations of the environmental factors, such as the variations of temperature, humidity, air flow, and the printing platform vibration due to stage movement, might affect printing accuracy[12]. It also took some time to achieve and maintain a steady flow rate and stage speed, especially for high viscous biopolymer solutions. Besides, corona discharge phenomena are quite common when using PCL/gliadin and PCL/zein inks. This is ascribed to residual charges remained in the peptide chains of gliadin or zein protein, which alters the electrical properties of the composite inks. When the accumulated charges on the droplet surface at the nozzle tip exceeded a critical value, the corona discharge could be observed. If this discharge lasts for a longer time, the EHDP fabrication system can be damaged.

To achieve a reliable fabrication process, it is essential to develop a system to monitor and identify the status of triggered jet and cone. In the developed system, the jet and cone images were recorded using digital microscope (Supereyes B011 digital camera with 1 – 500 magnifications and 30 frames/s) to observe the details of Taylor cone and jet region. To capture images, the camera position, focal length, and shooting angle should be calibrated by comparing the overlapping area of the grayscale nozzle image with a predefined position.

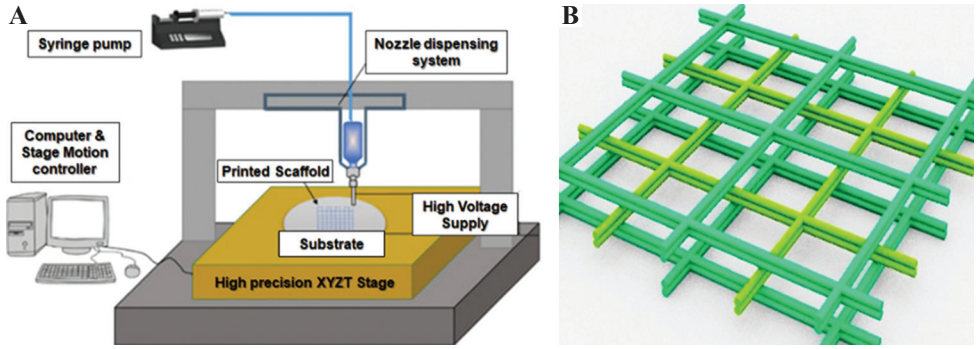


**Figure 1.** Electrohydrodynamic printing (EHDP) system and scaffold fabrication. (A) Schematic diagram of EHDP system. (B) Scaffold structure by fiber stacking.

To establish a viable manufacturing process and minimize defect-related loss in long time fabrication, the captured EHDP cone and jet images were applied to detect abnormal modes, as shown in **Figure 2A**. The identification task in this EHDP monitoring system involves the application of an image processing algorithm to extract relevant features and a recognition algorithm to determine the modes of Taylor cones. This is very similar to traditional fabrication process monitoring, where feature extraction and selection are applied to determine the input features of machining learning methods for effective condition identification[24,25].

**Figure 2B** shows a standard cone with a straight jet for EHDP scaffold fabrication. In the EHDP monitoring and identification system, various types of corona discharge were reported. As shown in **Figure 2C**, the corona discharge happened slightly below the needle tip at initial jetting process or during fabrication. Such discharge could be avoided by optimizing EHDP process parameters and environmental parameters. **Figure 2D** shows the current flow through the air from the region surrounding the jet to the grounded substrate. This reduced the surface charge density and increased the jet's lateral stability. Different from the above-mentioned two scenarios, a huge Taylor cone with serious discharge at the needle tip is shown in **Figure 2E**. To avoid possible damages of the EHDP fabrication system, we need to properly vary the biomaterial ink properties, process parameters, and environmental parameters.

Overall, this monitoring and identification system provides intuitive information of EHDP fabrication process and bridges the knowledge gap between the corona discharges and electrical properties of the composite materials. Researchers can evaluate new inks' property and stability during long time printing and gain additional insights into fundamental mechanism causing corona discharges. It can also assist new inks' fabrication process parameter optimization such as applied electric field between the nozzle and the substrate, solution feeding rate, programmed stage speed and moving path, temperature, and humidity.

## 3. Results and discussion

### 3.1. Composite scaffold structure and tensile test

The fabricated scaffold fibers with varied material compositions may influence cell-scaffold interactions. To investigate this factor, we prepared scaffolds using the same structural parameters (pore size, fiber diameter, and number of layers), and fabricated PCL, PCL/zein-10, PCL/zein-20, PCL/gliadin-10, and PCL/gliadin-20 scaffolds for comparison.

#### *(1) Composite scaffold structure analysis*

The printed scaffolds consist of 12 layers of fibers with a thickness of about 65 – 85 μm. The thickness of PCL, PCL/zein, and PCL/gliadin scaffolds is stated in **Table 1**. The fiber diameter of top layer is approximately 8.9 – 9.4 μm, which is close to typical cell size. Due to the impact of ejected filament onto the previously deposited fiber layers, the fiber diameter of the bottom layers is about twice the diameter of the top layer cross of all scaffolds. The porosity of these scaffolds is about 89 – 92.1%, which is in favor for exchanging nutrition and waste. In **Table 1**, the structural parameters such as fiber diameter, scaffold thickness, bulk density, and porosity are very similar for all the scaffolds. In other words, the proposed biomaterial inks with current components and portion do not influence the morphology of these scaffolds obviously.

As shown in **Figure 3**, PCL and PCL/gliadin scaffolds were observed using a scanning electron microscope (SEM, JSM-6510, JEOL, Japan) for morphology analysis. The pore size was precisely defined, and fibers were precisely stacked in a layer-by-layer manner. For the fabricated scaffolds using PCL/zein and PCL/gliadin inks, there was not much difference in terms of fiber diameter and cross-section structure. In general, these scaffold parameters are independent of the material compositions. The tensile properties of these scaffolds were compared and analyzed in sub-section.

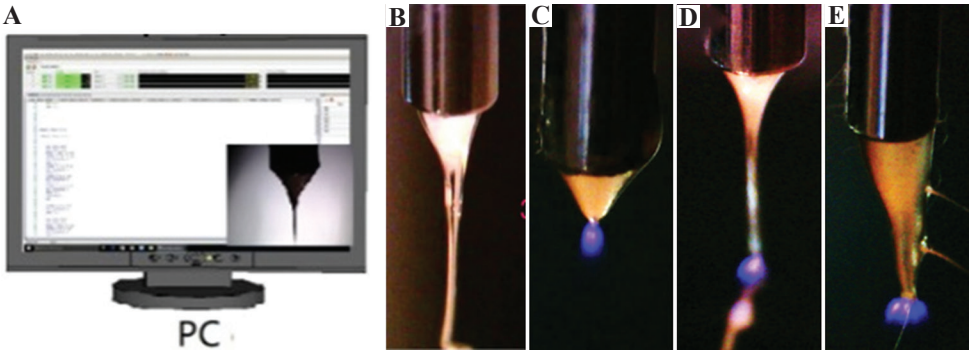


**Figure 2.** Electrohydrodynamic printing (EHDP) monitoring and discharging phenomena. (A) EHDP monitoring interface. (B) Standard cone. (C) Discharge at initial jet formation. (D) Discharge in fabrication. (E) Huge cone with discharge.

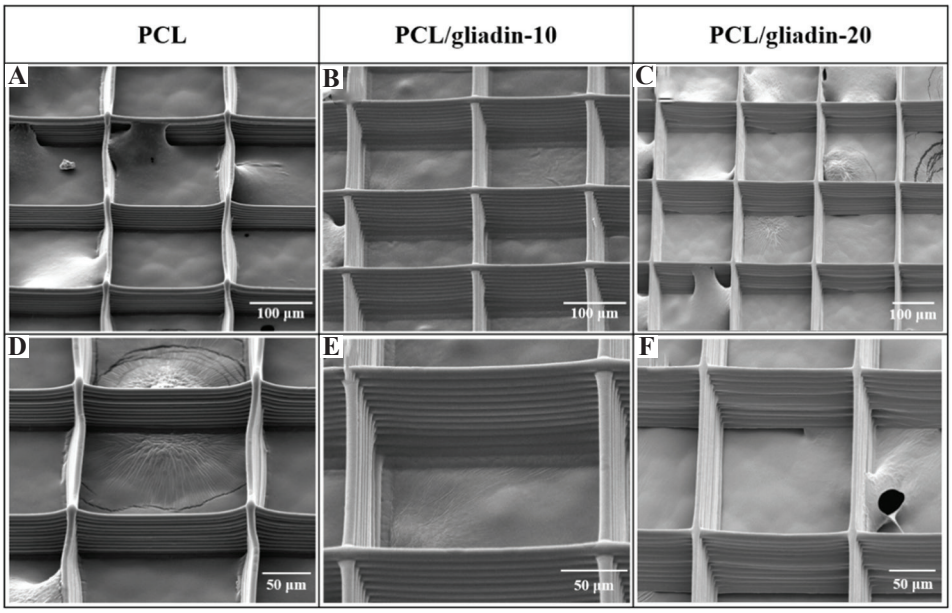


**Figure 3.** Scanning electron microscope images and their corresponding enlarged views of morphology. (A) and (D) poly(ε-caprolactone) (PCL). (B) and (E) PCL/gliadin-10. (C) and (F) PCL/glaidin-20 scaffolds.

**Table 1.** Morphological data of printed scaffolds

| Scaffolds | PCL | PCL/zein-10 | PCL-zein-20 | PCL/gliadin-10 | PCL/gliadin-20 |
|---|---|---|---|---|---|
| Fiber diameter (μm) | | | | | |
| Top layer | 8.9±1.1 | 9.0±0.7 | 9.0±1.1 | 9.4±0.7 | 9.1±1.1 |
| Bottom layer | 17.4±2.9 | 18.5±1.0 | 20.0±2.4 | 18.1±1.5 | 17.5v1.7 |
| Thickness (μm) | 67.8±7.4 | 72.4±3.5 | 77.6±2.4 | 72.7±2.9 | 75.2±3.3 |
| Bulk density (kg/ $m^3$) [1] | 1100 | 1118 | 1137 | 1130 | 1162 |
| Porosity (%) | 91.7±0.3 | 92.1±0.2 | 91.7±0.5 | 89.0±0.5 | 89.6±1.1 |

[1]Bulk density is estimated based on the densities of PCL, zein, and gliadin in the scaffolds.

### *(2) Tensile properties of the composite scaffolds*

The scaffolds' tensile properties were examined using a universal testing machine (HD-B609B-S, HAIDA, China). The scaffolds were prepared in rectangular shape (4 × 2 cm) and stretched along the longer side. This test was to stretch the scaffolds with an initial gauge length of 20.0 mm at a speed of 1 mm/min and 10 mm/min for pre-loading and loading conditions.

The stress-strain curve of PCL, PCL/gliadin, and PCL/zein scaffolds is illustrated in **Figure 4** and tensile properties of scaffolds are summarized in **Table 2**. In general, PCL scaffold showed a typical amorphous

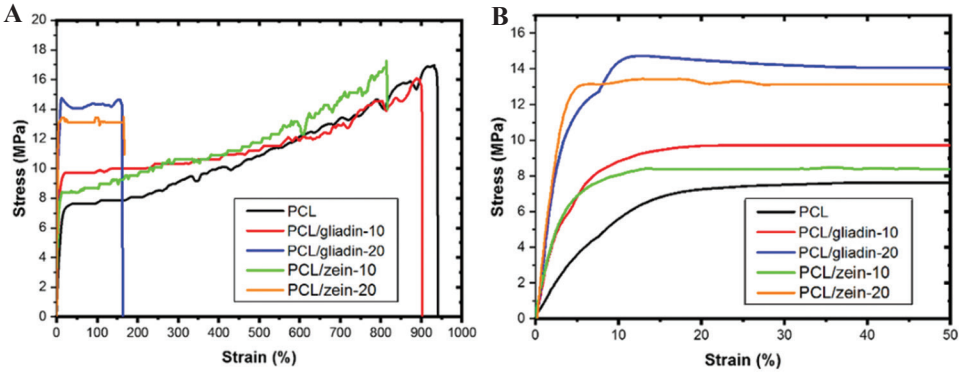


**Figure 4.** Tensile test of printed scaffolds (A) Stress-strain curve, (B) Enlarged view of initial range.

**Table 2.** Tensile properties of PCL, PCL/zein, and PCL/gliadin scaffolds

| Scaffolds | PCL | PCL/zein-10 | PCL/zein-20 | PCL/gliadin-10 | PCL/gliadin-20 |
|---|---|---|---|---|---|
| Young's modulus (MPa) | 101.3±6.5 | 241.4±7.9 | 338.7±38.9 | 265.3±27.8 | 465.3±50.9 |
| Yield stress (MPa) | 4.5±0.5 | 6.3±0.3 | 14.2±0.6 | 7.2±0.7 | 15.0±0.6 |
| Yield strain (%) | 6.5±0.5 | 5.4±0.7 | 6.0±1.0 | 4.7±0.6 | 5.4±0.4 |
| Ultimate stress (MPa) | 17.1±0.5 | 15.9±0.5 | 14.3±0.8 | 15.7±0.8 | 14.5±0.7 |
| Ultimate strain (%) | 994.4±54.7 | 802.8±59.1 | 167.0±50.9 | 891.2±31.8 | 120.8±26.0 |

polymer behavior with three phases, including elastic deformation, yielding, and prolonged strain hardening. The Young's modulus of this PCL scaffold was about 101.3 ± 6.5 MPa, whereas the yield stress and strain were 4.5 ± 0.5 MPa and 6.5 ± 0.5%, respectively. The ultimate stress and strain of the PCL scaffolds were 17.1 ± 1.0 MPa and 994.4 ± 54.7%, which were about 4 and 150 times higher than that at the yield point. These results suggest that PCL is a ductile material with superior roughness because of the reorientation of polymer chains during stretching. When incorporating gliadin nanoparticles into the composite ink, the Young's modulus values of PCL/gliadin-10 and PCL/gliadin-20 scaffolds dramatically increased to 265.3 ± 27.8 MPa and 465.3 ± 50.9 MPa, respectively. The ultimate strain of PCL/gliadin-20 scaffold dropped to 120.8 ± 26.0 MPa, which is only about one-eighth of that of PCL, whereas the ultimate strain of PCL/gliadin-10 scaffolds remained at high level of 891.2 ± 31.8 MPa. The results showed that PCL/gliadin-20 scaffold became stiffer and brittle, while PCL/gliadin-10 scaffold was still ductile with improved hardness. The gliadin nanoparticles could self-assemble into nanosized structures on accounts of the amphiphilic nature of plant proteins in the solution[21]. These nanoparticles form strong intermolecular interactions with PCL polymer chains and increase the mechanical properties of this PCL/gliadin-10 scaffold, that is, Young's modulus and yield stress. This is similar to incorporating inorganic nanoparticles, such as bioactive glass, to improve the mechanical performance of PCL[26]. In addition, the overall elongation is sacrificed when these nanoparticles start to agglomerate at higher concentration and become larger partial continuous phase in some regions.

The tendency of PCL/zein-10 scaffold's stress-strain curve was very similar to that of PCL/gliadin-10 scaffold, since the uniformly dispersed zein nanoparticles in the composite could link the entangled PCL chains through molecular interactions. This strengthening effect increased both Young's modulus and yield stress. Similar to PCL/gliadin-20 scaffold, the toughness of PCL/zein-20 scaffold was sacrificed somehow because of larger portion of zein particles.

Mechanical stimulation is one of the critical elements in the complex microenvironment during cell culture. Since the chemical composition and proportion of composite materials can tune the stiffness, Young's modulus, and strain of the fabricated scaffolds, diverse mechanical stimuli can be created for cell behavior studies. For example, the stiffness of cell local environment can be used to investigate its influence on cellular traction force to regulate cell migration. However, such level of measurement is currently not available in 3D environment.

## 3.2. Composite scaffolds' cell culture study

Scaffolds' biological studies usually involve the examination of their biocompatibility and biodegradation. The scaffold biodegradation is one of the key factors in tissue regeneration since it provides temporary support for tissue growth and infiltration on implantation and

degrades at a proper rate during tissue regeneration process. This is not a serious issue for cell culture studies since scaffolds are only used for a short time to produce *in vitro* models.

A well-known cell line derived from mouse embryo cells, named NIH/3T3 cell, was cultured on PCL, PCL/gliadin, and PCL/zein scaffolds for biocompatibility evaluation. Due to the concern of side effects from gliadin in cell growth, the cytotoxicity of PCL/gliadin scaffolds was evaluated before cell culture studies.

### *(1) Cytotoxicity assay of gliadin released from PCL/gliadin scaffolds*

The cytotoxicity of the gliadin released from PCL/gliadin scaffolds on NIH/3T3 fibroblast cell was evaluated through colorimetric MTT assay. As shown in **Figure 5A**, the cell viability of NIH/3T3 cells was higher than 95% when incubating together with PCL or PCL/gliadin-10 scaffolds. The cell viability for PCL/gliadin-10 scaffolds was slightly higher than that of the control group (cell culture in medium), while this value was only about 85% for PCL/gliadin-20 scaffolds. This suppressive effect was caused increased release of gliadin from the PCL/gliadin-20 scaffold since its corresponding weight loss in 72 h was obviously bigger than that of PCL/gliadin-10.

The weight loss of PCL/gliadin scaffolds was measured by immersing them in phosphate-buffered saline (PBS, 10 mM, pH 7.4) with the addition of 1% antibiotics at an incubator (37°C). As in **Figure 5B**, the weight loss of PCL scaffold versus time was negligible, while the weight loss for PCL/gliadin-10 and PCL/gliadin-20 scaffolds was up to 14.5% and 21.2%, respectively, in 120 h. Nearly 90% of the total weight loss happened in the first 20 h. Meanwhile, the release of gliadin did not change the pH value of the solution as gliadin is neutral substance in the solution.

### *(2) Cell viability and proliferation studies in the PCL/gliadin scaffolds*

The cellular interactions of these fabricated PCL/gliadin scaffolds were further studied in this sub-section. The influence of gliadin component was investigated by directly culturing NIH/3T3 cells on the PCL/gliadin scaffolds. The scaffolds were cut into unified round specimens and inserted in the ultralow attachment culture plate. A small volume of cell suspension was directly pipetted onto the specimen in each well for cell seeding. After incubation for few hours, the culture medium was added, and some cells adhered onto the scaffold fibers.

Cell seeded scaffolds were visualized by confocal laser scanning microscopy (CLSM, LSM-880, ZEISS, Germany). After fixation in paraformaldehyde, the cell nuclei and membrane were stained with Hoechst 33342 and DiI dye, which emit blue and red fluorescence, respectively, on laser excitation. **Figure 6A** shows the CLSM images of cell cultured on PCL and PCL/gliadin scaffolds on days 1, 3, 7, and 14. On day 1, the spheroid cells could partially attach onto the scaffolds. After 3 days, most of the attached cells started to spread, orient, elongate along the fiber directions, and extend the filopodia at leading edge to grab on the adjacent fibers. This resembles fibroblast migration *in vivo* with front-end/back-end polarity[27]. The cell adhesion and proliferation were not homogeneous on the first few days because of uneven cell distribution during initial cell seeding. From day 3 to day 7, the fibroblasts actively proliferated from the scaffold's side walls to the center of pores, formed a unique circular structure, and eventually merged to form a cellular film. Finally, a film-like cell sheet was observed in each cultured scaffold on day 14.

A colorimetric cell proliferation assay (CellTiter 96® AQueous One Solution) was applied to count cell numbers. In cell culture experiments, the ultra-low attachment culture plate (Corning 3473) was used for

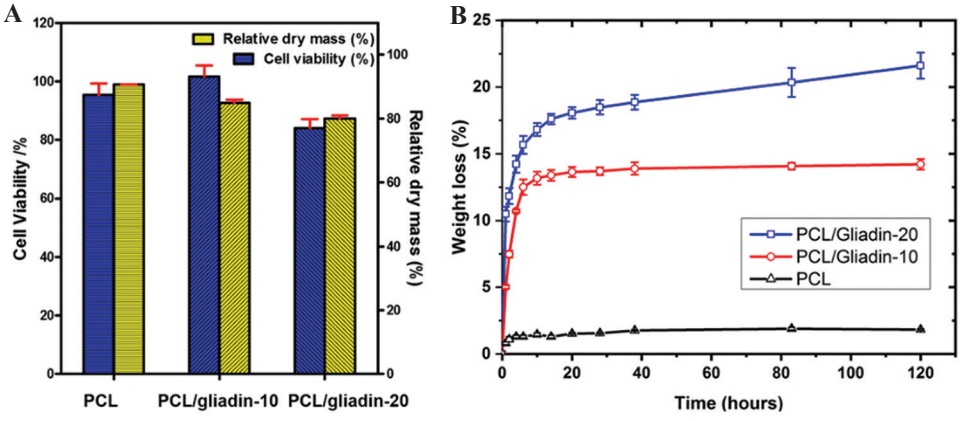


**Figure 5.** *In vitro* cytotoxicity test (A) Cell viability and relative dry mass loss after seeding cells on poly(ε-caprolactone) (PCL) and PCL/gliadin scaffolds for 72 h; (B) weight loss profile of PCL and PCL/gliadin scaffolds in phosphate-buffered saline.

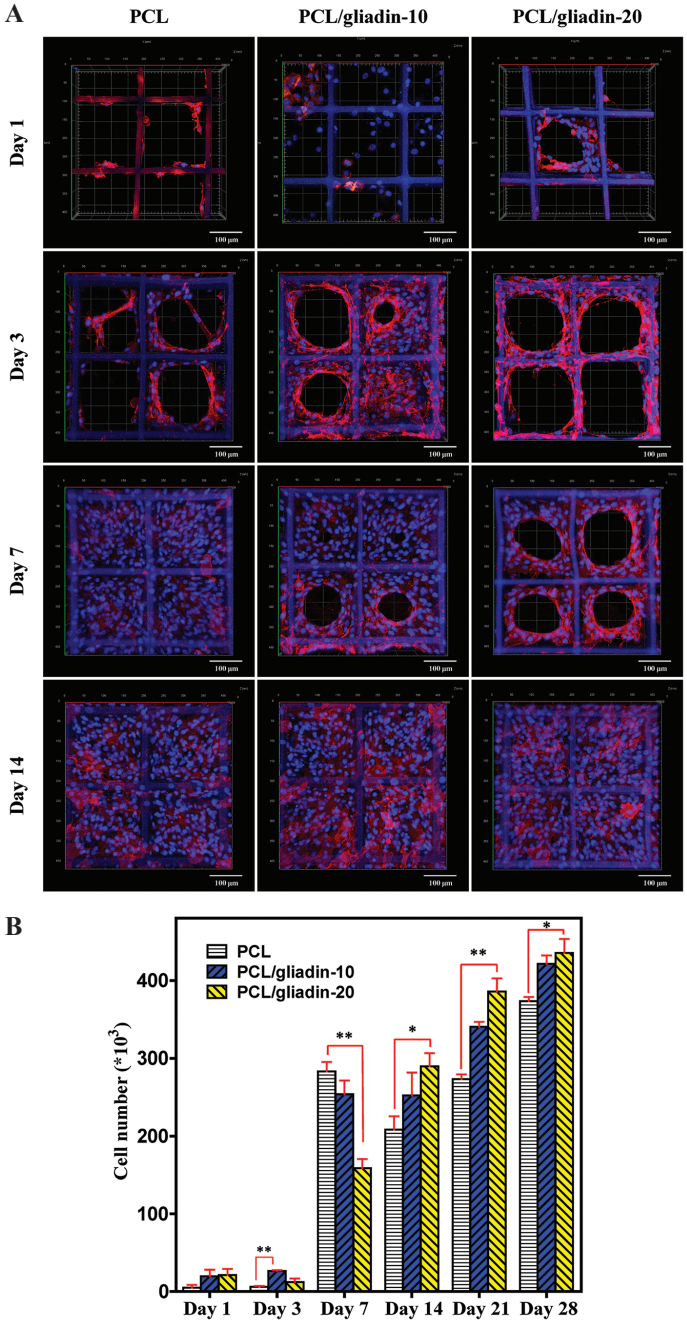


**Figure 6.** 3D cell culture study on gliadin containing scaffolds (A) Confocal laser scanning microscopy images of NIH/3T3 cell cultured on poly(ε-caprolactone) (PCL) and PCL/gliadin scaffolds. (B) NIH/3T3 cell numbers on PCL and PCL/gliadin scaffolds by CellTiter 96® AQueous One Solution assay ($n = 5$, $^*P < 0.05$, $^{**}P < 0.01$).

cell seeding. For this kind of culture plate, cells were unable to attach onto the bottom substrate. They either adhered onto the scaffold fibers or gathered to form cell spheroids that floated in the medium. Before performing cell counts, the cell seeded scaffolds were washed with PBS thrice to get rid of unattached cells and transferred to a new plate for a colorimetric cell counting assay. Thus, only the cells that attached onto the scaffold were counted for the comparison of cell numbers.

As illustrated in **Figure 6B**, the number of cell attached to the gliadin-containing scaffolds was approximately 4 times higher than that of the PCL scaffolds on day 1. This might be attributed to the improved hydrophilicity of the fiber surface, and certain amino acid residues of gliadin might act as anchor points for cell recognition and binding. On day 3, the cells adapted to the microenvironment and the number of cells that attached to the PCL and PCL/gliadin-10

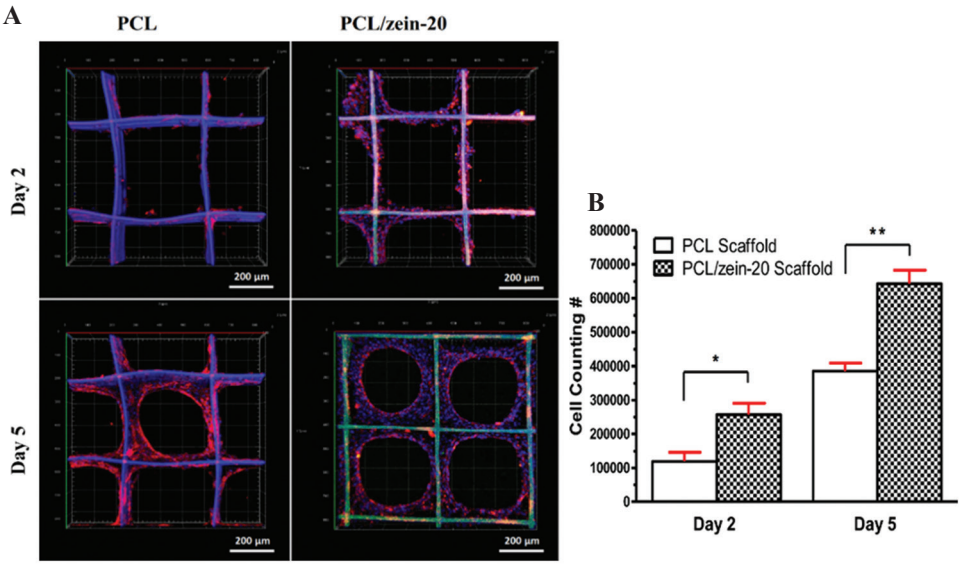


**Figure 7.** 3D cell culture study on zein containing scaffolds (A) Confocal laser scanning microscopy images of NIH/3T3 cell culture on poly(ε-caprolactone) (PCL) and PCL/zein-20 scaffolds. (B) NIH/3T3 cell number on PCL and PCL/zein-20 scaffolds.(n = 3, $*P < 0.05$, $**P < 0.01$). (Reproduced from Ref. Jing *et al*.[23] with permission).

scaffolds slightly increased. However, the cell number on the PCL/gliadin-20 scaffolds declined by around 40%, which is consistent with the results of cytotoxicity assay in **Figure 5.** This growth inhibition effect is caused by increased release of gliadin component. From day 7 to day 28, the cell number continued to increase, and the biggest increase was observed from the PCL/gliadin-20 scaffolds. This is attributed to the larger number of nano-pores and cracks created by the released gliadin which facilitate cell migration, proliferation, and infiltration.

In general, the gliadin-containing scaffolds can promote cell adhesion of NIH/3T3 cells. It can facilitate cell proliferation more effectively than PCL for relatively long-term cell culture until week 4. The inhibition effect from PCL/gliadin-20 scaffold only shows at the earlier stage.

### *(3) Cell viability and proliferation studies in PCL/zein scaffolds*

Zein is almost insoluble in water or PBS solution; therefore, the evaluation of weight loss of PCL/gliadin in cell culture was not applicable for PCL/zein scaffolds. Since no cytotoxicity of zein has been reported in previous studies[23], we evaluated biological performance of fabricated PCL/zein scaffolds directly. **Figure 7A** shows the CLSM images of seeding NIH/3T3 cells on PCL and PCL/zein-20 scaffolds on different days and **Figure 7B** shows the corresponding cell counting results. On day 2, NIH/3T3 cells were inclined to adhere onto the side surface of these scaffolds and the number of cells on the PCL/zein-20 scaffold was about twice of that on the PCL scaffolds. The cell affinity increased with zein portion in the scaffolds. On day 5, NIH/3T3 cells distributed homogeneously within the scaffolds and formed circular cell clusters. Eventually, cellular films could be observed within the scaffold pores. Seemingly, zein-containing fiber surface was more suitable for cell recognition and adhesion due to the functional groups from the amino acid side chains. The cell affinity toward scaffold could be adjusted by varying weight percentage of zein in the composite inks.

### *(4) Plant protein nanoparticles in cell culture applications*

Plant protein nanoparticles affect scaffolds' cell culture applications through protein particle signaling, surface morphology change, and scaffold degradation after the release of nanoparticles. Fibrous scaffold composition has a profound influence on cell behavior such as signaling and contact guidance[1]. This inspires novel strategies to manipulate fiber surface with chemical stimuli for enhanced cell attachment and proliferation. The composite scaffolds containing plant protein can benefit cell culture process in two steps. First, the fiber-containing protein nanoparticles favor cell attachment and colonization. As the key factor to improve scaffolds' cell affinity at the initial stage, this effect can be modulated by regulating the density, size, and dimensional scale of nanoparticles. With the increasing applications of plant protein nanoparticles in developing composite biomaterial inks, intriguing ECM-mimicking fibrous scaffolds can be created with improved cell–scaffold interface.

Both zein and gliadin particles are prone to self-assemble to nanospheres in biomaterial inks because

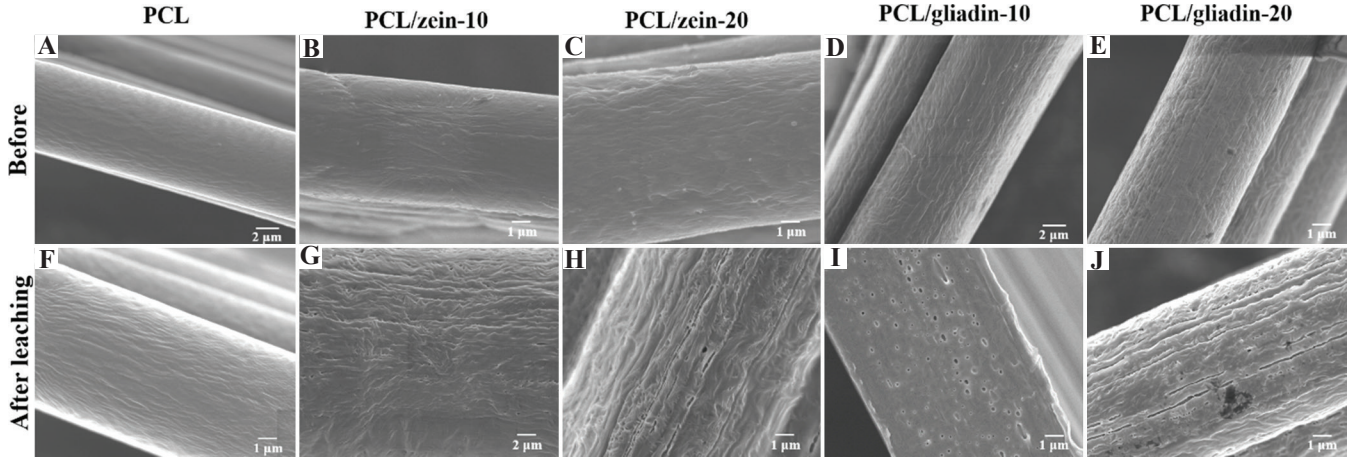


**Figure 8.** Fiber surface morphological changes of before and after the leaching treatment for 48 h. (A) and (F) poly(ε-caprolactone) (PCL). (B) and (G) PCL/zein-10. (C) and (H) PCL/zein-20. (D) and (I) PCL/gliadin-10. (E) and (J) PCL/gliadin-20. PCL/gliadin and PCL/zein scaffolds were leached in culture media and 70% ethanol, respectively. (PCL scaffold was used as control).

of their amphiphilicity[17]. It is difficult to compare the cellular behaviors of zein and gliadin on PCL/zein and PCL/gliadin scaffolds in the same way, as gliadin can quickly dissolve in the culture medium but zein has poor water solubility. Hence, leaching treatment was applied to simulate the surface morphology change of scaffolds *in vitro*. Before the leaching treatment, the PCL, PCL/zein, and PCL/gliadin scaffolds were dried *in vacuo* at 40°C until they reached a constant weight. Then, the scaffolds were completely immersed in 70% ethanol with shaking (80 rpm) for 48 h. The solution was replenished every 12 h. After treatment, the scaffolds were washed with deionized water thrice and then dried *in vacuo* until they reached a constant weight. Using this method, nanoparticles on the composite scaffold fiber surface were released into the culture medium, and nanopores and cracks were generated.

According to **Figure 8A-E**, surface morphology of fibers was almost the same for all the scaffold materials because relatively small portion of nanoparticles in the composite ink materials was not sufficient to engender noticeable changes. As shown in **Figure 8A and 8F**, no obvious change was found on PCL scaffold fiber surface before and after the leaching treatment since PCL cannot dissolve in ethanol. The size and density of gliadin and zein particles could be speculated from the surface morphology change of fibers, as shown in **Figure 8G-J**, through leaching. Based on the voids on the fiber surface (**Figure 8G-8J**), it can be speculated that both zein and gliadin can self-assemble into nanoparticles in the composite ink, which can influence mechanical properties of printed scaffolds. Moreover, higher density of nanopores and cracks could be observed on PCL/zein-20 and PCL/gliadin-20 scaffolds compared with those observed on PCL/zein-10 and PCL/gliadin-10 scaffolds. The scale of such nanopores was also larger for the PCL/zein-20 and PCL/gliadin-20 scaffolds, which is due to the increasing portion and size of plant protein particles in the composite inks. For example, the average pore size of nanopores on **Figure 8I and 8J** is 133.1 ± 47.4 nm and 209.2 ± 76.2 nm, respectively. These holes and fissures interconnected with each other, generated a highly cavernous structure, and increased surface area exponentially; all of which significantly facilitated cell migration, proliferation, and infiltration.

In general, the developed composite scaffolds degrade in two interrelated processes. First, zein and gliadin particles can be released from scaffold fiber surface under physiological environment, but in different ways. Since gliadin is a water-soluble protein, its particles from PCL/gliadin scaffolds can be dissolved in PBS solution. For PCL/zein scaffolds, various proteases can hydrolyze zein into peptides or amino acids. Thus, nanopores and cracks on the fiber surface can be observed on both PCL/zein and PCL/gliadin scaffolds. Second, such nanoporous surface can accelerate the composite scaffolds' degradation, since PCL polymer chains might be synchronously released into solution when zein or gliadin domain in the composite is degraded as a result of molecular level blending. Thus, the degradation rate of the composite scaffolds can be controlled by adjusting the mixing ratio of plant protein and PCL in the biomaterial ink. In general, the composite material scaffolds degrade faster than the pure PCL scaffolds with the same scaffold structural parameters.

Plant proteins have been used to develop composite scaffolds for several reasons, including their biocompatibility, biodegradability, safety, low cost, processibility, and ductility[28]. Nevertheless, the possible immunogenicity effects restrict their biomedical applications. Of course, whether the occurrence of immune response depends on the dose of plant protein

within the scaffolds still requires further and thorough investigations. The availability of a few synthetic biopolymers and plant proteins for developing composite materials has given us the opportunity to try out different permutations in an attempt to fine-tube mechanical properties and biological performance of the scaffolds. The purity level of these plant proteins may also affect their physicochemical properties and act as a limiting factor in their wide usage. More researches are scaling up the current protein extraction and purifying techniques and clinical trials on more composite scaffolds are expected soon.

## 4. Conclusion

Plant proteins, such as zein and gliadin, have been reported to play a critical role in regulating cell behaviors. Their interaction that occurs at nanoscale has not been comprehensively discussed in the context of fibrous scaffolds. Because of the unique advantages of such plant proteins, we explore the possibilities of utilizing them as scaffold materials for cell culture applications. Two types of plant protein-based composite inks, called the PCL/gliadin and PCL/zein, were prepared. The corresponding scaffolds were fabricated using EHDP technology. A monitoring and identification system was developed to optimize the corresponding scaffold fabrication process. Both PCL/gliadin-10 and PCL/zein-10 scaffolds have enhanced tensile strength and cell viability in terms of cell affinity and proliferation. Compared with PCL scaffold, the PCL/gliadin-20 and PCL/zein-20 scaffolds are brittle and stiffer. Moreover, the proportion of plant proteins can be altered to control the tensile strength and cell viability of these composite scaffolds. Thus, the composite materials, PCL/gliadin-10 and PCL/zein-10, are recommended for tissue engineering as they can not only improve scaffolds' mechanical strength to support cell growth but also exhibit favorable biocompatibility for cell culture applications. The developed composite scaffolds may provide valuable *in vitro* platform to study cell biology in 3D microenvironment. With the increasing applications of plant protein nanoparticles in developing new composite biomaterial inks, intriguing ECM-mimicking fibrous scaffolds can be created with improved cell–scaffold interface, which can be used to culture diverse cells and form organoids.

## Acknowledgments

This work is financially supported by the Key Program Special Fund in Xi'an Jiaotong-Liverpool University (XJTLU) under Grant KSF-A-09 and KSF-E-37.

## Conflict of interest

The authors declare no conflicts of interest.

## Author contribution

L.J., H.L., and X.W. designed the overall experimental plan and performed experiments. L.J. interpreted data and wrote the manuscript with support from J.S. and H.L. J.S. and D.H. supervised the project and conceived the original idea. All authors read and approved the manuscript.

## References

1. Hutmacher DW, 2001, Scaffold Design and Fabrication Technologies for Engineering Tissues State of the Art and Future Perspectives. *J Biomater Sci Polym Ed*, 12:107–24. http://doi.org/10.1163/156856201744489.
2. Pampaloni F, Reynaud EG, Stelzer EH, 2007, The Third Dimension Bridges the Gap between Cell Culture and Live Tissue. *Nat Rev Mol Cell Biol*, 8:839–45. http://doi.org/10.1038/nrm2236.
3. Walpita D, Hay E, 2002, Studying Actin-dependent Processes in Tissue Culture. *Nat Rev Mol Cell Biol*, 3:137–41. http://doi.org/10.1038/nrm727.
4. Gudjonsson T, Rønnov-Jessen L, Villadsen R, *et al.*, 2002, Normal and Tumor-derived Myoepithelial Cells Differ in their Ability to Interact with Luminal Breast Epithelial Cells for Polarity and Basement Membrane Deposition. *J Cell Sci*, 115:39.
5. Dhiman HK, Ray AR, Panda AK, 2005, Three-dimensional Chitosan Scaffold-based MCF-7 Cell Culture for the Determination of the Cytotoxicity of Tamoxifen. *Biomaterials*, 26:979–86. http://doi.org/10.1016/j.biomaterials.2004.04.012.
6. Baker BM, Chen CS, 2012, Deconstructing the Third Dimension-how 3D Culture Microenvironments Alter Cellular Cues. *J Cell Sci*, 125:3015–24. http://doi.org/10.1242/jcs.079509.
7. Ma PX, 2004, Scaffolds for Tissue Fabrication. *Mater Today*, 7:30–40.
8. Chia HN, Wu BM, 2015, Recent Advances in 3D Printing of Biomaterials. *J Biol Eng*, 9:4.
9. Ozbolat IT, Hospodiuk M, 2016, Current Advances and Future Perspectives in Extrusion-Based Bioprinting. *Biomaterials*, 76:321–43. http://doi.org/10.1016/j.biomaterials.2015.10.076.
10. Ng WL, Lee JM, Zhou M, *et al.*, 2020, Vat Polymerization-based Bioprinting-Process, Materials, Applications and Regulatory Challenges. *Biofabrication*, 12:022001. http://doi.org/10.1088/1758-5090/ab6034.
11. Onses MS, Sutanto E, Ferreira PM, *et al.*, 2015, Mechanisms, Capabilities, and Applications of High-Resolution

Electrohydrodynamic Jet Printing. *Small*, 11:4237–66. http://doi.org/10.1002/smll.201500593.

12. Liu H, Vijayavenkataraman S, Wang D, *et al.*, 2017, Influence of Electrohydrodynamic Jetting Parameters on the Morphology of PCL Scaffolds. *Int J Bioprint*, 3:72–82. http://doi.org/10.18063/ijb.2017.01.009.
13. Guvendiren M, Molde J, Soares RMD, *et al.*, 2016, Designing Biomaterials for 3D Printing. *ACS Biomater Sci Eng*, 2:1679–93. http://doi.org/10.1021/acsbiomaterials.6b00121.
14. Sun J, Vijayavenkataraman S, Liu H, 2017, An Overview of Scaffold Design and Fabrication Technology for Engineered Knee Meniscus. *Materials* (*Basel*), 10:29. http://doi.org/10.3390/ma10010029.
15. Woodruff MA, Hutmacher DW, 2010, The Return of a Forgotten Polymer Polycaprolactone in the 21st Century. *Prog Polym Sci*, 35:1217–56. http://doi.org/10.1016/j.progpolymsci.2010.04.002.
16. Lam CX, Hutmacher DW, Schantz JT, *et al.*, 2009, Evaluation of Polycaprolactone Scaffold Degradation for 6 Months *In Vitro* and *In Vivo*. *J Biomed Mater Res A*, 90:906–19.
17. Wan ZL, Guo J, Yang XQ, 2015, Plant Protein-based Delivery Systems for Bioactive Ingredients in Foods. *Food Funct*, 6:2876–89. http://doi.org/10.1039/c5fo00050e.
18. Anderson TJ, Lamsal BP, 2011, REVIEW: Zein Extraction from Corn, Corn Products, and Coproducts and Modifications for Various Applications: A Review. *Cereal Chem J*, 88:159–73. http://doi.org/10.1094/cchem-06-10-0091.
19. Paliwal R, Palakurthi S, 2014, Zein in Controlled Drug Delivery and Tissue Engineering. *J Control Release*, 189:108–22. http://doi.org/10.1016/j.jconrel.2014.06.036.
20. He M, Jiang H, Wang R, *et al.*, 2017, Fabrication of Metronidazole Loaded Poly (ε-Caprolactone)/Zein Core/Shell Nanofiber Membranes Via Coaxial Electrospinning for Guided Tissue Regeneration. *J Colloid Interface Sci*, 490:270–8. http://doi.org/10.1016/j.jcis.2016.11.062.
21. Urade R, Sato N, Sugiyama M, 2018, Gliadins from Wheat Grain: An Overview, from Primary Structure to Nanostructures of Aggregates. *Biophys Rev*, 10:435–43. http://doi.org/10.1007/s12551-017-0367-2.
22. Koning F, 2015, Adverse Effects of Wheat Gluten. *Ann Nutr Metab*, 67 Suppl 2:8–14.
23. Jing L, Wang X, Liu H, *et al.*, 2018, Zein Increases the Cytoaffinity and Biodegradability of Scaffolds 3D-Printed with Zein and Poly(epsilon-caprolactone) Composite Ink. *ACS Appl Mater Interfaces*, 10:18551–9. http://doi.org/10.1021/acsami.8b04344.s001.
24. Sun J, Hong GS, Rahman M, *et al.*, 2005, Improved Performance Evaluation of Tool Condition Identification by Manufacturing Loss Consideration. *Int J Prod Res*, 43:1185–204.
25. Jie S, Hong GS, Rahman M, *et al.*, 2002, Feature Extraction and Selection in Tool Condition Monitoring System. In: Australian Joint Conference on Artificial Intelligence, Springer, Berlin, Germany, pp. 487-497. http://doi.org/10.1007/3-540-36187-1_43.
26. Castro AG, Diba M, Kersten M, *et al.*, 2018, Development of a PCL-silica Nanoparticles Composite Membrane for Guided Bone Regeneration. *Mater Sci Eng C Mater Biol Appl*, 85:154–61.
27. Meshel AS, Wei Q, Adelstein RS, *et al.*, 2005, Basic Mechanism of Three-dimensional Collagen Fibre Transport by Fibroblasts. *Nat Cell Biol*, 7:157–64. http://doi.org/10.1038/ncb1216.
28. Reddy N, Yang Y, 2011, Potential of Plant Proteins for Medical Applications. *Trends Biotechnol*, 29:490–8.

RESEARCH ARTICLE

# Biodegradation, Antibacterial Performance, and Cytocompatibility of a Novel ZK30-Cu-Mn Biomedical Alloy Produced by Selective Laser Melting

**Bin Xie[1], Ming-Chun Zhao[1], Rong Xu[1], Ying-Chao Zhao[1], Dengfeng Yin[1]*, Chengde Gao[1], Andrej Atrens[2]**

[1]School of Materials Science and Engineering, Central South University, Changsha 410083, P.R. China
[2]School of Mechanical and Mining Engineering, University of Queensland, Brisbane, Qld 4072, Australia

**Abstract:** In the present study, an antibacterial biomedical magnesium (Mg) alloy with a low biodegradation rate was designed, and ZK30-0.2Cu-xMn (x = 0, 0.4, 0.8, 1.2, and 1.6 wt%) was produced by selective laser melting, which is a widely applied laser powder bed fusion additive manufacturing technology. Alloying with Mn evidently influenced the grain size, hardness, and biodegradation behavior. On the other hand, increasing Mn content to 0.8 wt% resulted in a decrease of biodegradation rate which is attributed to the decreased grain size and relatively protective surface layer of manganese oxide. Higher Mn contents increased the biodegradation rate attributed to the presence of the Mn-rich particles. Taken together, ZK30-0.2Cu-0.8Mn exhibited the lowest biodegradation rate, strong antibacterial performance, and good cytocompatibility.

**Keywords:** Magnesium alloy; Selective laser melting; Biodegradation; Antibacterial activity; Grain refinement

***Correspondence to:** Dengfeng Yin, School of Materials Science and Engineering, Central South University, Changsha 410083, P.R. China; 206191@csu.edu.cn.

**Received:** June 21, 2020; **Accepted:** August 28, 2020; **Published Online:** October 30, 2020

**Citation:** Xie B, Zhao MC, Xu R, *et al.,* 2021, Biodegradation, Antibacterial Performance and Cytocompatibility of a Novel ZK30-Cu-Mn Biomedical Alloy Produced by Selective Laser Melting. *Int J Bioprint,* 7(1):300.http://doi.org/10.18063/ijb.v7i1.300

## 1. Introduction

Magnesium (Mg) alloy is a new metal implant material that has suitable rates of biodegradation and good biocompatibility[1-4]. The further research is the development of antibacterial Mg alloys, such as Cu-containing Mg alloys. These are promising biodegradable antibacterial implant materials[5-7] because Cu can provide an antibacterial effect which can resolve clinical infection in bone regeneration and in other orthopedic applications. However, the degradation rate of Cu-containing Mg alloys is very rapid because the Cu-containing intermetallic compounds cause microgalvanic corrosion[5-7]. Alloying has been widely used to ameliorate the degradation rate of Mg alloys.

Alloying with Mn may refine the grain size and decrease the corrosion rate[8-10]. Moreover, Mn is an essential trace element in the human body and the Mn that is released during Mg alloy degradation is non-toxic to human body[11]. Appropriate Mn level can promote the growth and development of bones and improve hematopoietic function of the body[12]. However, the uniform dispersion of Mn in Mg alloys remains a big challenge in conventional casting process because Mn reduces the fluidity of Mg alloys which facilitates Mn segregation[13]. Hence, it is necessary to develop a method to produce homogeneous Mn-containing Mg alloys.

Selective laser melting (SLM) as a widely applied laser powder bed fusion metallic additive manufacturing technology[14-22] can rapidly melt mixed powders of Mn and Mg alloys and cause rapid solidification in the melt pool, resulting in a homogenous microstructure with fine grains. Therefore, SLM can produce homogeneous Mn-containing Mg alloys that are expected to have a refined grain size and a lower corrosion rate. Furthermore, grain refinement can increase the mechanical properties.

As stated above, alloying Mn into a antibacterial Cu-containing Mg alloy using SLM was suggested and investigated in this article to decrease the corrosion rate

and retain the antibacterial activity of the Cu-containing Mg alloy. This method can produce antibacterial Mg-based alloys with the desired lower corrosion rate. Furthermore, mechanical properties may be improved by alloying and grain refinement. Previous work indicated that ZK30 (Mg-3Zn-0.5Zr) had good mechanical properties and biodegradation resistance[13,23]. When Cu was added to ZK30 by SLM, SLMed ZK30-0.2Cu had a uniform microstructure, good cytocompatibility, and antibacterial performance[23].

In this study, SLM was used to produce antibacterial Mg alloys from Cu powder (0.2 wt.% Cu), Mn powder (0, 0.4, 0.8, 1.2, and 1.6 wt.% Mn), and ZK30 powder. The microstructure, hardness, biodegradation, antibacterial performance, and cytotoxicity of these alloys were investigated. This proposed method is a new approach for the composition design and the manufacturing process to develop novel antibacterial Mg-based biodegradable alloys.

## 2. Materials and methods

### 2.1. Materials preparation

Gas atomized spherical ZK30 powder, pure Cu powder (99.9%), and irregularly shaped pure Mn powder (99.9%) were used. The composition of ZK30 powder is presented in **Table 1**. The ZK30 powder was mechanically mixed with 0.2 wt% Cu powder and different content of Mn powder (0, 0.4, 0.8, 1.2, and 1.6 wt%) was added by ball milling[14] at a rotation rate of 150 rpm in the atmosphere of $SF_6$ (1 vol%) and $CO_2$ (balance) for 180 min. ZK30-0.2Cu-xMn alloys (x = 0, 0.4, 0.8, 1.2, and 1.6) were produced using a self-regulating SLM system[24] in a chamber filled with high purity argon. The fiber laser had an output power of 500 W and a wavelength of 1064 nm. The minimum focused spot diameter of laser beam was 50 μm. The parameters of the process are as follows: The spot size was 150 μm, scanning speed was at 200 mm/min, laser power was 80 W, and the specimen size is 8 mm × 8 mm × 5 mm.

### 2.2. Microstructural and mechanical characterizations

The specimens of the SLMed ZK30-0.2Cu-xMn alloys were metallurgically ground and polished and etched in a solution of nitric acid and alcohol (4 mL nitric acid and 96 mL ethanol) for 5 – 10 s. The microstructures were characterized using optical microscopy (OM, Leica DMI 3000 L) and scanning electron microscopy (SEM, JSM-5600LV, JEOL Co., Tokyo, Japan) equipped with energy dispersive spectroscopy (EDS, JSM-5910LV, JOEL Ltd., Japan). Intermetallic second phases were analyzed using X-ray diffraction (XRD) monochromatic Cu-Kα radiation at 15 mA and 30 kV, with scattering angles ranging from 10° to 80°, step size 0.02° and scanning speed 8°/min. The hardness was measured using a microhardness tester for 10 s under 2.942 N load.

### 2.3. Electrochemical tests

The electrochemical behavior of SLMed ZK30-0.2Cu-xMn alloys at room temperature in simulated body fluid (SBF) was characterized by potentiodynamic polarization curves, measured using an electrochemical workstation (MULTI AUTOLAB M204). The ionic concentrations of the standardized SBF solution that corresponds to the concentration of the ions in the blood are shown in **Table 2**. The specimen with the exposed area of 0.8 mm × 0.8 mm was encapsulated with epoxy resin and a Cu wire was used as the conducting wire. The polarization curve was measured by a three-electrode configuration. The specimen was the working electrode (WE), a platinum gauze (25 mm × 25 mm; 60 mesh) was the counter electrode (CE). A saturated Ag/AgCl electrode (in saturated KCl) was the reference electrode (RE). Potentiodynamic polarization curves were measured at a scan rate of 5 mV/s after the specimen was immersed for 2500 s at the open circuit potential and steady corrosion conditions had been established. The biodegradation rate ($P_i$, mm year$^{-1}$) was calculated from the corrosion current density ($i_{corr}$, mA cm$^{-2}$), using[25,26]:

$$P_i = 22.85\, i_{corr} \quad \text{(i)}$$

### 2.4. Immersion tests

Immersion tests were conducted on the basis of ASTM G31-72 (the ratio of the solution volume [mL] to specimen surface area [cm$^2$] was 30:1) in SBF solution for 168 h. The initial weight of specimen was recorded before immersion, the degradation solution was refreshed every 24 h to keep the pH value at about 7.4. Funnels were used to collect the evolved hydrogen by covering the samples. The specimen was cleaned using acetone and water to remove the corrosion products and then weighed. The biodegradation rate ($P_h$, mm y$^{-1}$) was calculated from hydrogen evolution rate ($V_h$, ml/cm$^2$ day) and the biodegradation rate ($P_w$, mm year$^{-1}$) was calculated from the weight loss rate ($\Delta W$, mg cm$^{-2}$ d$^{-1}$) using[25,26]:

**Table 1.** The composition of the ZK30 powder (wt%)

| Powder | Mg | Zn | Zr | Al | Cu | Fe | Mn | Ni | Si |
|---|---|---|---|---|---|---|---|---|---|
| ZK30 | 96.34 | 3.16 | 0.48 | 0.002 | 0.002 | 0.01 | 0.0068 | 0.0036 | 0.01 |

**Table 2.** The ion concentrations of SBF and human blood plasma according to the ISO standard ($10^{-3}$ mol/L)

| Ion | SBF (pH 7.40) | Blood plasma (pH 7.2–7.4) |
|---|---|---|
| $Na^+$ | 142 | 142 |
| $K^+$ | 5.0 | 5.0 |
| $Mg^{2+}$ | 1.5 | 1.5 |
| $Ca^{2+}$ | 2.5 | 2.5 |
| $Cl^-$ | 148 | 103 |
| $HCO_3^-$ | 4.2 | 27 |
| $HPO_4^{2-}$ | 1.0 | 1.0 |
| $SO_4^{2-}$ | 0.5 | 0.5 |

$$P_h = 2.279 V_h \quad \text{(ii)}$$

$$P_w = 2.1\ \Delta W \quad \text{(iii)}$$

The surface morphologies and corrosion products of the specimens after immersion were characterized by SEM with EDS and X-ray photoelectron spectroscopy (XPS). The XPS measurements were achieved using an X-ray source of Mg Kα (1253.6 eV). The binding energy of the measurement was corrected by the binding energy of $C_{1s}$ of hydrocarbons (284.6 eV) absorbed on the surface.

## 2.5. Antibacterial properties

*Staphylococcus aureus* (*S. aureus*, ATCC 25923) is one of the most common bacteria causing infection and was, therefore, used as a model bacterium. The preparation method of SLMed ZK30-0.2Cu-xMn alloy extracts for antibacterial test was as follows. After disinfection by ultraviolet radiation, all the samples and control groups were cultured in SBF solution with *S. aureus* in three replicates and placed in a 12-well untreated polystyrene plate. Each well contained sample and *S. aureus* suspension with a concentration of  with a concentration of $1^{-10} \times 10^5$ colony-forming unit (CFU)/ml prepared using sterile SBF solution. The ratio of the specimen surface are ($cm^2$) to the  solution volume (mL) were 1.25 $cm^2$/mL. The plates were kept at constant temperature for 4, 12, 48, 72, and 96 h at 37 ± 0.5°C. Bacterial cell density in the SBF solution was evaluated by bacterial counting after each culture period. Before calculating the number of colonies, the suspension was diluted to $1^{-10} \times 10^3$ CFU/ml, and 0.05 ml suspension was added to the LB nutrient agar plate, which was carefully spread and plated and then incubated for 24 h at 37 ± 0.5°C.

## 2.6. Cytocompatibility

Cell compatibility, which is essential for biomedical implant materials, was studied using the MG63 osteosarcoma cells. The cytocompatibility was evaluated by carrying out cell proliferation assay and fluorescence live/dead staining assay. The extracts of SLMed ZK30-0.2Cu-xMn alloys were extracted in the humidified atmosphere containing 5% $CO_2$ at 37°C for 24 h using Dulbecco's Modified Eagle's Medium as extraction medium with an extraction rate of 1.25 $cm^2$/ml. The supernatant was extracted, centrifuged, and filtered to produce the extract. The extract was refrigerated at 4°C to prepare for cell viability test. CCK-8 assays were used to examine the proliferation of MG63 cells cultured in SLMed ZK30-0.2Cu-xMn and Ti extracts. The fluorescence live/dead staining assay was performed based on the following procedures. Cells were cultured on a 96-well plate at the density of $5 \times 10^3$ cells per 100 ml for 24 h to ensure cell adherence. The medium was then replaced by 100 μL extract. After 1 day and 3 days of incubation, the cell viability was determined by live/dead staining.

# 3. Results

## 3.1. Microstructure

**Figure 1** shows optical microstructures of the SLMed ZK30-0.2Cu-xMn alloys. The microstructures of all the alloys consist of fine equiaxed grains. The grain size decreased with increasing Mn content. The grain size of SLMed ZK30-0.2Cu was about 5 μm, as shown in **Figure 1A**, which was smaller than that obtained by traditional casting[27]. Increasing Mn contents decreased the grain size, as shown in **Figure 1B** through **Figure 1E**. The grain size of SLMed ZK30-0.2Cu-1.6Mn alloy was about 3 μm. This indicates that the incorporation of Mn into SLMed ZK30-0.2 Cu refines grain size. The small grain size produced by SLM is attributed to the rapid solidification of the melt pool. The additional grain refinement by alloying Mn is attributed to additional nucleation sites and grain boundary pinning effect provided by Mn, which can inhibit grain growth.

**Figure 2** shows the XRD patterns of the SLMed ZK30-0.2Cu-xMn alloys. The XRD patterns for SLMed ZK30-0.2Cu, SLMed ZK30-0.2Cu-0.4Mn, and SLMed ZK30-0.2Cu-0.8Mn included peaks of α-Mg, MgZnCu, and $MgZn_2$ phases. For a Mn content higher than 0.8 wt.%, SLMed ZK30-0.2Cu-xMn alloys (x = 1.2 and 1.6) also produced diffraction peaks of the α-Mn phases.

The microstructure of SLMed ZK30-0.2Cu-1.6Mn is presented at a higher magnification SEM micrograph in **Figure 3A**. Numerous irregularly shaped intermetallic phases were distributed inside the grains and along grain boundaries. The composition of the intermetallic phases at Point 1, Point 2, and Point 3 in **Figure 3A** is presented in **Figure 3B** determined from the EDS spectra. Point 1 (bright granular precipitate distributed along the grain boundaries) was composed of Zn and Mg; Point 2 (short bar-shaped precipitate distributed along the grain boundaries) was composed of Zn, Mg, and Cu; and Point

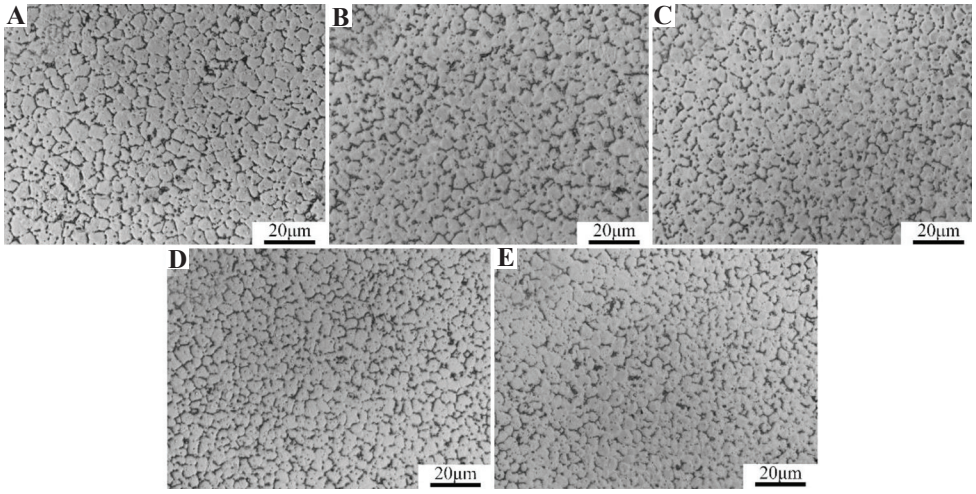


**Figure 1.** Optical microstructures of SLMed ZK30-0.2Cu-xMn. (A) x = 0, (B) x = 0.4, (C) x = 0.8, (D) x = 1.2, (E) x = 1.6.

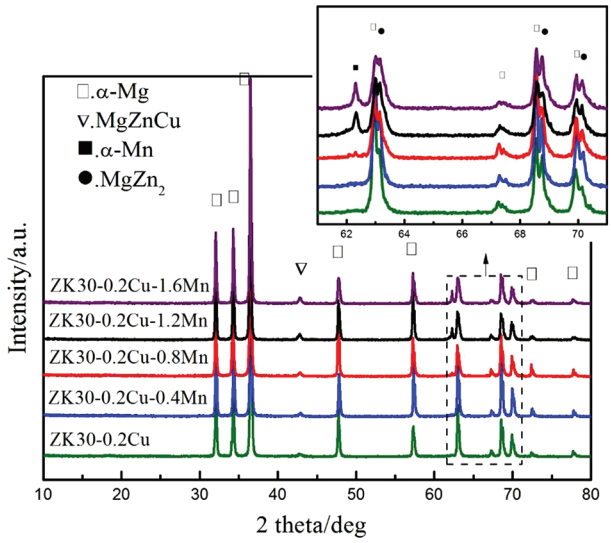


**Figure 2.** X-ray diffraction spectra of SLMed ZK30-0.2Cu-xMn.

3 (spheroidal precipitate scattered along grain boundaries and inside the grains) was composed of Mg and Mn. There was good agreement between the composition results determined respectively by EDS spectra and XRD patterns. This indicates the presence of $MgZn_2$, MgZnCu, and α-Mn phases in SLMed ZK30-0.2Cu-1.6Mn.

## 3.2. Hardness

**Figure 4** presents the Vickers hardness values measured on the polished surface of the SLMed ZK30-0.2Cu-xMn. The hardness of the SLMed ZK30-0.2Cu was 92 ± 3 HV, while a typical hardness of cast Mg alloys is ~70 HV[28]. This indicates that SLM significantly enhances the hardness of the Mg alloys which is attributed to the grain refinement introduced by rapid solidification during the SLM process.

The incorporation of Mn into ZK30-Cu by SLM further increased the hardness. The hardness increased with the Mn content to a maximum hardness of 117 ± 4 HV for the Mn content of 1.6 wt%. This hardness increase is attributed to grain refinement, solid solution strengthening, and second-phase strengthening due to the Mn incorporation. This indeed verifies that Mn is an effective reinforcement for Mg alloys and hardening is attained through the incorporation of Mn into the Mg alloy through SLM.

## 3.3. Biodegradation

**Figure 5** shows potentiodynamic polarization curves for SLMed ZK30-0.2Cu-xMn tested at 37 ± 0.5°C in the SBF solution. The incorporation of Mn into ZK30-0.2Cu by SLM resulted in a change in the corrosion potential ($E_{corr}$) and the corrosion current density ($i_{corr}$). The $E_{corr}$ increased with Mn content, which was attributed to the more positive electrochemical potential of Mn, compared to Mg. The $i_{corr}$ values were derived from the linear part of the cathodic branch of the polarization potential curves using Tafel extrapolation. The incorporation of Mn into ZK30-0.2Cu by SLM first decreased the $i_{corr}$ values. The $i_{corr}$ values of SLMed ZK30-0.2Cu and SLMed ZK30-0.2Cu-0.4Mn were 29 μA/cm² and 18 μA/cm², respectively. The $i_{corr}$ had the minimum value of 12 μA/cm², while Mn content was 0.8 wt.%. Thereafter, with Mn content increased to 1.2 wt% and 1.6 wt%, the $i_{corr}$ increased to 32 μA/cm² and 40 μA/cm², respectively, and was even higher than that for the SLMed ZK 30-0.2Cu without Mn. Using Equation 1, the biodegradation rates were calculated from the $i_{corr}$ values and are presented in **Table 3**.

**Figure 6** shows hydrogen evolution data (**Figure 6A**) and weight loss data (**Figure 6B**) of the SLMed specimens immersed in SBF for 168 h (i.e., 7 days). All the SLMed

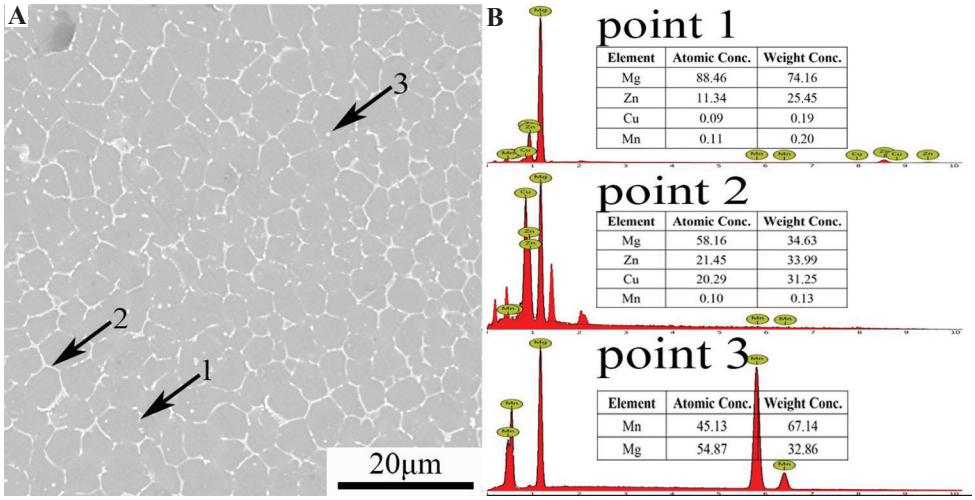


**Figure 3.** (A) Scanning electron microscopy microstructure and (B) energy-dispersive spectroscopy spectra of points 1~3 of SLMed ZK30-0.2Cu-1.6Mn.

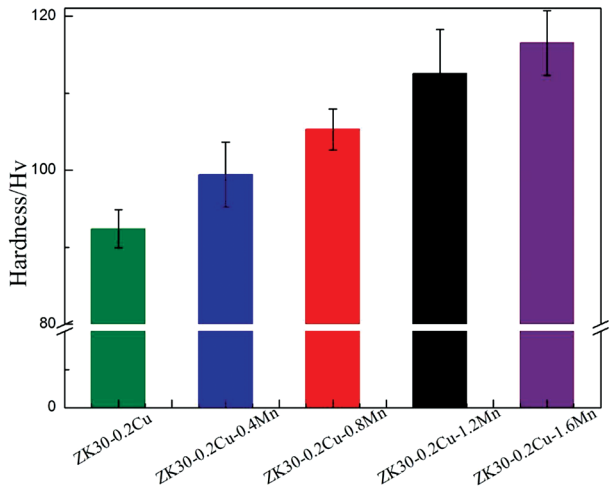


**Figure 4.** Hardness of SLMed ZK30-0.2Cu-xMn.

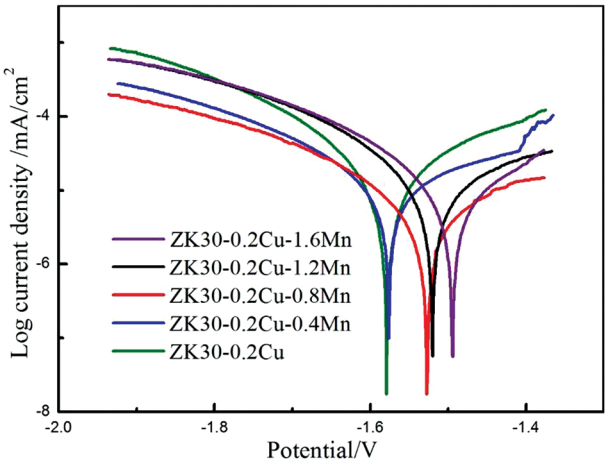


**Figure 5.** Potentiodynamic polarization curves of SLMed ZK30-0.2Cu-xMn.

alloys exhibited an increase in hydrogen evolution volume with immersion time increased, but the rate of hydrogen evolution was fast at the initial 120 h period and then slowed down when immersion time increased, which might be attributed to a slightly increased protectiveness of corrosion layers, which could prevent the corrosion from penetrating into the Mg matrix and thus decrease the corrosion rate. The incorporation of Mn into ZK30-0.2Cu by SLM significantly influenced the hydrogen evolution. The hydrogen evolution volume first decreased, reached a minimum the content of Mn increased to 08 wt%, and hereafter increased when Mn content further increased. There was a direct correlation of the influence of the Mn content on the hydrogen evolution volume and the weight loss rate, that is, the weight loss rate first decreased and had the minimum with Mn content that was increased to 0.8 wt.% and hereafter decreased when Mn content further increased. The biodegradation rates, calculated from hydrogen evolution rate and weight loss rate using Equation 2 and Equation 3 respectively, are listed in **Table 3**.

The biodegradation rate determined by weight loss and hydrogen evolution showed generally good agreement, whereas the biodegradation rate derived from the polarization curves was apparently lower, which is commonly observed[29,30]. However, these methods showed the same trends. In view of the above, SLMed ZK30-0.2Cu-0.8Mn had the lowest biodegradation rate, and the biodegradation rates of SLMed ZK30-0.2Cu-xMn alloys in a decreasing order are shown as follows: SLMed ZK30-0.2Cu-1.6Mn >SLMed ZK30-0.2Cu-1.2Mn >SLMed ZK30-0.2Cu >SLMed ZK30-0.2Cu-0.4Mn > SLMed ZK30-0.2Cu-0.8Mn.

**Figure 7** shows the surface appearances of the SLMed ZK30-0.2Cu-xMn specimens after immersion in the SBF solution for 48 h. **Figure 7A** shows that numerous

**Table 3.** Corrosion rate of SLMed ZK30-0.2Cu-xMn

| Materials | ZK30-0.2Cu | ZK30-0.2 Cu-0.4Mn | ZK30-0.2 Cu-0.8Mn | ZK30-0.2 Cu-1.2Mn | ZK30-0.2 Cu-1.6Mn |
|---|---|---|---|---|---|
| $V_h$ (ml [cm$^2$ day]$^{-1}$) | 0.67±0.03 | 0.56±0.03 | 0.48±0.06 | 0.71±0.04 | 0.93±0.04 |
| $P_h$ (mm year$^{-1}$) | 1.53±0.07 | 1.28±0.07 | 1.09±0.14 | 1.62±0.09 | 2.12±0.09 |
| ΔW (mg [cm$^2$ day]$^{-1}$) | 0.68±0.01 | 0.59±0.02 | 0.47±0.01 | 0.73±0.02 | 0.8±0.02 |
| $P_w$ (mm/year) | 1.43±0.02 | 1.24±0.04 | 0.99±0.02 | 1.53±0.04 | 1.68±0.04 |
| $I_{corr}$ (μA cm$^{-2}$) | 29 | 18 | 12 | 32 | 40 |
| $P_i$ (mm year$^{-1}$) | 0.7 | 0.4 | 0.3 | 0.7 | 0.9 |

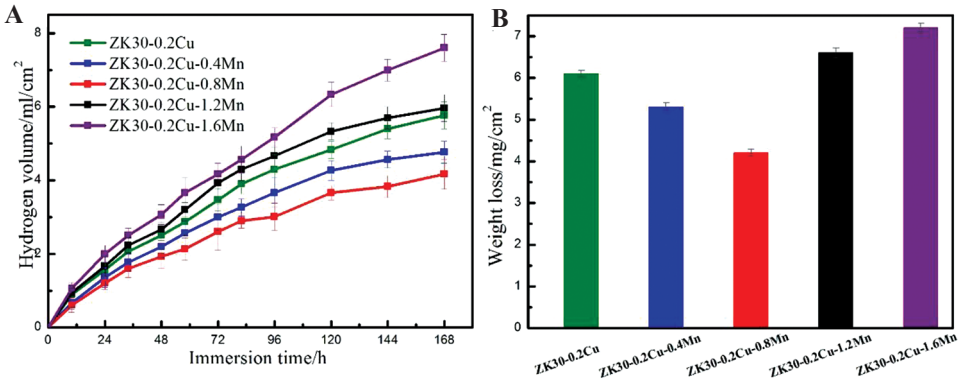


**Figure 6.** Biodegradation behaviors: (A) Hydrogen evolution, (B) weight loss.

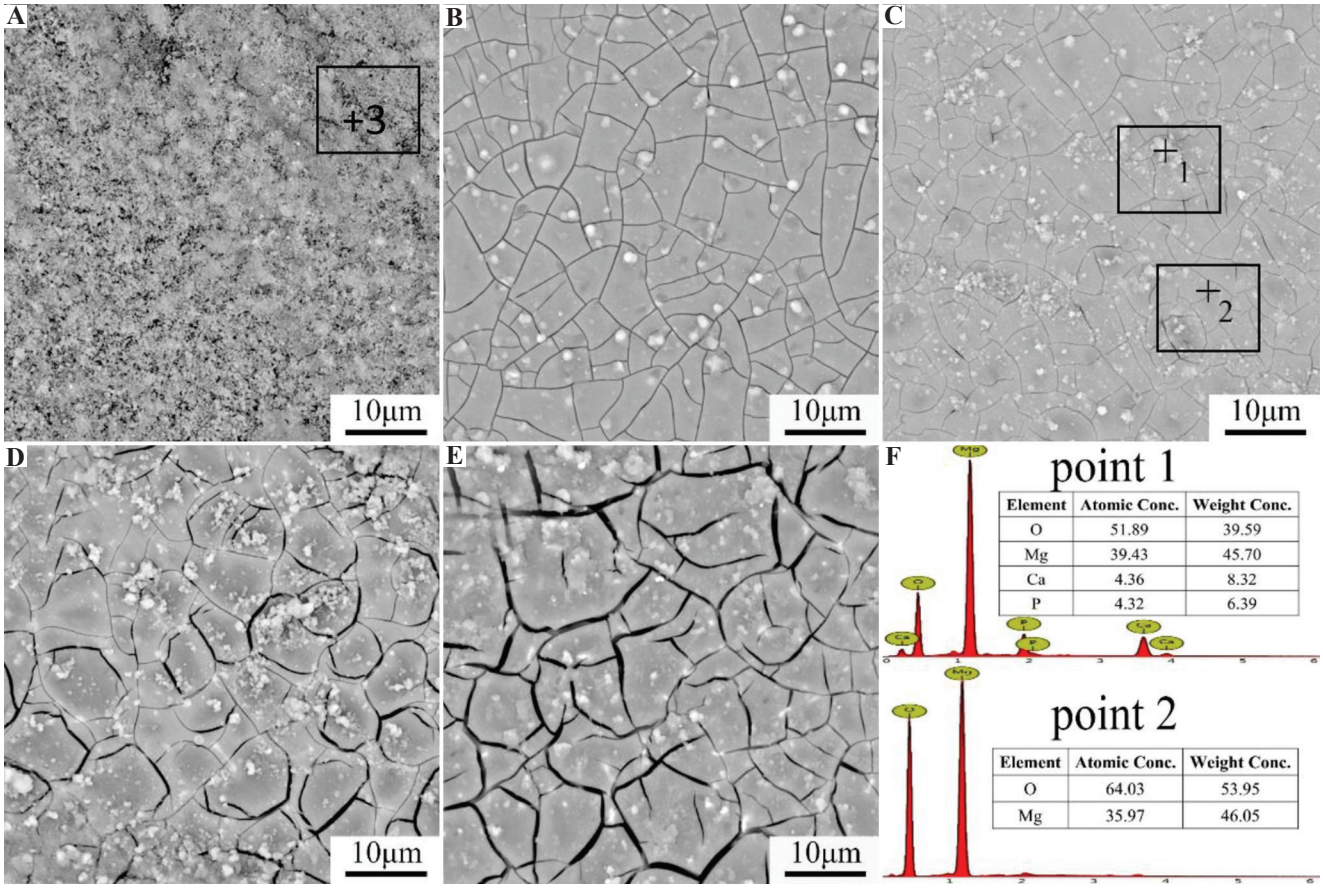


**Figure 7.** Scanning electron microscopy appearance of corroded surfaces of SLMed ZK30-0.2Cu-xMn (A) x = 0, (B) x = 0.4, (C) x = 0.8, (D) x = 1.2, (E) x = 1.6 and (F) energy-dispersive spectroscopy spectra of points 1~2.

loose corrosion products covered the entire surface of the SLMed ZK30-0.2Cu specimen. The Mn-containing alloys did not have these loose corrosion products, but contained some discontinuous white products distributed as a continuous mud-cracked film, as shown in **Figure 7B-E**. The corrosion products on SLMed ZK30-0.2Cu-0.4Mn and SLMed ZK30-0.2Cu-0.8Mn were intact and compact, and there were no loose corrosion products (**Figure 7B and C**), which implied that the corrosion of SLMed ZK30-0.2Cu-0.4Mn and SLMed ZK30-0.2Cu-0.8Mn was relatively slight, compared to SLMed ZK30-0.2Cu. The surface of the alloy containing a Mn content of 1.2 wt.% contained microcracks (**Figure 7D**). With the Mn content further increased to 1.6 wt%, the microcracks became larger and deeper (**Figure 7E**). The compositions of corrosion layers on the corroded surfaces were analyzed using EDS. The EDS spectra in Point 1 and Point 2 in **Figure 7C** confirmed that the regular corrosion layers and the discontinuous white products on the corroded surface of SLMed ZK30-0.2Cu-0.8Cu specimens contained "O, Mg, Ca, and P" and "O and Mg," respectively. The Ca and P elements were present on the corroded surface, indicating that Ca-P compounds precipitated on the surface of the hydroxide corrosion layers as the corrosion continued[31]. The EDS spectra of Point 3 in **Figure 7A** confirmed that the corrosion products on the corroded surface of SLMed ZK30-0.2Cu contained "O and Mg," similar to the EDS spectra of Point 2.

### 3.4. Antibacterial activity against *S. aureus*

**Figure 8** shows the colonies of *S. aureus* cultured on the blank control, on pure Mg and on SLMed ZK30-0.2Cu-0.8Mn for 24 h and 72 h. There were a large number of colonies on the blank control. There were fewer colonies on the pure Mg. There were very few colonies on the SLMed ZK30-0.2Cu-0.8Mn after 24 h and almost no colonies after 72 h.

**Figure 9A** shows the number of *S. aureus* CFU/ml in extracts of the blank control, the pure Mg, and the SLMed ZK30-0.2Cu-0.8Mn at different time intervals without adjusting pH. The number of the colonies of *S. aureus* in the control group did not change significantly with increasing time, while the number of colonies on pure Mg and SLMed ZK30-0.2Cu-0.8Mn decreased gradually. Particularly, the colonies on SLMed ZK30-0.2Cu-0.8Mn decreased to zero after 72 h. The colonies in the neutral environments (at pH 7.4) are shown in **Figure 9B**. The colonies of the control and pure Mg did not change significantly with increasing time, while that on SLMed ZK30-0.2Cu-0.8Mn declined gradually, dropping sharply after 72 h and to zero after 96 h. This demonstrated the good antibacterial efficacy of SLMed ZK30-0.2Cu-0.8Mn.

### 3.5. Cytocompatibility

**Figure 10** shows the results of CCK-8 assay of MG63 cells, which were cultured on the samples for 1, 4, and 7 days. The number of live cells was proportional to the absorbance (or optical density). This indicates that the number of live cells on all the samples gradually increases with the increase of culture time, suggesting that they are all cytocompatible. From the 1st day to the 7th day, the relative proliferation rate of the MG63 cells in the six extract groups showed a similar growth trend. There was

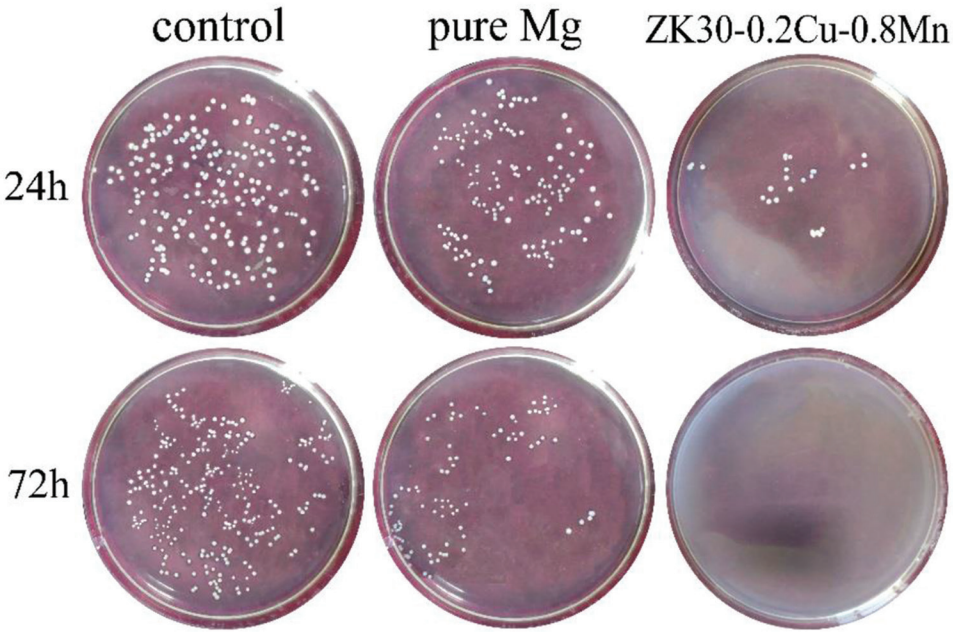


**Figure 8.** The growth of bacteria colonies on agar plates cocultured with *Staphylococcus aureus* at 37°C for 24 h and 72 h.

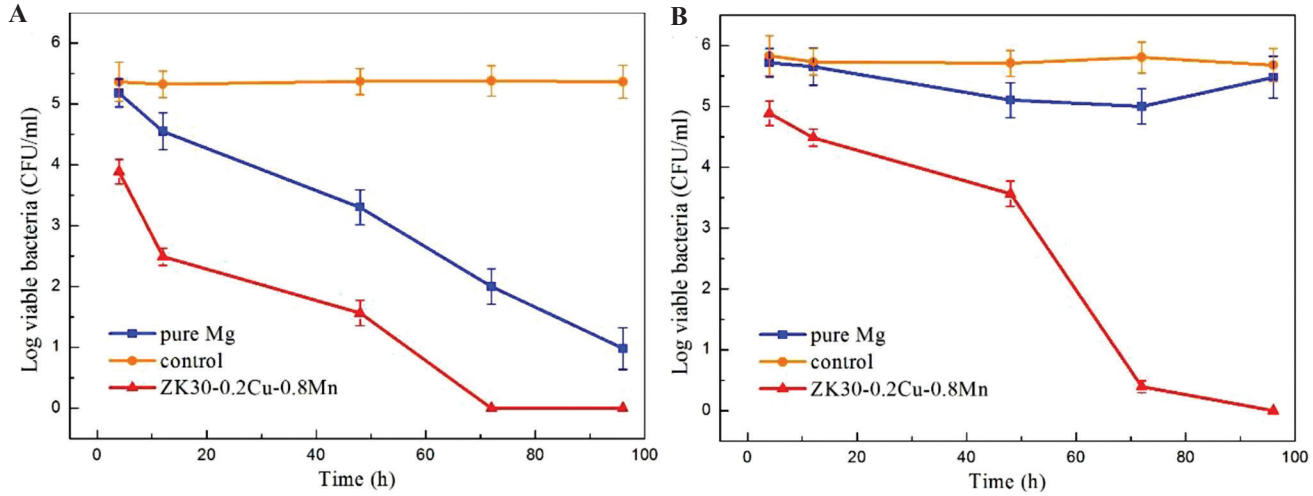


**Figure 9.** Number of colony-forming units/mL of *Staphylococcus aureus* after incubation with different samples at (A) uncontrolled pH values and (B) neutral pH of 7.4.

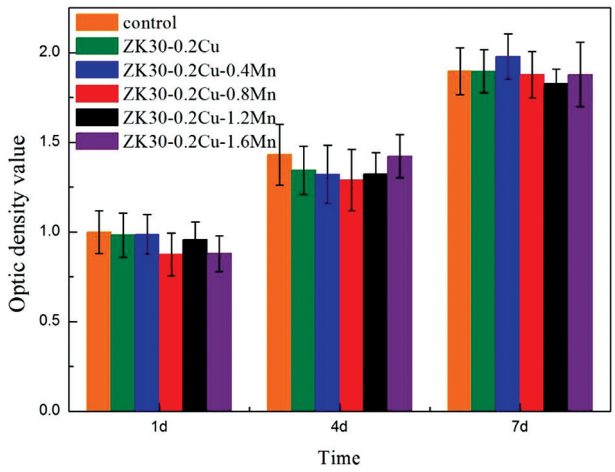


**Figure 10.** Optical density values for MG63 cells incubated in Ti and SLMed ZK30-0.2Cu-xMn extracts for 1, 4, and 7 days.

no apparent difference in the cell proliferation number between SLMed ZK30-0.2Cu-xMn and Ti extracts at different time points. This indicates that SLMed ZK30-0.2Cu-xMn is suitable for cell growth without cytotoxicity as well as Ti extract.

**Figure 11** shows the fluorescence live/dead staining results of MG63 cells, which were cultured after 1 and 3 days. Live cells were indicated by green fluorescence staining with calcein-AM, while dead cells by red staining with EthD-1. There was no evident indication of dead cells. The cells cultured on all the SLMed alloys had a well spread morphology, exhibiting no apparent difference among them and MG63 cells cultured in the extract had a morphology with spindle and round shapes which was in accordance with the morphology of normal cells. The cells showed good growth patterns and the number of cells increased obviously as incubation time increased.

The results of the cell proliferation assays and the fluorescence staining imaging indicated that SLMed ZK30-0.2Cu-xMn has suitable cytocompatibility as expected, because all elements in the SLMed alloys are cytocompatible.

## 4. Discussion

This current study successfully used SLM to fabricate ZK30-0.2Cu-xMn with various Mn concentrations (0.4, 0.8, 1.2, and 1.6 wt%), which exhibited strong antibacterial ability and good cytocompatibility. Mg-based alloys are attractive candidates for metallic implant biodegradable materials if the rate of the biodegradation can be decreased. The decrease of the biodegradation rate was examined by adding Mn by SLM for antibacterial Cu-containing Mg alloys in this study.

After the SLMed ZK30-0.2Cu-xMn specimens were immersed in the SBF solution, the corrosion reactions given by Equation 4, Equation 5, and Equation 6 in the following occurred and the surface hydroxide layer formed. The hydroxide layer was loose (**Figure 7A**) and provided little corrosion protection. As corrosion continued, hydroxyapatite formed due to the reaction between hydroxide in the corrosion product, $HPO_4^{2-}$ (or $PO_4^{3-}$) and $Ca^{2+}$ in the SBF, which resulted in the precipitation of Ca/P hydroxide on the surface of the hydroxide layer according to Equation vii[32]. This was substantiated by the EDS spectra shown in **Figure 7F**, which indicated that the corrosion products are mainly composed of O, Mg, Ca, and P.

$$Mg^{2+} - 2e^- \rightarrow Mg^{2+} \quad \text{(iv)}$$

$$2H_2O + O_2 + 4e^- \rightarrow 4OH^- \quad \text{(v)}$$

$$Mg^{2+} + 2OH^- \rightarrow Mg(OH)_2 \quad \text{(vi)}$$

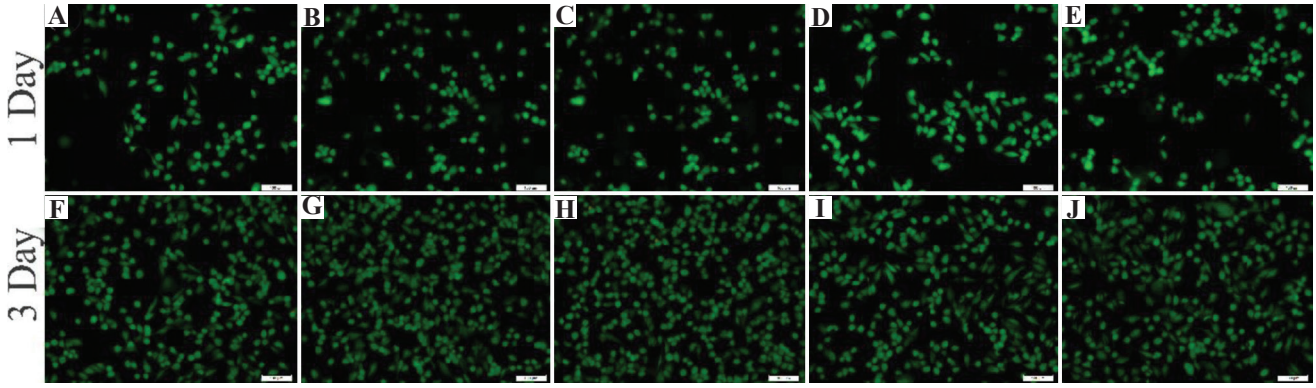


**Figure 11.** The live (green)-dead (red) staining of the MG63 cells cultured for 1 day and 3 days in the presence of (A) and (F) SLMed ZK30-0.2Cu; (B) and (G) SLMed ZK30-0.2Cu-0.4Mn; (C) and (H) SLMed ZK30-0.2Cu-0.8Mn; (D) and (I) SLMed ZK30-0.3Cu-1.2Mn; (E) and (J) SLMed ZK30-0.3Cu-1.6Mn.

$$10\ Ca^{2+} + 6\ PO_4^{3-} + 2\ OH^- \rightarrow Ca_{10}(PO_4)_6(OH) \quad \text{(vii)}$$

The results from the polarization curves (**Figure 5**), hydrogen evolution (**Figure 6A**), and weight loss (**Figure 6B**) showed that alloying with Mn had a significant effect on the biodegradation of SLMed ZK30-0.2Cu-xMn. With increasing Mn concentration, the biodegradation rate first decreased and reached a minimum value at a Mn content of 0.8 wt%. These results were consistent with the literature[33,34], which reported that small additions of Mn to Mg alloys decreased the corrosion rate by refining the microstructure. **Figure 1** shows that the incorporation of Mn substantially decreased the grain size. The fine-grained microstructure contained more grain boundaries and acted as a physical corrosion barrier to prevent corrosion[35]. In addition, the grain refinement reduced the mismatch stress between the surface layer and the Mg substrate to inhibit pitting initiation[36]. Therefore, grain refinement due to Mn addition can significantly decrease the biodegradation rate of SLMed ZK30-0.2Cu-xMn.

The surface corrosion appearances (**Figure 7**) showed that the addition of Mn promoted the formation of an intact compact layer of surface corrosion products, thereby providing better corrosion protection. However, Mn was not detected in the corrosion products on the corroded surface of SLMed ZK30-0.2Cu-xMn by the EDS, as shown in **Figure 7F**. The corrosion products were further examined by XPS. **Figure 12** shows the results of XPS analysis of the chemical compositions of Mg, Mn, and O in the corrosion products on SLMed ZK30-0.2Cu-0.8Mn by an analysis of the Mg 1s, Mn 2p, and O 1s peaks. The wide Mg 1s peak was composed of $Mg(OH)_2$ at 523.4 eV and MgO at 530.4 eV. The two constituent peaks of Mn $2p_{1/2}$ at 654.2 eV and Mn $2p_{3/2}$ at 641.9 eV in the Mn 2p indicated the existence of MnO and $MnO_2$, respectively. The O 1s peak was composed of three constituent peaks of $MnO_x$ at 529.4 eV, MgO at 530.4 eV, and $Mg(OH)_2$ at 532.4 eV. Consequently, in addition to $Mg(OH)_2$ and MgO, manganese oxides were certainly present in the corrosion products. Manganese oxides in the corrosion products were detected by XPS but could not be detected by EDS. One of the most likely reasons was that the manganese oxide layer was attached to the substrate and was covered by loose $Mg(OH)_2$ and accordingly the thickness of the corrosion layer exceeded the limit of EDS detection. In addition, there was probably only Mn oxide layer. When Mg alloys were immersed in SBF, the biodegradation of Mg was severe due to easy penetration of the oxide/hydroxide products by destructive $Cl^-$ ions and the formation of a chloride salt ($MgCl_2$), that is, the destructive $Cl^-$ ions existing in the SBF transformed $Mg(OH)_2$ into the more soluble $MgCl_2$ as given by Equation 8.

$$Mg^{2+} + 2Cl^- \rightarrow MgCl_2 \quad \text{(viii)}$$

Nam *et al.* demonstrated that in 0.6 M NaCl solution, Mn alloying into a Mg-5Al-based alloy inhibited the penetration of $Cl^-$ ions[37]. Metalnikov *et al.* further proposed that in 3.5 wt% NaCl solution saturated with $Mg(OH)_2$, Mn alloying into a Mg-5Al-based alloy could cause the formation of a relatively protective oxide film[38]. Therefore, in the present work, the formation of a manganese oxide layer on SLMed ZK30-0.2Cu-xMn was also expected to significantly decrease the biodegradation rate in SBF containing $Cl^-$ ions. This was supported by the results of the surface corrosion morphologies (**Figure 7**) and biodegradation rate from electrochemical tests and immersion tests (**Figure 6**), in which the SLMed ZK30-0.2Cu-0.8Mn specimens had an intact compact corroded surface layer and the lowest biodegradation rate.

The SLMed ZK30-0.2Cu-xMn is a multiphase alloy, in which different microconstituents, that is, the Mg matrix and the second phases may cause strong micro galvanic corrosion. As shown in **Figure 2**, the diffraction peaks of the Mn phase could be identified only when the Mn content was >0.8 wt.%. This indicates that the Mn element could completely dissolve in Mg matrix

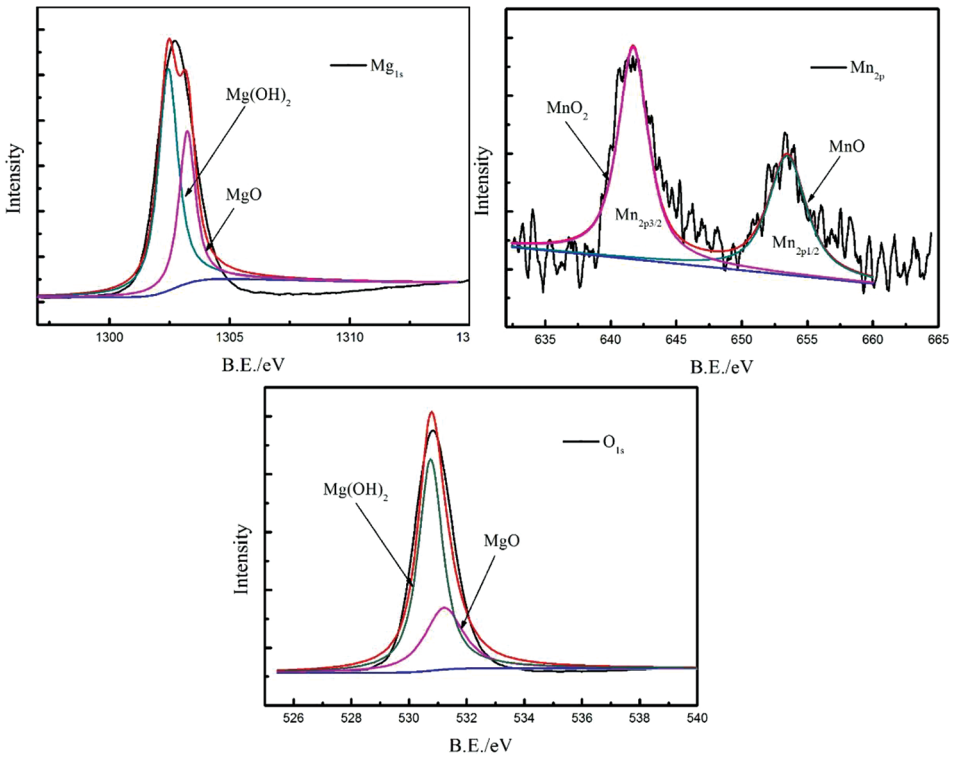


**Figure 12.** X-ray photoelectron spectroscopy analysis of corrosion products on SLMed ZK30-0.2Cu-0.8Mn.

if the Mn content was less than 0.8wt%, due to the rapid solidification by the SLM processing and formed supersaturated solid solutions. In contrast, a Mn content >0.8 wt% resulted in the formation of a small amount of Mn phase, which could not dissolve in the Mg matrix and precipitated after the rapid solidification. The precipitated Mn phase served as a cathode and the Mg matrix as anode formed a galvanic couple, which increased the biodegradation rate. Consequently, the biodegradation rate first decreased, with Mn content increased and reached a minimum while Mn content was 0.8 wt% and then increased with the Mn content. Furthermore, the precipitated Mn phase formed a weak interface with the adjacent Mg where the cracks were easily initiated. **Figure 7D and 7E** shows some microcracks on the corroded surfaces of SLMed ZK30-0.2Cu-1.2Mn and SLMed ZK30-0.2Cu-1.6Mn, which were generated due to the dehydration of the corrosion product layer by drying[39]. The existence of microcracks caused the matrix to contact the SBF directly and accelerated the corrosion. The microcracks of the corroded surfaces became larger and deeper when Mn content increased from 1.2 wt% to 1.6 wt%, accompanied by an increased biodegradation rate. Even so, for SLMed ZK30-0.2Cu-1.6Mn, some local areas presented microcracks, while some other areas were still covered by an integrated compact surface corrosion layer (**Figure 7E**), which was formed due to the Mn content as described above. As a consequence, for SLMed ZK30-0.2Cu-xMn, the influence of grain refinement and the relatively protective manganese oxide layer on the increase of the biodegradation resistance counteracted the influence of the undissolved Mn phase on the decrease of biodegradation resistance; therefore, SLMed ZK30-0.2Cu-0.8Mn has the lowest biodegradation rate.

## 5. Conclusion

Novel antibacterial ZK30-0.2Cu-xMn alloys with fine equiaxed grains were successfully fabricated by SLM. Alloying with Mn has an evident influence on grain size, hardness, and biodegradation rate of SLMed ZK30-0.2Cu-xMn alloys. Alloying with Mn decreases the grain size and produces a relatively protective manganese oxide film, which significantly decreases the biodegradation rate of SLMed ZK30-0.2Cu-xMn alloys. Undissolved Mn increases the biodegradation rate of SLMed ZK30-0.2Cu-xMn. The optimum Mn content is 0.8 wt.%. SLMed ZK30-0.2Cu-0.8Mn has the lowest biodegradation rate. SLMed ZK30-0.2Cu-0.8Mn exhibits strong antibacterial ability and good cytocompatibility, indicating their future prospects for bone implants.

## Conflict of interest

There are no conflicts of interest to declare.

## References


1. Johnston S, Shi Z, Venezuela J, *et al.*, 2019, Investigating Mg Bio-corrosion *In Vitro*: Lessons Learned and Recommendations. *JOM*, 71(4):1406–13. https://doi.org/10.1007/s11837-019-03327-9
2. Zheng Z, Zhao MC, Tan L, *et al.*, 2020, Corrosion Behavior of a Self-Sealing Coating Containing $CeO_2$ Particles on Pure Mg Produced by Micro-Arc Oxidation. *Surf Coat Technol*, 386:125456. https://doi.org/10.1016/j.surfcoat.2020.125456
3. Lopes DR, Silva CL, Soares RB, *et al.*, 2019, Cytotoxicity and Corrosion Behavior of Magnesium and Magnesium Alloys in Hank's Solution after Processing by High-Pressure Torsion. *Adv Eng Mater*, 21(8):1900391. https://doi.org/10.1002/adem.201900391
4. Rua JM, Zuleta AA, Ramirez J, *et al.*, 2019, Micro-Arc Oxidation Coating on Porous Magnesium foam and its Potential Biomedical Applications. *Surf Coat Technol*, 360:213–21. https://doi.org/10.1016/j.surfcoat.2018.12.106
5. Yan X, Zhao M, Yang Y, *et al.*, 2019, Improvement of Biodegradable and Antibacterial Properties by Solution Treatment and Micro-Arc Oxidation (MAO) of a Magnesium Alloy with a Trace of Copper. *Corros Sci*, 156:125–38. https://doi.org/10.1016/j.corsci.2019.05.015
6. Liu C, Fu X, Pan H, *et al.*, 2016, Biodegradable Mg-Cu Alloys with Enhanced Osteogenesis, Angiogenesis, and Long-Lasting Antibacterial Effects. *Sci Rep*, 6:27374. https://doi.org/10.1038/srep27374
7. Yan X, Wan P, Tan L, *et al.*, 2018, Influence of Hybrid Extrusion and Solution Treatment on the Microstructure and Degradation Behavior of Mg-0.1Cu Alloy. *Mater Sci Eng B*, 229:105–17.
8. Gu X, Zheng Y, Cheng Y, *et al.*, 2009, *In Vitro* Corrosion and Biocompatibility of Binary Magnesium Alloys. *Biomaterials*, 30:484–98. https://doi.org/10.1016/j.biomaterials.2008.10.021
9. Ha HY, Kim HJ, Baek SM, *et al.*, 2015, Improved Corrosion Resistance of Extruded Mg-8Sn-1Zn-1Al Alloy by Microalloying with Mn. *Scr Mater*, 109:38–43. https://doi.org/10.1016/j.scriptamat.2015.07.013
10. Yang Y, Wu P, Wang Q, *et al.*, 2016, The Enhancement of Mg Corrosion Resistance by Alloying Mn and Laser-Melting. *Materials*, 9:216. https://doi.org/10.3390/ma9040216
11. Leach RM, Muenster AM, Wien EM, 1969, Studies on the Role of Manganese in Bone Formation: II. Effect upon Chondroitin Sulfate Synthesis in Chick Epiphyseal Cartilage. *Arch Biochem Biophys*, 133(1):22–8.
12. Liu Y, Koltick D, Byrne P, *et al.*, 2013, Development of a Transportable Neutron Activation Analysis System to Quantify Manganese in Bone *In Vivo*: Feasibility and Methodology. *Physiol Meas*, 34(12):1593. https://doi.org/10.1088/0967-3334/34/12/1593
13. Li WX, 2005, Magnesium and its Alloys. Central South University Press, Changsha.
14. Yu WH, Sing SL, Chua CK, *et al.*, 2019, Particle-Reinforced Metal Matrix Nanocomposites Fabricated by Selective Laser Melting: A State of the Art Review. *Prog Mater Sci*, 104:330–79. https://doi.org/10.1016/j.pmatsci.2019.04.006
15. Li X, Tan Y, Willy H, *et al.*, 2019, Heterogeneously Tempered Martensitic High Strength Steel by Selective Laser Melting and its Micro-Lattice: Processing, Microstructure, Superior Performance and Mechanisms. *Mater Des*, 178:107881. https://doi.org/10.1016/j.matdes.2019.107881
16. Zhao Y, Tang Y, Zhao M, *et al.*, 2019, Graphene Oxide Reinforced Iron Matrix Composite with Enhanced Biodegradation Rate Prepared by Selective Laser Melting. *Adv Eng Mater*, 21(8):1900314. https://doi.org/10.1002/adem.201900314
17. Gao C, Yao M, Li S, *et al.*, 2019, Highly Biodegradable and Bioactive Fe-Pd-Bredigite Biocomposites Prepared by Selective Laser Melting. *J Adv Res*, 20:91–104. https://doi.org/10.1016/j.jare.2019.06.001
18. Sing SL, Huang S, Yeong WY, 2020, Effect of Solution Heat Treatment on Microstructure and Mechanical Properties of Laser Powder Bed Fusion Produced Cobalt-28Chromium-6Molybdenum. *Mater Sci Eng A*, 769:138511. https://doi.org/10.1016/j.msea.2019.138511
19. Tan JH, Sing SL, Yeong WY, 2020, Microstructure Modelling for Metallic Additive Manufacturing: A Review. *Virtual Phys Prototyp*, 15(1):87–105. https://doi.org/10.1080/17452759.2019.1677345
20. Li X, Tan Y, Wang P, *et al.*, 2020, Metallic Microlattice and Epoxy Interpenetrating Phase Composites: Experimental and Simulation Studies on Superior Mechanical Properties and their Mechanisms. *Compos Part A Appl Sci Manuf*, 135:105934. https://doi.org/10.1016/j.compositesa.2020.105934
21. Nie XJ, Chen Z, Qi Y, *et al.*, 2020, Effect of Defocusing Distance on Laser Powder Bed Fusion of High Strength Al-Cu-Mg-Mn Alloy. *Virtual Phys Prototyp*, 15(3):325–39. https://doi.org/10.1080/17452759.2020.1760895

22. Huang S, Sing SL, Looze G, *et al.*, 2020, Laser Powder Bed Fusion of Titanium-Tantalum Alloys: Compositions and Designs for Biomedical Applications. *J Mech Behav Biomed Mater*, 108:103775. https://doi.org/10.1016/j.jmbbm.2020.103775
23. Xu R, Zhao M, Zhao Y, *et al.*, 2019, Improved Biodegradation Resistance by Grain Refinement of Novel Antibacterial ZK30-Cu Alloys Produced Via Selective Laser Melting. *Mater Lett*, 237:253–7. https://doi.org/10.1016/j.matlet.2018.11.071
24. Zhao YC, Tang Y, Zhao MC, *et al.*, 2020, Study on Fe-xGO Composites Prepared by Selective Laser Melting: Microstructure, Hardness, Biodegradation and Cytocompatibility. *JOM*, 72:1163–74. https://doi.org/10.1007/s11837-019-03814-z
25. Zhao Y, Zhao M, Xu R, *et al.*, 2019, Formation and Characteristic Corrosion Behavior of Alternately Lamellar Arranged α and β in As-Cast AZ91 Mg Alloy. *J Alloys Compd*, 770:549–58. https://doi.org/10.1016/j.jallcom.2018.08.103
26. Zhao MC, Liu M, Song GL, *et al.*, 2008, Influence of the β-Phase Morphology on the Corrosion of the Mg Alloy AZ91. *Corros Sci*, 50:1939–53.
27. Li Z, Chen M, Li W, *et al.*, 2017, The Synergistic Effect of Trace Sr and Zr on the Microstructure and Properties of a Biodegradable Mg-Zn-Zr-Sr Alloy. *J Alloys Compd*, 702:290–302. https://doi.org/10.1016/j.jallcom.2017.01.178
28. Zhang X, Hua L, Liu Y, 2012, FE simulation and Experimental Investigation of ZK60 Magnesium Alloy with Different Radial Diameters Processed by Equal Channel Angular Pressing. *Mater Sci Eng A*, 535:153–63. https://doi.org/10.1016/j.msea.2011.12.057
29. Zhao MC, Schmutz P, Brunner S, *et al.*, 2009, An Exploratory Study of the Corrosion of Mg Alloys During Interrupted Salt Spray Testing. *Corros Sci*, 51(6):1277–92. https://doi.org/10.1016/j.corsci.2009.03.014
30. Tao JX, Zhao M, Zhao Y, *et al.*, 2020, Influence of Graphene Oxide (GO) on Microstructure and Biodegradation of ZK30-xGO Composites Prepared by Selective Laser Melting. *J Magnes Alloys*, 8(3):952–62. https://doi.org/10.1016/j.jma.2019.10.004
31. Zhao MC, Zhao YC, Yin DF, *et al.*, 2019, Biodegradation Behavior of Coated As-Extruded Mg-Sr Alloy in Simulated Body Fluid. *Acta Metall Sin* (*Engl Lett*), 32:1195–206. https://doi.org/10.1007/s40195-019-00892-5
32. Atrens AD, Gentle I, Atrens A, 2015, Possible Dissolution Pathways Participating in the Mg Corrosion Reaction. *Corros Sci*, 92:173–81. https://doi.org/10.1016/j.corsci.2014.12.004
33. Song GL, Atrens A, 1999, Corrosion Mechanisms of Magnesium Alloys. *Adv Eng Mater*, 1:11–33. https://doi.org/10.1002/(sici)1527-2648(199909)1:1<11::aid-adem11>3.0.co;2-n
34. Esmaily M, Svensson JE, Fajardo S, *et al.*, 2017, Fundamentals and Advances in Magnesium Alloy Corrosion. *Prog Mater Sci*, 89:92–193. https://doi.org/10.1016/j.pmatsci.2017.04.011
35. Zhang W, Tan LL, Li DR, *et al.*, 2019, Effect of Grain Refinement and Crystallographic Texture Produced by Friction Stir Processing on the Biodegradation Behavior of a Mg-Nd-Zn Alloy. *J Mater Sci Technol*, 35(5):777–83. https://doi.org/10.1016/j.jmst.2018.11.025
36. Kirkland NT, Waterman J, Birbilis N, *et al.*, 2012, Buffer-Regulated Bio-corrosion of Pure Magnesium. *J Mater Sci Mater Med*, 23(2):283–91.
37. Nama ND, Mathesh M, Forsyth M, *et al.*, 2012, Effect of Manganese Additions on the Corrosion Behavior of an Extruded Mg-5Al Based Alloy. *J Alloys Compd*, 542:199–206. https://doi.org/10.1016/j.jallcom.2012.07.083
38. Metalnikov P, Ben-Hamua G, Templeman Y, *et al.*, 2018, The Relation between Mn Additions, Microstructure and Corrosion Behavior of New Wrought Mg-5Al Alloys. *Mater Charact*, 145:101–15. https://doi.org/10.1016/j.matchar.2018.08.033
39. Baril G, Pebere N, 2001, The Corrosion of Pure Magnesium in Aerated and Deaerated Sodium Sulphate Solutions. *Corros Sci*, 43(3):471–84. https://doi.org/10.1016/s0010-938x(00)00095-0

RESEARCH ARTICLE

# Investigation of Ceramic Dental Prostheses Based on $ZrSiO_4$-Glass Composites Fabricated by Indirect Additive Manufacturing

**Marlon Wesley Machado Cunico[1,2]***

[1]Department of Mechanical Engineering, FAE University Center, Curitiba, Parana, Brazil
[2]Concep3D Research and Development, Curitiba, Parana, Brazil

**Abstract:** Dental prosthesis and restoration technologies have been developed in the past years. Despite the advantages of additive manufacturing, computer-aided design, and computer-aided manufacturing technologies are still the dominant type of method for fabricating prostheses. Therefore, the main goal of this study is to assess the feasibility of using indirect fused deposition modeling to fabricate dental prosthesis made of $ZrSiO_4$-glass composites. To achieve this goal, filaments were filled by 90% of $ZrSiO_4$ and 50 μm glass spheres to fabricate prosthesis. Multivariable approach was applied to evaluate the feasibility of the proposed method. Holding temperature, holding time, heating rate, and cooling rate were considered the control factors, while shrinkage, flexural strength, and process feasibility were the study responses. In addition, the flexural strength of materials was found between 25 and 85 MPa, while shrinkage fluctuated between 10 and 25%.

**Keywords:** Fused deposition modeling ceramic sintering; Additive manufacturing; Ceramics

***Correspondence to:** Marlon Wesley Machado Cunico, Department of Mechanical Engineering, FAE University Center, Curitiba, Parana, Brazil; marloncunico@yahoo.com.br

**Received:** September 29, 2020; **Accepted:** October 20, 2020; **Published Online:** November 26, 2020

**Citation:** Cunico MWM., 2021, Investigation of Ceramic Dental Prostheses Based on $ZrSiO_4$-Glass Composites Fabricated by Indirect Additive Manufacturing. *Int J Bioprint,* 7(1):315. http://doi.org/10.18063/ijb.v7i1.315

## 1. Introduction

In the past few years, additive manufacturing (AM) technologies have started playing an important role in several industrial and health-care segments[1]. In addition, development of dental materials and applications signifies the advent of digital fabrication through which the dental implants are mainly fabricated by computer-aided design and computer-aided manufacturing (CAD/CAM) techniques coupled with three-dimensional (3D) scanning[2,3].

**Table 1** shows the most common techniques that are used in accordance with the type of dental prosthesis. Possibly, CAD/CAM is currently the most used technique in prosthodontics[4]. Although AM is still used in the fabrication of medical/dental models and temporary dentures, its mechanical strength is usually inferior to that of CAD/CAM technologies and no sufficient clinical records regarding its application are available[2-5]. In spite of that, CAD/CAM techniques also show some disadvantages, such as requirement of highly trained professional to operate 5-axis computer numerical control, high cost of raw material, excessive waste generation, high cost of maintenance, and short lifetime of tooling. On the other hand, AM could improve the fabrication of dental prosthesis by increasing automation, flexibility, shape freedom, and fabrication speed. Apart from manufacturing and product development, AM is also in applied in different areas, such as aerospace, electronics, medical applications, and tissue engineering[6-15].

After weighing the pros and cons of either technique, several aspects of AM technologies, such as mechanical strength, type of material, bio-reactivity, and cost, still remain as the challenges awaiting to be addressed[18]. For that reason, AM technologies are widely used for: provisional crown and bridge restorations, casting patterns, dental models, surgical guide, and splints. On the other hand, further development of AM technologies

**Table 1.** State of the art of prosthodontical technologies

| | | Classic dentistry technologies | | | | Additive manufacturing technologies | | | | | |
|---|---|---|---|---|---|---|---|---|---|---|---|
| | | Sintering | slip casting and Casting | Hot-pressed/ injection molded ceramics | CAD/ CAM[1] | SLM[2] | SLS[3] | BindJet direct or infiltrated | Multijet | SLA/DLP[4]- direct or wax-like castable | FDM[5]/ extrusion-based |
| Applications | Crown and bridges | [16] | [16,17] | [17] | [3,16-19] | [18,19] | [19] | | | | |
| | Denture | [16] | [17] | [17] | [3,16-19] | [18,19] | [19] | | | | |
| | Denture holder | [16] | | [17] | [3,16-19] | [18,19] | | | | | |
| | Copings | [16] | [17] | | [3,16-19] | [18,19] | | | | | |
| | Casting patterns/lost wax | [16] | | [16] | [3,18] | | | | [18,19] | [18,19] | |
| | Provisional temporary crown | | | | [18] | | [20] | | [2] | [2,18] | |
| | Dental model | | | | [18] | | | | [2,18,20] | [2,18] | |
| | Surgical guide | | | | [3,18] | | | | [2,18] | [18] | [18] |
| | Surgical guide plate | | | | [3,18] | | [2] | [2] | [2] | [2] | [18] |
| | Splints | | | | [18] | | | | [2,18] | [2,18] | [18] |
| | Prosthetic constructions | | | | [18] | | | | | | |
| Materials | All-ceramic | [18] | [18] | [17] | [18,20] | | [18] | | | | |
| | Porcelain | [18] | [18] | [17] | [18] | | | | | | [18] |
| | Y-TZP[6] | [18] | [18] | | [18] | | | | | | |
| | Metallic | [18] | [18] | | [18,20] | [2,18] | | | | | |
| | Glass-ceramic | [18] | [18] | [17] | [18,20] | | [18] | [18] | [19,20] | | |
| | Polymer-ceramic composite | [18] | [18] | | [16,18,20] | | [18] | [18] | | [2,3,18,19] | |
| | Metal-ceramic composite | [18] | [18] | | [16,18,20] | | [18] | | | | |
| | Polymeric material | | | | [18] | | [18] | [18] | [18,19] | [2,3,18,19] | |

1- CAD, Computer-aided design; CAM, Computer-aided manufacturing; 2-SLM, Selective laser melting; 3-Selective laser sintering; 4-SLA, SLA, Stereolithography apparatus/DLP, Digital light projector; 5-FDM, Fused deposition modeling; 6-YTZP, Yttria stabilized zirconia.

is still need warranted to perfect their applications in the fabrication of dental implants, crown, and bridges denture and prosthetic constructions. Therefore, the main goal of this study is to propose and investigate the feasibility of a novel fabrication method based on $ZrSiO_4$-glass composite in dental prosthesis applications, such as crowns, coupings, bridges, and dentures. The schematic of this method is illustrated in **Figure 1**.

In this method, the collapsible $ZrSiO_4$ mold of negative of crown or bridge was fabricated by AM based on fused filament fabrication (FFF). The negative cavity was filled by lanthanum glass powder and sintered subsequently. In the end, the pieces were heated to debind the negative structure and then create sintered composite pieces.

It is also important to note that several AM techniques, such as inkjet printing and stereolithography, generate objects with higher resolution than manufacturing by FFF. However, these techniques are restricted by photopolymeric resins and slurry-based techniques. For that reason, they are mainly used for casting patterns, lost wax (resin), and investment casting[19,20]. In addition, in spite of high resolution, these AM techniques (stereolithography apparatus and Inkjet printing) imply on dimensional and geometrical accuracy equivalent to FFF techniques[21-23]. In fact, the high resolution has been shown to influence the roughness, rather than the dimensional accuracy[21-23]. Besides low cost, AM based on FFF is able to fabricate objects with high amount of ceramic and metallic in their composition[24-26]. Thus, this technique is suitable for fabrication of collapsible molds made of ceramics or metallic material with high temperature resistance.

To evaluate the feasibility of this technique, we applied multivariable approach to investigate the main effect of control factors on responses. Holding temperature, holding time, heating rate, cooling rate, and shrinkage chamber were the control factors while shrinkage, flexural strength, and process feasibility were the study responses. The fabrication parameters, formulation of materials, flexural testing specimen shape, and crown shape were kept constant. This study helped determine whether the proposed method of indirect AM is feasible to fabricate ceramic dental prosthesis.

## 2. Materials and methods

To investigate the feasibility of the proposed method in addition to the main effect of control factors on responses, we applied a $2^k$ multivariable methodology (full design with body central point) where holding temperature ($T_h$), holding time ($t_h$), heating rate ($R_h$), and cooling rate ($R_c$) were the control factors. In addition, we also defined three screening steps in augmented design approach to minimize the holding time and maximize the densification and mechanical properties.

The levels and values of each control factor are presented in **Table 2**. The values of holding temperature are between the activation temperature of glass and $ZrSiO_4$ (700°C) and the melting temperature of glass (1078°C).

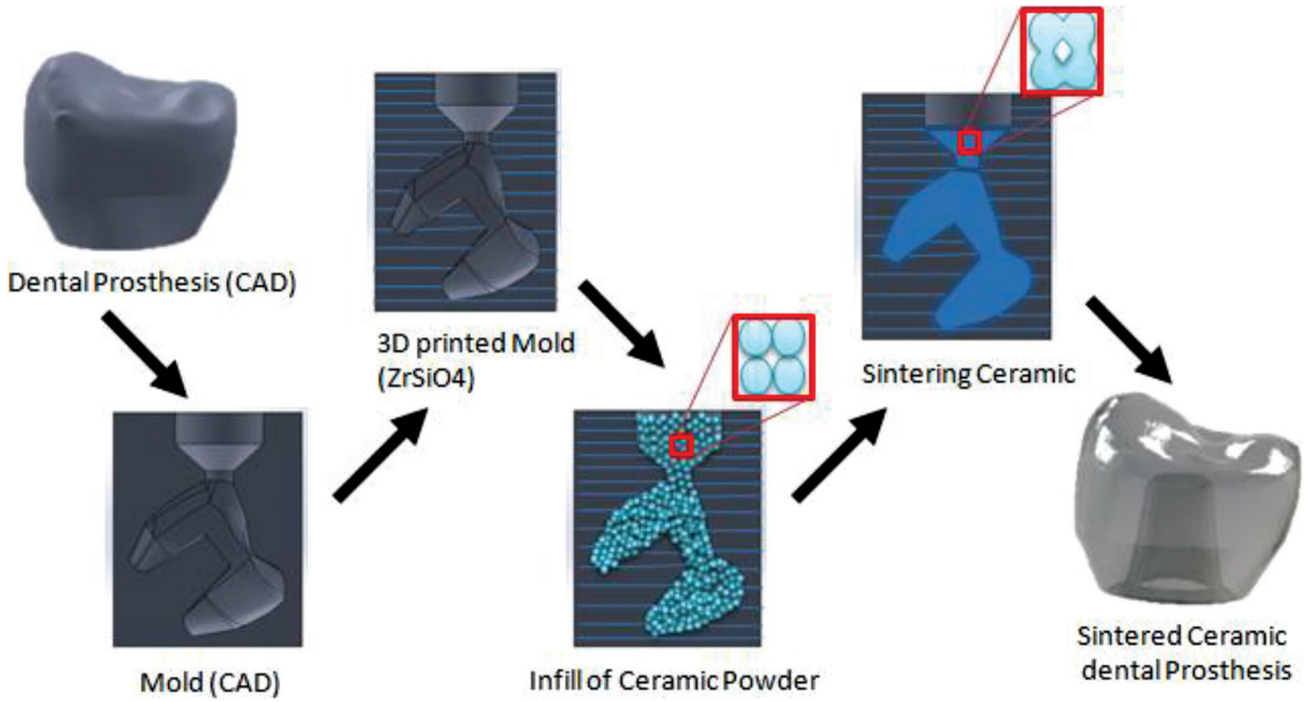


**Figure 1.** Schematic diagram of the fabrication of ceramic dental prosthesis using indirect additive manufacturing.

This also indicates that the cooling time enhanced two types of heat treatment (quenching for fast cooling and annealing for slow cooling). Therefore, the effect of such treatments on crystallization level, mechanical strength, and geometry distortion can be evidenced. On the other hand, holding time and heating rate are expected to affect the sinterization parameters, such as nucleation, grain growth, and diffusion.

For the sintering process, we used a 2000 W electrical Furnace PID controller with 4 ramps curves and insulation muffle. The main control parameters and schematic sintering temperature curves that we applied in this study are illustrated in **Figure 2**.

The flexural testing was performed in accordance with ISO 6872 in an EMIC DL10000 universal testing machine. We used MATLAB software for the image processing, and the image acquisition was performed using optical microscope Digital Avangard Optics AN-E500 (AVANGARD 2011), which a magnitude of up to ×500 of amplification. For the gravimetric analysis (drying monitoring), we used a 0.005 g error scale. To identify dimensional distortions of the specimen, we used both 0.05 mm caliper and computational image processing to measure the specimen dimensions. After measuring, we used MATLAB software to perform statistical analysis and evidence the geometrical variation of object external contour. To measure feasibility response, we established a scale from 0 to 1 in which level 1 indicates that the object has no significant distortions and is feasible to be used; level 0.75 exposes minor distortion which corresponds to 5% of distortion; and level 0.5 indicates that the object has 10% of distortion. It is important to note that the measurement of feasibility response was used to analyze non-volumetric distortions and compare CAD models

**Table 2.** Experiment design

| | | Level | | |
|---|---|---|---|---|
| | Control factors | −1 | 0 | 1 |
| 1st step | | | | |
| | Heating rate (Hrate) (°C/min) | 2 | 3.5 | 5 |
| | Holding temperature (Thold) (°C) | 700 | 800 | 900 |
| | Holding time (thold ) (h) | 1 | 2.5 | 4 |
| | Cooling rate(Crate) (°C/min) | 2 | | 30 |
| 2nd step | | | | |
| | Holding temperature(Thold) (°C) | 700 | 750 | 800 |
| | Holding time(thold) (h) | 1 | 1.75 | 2.5 |
| 3rd step | | | | |
| | Holding temperature(Thold) (°C) | 700 | 725 | 750 |
| | Holding time(thold) (h) | 2.5 | 2.875 | 3.25 |

Where: $T_{hold}$ is the holding temperature – period of time where the temperature is kept constant; $t_{hold}$ is the holding time or plato time – temperature which is kept constant during a period of time; $H_{rate}$ is the heating rate of sintering furnace; $C_{rate}$ or k is the cooling rate of object.

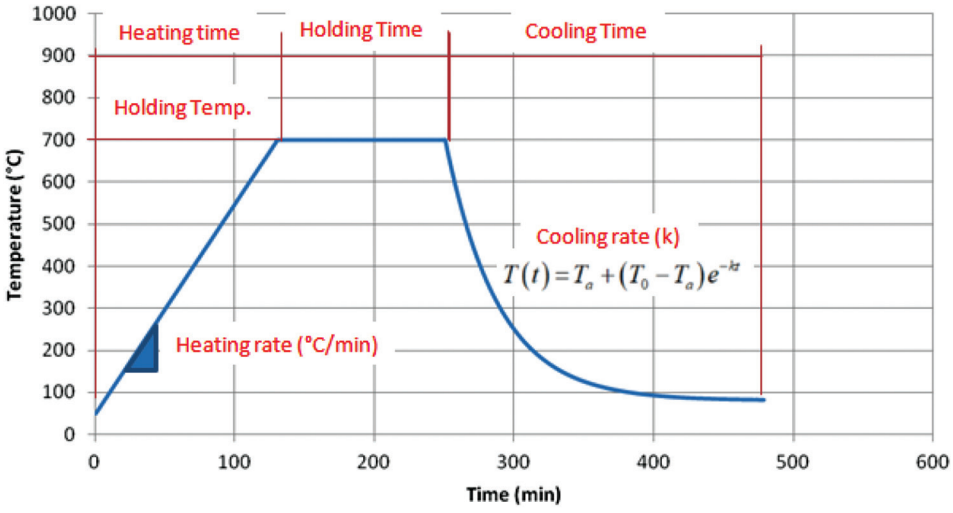


**Figure 2.** Illustration of sintering temperature curves and control factors: Holding temperature ($T_{hold}$), holding time ($t_{hold}$), cooling rate (k), and heating rate ($H_{rate}$).

adjusted by shrinkage factor, although shrinkage is a sort of volumetric distortion.

For specimen's fabrication, we used a fused deposition modeling process and filament filled by 90% of $ZrSiO_4$. The main process parameters remained constant, where extrusion temperature was 220°C, layer thickness was 0.1 mm, distance between filaments was 0.2 mm, and nozzle diameter was 0.4 mm. In addition, we have also considered no support material and no retract to build the specimens. In all the cases, the extrusion temperature and chamber temperature were also kept constant, while no bed temperature was established. The fabrication environment was also controlled at 25°C (room temperature) and 50% of relative humidity.

The repeatability and error of the AM-generated mold were also identified before performing the study. Ten samples of the mold were fabricated, and their external and internal geometry was measured. The internal geometry was evaluated by transversal cuts, which helped to ensure that the divergence between CAD- and AM-generated molds was up to 0.15 mm besides an error of 2% in the small dimension of mold.

## 3. Results and discussion

In general, the evaluation of concept feasibility was satisfactory, whereas a feasible process window was identified. From geometric point of view, the crown was obtained in low sintering temperatures because high levels of temperature distorted the geometry due to excessive melting and high shrinkage.

With regard to the main effect of control factors on the feasibility, mechanical strength and shrinkage, holding temperature had the strongest effect on the feasibility and flexural strength in comparison with the other control factors (**Figure 3**). On the other hand, holding time affects shrinkage the most. It shows that holding time and holding temperatures are the most relevant factors for the augmented design. Therefore, the second design of experiments screening increased the experiment resolution for holding temperature and holding time. The flexural strength was also affected by heating rate, indicating that densification of material might have reduced the strength of material.

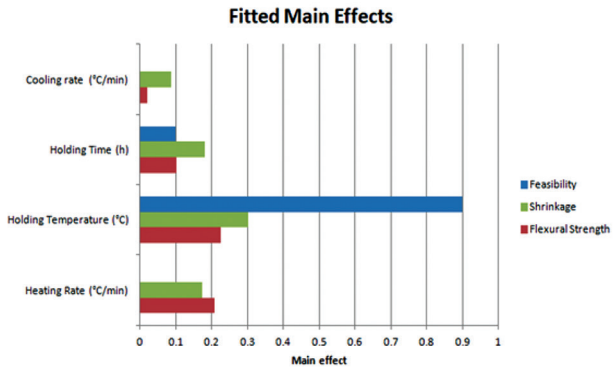


**Figure 3.** Main effect of control parameter on feasibility, flexural strength, and shrinkage.

In parallel with the feasibility of the proposed concept, high temperature implies on the unfeasibility of concept regardless of time holding, cooling rate, and heating rate (**Figure 4**). In this study, the holding temperature was the most relevant parameter for feasibility, followed by holding time. In contrast, heating and cooling rates were found not to affect the feasibility. From the geometric point of view, our analysis revealed that the shrinkage varied from 13.4% to 27% into the feasible area. The lowest value of shrinkage was found in a condition when the heating rate equals to 5°C/min, holding temperature 700°C, holding time 3.2 h, and cooling rate 30°C/min, whereas the highest value was found in a condition when the heating rate equals to 2°C/min, holding temperature 700°C, holding time 4 h, and cooling rate 2°C/min.

**Figure 4** shows the main effect of control parameter shrinkage. The holding temperature was the most relevant factor for the shrinkage, while the heating rate showed the smallest effect among the control parameters. With respect to material mechanical strength, **Figure 4** also presents the main effect of control parameter on flexural strength. The temperature and heating rate were the most relevant factors for mechanical strength, while cooling rate presented the smallest effect among the control parameters. The mean values of flexural strength varied from 25 to 82 MPa, where the lowest values were found in low holding temperatures (700°C) and short holding time (1 h). On the other hand, the highest values were obtained by long hold time (1 h) and 800°C of holding temperature. It is also important to indicate that this process did not evaluate the effects of neither heating treatment nor material. Therefore, further studies are still needed for incorporating the use of stronger materials and heating treatments in this concept.

In addition, **Figure 5** shows a comparison diagram of geometrical concept for feasibility as a function of holding temperature and holding time. In this figure, a feasibility line separates the results which were considered feasible and unfeasible from the geometrical point of view.

In addition, the feasibility was also separated in two areas. High grain growth was obtained at low temperature (700°C) during long holding time (4 h), producing specimen with high densification. On the other hand, low grain growth was obtained at low temperatures (700°C) during short periods of time (1 h), producing specimen with low densification. Of note, the central point of the study indicated a limit of feasibility so that the sintering process can be directly correlated to the absorbed energy as a function of time and temperature. The unfeasible

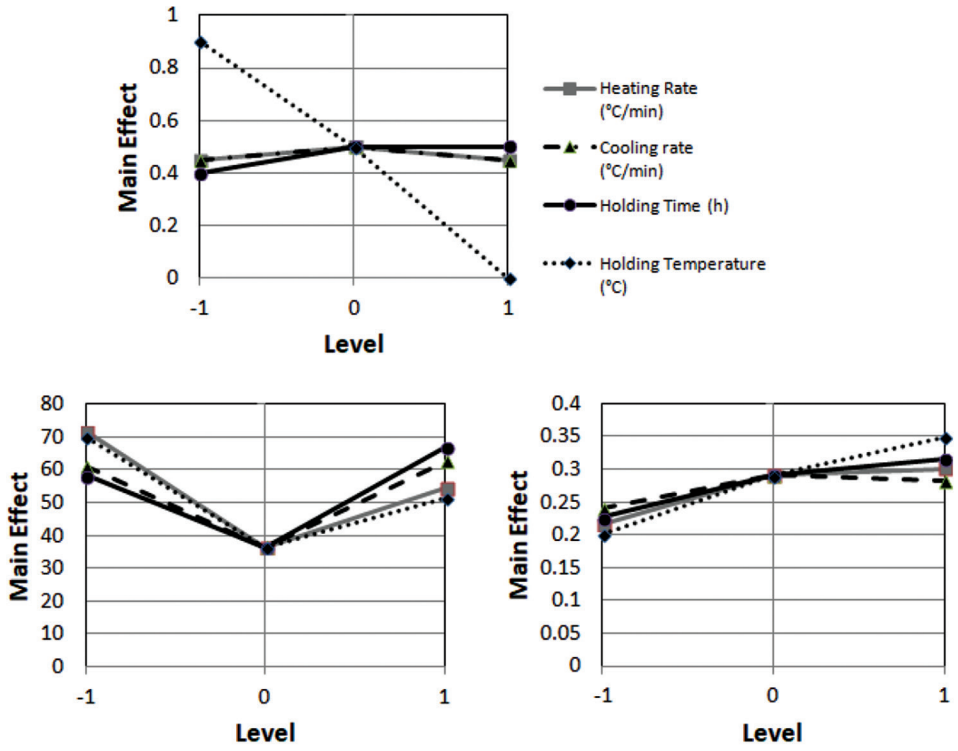


**Figure 4.** Standardized main effect of control factors on feasibility, flexural strength, and shrinkage.

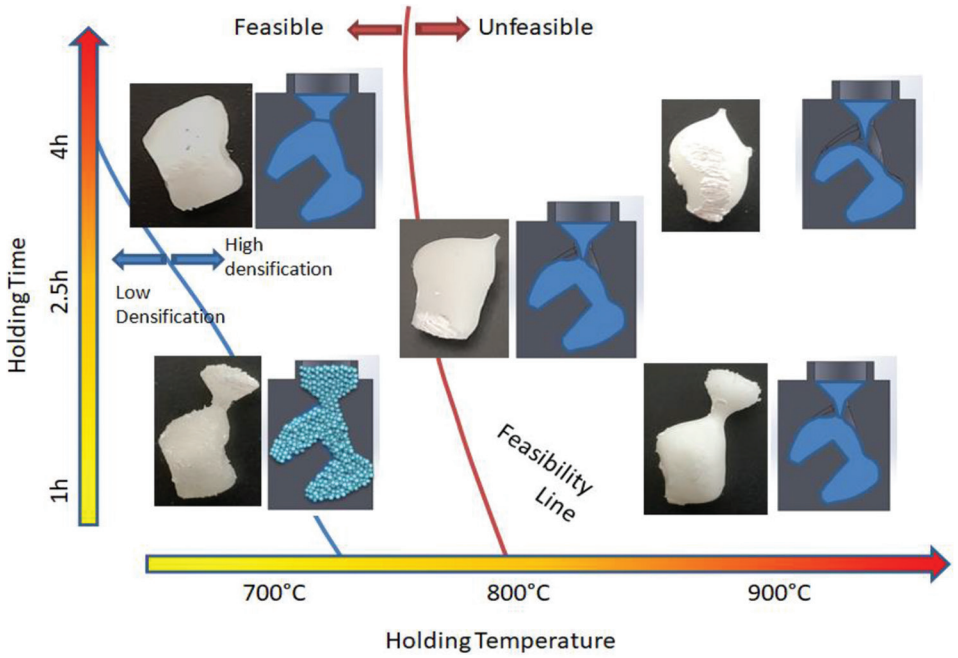


**Figure 5.** Comparison diagram of proposal feasibility as a function of holding temperature and holding time.

area was highlighted by high densification and excess of deformation due to a decrease in viscosity. In addition, this reduction indicated mold infiltration and subsequent incrustation of collapsed mold on object surface. The materials obtained at high temperature with long holding time were of high densification and grain size and were bigger than the grain in material produced at low temperatures. This situation is shown in **Figure 6**, where the comparison of material densification and grain size is presented.

To better understand the behavior of material properties as a function of holding temperature and holding time, **Figure 7** shows the contour diagrams of feasibility, shrinkage, and flexural strength and presents an overlapping diagram indicating the process window from where high values can be obtained.

According to **Figure 7**, high values of feasibility flexural strength and low values of shrinkage can be obtained with holding time at around 1.5 h and holding temperature at around 750°C. In this case, values of flexural strength fluctuate around 65 MPa, while the shrinkage values around 13%. The feasibility ratio was considered higher than 0.9. It is important to note that the feasibility level indicates the compatibility between the physical model and the CAD 3D model. Therefore, the distortion between the physical model and the 3D model adjusted with volumetric shrinkage is lower than 10% for the feasibility level which is higher than 0.9. That represents an error up to 0.1 mm in the smallest analyzed dimension of the samples. Another important point on this matter is the potential minimization of shrinkage factor in accordance with the type and formulation of ceramic material and the size of powder grain. Nonetheless, further efforts are still needed to improve material properties and process aspects, such as mechanical strength, biocompatibility, physical, and chemical properties.

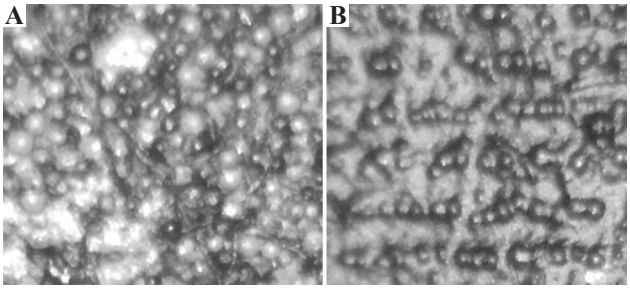


**Figure 6.** Comparison between low (A) and high (B) densification.

**Figure 8** shows the comparison in flexural strength between the proposed method and other typical methods that are used for fabricating dental prosthesis. It is important to see that our current results identified values

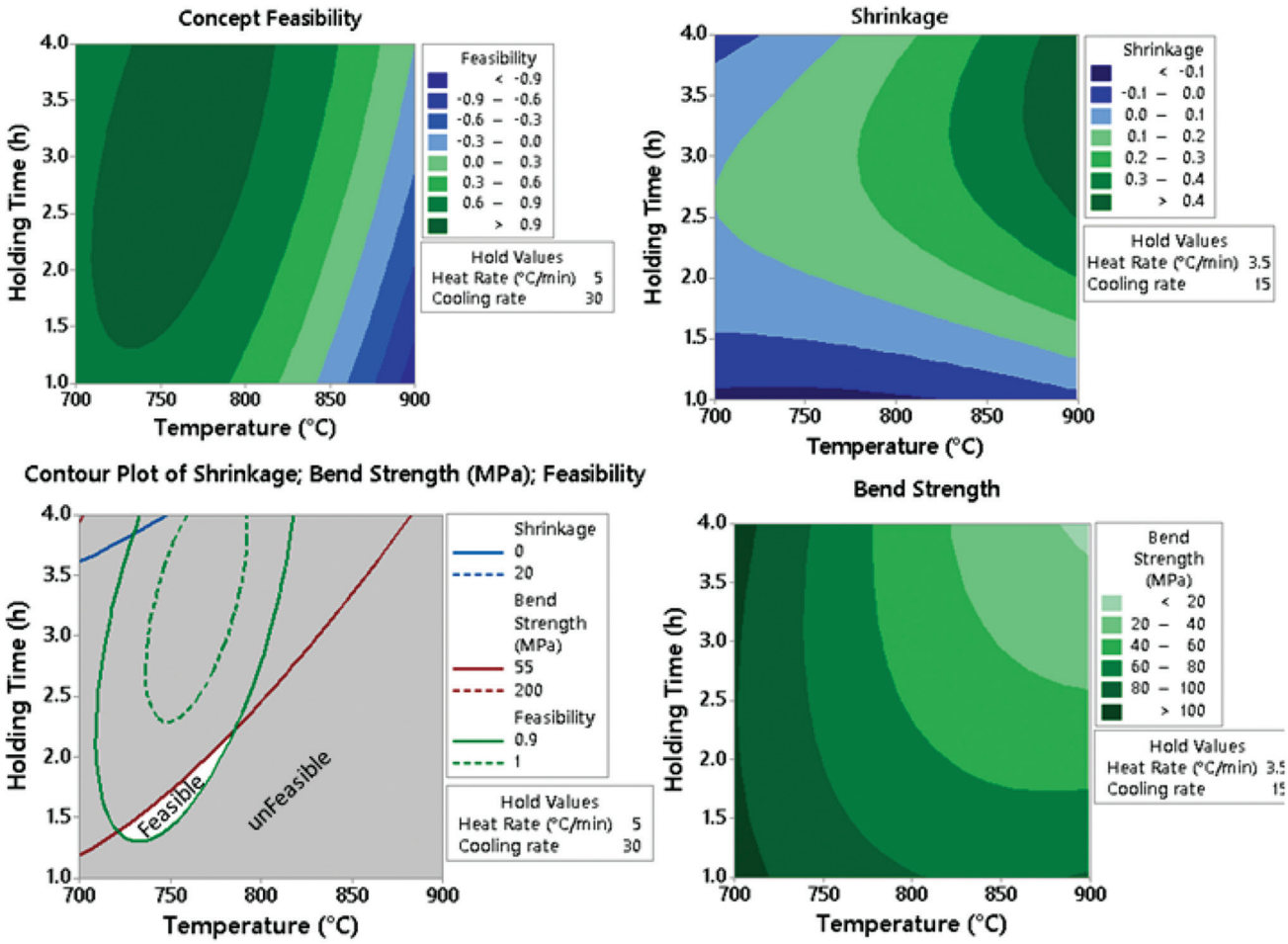


**Figure 7.** Contour diagrams of flexural strength, feasibility, shrinkage, and the overlapping diagram with combination of high values.

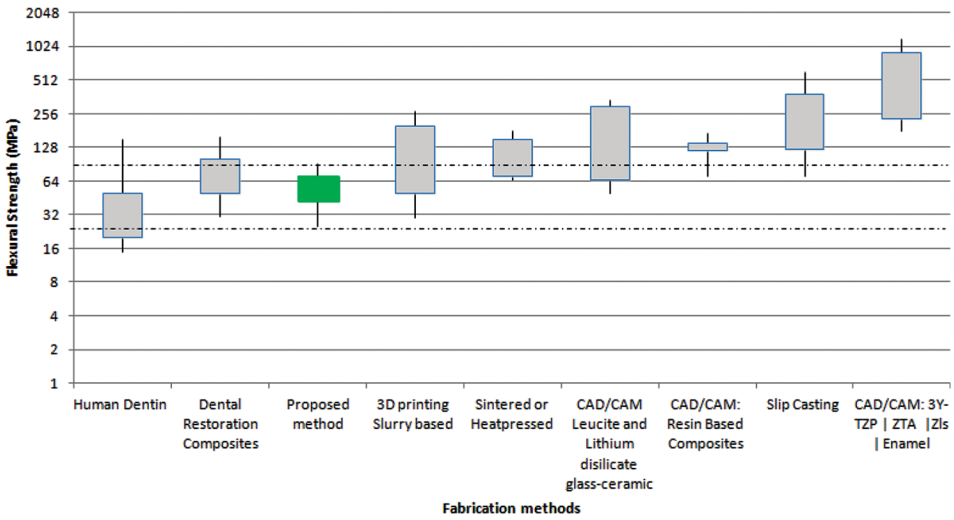


**Figure 8.** Flexural strength of the proposed method and typical dental prosthesis[3,17,28-37].

**Figure 9.** ZrSiO4-glass composite-based prosthetic crowns fabricated by indirect fused deposition modeling collapsible tool. The crown on the left side is of high grain densification with no finishing and the crown on the right side is of low grain densification with no finishing.

that are comparable to the typical dental applications. Therefore, further studies might increase the flexural strength up to the level of slip casting strength. It is also important to note that the volumetric shrinkage for typical CAD/CAM dental application varies from 5 to 30% [3,4,17,27]. Therefore, the range of values found in this work (13 – 25%) is compatible with the current state of art, indicating potential application in the field.

This concept has been shown to work and open a new possibility to fabricate glass-ceramic materials by AM technologies using collapsible ceramic mold, as presented in **Figure 9**. In this figure, two prosthetic crowns with no finishing were presented. The left-side crown presents high grain densification while the right-side crown with low grain densification. Both crowns have no layer marks, as the sintering process merged powder grain and created object superficial tension which inhibits the occurrence of mold layer marks. In addition, it is also known that after the fabrication of the dental prosthesis, the typical dental applications (CAD/CAM, slip casting, *etc.*) are coupled with several stages of finishing and making-up that improve the esthetic appearance of the prosthesis so that they mimic the original human dent[38]. Therefore, the geometrical characteristics, mechanical properties, and biocompatibility are the most important aspects to be considered in this type of application. Despite the preliminary results on the feasibility of the proposed method, further studies are still needed to improve mechanical strength, diversify the glass-ceramic materials, applications, and biocompatibility.

## 4. Conclusions

Collectively, this study assessed the feasibility of the glass-ceramic fabrication based on collapsible AM mold of $ZrSiO_4$. The working proof generates new perspectives to AM in dentistry, ceramics, and medical applications, whereas collapsible AM molds, such as we method used in this study, can support fabrication up to 2300°C.

This study also identified that the holding temperature is the factor that mostly influences the feasibility, strength, and shrinkage, followed by holding time which directly affects the material densification and grain growth. Besides, long time periods and high temperatures increase the densification and soften the material, leading to distorted geometry, and making the method unfeasible. On the other hand, flexural strength fluctuates between 25 and 82 MPa and can be highly affected by heating rate and cooling rate. Further studies are required to investigate the role of heating treatments and increase mechanical and geometrical properties, as

well as incorporate new materials and applications for screening.

## Acknowledgment

We would like to thank Concep3D R&D and FAE Centro Universitário for their support and infrastructure.

## Conflicts of interest

No conflicts of interest were reported by the authors.

## Author contributions

All the stages of this study were performed only by the author.

## References

1. Cunico MW, de Carvalho J, 2016, Development of Novel Additive Manufacturing Technology: An Investigation of a Selective Composite Formation Process. *Rapid Prototyp J*, 22:51–66. https://doi.org/10.1108/rpj-04-2014-0049
2. Sulaiman TA, 2020, Materials in Digital Dentistry a Review. *J Esthet Restor Dent*, 32:171–81.
3. Li RW, Chow TW, Matinlinna JP, 2014, Ceramic Dental Biomaterials and CAD/CAM Technology: State of the Art. *J Prosthodont Res*, 58:208–16. https://doi.org/10.1016/j.jpor.2014.07.003
4. Karthick A, Malarvizhi D, Tamilselvi R, *et al*., 2019, Ceramics in dentistry? A review. *Indian J Public Health Res Dev*, 10:6065.
5. Gali S, Sirsi S, 2015, 3D Printing: The Future Technology in Prosthodontics. *J Dent Orofac Res*, 11:37–40.
6. Uriondo A, Esperon-Miguez M, Perinpanayagam S, 2015, The Present and Future of Additive Manufacturing in the Aerospace Sector: A Review of Important Aspects. *Proc Inst Mech Eng G*, 229:2132–47. https://doi.org/10.1177/0954410014568797
7. Najmon JC, Raeisi S, Tovar A, 2019, Review of Additive Manufacturing Technologies and Applications in the Aerospace Industry. In: Additive Manufacturing for the Aerospace Industry. Elsevier, Amsterdam, Netherlands, pp. 7–31. https://doi.org/10.1016/b978-0-12-814062-8.00002-9
8. Espera AH, Dizon JR, Chen Q, *et al*., 2019, 3D-printing and Advanced Manufacturing for Electronics. *Prog Addit Manuf*, 4:245–67. https://doi.org/10.1007/s40964-019-00077-7
9. Saengchairat N, Tran T, Chua CK, 2017, A Review: Additive Manufacturing for Active Electronic Components. *Virtual Phys Prototyp*, 12:31–46. https://doi.org/10.1080/17452759.2016.1253181
10. Ng WL, Chua CK, Shen YF, 2019, Print me an Organ! Why we are not there yet. *Prog Polym Sci*, 97:101145. https://doi.org/10.1016/j.progpolymsci.2019.101145
11. Lee JM, Ng WL, Yeong WY, 2019, Resolution and Shape in Bioprinting: Strategizing Towards Complex Tissue and Organ Printing. *Appl Phys Rev*, 6:011307. https://doi.org/10.1063/1.5053909
12. Prinz FB, 1997, Rapid Prototyping in Europe and Japan. *Center Adv Technol*, 1997:102.
13. Vandenbroucke B, Kruth JP, 2007, Selective Laser Melting of Biocompatible Metals for Rapid Manufacturing of Medical Parts. *Rapid Prototyp J*, 13:196–203. https://doi.org/10.1108/13552540710776142
14. Wong J, 2010, Biocompatible Tantalum Fiber Scaffolding for Bone and Soft Tissue Prosthesis, Google Patents.
15. Mueller B, 2012, Additive Manufacturing Technologies: Rapid Prototyping to Direct Digital Manufacturing. *Assembly Autom*, 32:3332. https://doi.org/10.1108/aa.2012.03332baa.010
16. Anusavice KJ, 2013, Phillips Materiais Dentários. Elsevier, Brasil.
17. Denry IL, 1996, Recent Advances in Ceramics for Dentistry. *Crit Rev Oral Biol Med*, 7:134–43.
18. Lin L, Fang Y, Liao Y, *et al*., 2019, 3D Printing and Digital Processing Techniques in Dentistry: A Review of Literature. *Adv Eng Mater*, 21:1801013. https://doi.org/10.1002/adem.201801013
19. Torabi K, Farjood E, Hamedani S, 2015, Rapid Prototyping Technologies and their Applications in Prosthodontics, a Review of Literature. *J Dent*, 16:1.
20. Denry I, Kelly J, 2014, Emerging Ceramic-based Materials for Dentistry. *J Dent Res*, 93:1235–42. https://doi.org/10.1177/0022034514553627
21. Ishida Y, Miyasaka T, 2016, Dimensional Accuracy of Dental Casting Patterns Created by 3D Printers. *Dent Mater J*, 35:250–6. https://doi.org/10.4012/dmj.2015-278
22. Shujaat S, Shaheen E, Novillo F, *et al*., 2020, Accuracy of Cone Beam Computed Tomography Derived Casts: A Comparative Study. *J Prosthet Dent*, 2020:21. https://doi.org/10.1016/j.prosdent.2019.11.021
23. Dikova T, Dzhendov DA, Ivanov D, *et al*., 2018, Dimensional Accuracy and Surface Roughness of Polymeric Dental Bridges Produced by Different 3D Printing Processes. *Arch*

*Mater Sci Eng*, 94:65–75.
https://doi.org/10.5604/01.3001.0012.8660

24. Thompson Y, Gonzalez-Gutierrez J, Kukla C, *et al*., 2019, Fused Filament Fabrication, Debinding and Sintering as a Low Cost Additive Manufacturing Method of 316L Stainless Steel. *Addit Manuf*, 30:100861.
https://doi.org/10.1016/j.addma.2019.100861
25. Saude N, Ibrahim M, Ibrahim MH, 2014, Mechanical Properties of Highly Filled Iron-ABS Composites in Injection Molding for FDM Wire Filament. *Mater Sci Forum*, 773–774:448–53.
https://doi.org/10.4028/www.scientific.net/msf.773-774.448
26. Abdullah AM, Rahim TN, Mohamad D, *et al*., 2017, Mechanical and Physical Properties of Highly $ZrO_2$/β-TCP Filled Polyamide 12 Prepared via Fused Deposition Modelling (FDM) 3D Printer for Potential Craniofacial Reconstruction Application. *Mater Lett*, 189:307–9.
https://doi.org/10.1016/j.matlet.2016.11.052
27. Denry I, Kelly JT, 2008, State of the Art of Zirconia for Dental Applications. *Dent Mater*, 24:299–307.
https://doi.org/10.1016/j.dental.2007.05.007
28. Coldea A, Swain MV, Thiel N, 2013, Mechanical Properties of Polymer-infiltrated-ceramic-network Materials. *Dent Mater*, 29:419–26.
https://doi.org/10.1016/j.dental.2013.01.002
29. Junior SA, Zanchi CH, de Carvalho RV, *et al*., 2007, Flexural Strength and Modulus of Elasticity of Different Types of Resin-based Composites. *Braz Oral Res*, 21:16–21.
https://doi.org/10.1590/s1806-83242007000100003
30. Silva LH, de Lima E, de Paula Miranda RB, *et al*., 2017, Dental Ceramics: A Review of New Materials and Processing Methods. *Braz Oral Res*, 31:e58.
31. Abd El-Ghany OS, Sherief AH, 2016, Zirconia Based Ceramics, Some Clinical and Biological Aspects. *Future Dent J*, 2:55–64.
https://doi.org/10.1016/j.fdj.2016.10.002
32. Bicalho LA, Baptista CA, Barboza MJ, *et al*., 2011, $ZrO_2$-Bioglass Dental Ceramics: Processing, Structural and Mechanics Characterization. In: Advances in Ceramics Electric and Magnetic Ceramics, Bioceramics, Ceramics and Environment. InTech, Rijeka, Croatia.
https://doi.org/10.5772/22334
33. Christel P, Meunier A, Heller M, *et al*., 1989, Mechanical Properties and Short-term *In Vivo* Evaluation of Yttrium-oxide-partially-stabilized Zirconia. *J Biomed Mater Res*, 23:45–61.
https://doi.org/10.1002/jbm.820230105
34. Guazzato M, Albakry M, Ringer SP, *et al*., 2004, Strength, Fracture Toughness and Microstructure of a Selection of All-ceramic Materials. Part I. Pressable and Alumina Glass-infiltrated Ceramics. *Dent Mater*, 20:441–8.
https://doi.org/10.1016/j.dental.2003.05.003
35. Guazzato M, Albakry M, Ringer SP, *et al*., 2004, Strength, Fracture Toughness and Microstructure of a Selection of All-ceramic Materials. Part II. Zirconia-Based Dental Ceramics. *Dent Mater*, 20:449–56.
https://doi.org/10.1016/j.dental.2003.05.002
36. Ilie N, Hickel R, 2009, Investigations on Mechanical Behaviour of Dental Composites. *Clin Oral Investig*, 13:427.
https://doi.org/10.1007/s00784-009-0258-4
37. Galante R, Figueiredo-Pina CG, Serro AP, 2019, Additive Manufacturing of Ceramics for Dental Applications: A Review. *Dent Mater*, 35:825–46.
https://doi.org/10.1016/j.dental.2019.02.026
38. Virdi M, 2015, Emerging Trends in Oral Health Sciences and Dentistry. IntechOpen, London, pp. 854.

RESEARCH ARTICLE

# 3D-printed HA15-loaded β-Tricalcium Phosphate/ Poly (Lactic-co-glycolic acid) Bone Tissue Scaffold Promotes Bone Regeneration in Rabbit Radial Defects

**Chuanchuan Zheng[1†], Shokouh Attarilar[2†], Kai Li[3†], Chong Wang[4], Jia Liu[1*], Liqiang Wang[5], Junlin Yang[2], Yujin Tang[1*]**

[1]Department of Orthopedics, Affiliated Hospital of Youjiang Medical University for Nationalities, Baise, Guangxi, 533000, China
[2]Department of Pediatric Orthopaedics, Xinhua Hospital Affiliated to Shanghai Jiao Tong University School of Medicine, Shanghai, 200092, China
[3]Academy of Orthopedics, Guangdong Province, Guangdong Provincial Key Laboratory of Bone and Joint Degeneration Diseases, The Third Affiliated Hospital of Southern Medical University, Guangzhou 510000, China.
[4]School of Mechanical Engineering, Dongguan University of Technology, Dongguan, Guangdong, 523808, China
[5]State Key Laboratory of Metal Matrix Composites, School of Material Science and Engineering, Shanghai Jiao Tong University, Shanghai, 200240, China
[†]*These authors contributed equally to this work.*

**Abstract:** In this study, a β-tricalcium phosphate (β-TCP)/poly (lactic-co-glycolic acid) (PLGA) bone tissue scaffold was loaded with osteogenesis-promoting drug HA15 and constructed by three-dimensional (3D) printing technology. This drug delivery system with favorable biomechanical properties, bone conduction function, and local release of osteogenic drugs could provide the basis for the treatment of bone defects. The biomechanical properties of the scaffold were investigated by compressive testing, showing comparable biomechanical properties with cancellous bone tissue. Furthermore, the microstructure, pore morphology, and condition were studied. Moreover, the drug release concentration, the effect of anti-tuberculosis drugs *in vitro* and in rabbit radial defects, and the ability of the scaffold to repair the defects were studied. The results show that the scaffold loaded with HA15 can promote cell differentiation into osteoblasts *in vitro*, targeting HSPA5. The micro-computed tomography scans showed that after 12 weeks of scaffold implantation, the defect of the rabbit radius was repaired and the peripheral blood vessels were regenerated. Thus, HA15 can target HSPA5 to inhibit endoplasmic reticulum stress which finally leads to promotion of osteogenesis, bone regeneration, and angiogenesis in the rabbit bone defect model. Overall, the 3D-printed β-TCP/PLGA-loaded HA15 bone tissue scaffold can be used as a substitute material for the treatment of bone defects because of its unique biomechanical properties and bone conductivity.

**Keywords:** Three-dimensional printing; β-tricalcium phosphate; HA15; Endoplasmic reticulum stress; Bone defect

***Correspondence to**: Yujin Tang, Department of Orthopedics, Affiliated Hospital of Youjiang Medical University for Nationalities, Baise, Guangxi, 533000, China; tangyujin1967@163.com. Jia Liu, Department of Orthopedics, Affiliated Hospital of Youjiang Medical University for Nationalities, Baise, Guangxi, 533000, China; liujia0111@live.cn

**Received:** October 30, 2020; **Accepted:** November 23, 2020; **Published Online:** January 20, 2021

**Citation:** Zheng C, Attarilar S, Li K, *et al*., 2021, 3D-printed HA15-loaded β-Tricalcium Phosphate/Poly (Lactic-co-glycolic acid) Bone Tissue Scaffold Promotes Bone Regeneration in Rabbit Radial Defects. *Int J Bioprint*, 7(1):317.http://doi.org/10.18063/ijb.v7i1.317

## 1. Introduction

Bone defects, which are of prominent importance, refer to a range of injuries that happen due to different reasons, including bone atrophy, trauma, benign and malignant tumors, and periodontal disease[1]. In this regard, an autologous bone graft is a unique standard of the hard tissue transplantation treatment, especially for bone defects[2].

These autologous bone grafts have numerous biological benefits over heterologous and synthetic bone substitutes due to their excellent combination of osteogenic, osteoinductive, and osteoconductive characteristics[3,4]. Despite these advantages, bone transplantation can lead to issues, such as bleeding, hematoma, infection, and chronic pains. Furthermore, this form of treatment is restrained by the donor sources and high costs of surgery[5,6]. Considering these issues and the great demand for treatment of bone defects, the need for modern designs and new strategies has been elevated to an urgent status, specifically for large-area bone defects. In this relation, bone tissue engineering is considered one of the most promising alternative approach for bone defect repairment[7]. One of the aims of bone tissue engineering is to fabricate osteoconductive scaffolds along with the successful delivery of osteogenic cells and biological factors[8].

The scaffold design should be able to accommodate living cells and guide their growth, and assist tissue regeneration in three dimensions[9,10]. The fabrication techniques also have a great impact on scaffold properties[11]. Moreover, the material and method selection must be designed according to specific demands of tissue (structural and metabolic)[12]. According to the biomimetic scaffold production protocols, the prepared scaffold must maintain a sufficient area for cell adhesion and proliferation, exchange of gaseous species, with the optimized surface-to-volume ratio and the degradation rate that matches tissue formation rate[13]. The scaffold's porosity, surface chemistry, morphology, three dimensional (3D) structure, immunogenicity, and mechanical properties have an extensive impact on the matrix properties in the biological artificial bone substitutes[14]. As yet, a wide array of materials has been used as matrix in bone tissue engineering, including natural polymers and their monomers (elastin, chitosan, silk, collagen, gelatin, etc.)[15], synthetic biodegradable polymers (polylactides, polycaprolactone, polypropylene fumarate, polyethylene glycol, etc.)[16], inorganic compounds of bone extracellular matrix (calcium phosphates, β-tricalcium phosphate [β-TCP], hydroxyapatite [HA], calcium carbonate, etc.)[17], and signaling molecules (RGD proteins and various growth factors)[18]. It was clear that bone tissue engineering scaffolds should imitate the composition and structure of natural bone tissue mostly by engaging biodegradable polymer matrix and inorganic bioactive fillers in 3D composite porous scaffolds.

The utilization of β-TCP and poly (lactic-co-glycolic acid) (PLGA) is very common due to their beneficial aspects. The β-TCP has found many applications in load-bearing orthopedic implants because of its compositional analogy to natural bone, osteoconductivity, and tailorable bioresorbability[19,20]. Furthermore, the PLGA is considered one of the base biomaterials because of its biocompatibility, potential for tailoring its biodegradation rate, Food and Drug Administration certification for clinical use in humans, surface modification ability, and the ease of export to other countries[21]. In addition, HA15 is an efficient inhibitor of endoplasmic reticulum (ER) chaperone protein glucose regulatory protein 78 (GRP78, also known as BiP), which can prohibit the ATPase activity of BiP and trigger the ER stress. Through ER stress, the cells activate unfolded protein response (UPR) and other signaling pathways in reaction to misfolded and unfolded protein aggregation in the ER cavity and the disorder of calcium balance.

Many stress responses can activate ER stress, thus could be called UPR[22-24]. UPR is mediated by three major signaling cascades that are triggered by the so-called ER pressure sensors, such as double-stranded RNA activated protein kinase R (like endothelial reticulum kinase [PERK]), inositol-dependent enzyme 1 α (IRE1 α), and activating transcription factor 6 (ATF6). PERK, IRE1 α, and ATF6 are ER membrane proteins, which are known to form complexes with BiP in a steady-state condition. The increased demand for protein folding leads to activation of PERK, IRE1 α, and ATF6, subsequently activating their downstream influencers to alleviate protein toxic stress on ER and restore ER homeostasis[25,26]. In this regard, HA15 can bind to the ATP enzyme of BiP and inhibit its activity, leading to BiP separation from PERK, IRE1 α, and ATF6 that elicits ER stress and UPR[27]. The dissociation of BiP can activate PERK that subsequently phosphorylates eIF2 α, leading to the inhibition of protein synthesis, which is conducive to the folding of proteins in the ER. Unlike most proteins, the phosphorylated eIF2 α selectively promotes the translation of ATF 4. Since the ATF4 has an upstream open reading frame in its fifth untranslated region, under normal circumstances, these upstream open reading frames would prevent the translation of ATF4. Phosphorylated eIF2 α can promote ribosome binding to the open reading frame of ATF4, inducing the expression of ATF4 mRNA and increasing the translation of ATF4. ATF4 and runt-related transcription factor 2 (Runx2) can interact with osteoblast-specific actin element 1 (OSE1) and osteoblast-specific actin element 2 (OSE2), respectively, in the osteocalcin (OCN) promoter region. This can induce the expression of osteoblast-specific OCN along with bone matrix mineralization promotion, osteoblast differentiation regulation, and bone formation[28,29]. Therefore, HA15 can promote osteoblast differentiation through the PERK-eIf2 α-ATF4 pathway. It was known that the accumulation of misfolded protein in the ER may lead to the secretion of HSPA5/BiP (GRP78) from ERN1/IRE1, allowing homodimerization and subsequent activation of ERN1/IRE1. This event has an auxiliary role in the post-translational transport of small presecretory proteins across the ER. Furthermore, the HSPA5 gene is overexpressed due to UPR under the cellular stress conditions[30-32]; therefore, the expression of

HSPA5 gene is a reliable indicator of ER stress in human diseases[33]. Furthermore, HSPA5 promotes cell survival and drug resistance under ER stress conditions[34]. Hence, it seems that β-TCP/PLGA-loaded HA15 material targeting HSPA5 which is a master regulator of the anti-apoptotic UPR signaling network[35] can be a good therapeutic option for bone defect problems.

In this study, we constructed a 3D-printed β-TCP/PLGA-loaded HA15 targeting HSPA5 bone tissue scaffold according to a rabbit model of radial bone defect and performed the implantation. The effect of 3D-printed β-TCP/PLGA-loaded HA15 bone tissue scaffold on bone defect treatment and the healing condition is thoroughly discussed in this article. This study also provides a theoretical and experimental guideline for the treatment of bone defect with drug-loaded biomaterials that may be a promising treatment of bone lesions.

## 2. Materials and methods

### 2.1. Scaffold fabrication

The 3D-printed bone tissue scaffold formation procedure along with *in vitro* and *in vivo* experiments is briefly shown in **Figure 1**. First, 3 g of PLGA (Shandong Medical Device Company, P.R. China) with an inherent viscosity of 0.6–0.8 dL/g was dissolved in 10 mL of dichloromethane (DCM). Then, 3 g of β-TCP was added to prepare PLGA/DCM solution, which was subject to a 20-min ultra-sonication. After that, 200 μg of HA15 was added to 1.5 ml of deionized water to form an aqueous solution. The HA15 aqueous solution was mixed with β-TCP/PLGA/DCM composite solution with the assistance of ultra-sonication to form uniform HA15/water/TCP/PLGA/DCM composite emulsions as printing inks. The inks were subsequently added into a 20 mL syringe connected to a V-shape nozzle (inner diameter: 0.4 mm). A pre-designed STL file shown in **Figure 2D and E** with dimensions of sample and multi-section views was imported in a cryogenic 3D printer (Shenzhen Creality 3D Technology Co., Limited, P.R. China) and cylindrical scaffolds with 3D grid patterns were printed. The printing procedure was carried out according to the pre-set parameters; the feed speed was 0.005 mL/s and the printing speed was 8 mm/s. Finally, a cylindrical scaffold with a diameter of 4 mm and a height of 15 mm were obtained (**Figure 2**). The printed scaffolds were freeze-dried for 24 h to remove all DCM.

### 2.2. Detection using scanning electron microscope

Scanning electron microscopy (SEM) (TESCAN-Vega 3 system) was used to observe the pore structure and micro-morphology of the prepared 3D-printed scaffold as well as the scaffold aperture size, pore connectivity, and surface morphology of pore walls. The Nano Measurer 1.2 was used to perform aperture measurement on the SEM micrograph of the bracket. In this regard, 30 measurement holes were randomly selected to calculate the mean and standard deviations (SD) to make a preliminary assessment of the aperture range.

### 2.3. Mechanical properties of scaffolds

An electronic universal testing machine was used to test the mechanical response of the bone tissue scaffolds with a dimension of 15 mm × 3 mm × 2 mm according to the GB/T1041-1992 Chinese standard protocol. The prepared sample was inserted in the testing area and the compression loading was conducted with a speed of 0.5 mm/min until the complete deformation, then the strength and modulus of the scaffold were measured.

### 2.4. *In vitro* experiments

#### *(1) Cell culture*

Murine mesenchymal stem cell line C3H10 was incubated under the standard condition in DMEM medium supplemented with 10% fetal bovine serum, 100 U/ml penicillin G, and 100 mg/ml streptomycin. To seed the C3H10 cells onto the 3D-printed scaffolds, the scaffolds were sterilized with ultraviolet light and 70% ethanol and were placed in 24-well tissue culture plates. For cell seeding, samples were pre-soaked in DMEM complete culture medium for 24 h. Subsequently, 1 mL complete culture medium ($3 \times 10^4$ C3H10 cells) was poured on the top surface of the scaffolds. Then, the samples were incubated for 2 h to permit the cells to attach the scaffolds. The cells were stimulated with two concentrations of leaching solution from β-TCP/PLGA/HA15 scaffolds; the scaffold was infiltrated with 5 ml (HA15-1) or 10 ml (HA15-2) culture medium for 48 h.

#### *(2) siRNA knockdown*

We transiently transfected C3H10T1/2 cells with HSPA5 siRNA using Lipofectamine RNAiMAX (Invitrogen, Carlsbad, CA, USA) in Opti-MEM medium (Invitrogen), according to the manufacturer's instructions. The sequences of HSPA5 siRNA are as follows: Forward, 5'-AAGGUUACCCAUGCAGUUGTT-3' and reverse, 5'-AGAUUCAGCAACUGGUUAAAGTT-3'. Universal Non-targeting Control siRNA was considered and used as the control for non-sequence-specific effects. The capability of siRNA knockdown was evaluated by Western blotting. Each experiment was performed in triplicates.

#### *(3) Western blot analysis*

Cells were lysed in 2% sodium dodecyl sulfate (SDS) with 2 M urea, 10% glycerol, 10 mM Tris–

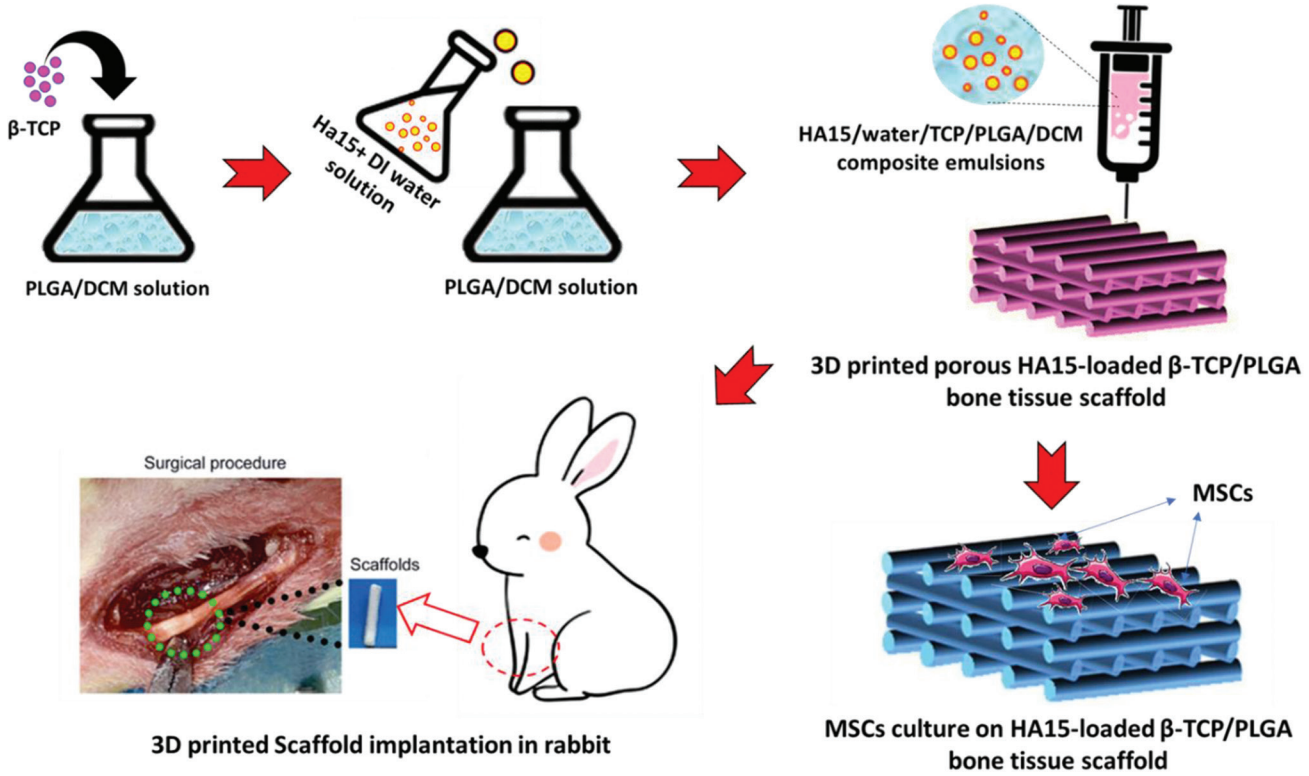


**Figure 1.** Production procedure of 3D-printed porous HA15-loaded β-tricalcium phosphate/poly (Lactic-co-glycolic acid) bone tissue scaffold along with *in vitro* mesenchymal stem cells (MSCs) culture and *in vivo* scaffold implantation in rabbit.

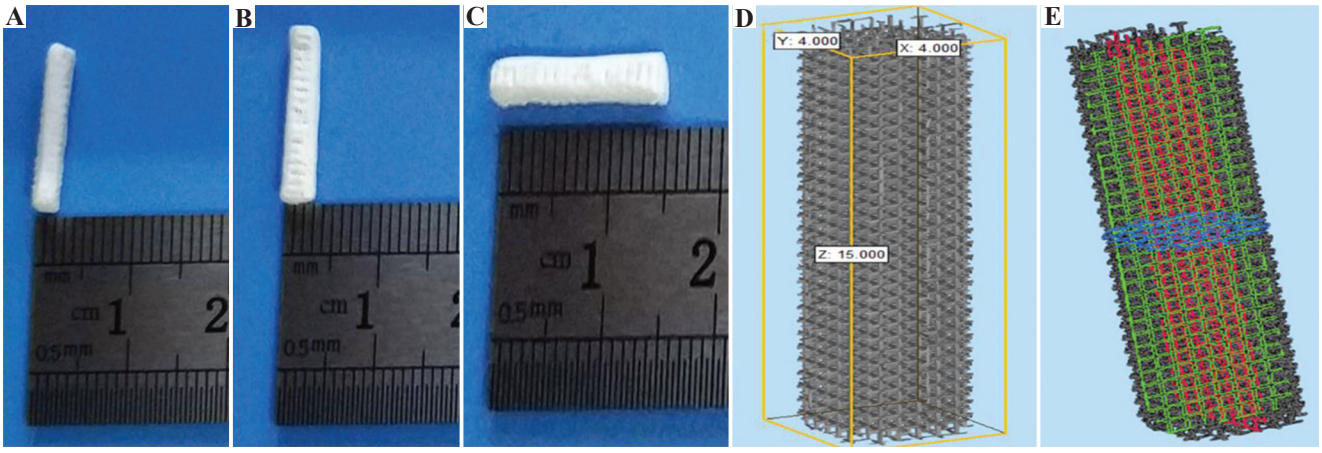


**Figure 2.** Prepared scaffolds. (A) β-tricalcium phosphate/poly (Lactic-co-glycolic acid)β-(TCP/PLGA) and (B) β-TCP/PLGA/HA15 samples; (C) the length of scaffolds; (D) pre-designed STL files showing the dimensions in mm; (E) STL file showing the multiple sections of sample: red for X section, green Y section, and blue for Z section.

HCl (pH 6.8), 10 mM dithiothreitol, and 1 mM phenylmethylsulfonyl fluoride. Proteins were separated by 10% SDS-polyacrylamide gel electrophoresis. After electrophoresis, proteins were transferred onto the membranes (Bio-Rad Laboratories, Hercules, CA, USA) using the wet transfer method. Each membrane was blocked using TBST (100 mM Tris–HCl pH 7.5, 150 mM NaCl, and 0.05% Tween 20) and 5% non-fat dried milk for 1 h at room temperature, and incubated with primary antibodies overnight on a shaker at 4°C. The membrane was incubated with HRP-coupled secondary antibody for 1 h at room temperature. Following this, membranes were treated with enhanced chemiluminescence reagents (ECL Kit, Amersham Biosciences, Piscataway, NJ, USA) and the proteins were detected using chemiluminescence technique.

#### *(4) Gene expression and real-time polymerase chain reaction (PCR) analysis*

The expression of osteogenic genes, including OCN, HSPA5, bone morphogenetic protein 2 (BMP2), alkaline phosphatase (ALP), collagen type I (col1a1), transcription factor Sp7 (Osterix), and Runx2, in C3H10 cells cultured on various specimens was analyzed by real-time PCR assay. After culturing for 7 days, total RNA was extracted using Trizol reagent from cells. The concentration of RNA was measured by a NanoDrop spectrophotometer (Thermo Fisher Scientific, USA). The primers used are shown in **Table 1**.

#### *(5) Alizarin red S staining*

Following osteogenic induction for 14 days, the cells were placed in 48-well plates (3-wells for each group) and fixed with 4% paraformaldehyde (PFA) for 20 min, and then rinsed twice with phosphate buffered saline (PBS). After that, the cells were stained using 40 mM alizarin red working solution for 10 min at room temperature. The cells were then rinsed twice with PBS and visualized under a light microscope. Next, 100 mmol/l cetylpyridinium chloride was poured into each well and semi-quantitative analyses were done by optical density measurement at 560 nm.

#### *(6) Immunofluorescence analysis*

For immunofluorescence analysis, after incubation with primary antibodies, followed by Alexa Fluor 594 donkey anti-mouse IgG1 (Life Technologies, Carlsbad, CA, USA) and Alexa Fluor 488 goat anti-mouse IgG2b (Life Technologies) secondary antibodies, cells were washed 3 times in PBS, after which nuclei were counterstained with 4',6-diamidino-2-phenylindole (Life Technologies). Images were obtained on a confocal laser-scanning microscope (Olympus, Tokyo, Japan).

### 2.5. *In vivo* experiments

#### *(1) Radial defect treatment of rabbit*

All *in vivo* animal experiments were conducted under the "Regulations on the Administration of Laboratory Animals" approved by the State Council, issued by the National Science and Technology Commission and approved by the Experimental Animal Ethics Committee of Youjiang Nationalities Medical College. Six New Zealand white rabbits, with an average weight of 2.5 ± 0.5kg, that were used in this experiment were provided by the Science Experiment Center of Youjiang Nationalities Medical College. Among them, the male rabbits and female rabbits were divided into β-TCP/groups using the random number method; these groups were PLGA/HA15 group, β-TCP/PLGA group, and bone defect group. The rabbits were assigned to either left or right radial defect model group using the random numbering method. The rabbits were anesthetized with 3% pentobarbital sodium at 20 mg/kg through ear intravenous injection (**Figure 3A**). The rabbits were fixed in the supine position and the forearm hairs were shaved to reveal the surgery site, which was disinfected with 2% iodine tincture 3 times. About 75% alcohol was used for deiodination. The corneal reflex of animals was observed to check if they were ready for surgery. The surgery began with a 2.0 cm long incision parallel to the radius of the forearm in the middle and upper segment of the forearm. Then, the subcutaneous tissue and muscle space were separated to expose the radius, after that the periosteum of the radius was cut (**Figure 3B**). An orthopedic mini-drill was used to cut a radius of about 1.5 cm in the upper-middle segment of the radius, and then the surgical site was rinsed with 0.9% sodium chloride solution. The samples were implanted at this site (indicated by a circle in **Figure 3C**). The subcutaneous tissue was sewed with 4-0 absorbable risk (**Figure 3D**). The incision was sutured with No. 0 suture and the wound was then disinfected and bandaged. The rabbits were kept in separate cages and each was administered an intramuscular penicillin injection at a dose of $1.6 \times 10^6$ units/day for 3 days post-surgery. All the animals were sacrificed 12 weeks after surgery by air embolization at the ear's marginal vein. The original surgical site was incised to observe the healing condition of the local bone defects. The surgical process is shown in **Figure 3**.

#### *(2) Micro-computed tomography (micro-CT) scan*

All experimental animals were subjected to 40-row micro-CT scanning through SIEMENS Inveon MMCT micro-CT instrument with working parameters of voltage and power of 55 kV and 80 W, respectively. Furthermore, the 3D reconstruction examination of the surgical sites was performed 12 weeks after surgery to thoroughly clarify the specific and intuitive bone callus growth and healing condition at the bone defect. Moreover, the quantitative analysis of bone volume/total volume (BV/TV), bone mineral density, trabecular thickness, and the structural model index was done according to the Hedberg's standard for evaluating the condition of new bone area.

#### *(3) Microfil angiography and micro-CT imaging*

The anesthetizing procedure was carried out according to a previously described method. The abdomen was fixed upward on the plate and the skin and muscle layer was cut along the midline of the abdomen. Then, the diaphragm was cut and the heart was exposed afterward. The heart was fixed with hemostatic forceps, and inserted with a 23G needle. The right atrial appendage in the left ventricle was cut with ophthalmic scissors. Subsequently, the infusion

**Table 1.** Primer sequences of osteogenic genes

| Osteogenic genes | Primer sequences |
|---|---|
| HSPA5 | F: 5'-CACGGTCTTTGACGCCAAG-3'<br>R: 5'-CCAAATAAGCCTCAGCGGTTT-3' |
| ALP | F: 5'-CGGATCCTGACCAAAAACC-3'<br>R: 5'-TCATGATGTCCGTGGTCAAT-3' |
| BMP2 | F: 5'-GAATGACTGGATCGTGGCACCTC-3'<br>R: 5'-GGCATGGTTAGTGGAGTTCAGGTG-3' |
| Col1α1 | F: 5'-CATGTTCAGCTTTGTGGACCT-3'<br>R: 5'-GCAGCTGACTTCAGGGATGT-3' |
| OCN | F: 5'-CACCATGAGGACCCTCTCTC-3'<br>R: 5'-TGGACATGAAGGCTTTGTCA-3' |
| Osterix | F: 5'-TCTCCATCTGCCTGACTCCT-3'<br>R: 5'-AGCGTATGGCTTCTTTGTGC-3' |
| Runx2 | F: 5'-GACTGTGGTTACCGTCATGGC-3'<br>R: 5'-ACTTGGTTTTTCATAACAGCGGA-3' |
| GAPDH | F: 5'-CATGTACGTTGCTATCCAGGC-3'<br>R: 5'-CTCCTTAATGTCACGCACGAT-3' |

F, forward; R, reverse; BMP2, bone morphogenetic protein 2; ALP, alkaline phosphate; col1a1, collagen type I; OCN; osteocalcin.

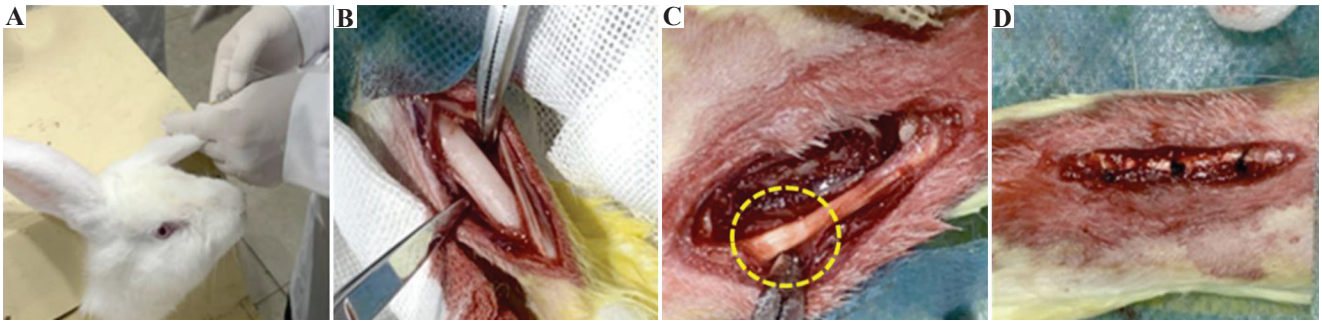


**Figure 3.** Surgery process on rabbit model. (A) Ear intravenous injection for anesthesia; (B) radius of the forearm in the middle and upper segment of the forearm; (C) sample implantation; (D) stitched wound.

pump was turned on and irrigated with saline until no red liquid flows out, and then it was changed to 4% PFA.

After the muscle tissue was fixed, the perfusion of 40-50 ml of mixed microfil liquid (solvent: solute=4:5, 1–2% coagulant added) was started. At the end of the perfusion process, the small blood vessels of the mesentery appeared yellow. Then, the rabbit corpse was placed in a 4°C refrigerator overnight. After the contrast agent was fixed, the rabbit upper limb was extracted to implement a micro-CT scan and observe the angiography.

### 2.6. Statistical analysis

The obtained results were expressed as mean ± SD. All the quantitative data were obtained from three or four independent experiments. The statistical analysis was performed using one-way analysis of variance followed by post-hoc tests. A value of $P < 0.05$ was regarded as significant.

## 3. Results and discussion

### 3.1. Characterizations of scaffolds

The pore structure of the 3D-printed scaffolds was evaluated using SEM. **Figure 4** shows the SEM micrographs of β-TCP/PLGA and β-TCP/PLGA/HA15 scaffolds. Both samples have 3D interconnected macropores with an acceptable shape tolerance and uniformity[36]. It can be observed that the number of distortions and defects is negligible and the 3D printing process has a good capability to produce this type of layer-by-layer β-TCP/PLGA scaffolds. The red dotted circles in **Figure 3** shows the near perfect pore morphologies. Also, the pores have rectangular shapes but are of varying sizes. The bigger pores have dimensions of about 200 μm ×180 μm while the smaller ones have dimensions in the range of ~100 μm × ~180 μm. This perfect pore structure maintains a large number of adhesion areas for cells.

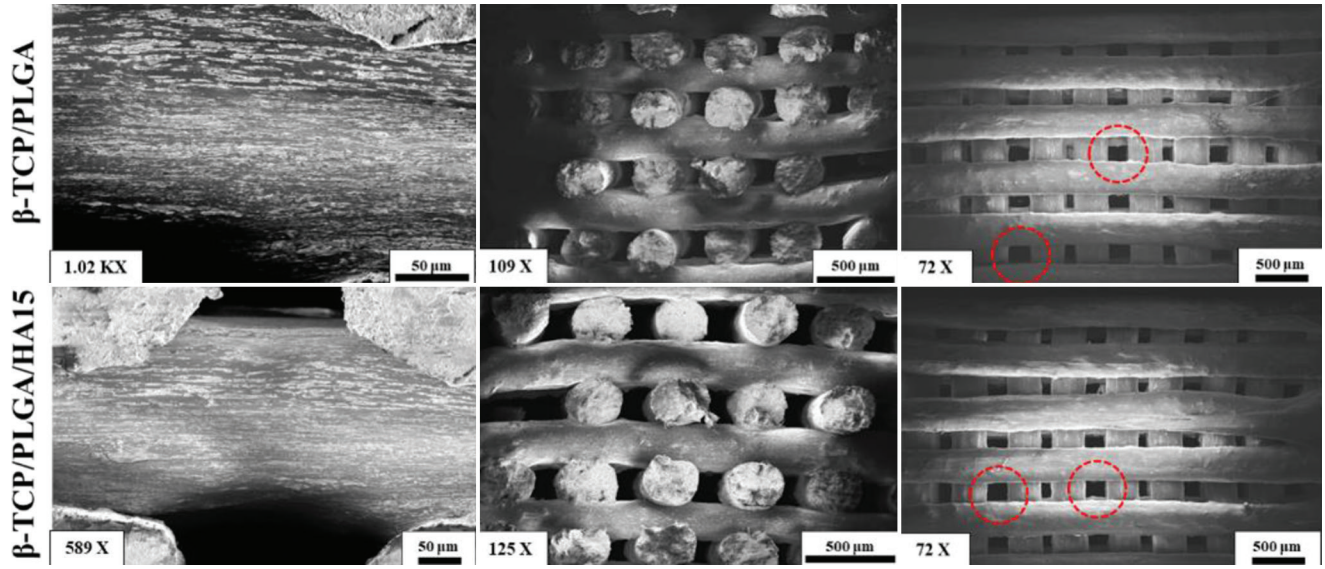


**Figure 4.** Scanning electron microscopy scanning results of the scaffolds with different magnifications. The upper row shows the β-tricalcium phosphate/poly (Lactic-co-glycolic acid) (β-TCP/PLGA) scaffolds and the bottom row shows the β-TCP/PLGA/HA15 scaffolds. The red dotted circles show the perfect pores.

### 3.2. Western blot

**Figure 5A** shows the qualitative western blot results of osteogenesis proteins after knockdown of HSPA5 in C3H10 cells (siRNA-transfected [Si-HSPA5]) and after being transfected with two concentrations of HA15 in stimulated osteogenic medium for 7 days. Both conditions (Si-HSPA5- and HA15-treated samples) exhibited expression for all osteogenic proteins tested, including HSPA5, OCN, Col1a1, Osterix, and β-actin. It was clearly seen that both Si-HSPA5- and HA15-treated samples did express a strong persistent signal for β-actin. Nevertheless, the Osterix has a considerable signal in both samples but it is more pronounced in Si-HSPA5. The Osterix expression is a general phenomenon in human bone tissues and Osterix as an important transcription factor is necessary for differentiation of osteoblasts[37]. Moreover, OCN as a sign of late osteoblast maturation and Col1a1 as the osteogenesis-related protein have considerably stronger signals compared to the negligible signals seen in the HA15-treated samples. It can be seen that Si-HSPA5 is more successful in silencing the HSPA5 proteins than HA15 treatment whereas HA15 can decrease the OCN and Col1a1 signals.

### 3.3. Gene expression

**Figure 5B** shows the mRNA expression of osteogenic genes in Si-HSPA5 and after 7 days treatment with two concentrations of leaching solution in C3H10 cells which is stimulated by the osteogenic medium. It was seen that all the osteogenic genes except HSPA5 were upregulated in both Si-HSPA5 and HA15 conditions compared to the control samples. The gene expression of ALP, which is an early marker of osteogenic differentiation[38], was upregulated about 3 folds in HA15-1 condition and about 0.17 fold in HA15-2 condition compared to the control sample (untreated condition and considered as natural healing). On the other hand, in the Si-HSPA condition, this increment was about 1.5 times compared to the control sample. Furthermore, the expression of OCN gene, which is a late marker of osteogenic differentiation[39], was increased for about 1.85 folds in Si-HSPA, and about 3 and 1.8 fold in HA15-2 and HA15-1 conditions, respectively. COL1A1 gene expression also showed considerable enhancement compared to control samples in all conditions. The reduction of HSPA5 in **Figure 5B** indicates a reduction of ER stress[40] and the improvement of drug performance.

### 3.4. Alizarin red S staining

The results of alizarin red staining showed enhanced calcium deposition in C3H10 cells that were transfected with Si-HSPA5 and two concentrations of leaching solution from β-TCP/PLGA/HA15 scaffolds on day 14, being greater in HA15-1 and Si-HSPA5 conditions (**Figure 5C**). Hence, the mineralization of extracellular matrix that usually happens during *in vitro* osteogenesis[41] can be improved by implementing HA15 and Si-HSPA5. The red spots, which serve as an indicator of calcium deposition and HA formation, considerably increased compared to control samples, indicating a better osteogenesis performance of all samples, especially the HA15-1 condition.

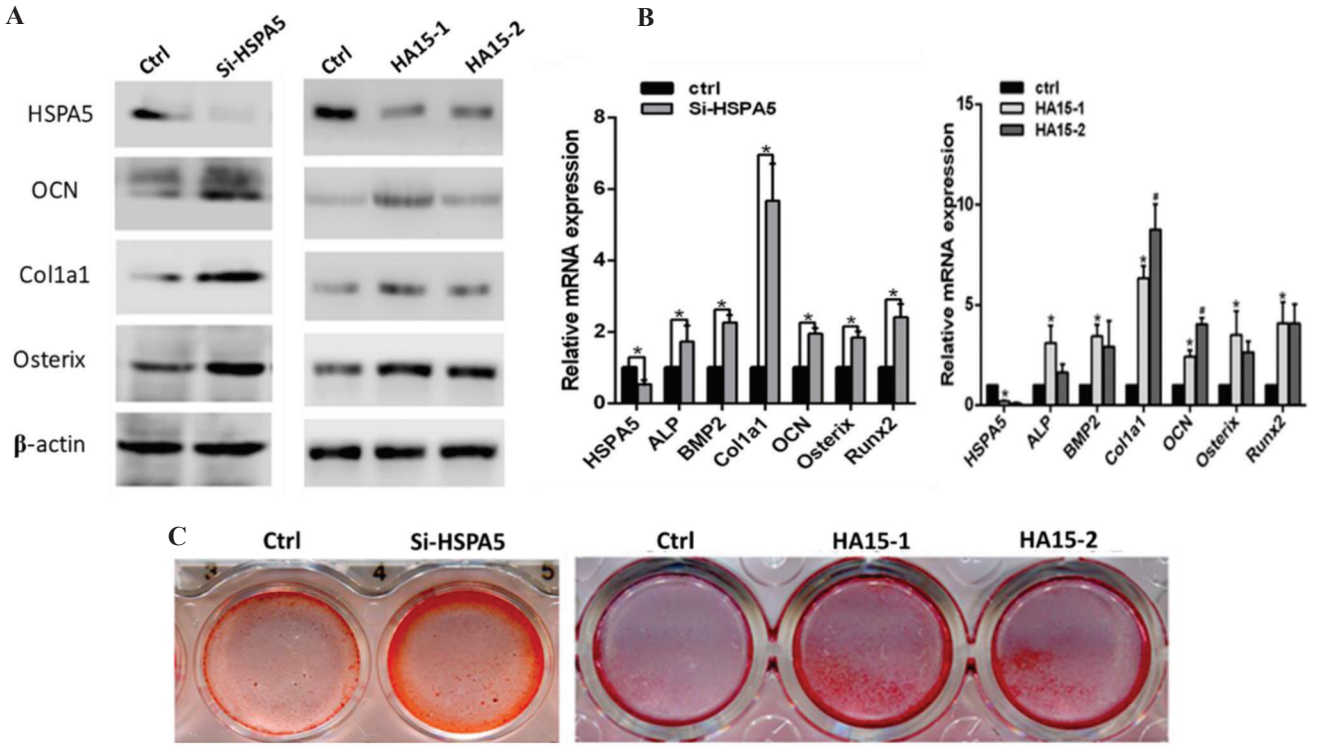


**Figure 5.** (A) Western blot analyses of osteogenic proteins after knockdown of HSPA5 in C3H10 cells (Si-HSPA5) and after treatment with two concentrations of leaching solution from β-tricalcium phosphate/poly (Lactic-co-glycolic acid)/HA15 scaffolds (HA15-1, HA15-2) in stimulated osteogenic medium for 7 days. (B) mRNA expression of osteogenic genes after knockdown of HSPA5, treatment with HA15-1 or HA15-2 in C3H10 cells and being stimulated by osteogenic medium for 7 days. (C) Alizarin red S staining of C3H10 cells with HSPA5 knockdown and treatment with HA15-1 or HA15-2 in osteogenic medium for 14 days.

### 3.5. Immunofluorescence staining

The OCN protein, DAPI, and HSPA5 were stained using immunofluorescence method and the co-localization of them was observed using confocal laser scanning microscope. The OCN proteins were marked by green fluorescence, HSPA5 by red color, and the nucleus labeled by DAPI as blue color. After merging all the immunofluorescence figures, it can be seen that OCN and HSPA5 were co-localized in cytoplasm and nucleus (**Figure 6**). Significantly stronger OCN staining was observed in the HA15 sample in comparison to the control, indicating a better osteogenic effect. Contrarily, the amount of HSPA5 was considerably decreased in the HA15 sample compared to the control. Thus, HA15 has the potential to improve osteogenesis and reduce HSAP5.

### 3.6. Mechanical properties

The mechanical compression performance of β-TCP/PLGA and β-TCP/PLGA/HA15 samples is listed in **Table 2** and their respective stress-strain curves are illustrated in **Figure 7**. The compression strengths of

**Table 2.** Compression mechanical results of β-TCP/PLGA and β-TCP/PLGA/HA15 scaffolds

| Scaffold | Young modulus (E) | Ultimate tensile strength (UTS) | Strain |
|---|---|---|---|
| β-TCP/PLGA | 27.86 | 0.366 MPa | 1.28% |
| β-TCP/PLGA/HA15 | 31.36 | 0.443 MPa | 8.6% |

β-TCP/PLGA and β-TCP/PLGA/HA15 samples were about 0.366 MPa and 0.443 MPa, respectively. It can be seen that the compression strength of the β-TCP/PLGA/HA15 scaffold is 19% higher than that of the β-TCP/PLGA and is considered more suitable for load-bearing applications, especially bone defects. Although β-TCP/PLGA has less Young's modulus and can inhibit stress shielding effect, this amount in β-TCP/PLGA/HA15 is not considerably high and it can still maintain good biomechanical properties. The compression strength and Young's modulus of these samples are comparable with those of cancellous bone tissue[42,43]; hence, they seem to be suitable for bone defect applications. Nonetheless, the performance of

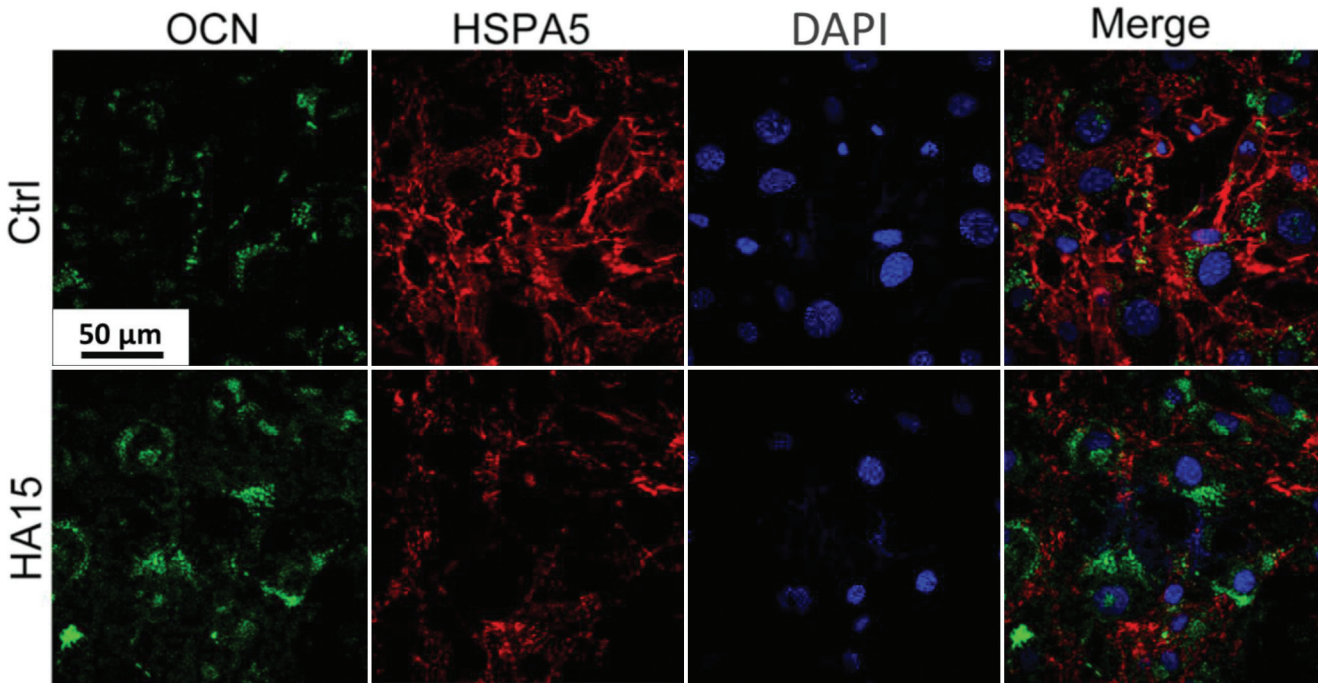


**Figure 6.** Immunofluorescence staining of OCN, HSPA5, and DAPI in C3H10 cells treated with leaching solution from β-tricalcium phosphate/poly (Lactic-co-glycolic acid)/HA15 scaffolds and osteogenic medium for 7 days.

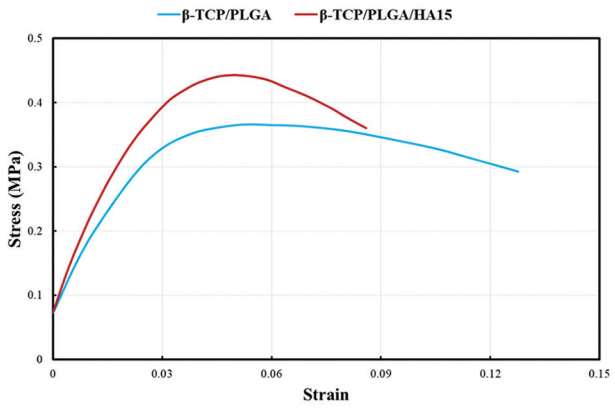


**Figure 7.** Mechanical compression stress-strain curve of β-tricalcium phosphate/poly (Lactic-co-glycolic acid) (β-TCP/PLGA) and β-TCP/PLGA/HA15 scaffolds.

β-TCP/PLGA/HA15 scaffold is better and should be the potential choice.

### 3.7. Micro-CT scan and microfil angiography of bone formation

After implantation of scaffolds and surgery procedure (**Figure 8A**), the BV fraction (%) of scaffolds was analyzed by micro-CT scan as shown in **Figure 8B**. Micro-CT scan experiment can accurately quantify the bone and its spatial growth and 3D distribution[44]. It can be seen that the samples have very different mineralization behavior. The extent of bone formation of the β-TCP/PLGA/HA15 sample was considerably higher than that of the β-TCP/PLGA and control sample 12 weeks after the surgery. The addition of HA15 considerably improved bone mineralization but the effect of β-TCP/PLGA seemed to be not significant. It should be considered that the scaffold material was mostly degraded after 12 weeks so it cannot be shown by micro-CT scans.

The 3D images of neovascularization (newly formed vessel-like structure) in the scaffold region are demonstrated in **Figure 8C**. There were considerably more newly formed vessels in the β-TCP/PLGA/HA15 and β-TCP/PLGA scaffolds compared to the control sample. The best performance was seen in the β-TCP/PLGA/HA15 sample. For more effective bone repair and regeneration, angiogenesis is essential. Moreover, vascularization leads to osteogenesis during tissue maturity and regeneration[45]. Reportedly, the neovascularization improvement could accelerate osteogenesis even before the establishment of local blood flow[46]. Hence, the formation of β-TCP/PLGA and β-TCP/PLGA/HA15 scaffolds could significantly enhanced bone regeneration. **Figure 9** shows the accumulative HA15 release profile of β-TCP/PLGA/HA15 scaffold in which it can be seen that about 73% of HA15 was released in 25 days. The rate of HA15 release was very fast in the 1st week, especially after 5 days, then it started to decrease. If the release rate of the substance was assumed to be constant after 7 days, 100% of the HA15 would be released after about 59 days.

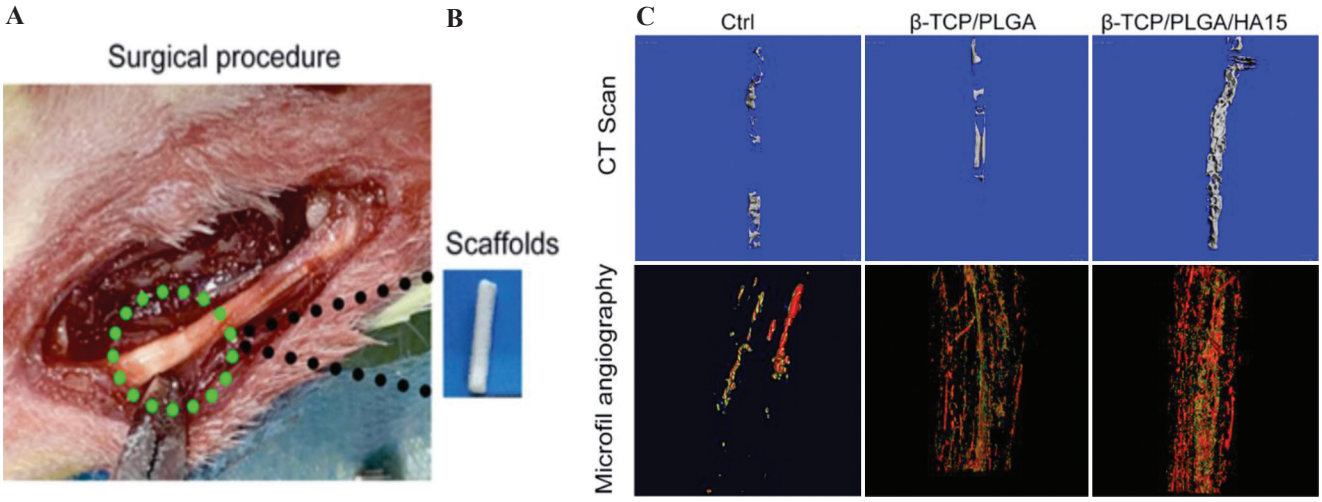


**Figure 8.** (A) Scaffold implantation surgical procedure in rabbits. (B) Micro-computed tomography (Micro-CT) scan images and quantification results of the defect area 12 weeks after the surgery; newly formed bone appeared as white dots on the CT images. (C) Microfil angiography and micro-CT imaging results of the rabbits.

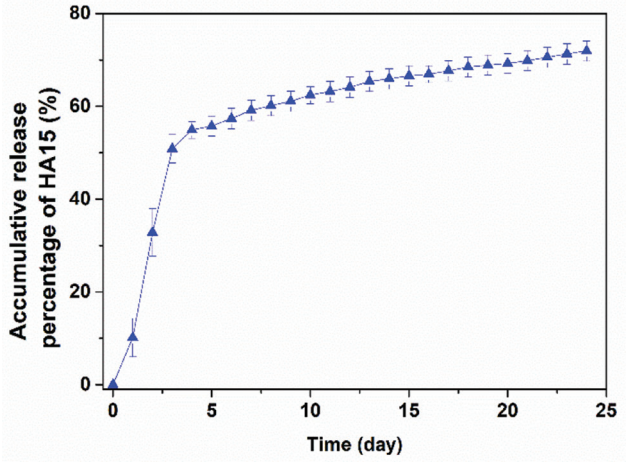


**Figure 9.** Accumulative HA15 release profile of β-tricalcium phosphate/poly (Lactic-co-glycolic acid)/HA15 scaffold.

## 4. Conclusion

In this study, a β-TCP/PLGA bone tissue scaffold loaded with osteogenesis-promoting drug HA15 was constructed by 3D printing technology. The scaffold loaded with the HA15 delivery system has favorable biomechanical properties comparable to those of the cancellous bone tissue and can promote cell differentiation into osteoblasts *in vitro* targeting HSPA5 and promote bone regeneration in a rabbit bone defect model. Moreover, this scaffold can enhance angiogenesis that has a significant role in more effective bone repair and regeneration. It was seen that HA15 can target HSPA5 to inhibit ER stress and promote osteogenesis, along with the inhibition of ER stress, reduced apoptosis, and induced autophagy *in vivo*. Overall, this study might provide a theoretical approach for the treatment of bone defects with HA15-loaded biomaterials.

## Conflicts of interest

The authors declare no conflicts of interest.

## References

1. Trejo-Iriarte CG, Serrano-Bello J, Gutiérrez-Escalona R, *et al*., 2019, Evaluation of Bone Regeneration in a Critical Size Cortical Bone Defect in Rat Mandible Using MicroCT and Histological Analysis. *Arch Oral Biol*, 101:165–71. https://doi.org/10.1016/j.archoralbio.2019.01.010
2. Tarafder S, Davies NM, Bandyopadhyay A, *et al*., 2013, 3D Printed Tricalcium Phosphate Bone Tissue Engineering Scaffolds: Effect of SrO and MgO Doping on *In Vivo* Osteogenesis in a Rat Distal Femoral Defect Model. *Biomater Sci*, 1:1250. https://doi.org/10.1039/c3bm60132c
3. Giannoudis PV, Dinopoulos H, Tsiridis E, 2005, Bone Substitutes: An Update. *Injury*, 36:S20–7. https://doi.org/10.1016/j.injury.2005.07.029
4. Pape HC, Evans A, Kobbe P, 2010, Autologous Bone Graft: Properties and Techniques. *J Orthop Trauma*, 24:S36–40. https://doi.org/10.1097/BOT.0b013e3181cec4a1
5. Ebraheim NA, Elgafy H, Xu R, 2001, Bone-Graft Harvesting From Iliac and Fibular Donor Sites: Techniques and Complications. *J Am Acad Orthop Surg*, 9:210–8. https://doi.org/10.5435/00124635-200105000-00007
6. Arrington ED, Smith WJ, Chambers HG, *et al*., 1996, Complications of Iliac Crest Bone Graft Harvesting. *Clin Orthop Relat Res*, 329:300–9. https://doi.org/10.1097/00003086-199608000-00037

7. Burg KJ, Porter S, Kellam JF, 2000, Biomaterial Developments for Bone Tissue Engineering. *Biomaterials*, 21:2347–59. https://doi.org/10.1016/S0142-9612(00)00102-2
8. Khojasteh A, Fahimipour F, Eslaminejad MB, *et al*., 2016, Development of PLGA-coated β-TCP Scaffolds Containing VEGF for Bone Tissue Engineering. *Mater Sci Eng C*, 69:780–8. https://doi.org/10.1016/j.msec.2016.07.011
9. Yang S, Leong KF, Du Z, *et al*., 2001, The Design of Scaffolds for Use in Tissue Engineering. Part I. Traditional Factors. *Tissue Eng*, 7:679–89. https://doi.org/10.1089/107632701753337645
10. Ng WL, Chua CK, Shen YF, 2019, Print me an Organ! Why we are not there YET. *Prog Polym Sci*, 97:101145. https://doi.org/10.1016/j.progpolymsci.2019.101145
11. Zhou H, Lawrence JG, Bhaduri SB, 2012, Fabrication Aspects of PLA-CaP/PLGA-CaP Composites for Orthopedic Applications: A Review. *Acta Biomater*, 8:1999–2016. https://doi.org/10.1016/j.actbio.2012.01.031
12. Hollister SJ, 2009, Scaffold Design and Manufacturing: From Concept to Clinic. *Adv Mater*, 21:3330–42. https://doi.org/10.1002/adma.200802977
13. Badekila AK, Kini S, Jaiswal AK, 2020, Fabrication Techniques of Biomimetic Scaffolds in Three-dimensional Cell Culture: A Review. *J Cell Physiol*, 2020:29935. https://doi.org/10.1002/jcp.29935
14. Logeart-Avramoglou D, Anagnostou F, Bizios R, *et al*., 2005, Engineering Bone: Challenges and for Bone Tissue Engineering and Regenerative Medicine: A Review. *J Cell Mol Med*, 9:72–84. https://doi.org/10.1111/j.1582-4934.2005.tb00338.x
15. Pina S, Oliveira JM, Reis RL, 2015, Natural-Based Nanocomposites. *Adv Mater*, 27:1143–69. https://doi.org/10.1002/adma.201403354
16. Asti A, Gioglio L, 2014, Natural and Synthetic Biodegradable Polymers: Different Scaffolds for Cell Expansion and Tissue Formation. *Int J Artif Organs*, 37:187–205. https://doi.org/10.5301/ijao.5000307
17. Shrivats AR, McDermott MC, Hollinger JO, 2014, Bone Tissue Engineering: State of the Union. *Drug Discov Today*, 19:781–86. https://doi.org/10.1016/j.drudis.2014.04.010
18. Winkler T, Sass FA, Duda GN, *et al*., 2018, A Review of Biomaterials in Bone Defect Healing, Remaining Shortcomings and Future Opportunities for Bone Tissue Engineering. *Bone Joint Res*, 7:232–43. https://doi.org/10.1302/2046-3758.73.BJR-2017-0270.R1
19. Nandi SK, Fielding G, Banerjee D, *et al*., 2018, 3D-Printed β-TCP Bone Tissue Engineering Scaffolds: Effects of Chemistry on *In Vivo* Biological Properties in a Rabbit Tibia Model. *J Mater Res*, 33:1939–47. https://doi.org/10.1557/jmr.2018.233
20. Liu Q, Cen L, Yin S, *et al*., 2008, A Comparative Study of Proliferation and Osteogenic Differentiation of Adipose-derived Stem Cells on Akermanite and β-TCP Ceramics. *Biomaterials*, 29:4792–99. https://doi.org/10.1016/j.biomaterials.2008.08.039
21. Gentile P, Chiono V, Carmagnola I, *et al*., 2014, An Overview of Poly(lactic-co-glycolic) Acid (PLGA)-Based Biomaterials for Bone Tissue Engineering. *Int J Mol Sci*, 15:3640–59. https://doi.org/10.3390/ijms15033640
22. Yadav RK, Chae SW, Kim HR, *et al*., 2014, Endoplasmic Reticulum Stress and Cancer. *J Cancer Prev*, 19 (2014) 75–88. https://doi.org/10.15430/JCP.2014.19.2.75.
23. Urra H, Dufey E, Avril T, *et al*., 2016, Endoplasmic Reticulum Stress and the Hallmarks of Cancer. *Trends Cancer*, 2:252–62. https://doi.org/10.1016/j.trecan.2016.03.007
24. Díaz-Villanueva J, Díaz-Molina R, García-González V, 2015, Protein Folding and Mechanisms of Proteostasis. *Int J Mol Sci*, 16:17193–230. https://doi.org/10.3390/ijms160817193
25. Sano R, Reed JC, 2013, ER Stress-induced Cell Death Mechanisms. *Biochim Biophys Acta Mol Cell Res*, 1833:3460–70. https://doi.org/10.1016/j.bbamcr.2013.06.028
26. Attarilar S, Yang J, Ebrahimi M, *et al*., 2020, The Toxicity Phenomenon and the Related Occurrence in Metal and Metal Oxide Nanoparticles: A Brief Review From the Biomedical Perspective. *Front Bioeng Biotechnol*, 8:822. https://doi.org/10.3389/fbioe.2020.00822
27. Cerezo M, Lehraiki A, Millet A, *et al*., 2016, Compounds Triggering ER Stress Exert Anti-Melanoma Effects and Overcome BRAF Inhibitor Resistance. *Cancer Cell*, 29:805–19. https://doi.org/10.1016/j.ccell.2016.04.013
28. Xiao G, Jiang D, Ge C, *et al*., 2005, Cooperative Interactions between Activating Transcription Factor 4 and Runx2/Cbfa1 Stimulate Osteoblast-specific Osteocalcin Gene Expression. *J Biol Chem*, 280:30689–96. https://doi.org/10.1074/jbc.M500750200
29. Wang W, Chen J, Hui Y, *et al*., 2018, Down-Regulation of miR-193a-3p Promotes Osteoblast Differentiation through up-regulation of LGR4/ATF4 Signaling. *Biochem Biophys Res Commun*, 503:2186–93. https://doi.org/10.1016/j.bbrc.2018.08.011

30. Zhang K, Kaufman RJ, 2004, Signaling the Unfolded Protein Response from the Endoplasmic Reticulum. *J Biol Chem*, 279:25935–8. https://doi.org/10.1074/jbc.R400008200
31. Ni M, Lee AS, 2007, ER Chaperones in Mammalian Development and Human Diseases. *FEBS Lett*, 581:3641–51. https://doi.org/10.1016/j.febslet.2007.04.045
32. Macario L, Alberto J, 2007, Molecular Chaperones: Multiple Functions, Pathologies, and Potential Applications. *Front Biosci*, 12:2588. https://doi.org/10.2741/2257
33. Hasnain SZ, Lourie R, Das I, *et al*., 2012, The Interplay between Endoplasmic Reticulum Stress and Inflammation. *Immunol Cell Biol*, 90:260–70. https://doi.org/10.1038/icb.2011.112
34. Chen Y, Mi Y, Zhang X, *et al*., 2019, Dihydroartemisinin-Induced Unfolded Protein Response Feedback Attenuates Ferroptosis via PERK/ATF4/HSPA5 Pathway in Glioma Cells. *J Exp Clin Cancer Res*, 38:402. https://doi.org/10.1186/s13046-019-1413-7
35. Uckun FM, Qazi S, Ozer Z, *et al*., 2011, Inducing Apoptosis in Chemotherapy-Resistant B-Lineage Acute Lymphoblastic Leukaemia Cells by Targeting HSPA5, a Master Regulator of the Anti-apoptotic Unfolded Protein Response Signalling Network. *Br J Haematol*, 153:741–52. https://doi.org/10.1111/j.1365-2141.2011.08671.x
36. Touri M, Kabirian F, Saadati M, *et al*., 2019, Additive Manufacturing of Biomaterials the Evolution of Rapid Prototyping. *Adv Eng Mater*, 21:1800511. https://doi.org/10.1002/adem.201800511
37. Nakashima K, Zhou X, Kunkel G, *et al*., 2002, The Novel Zinc Finger-Containing Transcription Factor Osterix is Required for Osteoblast Differentiation and Bone Formation. *Cell*, 108:17–29. https://doi.org/10.1016/S0092-8674(01)00622-5
38. Pirraco RP, Reis RL, Marques AP, 2013, Effect of Monocytes/Macrophages on the Early Osteogenic Differentiation of hBMSCs. *J Tissue Eng Regen Med*, 7:392–400. https://doi.org/10.1002/term.535
39. Catelas I, Sese N, Wu BM, *et al*., 2006, Human Mesenchymal Stem Cell Proliferation and Osteogenic Differentiation in Fibrin Gels *In Vitro*. *Tissue Eng*, 12:2385–96. https://doi.org/10.1089/ten.2006.12.2385
40. Scheiber AL, Guess AJ, Kaito T, *et al*., 2019, Endoplasmic Reticulum Stress is Induced in Growth Plate Hypertrophic Chondrocytes in G610C Mouse Model of Osteogenesis Imperfecta. *Biochem Biophys Res Commun*, 509:235–40. https://doi.org/10.1016/j.bbrc.2018.12.111
41. Tataria M, Quarto N, Longaker MT, *et al*., 2006, Absence of the p53 Tumor Suppressor Gene Promotes Osteogenesis in Mesenchymal Stem Cells. *J Pediatr Surg*, 41:624–632. https://doi.org/10.1016/j.jpedsurg.2005.12.001
42. Gerhardt LC, Boccaccini AR, 2010, Bioactive Glass and Glass-Ceramic Scaffolds for Bone Tissue Engineering. *Materials* (*Basel*), 3:3867–910. https://doi.org/10.3390/ma3073867
43. Nazarian A, von Stechow D, Zurakowski D, *et al*., 2008, Bone Volume Fraction Explains the Variation in Strength and Stiffness of Cancellous Bone Affected by Metastatic Cancer and Osteoporosis. *Calcif Tissue Int*, 83:368–79. https://doi.org/10.1007/s00223-008-9174-x
44. Lee JY, Son SJ, Son JS, *et al*., 2016, Bone-Healing Capacity of PCL/PLGA/Duck Beak Scaffold in Critical Bone Defects in a Rabbit Model. *Biomed Res Int*, 2016:1–10. https://doi.org/10.1155/2016/2136215
45. Collin-Osdoby P, 1994, Role of Vascular Endothelial Cells in Bone Biology. *J Cell Biochem*, 55:304–9. https://doi.org/10.1002/jcb.240550306
46. Chen SH, Lei M, Xie XH, *et al*., 2013, PLGA/TCP Composite Scaffold Incorporating Bioactive Phytomolecule Icaritin for Enhancement of Bone Defect Repair in Rabbits. *Acta Biomater*, 9:6711–22. https://doi.org/10.1016/j.actbio.2013.01.024

RESEARCH ARTICLE

# Powder Loading Effects on the Physicochemical and Mechanical Properties of 3D Printed Poly Lactic Acid/Hydroxyapatite Biocomposites

**Cyron L. Custodio[1,2], Phoebeliza Jane M. Broñola[1], Sharyjel R. Cayabyab[1], Vivian U. Lagura[1], Josefina R. Celorico[1], and Blessie A. Basilia[1,2]***

[1]Materials Science Division, Industrial Technology Development Institute, Department of Science and Technology, Bicutan, Taguig City 1631, Philippines
[2]School of Graduate Studies, Mapúa University, Manila 1002, Philippines

**Abstract:** This study presents the physicochemical and mechanical behavior of incorporating hydroxyapatite (HAp) with polylactic acid (PLA) matrix in 3D printed PLA/HAp composite materials. Effects of powder loading to the composition, crystallinity, morphology, and mechanical properties were observed. HAp was synthesized from locally sourced nanoprecipitated calcium carbonate and served as the filler for the PLA matrix. The 0, 5, 10, and 15 wt. % HAp biocomposite filaments were formed using a twin-screw extruder. The resulting filaments were 3D printed in an Ultimaker S5 machine utilizing a fused deposition modeling technology. Successful incorporation of HAp and PLA was observed using infrared spectroscopy and X-ray diffraction (XRD). The mechanical properties of pure PLA had improved on the incorporation of 15% HAp; from 32.7 to 47.3 MPa in terms of tensile strength; and 2.3 to 3.5 GPa for stiffness. Moreover, the preliminary *in vitro* bioactivity test of the 3D printed PLA/HAp biocomposite samples in simulated body fluid (SBF) indicated varying weight gains and the presence of apatite species' XRD peaks. The HAp particles embedded in the PLA matrix acted as nucleation sites for the deposition of salts and apatite species from the SBF solution.

**Keywords:** Hydroxyapatite; Polylactic acid; 3D printing; Simulated body fluid

***Correspondence to:** Blessie A. Basilia, Materials Science Division, Industrial Technology Development Institute, Department of Science and Technology, Bicutan, Taguig City 1631, Philippines; basiliablessie@gmail.com

**Received:** November 6, 2020; **Accepted:** January 15, 2021; **Published Online:** January 28, 2021

**Citation:** Custodio CL, Broñola PJM, Cayabyab SR, *et al.,* 2021, Powder Loading Effects on the Physicochemical and Mechanical Properties of 3D Printed Poly Lactic Acid/Hydroxyapatite Biocomposites. *Int J Bioprint*, 7(1):326. http://doi.org/10.18063/ijb.v7i1.326

## 1. Introduction

Additive manufacturing, popularly known as three-dimensional (3D) printing, is a relatively useful and modern technology that promises excellent complex architectural control without requiring molds or templates, and the ability to tailor-fit designs depending on the demands specified by the end-user. The fabrication technology is mostly used for rapid prototyping to realize proof of concept ideas before large scale manufacturing. Another notable use of 3D printing is in the low-volume production of specific parts for specialized needs.

Industries where 3D printing has been involved include aerospace, automotive and transportation[1,2], military, medicine[3,4], construction[5,6], practical household items, and even clothing. All 3D printing technology print the object on some build platform that adjusts in height equal to the thickness of the layer being printed[7]. The coordinated printing motion relies on a 3D pattern created with a computer-aided design (CAD) software. A variety of printing techniques have been available for research, such as stereolithography (SLA)[8], selective laser sintering (SLS)[9], and fused deposition modeling (FDM)[10], to name a few. SLA utilizes ultraviolet (UV) light to polymerize and cure its liquid photoactive

monomer resin. The liquid resin solidifies on exposure to a CAD-guided incident light[8]. SLS traces a CAD pattern using a laser beam onto the powder resin, thus selectively sintering the powders into a solid object[9]. FDM extrudes a thermoplastic filament into built materials and support structures layer by layer[10]. Current commodity thermoplastic filaments that are suitable for FDM printing include polypropylene, acrylonitrile butadiene styrene, polystyrene, polyvinyl alcohol, polyamide (PA or nylon), and polylactic acid (PLA).

PLA has been a common filament for FDM 3D printing, mainly because of its relatively lower processing temperature, dimensional reliability, acceptable print quality, and good mechanical performance. Its monomer, lactic acid, is produced by fermenting dextrose derived from renewable crop resources such as corn, starch, and sugarcane. Hence, PLA is widely known as a sustainable, non-toxic biocompatible, and biodegrading material. To date, PLA is often used for biomedical applications, such as bone tissue engineering[11], scaffolds[12], and implants fabrication. PLA-based implants benefit from the avoidance of stress shielding effects, which is a known disadvantage for metal implants. While implanted inside the body, PLA would also dissolve naturally and is susceptible to biodegradation, and their by-products are non-toxic. Although plates and screws made from PLA have been used to fixate jaw fractures without additional support, PLA still has some inherent drawbacks and limitations. As compared to more popular bone implant materials such as stainless steel and alloy metals, PLA is comparatively inferior by a large margin in terms of mechanical performance. Another difficulty of using pure PLA is the poor cell attachment and proliferation on the polymer's surface. To address these concerns, the physicochemical properties of pure PLA can be altered and improved by incorporating biocompatible ceramic fillers and reinforcements.

Ceramic materials, such as calcium phosphates, silica, and alumina, comprise the human bone tissue. Due to their biocompatibility, these ceramic compounds have been synthesized and used as implants for biomedical applications. Bioactive implants are often coated with a type of calcium phosphate called hydroxyapatite (HAp, $Ca_{10}(PO_4)_6(OH)_2$), a promising bone substitute mineral. However, HAp is neither used for load-bearing applications nor in its bulk form due to its inherent brittleness. Therefore, HAp is mostly used as surface coating for other biomaterials dedicated for bone grafting. As a filler or reinforcing material, HAp can act to improve the matrix material's biocompatibility[13], stimulate bone regeneration, and improve the stiffness, compressive, and bending strengths[14]. Artificial implants should mimic the mechanical properties of the natural bone as close as possible. The human bone has stiffness in the range of 17–20 GPa. The integration of hard HAp ceramics and polymeric PLA matrix allows for bone substitute materials that are flexible and strong[14].

Injection-molded PLA/HAp bioactive composites have been fabricated to be used as an internal fixation device for cancellous bone regeneration[15]. Micro and nanoscale-HAp particles have been incorporated to PLA through electrospinning. Both micro-HAp and nano-HAp have shown to improve the elastic modulus of the electrospun mats and acted as nucleating agents. However, micro-HAp induced brittleness due to the bigger geometry of the fillers which acted as defects rather than as reinforcements[13]. A study on 3D printed PLA scaffolds varied the printing orientations (0°, 45°, and 90°), followed by surface modification using HAp. The resulting scaffolds' compressive properties and cell proliferation were observed. It was found that the optimal printing orientation was 90° as it produced the highest compressive strength (53 MPa), while no cell deaths were observed and all live cells have attached to the scaffold surface, thus ensuring the non-toxicity of the HAp-modified 3D printed PLA scaffolds[12].

In this study, Hap-reinforced PLA matrix biocomposites have been fabricated to determine the effects of HAp powder loading to the physicochemical and mechanical properties of the resulting 3D printed composite (**Figure 1**). From locally sourced nanoprecipitated calcium carbonate (NPCC), as-synthesized HAp powders were mechanically mixed with PLA at different powder loadings, followed by extrusion into a filament, and lastly 3D printed. The effect of the PLA/Hap composition on the crystallinity, morphology, and mechanical properties was investigated.

## 2. Materials and methods

### 2.1. Materials

NPCC was locally sourced from the Philippines. PLA pellets (PLA, NatureWorks LLC, IngeoTM Biopolymer 2003D) were purchased from D&L Polymers & Colors, Inc. The following chemicals: Phosphoric acid ($H_3PO_4$, RCI Labscan Ltd.), ammonium hydroxide ($NH_4OH$, Loba Chemie Pvt. Ltd.), and ethanol ($CH_3CH_2OH$, Thermo Fisher Scientific), were used without further purifications. Distilled water was used in preparing the solutions and for the washing procedures.

### 2.2. Hydroxyapatite synthesis

Chemical precipitation technique was undertaken using aqueous solution of calcium hydroxide, $Ca(OH)_2$ and $H_3PO_4$. Before synthesis, $Ca(OH)_2$ was prepared from the calcination of NPCC to decompose $CaCO_3$ into CaO and $O_2$ (Eq. 2.1). This was followed by slaking to convert CaO into

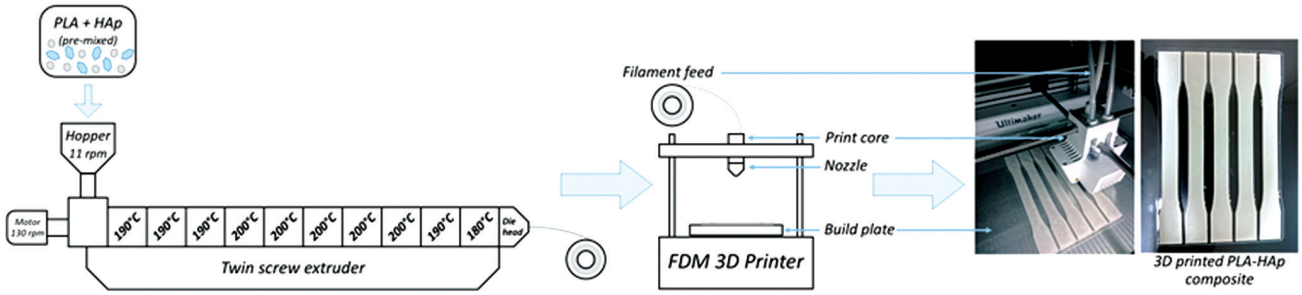


**Figure 1.** Schematic diagram of the polylactic acid/hydroxyapatite composite materials development process.

$Ca(OH)_2$ (Eq. 2.2). The obtained $Ca(OH)_2$ was dried and aqueous solution was prepared for the synthesis of HAp.

$$CaCO_3 \rightarrow CaO + CO_2 \quad (2.1)$$

$$CaO + H_2O \rightarrow Ca(OH)_2 \quad (2.2)$$

$$Ca(OH)_2 + H_3PO_4 \rightarrow Ca_{10}(PO_4)_6(OH)_2 \quad (2.3)$$

HAp was synthesized by mixing 1.5 M $Ca(OH)_2$ and 1 M $H_3PO_4$ (Eq. 2.3) at 40–50°C with continuous stirring. pH was monitored and maintained at 9–10 pH by dropwise addition of $NH_4OH$ to the mixture. The reaction required a 48-h maturation period, followed by washing with ethanol, and finally neutralized using deionized water. Then, the as-synthesized HAp was dried, ball milled, and then passed through an 80-mesh sieve. Final drying step was done at 80°C. Finally, the dried HAp powders were calcined at 1100°C.

## 2.3. Extrusion of the PLA/HAp composite filament

HAp powders were mechanically mixed with PLA pellets at different powder loadings (0, 5, 10, and 15 wt%) before extrusion and were labeled as PLA/0H, PLA/5H, PLA/10H, and PLA/15H, respectively (**Table 1**). A twin-screw extruder (Labtech Engineering Co. Ltd., Thailand) with a nominal screw diameter of 20 mm was used to composite the PLA/HAp mixture. Based on the calorimetric data of the PLA precursor, the input temperature profile of the 10 extruder's heating zone blocks was 190°C, 190°C, 190°C, 200°C, 200°C, 200°C, 200°C, 200°C, 190°C, and 180°C, respectively (**Figure 1**). The PLA/HAp mixture was fed onto the hopper, with an 11 rpm feed rate, and the screw speed set to 130 rpm. On exiting the nozzle, the filament goes into a water bath for cooling down, followed by passing through an air blower, before finally consolidating in a rotating spooler. The desired filament diameter was achieved by manually controlling the extruder motor and spooling speeds. Before printing, the PLA/HAp composite filaments were stored in an airtight dry box at room temperature to reduce the ambient moisture absorption.

**Table 1.** Sample nomenclature and composition.

| Sample | ID | % wt of HAp |
|---|---|---|
| PLA filled with 0% HAp | PLA/0H | 0 |
| PLA filled with 5% HAp | PLA/5H | 5 |
| PLA filled with 10% HAp | PLA/10H | 10 |
| PLA filled with 15% HAp | PLA/15H | 15 |

PLA, polylactic acid; HAp, hydroxyapatite

## 2.4. 3D printing of the PLA/HAp composite filament

The composited PLA/HAp blends were loaded and fed onto a 3D printer (Ultimaker S5, Netherlands) which operates based on a FDM technology. The printing parameters are listed in **Table 2**. Basically, the filament feed is re-extruded through a ruby-tipped CC print core that is specifically designed for composites, which had a 0.6 mm nozzle. Print core temperature was set at 200°C (±10), while the build plate was set to 60°C. A CAD file guided the precise movement of the print core assembly, which includes the extrusion nozzle. To compensate for any non-uniformity of the filament diameter and potential under-extrusion, the material flow rate was adjusted from 100 to 200% to achieve an acceptable and uniform print quality.

Dumbbell-shaped tensile test specimens were then 3D printed. The specimen dimensions were adopted from ASTM D638, and the generated 3D model (.stl) was digitally drafted through a CAD software such as SolidWorks (Dassault Systemes, France). The (.stl) file of the design was sliced using the software Cura, an open source 3D printing slicing application, which converted the (.stl) file into the printable (.ufp) file format.

## 2.5. Digital microscopy

The digital microscope VHX-7000 (Keyence Corporation, Japan) was used to observe the surface

**Table 2.** 3D printing parameters for FDM printing of PLA/HAp composites.

| Parameters | Settings |
|---|---|
| Layer height | 0.2 mm |
| Infill density | 100% |
| Infill pattern | Grid (45°, −45°) |
| Printing temperature | 210°C |
| Build plate temperature | 60°C |
| Print speed | 45 mm/s |
| Extrusion width (nozzle diameter) | 0.6 mm |

PLA, polylactic acid; HAp, hydroxyapatite; FDM, fused deposition modeling.

features and textures, depth profile, and fractured cross section of the 3D printed PLA/HAp composites, as well as the resulting scaffolds immersed in simulated body fluid (SBF) solutions. The samples were observed from 30× to 500× range.

## 2.6. Chemical composition

Attenuated total reflectance-Fourier transform infrared (ATR-FTIR) spectra were recorded across the 4000–600 $cm^{-1}$ frequency range, with 1–2 μ penetrating depth, and with 20 scans per sample at room temperature (23°C) using a Frontier FTIR spectrometer (PerkinElmer, USA). The synthesized HAp and 3D printed PLA/HAp composites were subjected to ATR-FTIR scans to determine the functional groups within the composite material.

## 2.7. Crystallinity

The diffraction patterns were obtained using a LabX X-ray diffraction (XRD)-6000 X-ray diffractometer (Shimadzu, Japan), with a Cu Kα radiation source at 40 kV operating voltage. The scanned range for all samples was from 2° to 60° (2θ) with a step size of 1°/min. The synthesized HAp, 3D printed PLA/HAp composites, and the biomineralized scaffolds were subjected to XRD characterization to confirm the presence of apatite species and their influence to the composite.

## 2.8. Mechanical properties

As adopted from ASTM D638, the tensile tests were carried out using a universal testing machine (Instron 5585H, USA), with a 10 kN static load cell, at a gauge length of 50 mm, and a strain rate of 5 mm/min. Tensile tests were done to determine the elastic modulus and tensile strength of the 3D printed PLA/HAp biocomposites. Five trials were tested for each sample, the average values reported, and the representative samples were plotted. Width and thickness of the test specimens were measured using a Mitutoyo digital caliper before testing. The tests were performed at room temperature and 54% relative humidity.

## 2.9. *In vitro* biomineralization

The bioactivities of the 3D printed scaffolds were assessed through immersion in SBF. The scaffolds were immersed in an SBF solution having a composition similar to what Rodriguez and Gatenholm reported[16], to determine the effect of increasing HAp powder loading to their biomineralization activity as a function of time. A liter of SBF solution was prepared by dissolving the analytic grade reagents (< 99%) in distilled water in the following order shown in **Table 3**.

In preparing the SBF solution, each reagent was added after the previous reagent has dissolved completely. The solution was prepared at 36.5°C under constant stirring. The pH of the solution was also adjusted to pH 7.4 using 1 M HCl solution and was kept refrigerated at 4°C before usage. The SBF is similar to the human blood plasma ionic concentration and composition. The samples were immersed in 15 mL of SBF solution and placed inside a dedicated oven set at 37°C for 24, 48, and 72 h to assess the growth and deposition of apatite species on the scaffold[17,18]. The SBF-immersed samples were retrieved from the solution and dried in the oven overnight, and finally characterized through digital microscopy, gravimetric analysis, and XRD.

# 3. Results and discussion

## 3.1. 3D printed PLA/HAp prototype

**Figure 2** shows the digital micrographs of the 3D printed PLA/HAp composites at different magnification levels, including the depth profile analysis. The top view of pure PLA (PLA/0H) was characterized by well-defined individual print beads, as the grid could be clearly seen both from 30× to 200× (**Figure 2A and B**), and even at the depth profile (**Figure 2E-F**). However, as the HAp loading was increased from 5 wt% to 15 wt%, the print beads were slowly disappearing and became less defined. Likewise, the surface finish oh PLA/5H, PLA/10H, and PLA/15H were more irregular and rougher than PLA/0H. The same visual trend could be seen at the depth profile, whereas the print bead gaps were slowly closing in and disappearing (**Figure 2L, R and X**). Hence, the 3D printed PLA/HAp composites were becoming more irregular as the HAp loadings were increased. Nonetheless, hydroxyapatite powders were seen from the composite surface with increasing frequency in accordance to the increasing HAp loading, although the distribution were irregular and agglomeration was present (**Figure 2H, J, N, P, T and V**).

Porosity and density are also some physical properties that must be considered, especially with polymer matrix composites. These properties can provide useful information in the prediction of the material's behavior, for instance, under mechanical stimuli. A denser material is usually a stronger one, and a porous material is usually

**Table 3.** Reagents and composition of the simulated body fluid solution.

| Chemical reagent | | Formula weight (g/mol) | Weight (g or mL in 1 L solution) |
|---|---|---|---|
| Sodium chloride | NaCl, Univar | 58.44 | 7.996 g |
| Sodium bicarbonate | $NaHCO_3$, Loba Chemie | 84.01 | 0.350 g |
| Potassium chloride | KCl, TPC | 74.55 | 0.224 g |
| Potassium phosphate dibasic anhydrous | $K_2HPO_4$, Loba Chemie | 174.18 | 0.228 g |
| Magnesium chloride hexahydrate | MgCl·6H2O, Loba Chemie | 203.3 | 0.305 g |
| Hydrochloric acid (1 M) | HCl, LabScan | 36.458 | 40 mL |
| Calcium chloride dihydrate | $CaCl_2 \cdot 2H_2O$, TPC | 147.02 | 0.278 g |
| Sodium sulfate anhydrous | $Na_2SO_4$, Fisher Scientific | 142.02 | 0.071 g |
| Tris buffer | $NH_2C(CH_2OH)_3$ Loba Chemie | 121.14 | 6.057 g |

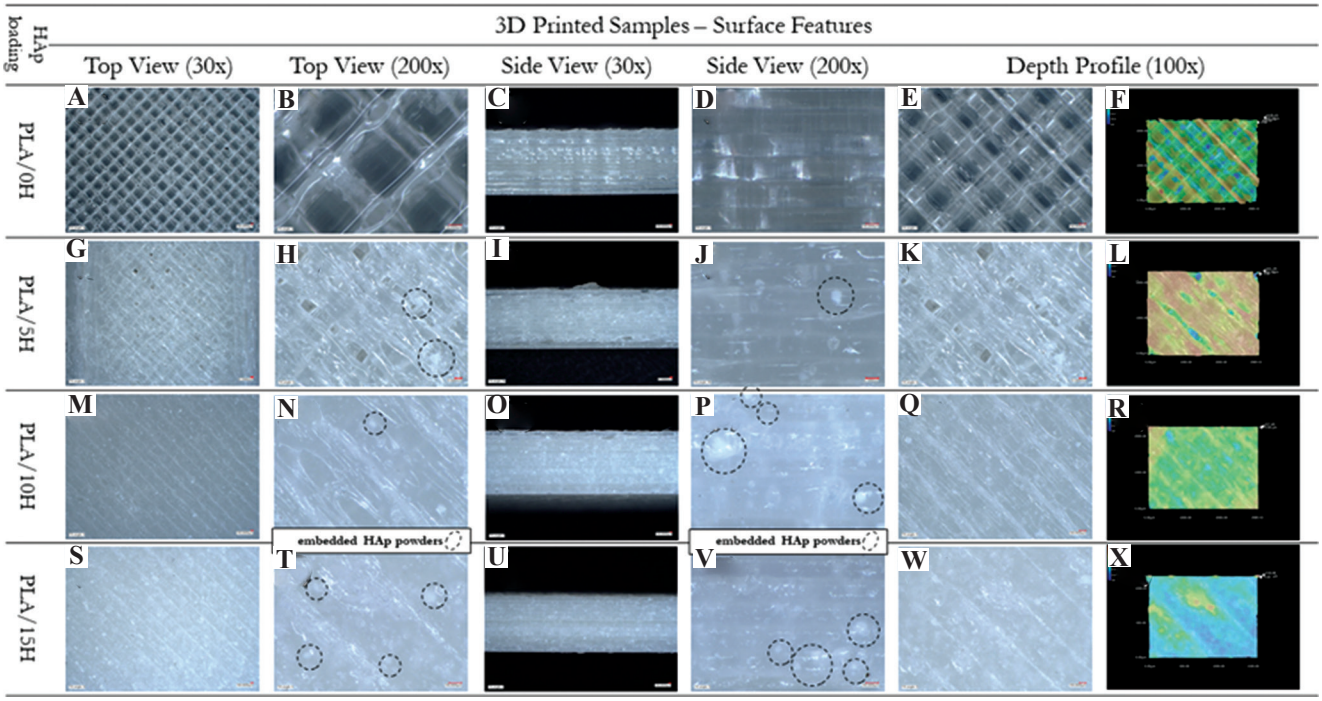


**Figure 2.** Digital micrographs of 3D printed polylactic acid (PLA)/hydroxyapatite: (A-F) PLA/0H; (G-L) PLA/5H; (M-R) PLA/10H; and (S-X) PLA/15H.

mechanically inferior. The experimental density and true porosity are presented in **Figures 3A and B**, respectively. We can see that as the HAp loading was increased, in an opposite manner the composites' density decreased. On the other hand, the porosity kept increasing, which means that more voids were forming as more HAp was added. Perhaps the tendency of HAp particles to agglomerate influenced the composites' microstructure and developed two kinds of sites that were agglomerated and areas that were porous as well. The true porosity was calculated using the following equation:

$$(\%)\mathrm{P} = 1 - \frac{\rho_{experimental}}{\rho_{theoretical}} \times 100 \qquad (3.1)$$

Where P refers to the true porosity (in percent), $\rho_{experimental}$ refers to experimental density, and $\rho_{theoretical}$ refers to theoretical density. The literature theoretical densities of $\rho_{PLA}$ and $\rho_{HAp}$ are 1.43 g•cm$^{-3}$ and 3.16 g•cm$^{-3}$, respectively[19].

## 3.2. Chemical composition

The changes in absorbance or absence of certain peaks in the FTIR spectra are presented in **Figure 4**. These absorption peaks can be attributed to functional groups that are present in HAp, in pure PLA, or in the composite material. Peaks and functional groups originating from PLA were located approximately at 2996 cm$^{-1}$ and 2945 cm$^{-1}$ ($CH_3$ stretching). The peaks at 1748 cm$^{-1}$,

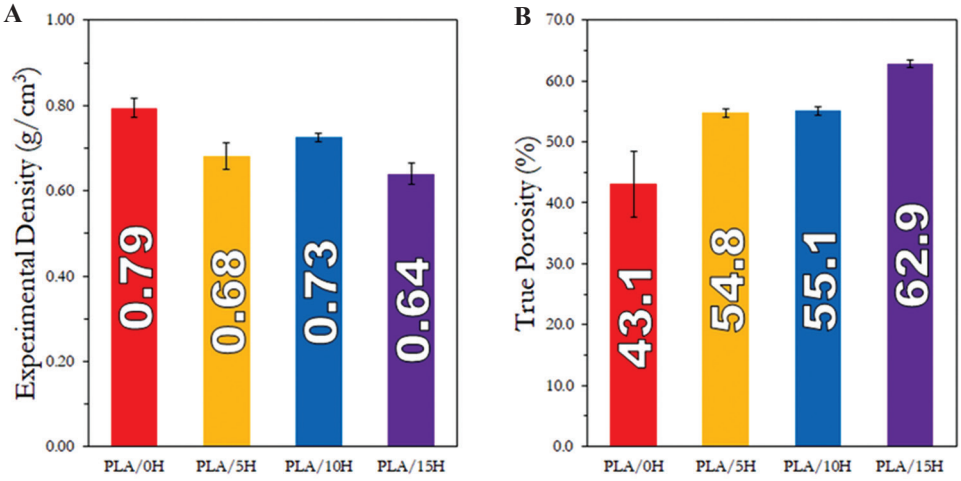


**Figure 3.** (A) Experimental density and (B) true porosity of the 3D printed polylactic acid /hydroxyapatite composites.

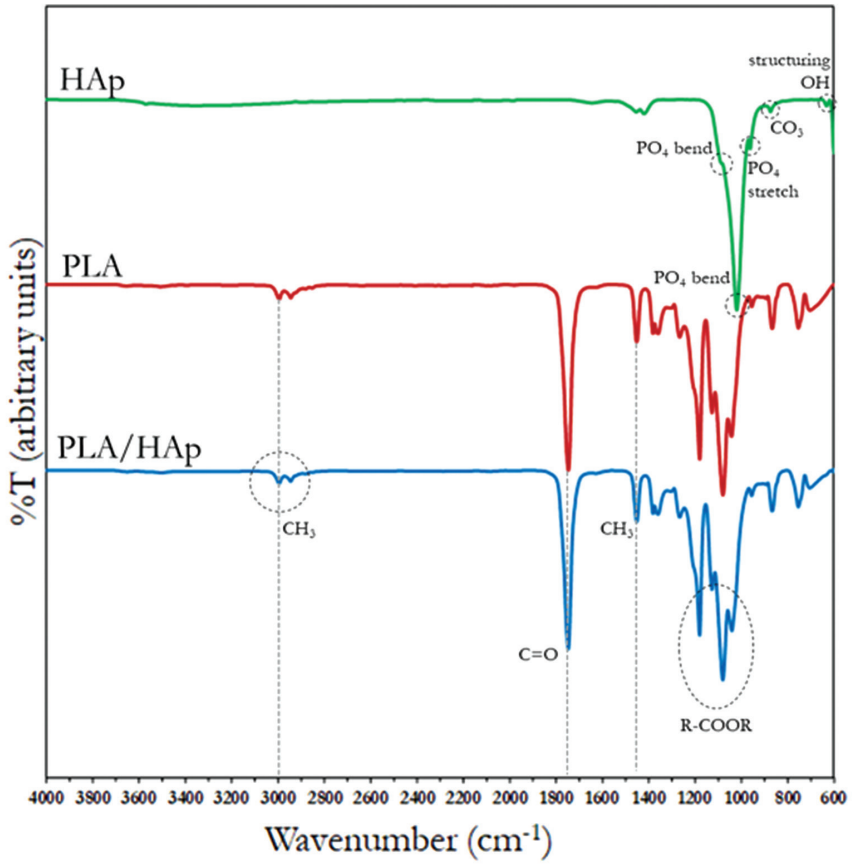


**Figure 4.** Fourier transform infrared spectra of hydroxyapatite (Hap), polylactic acid (PLA), and the 3D printed PLA/HAp composite (15 wt. %).

1181 $cm^{-1}$, 1127 $cm^{-1}$, and 1080 $cm^{-1}$ are identified as the backbone of ester groups of PLA[20]. Furthermore, 1748 $cm^{-1}$ pertains to C=O stretching vibrations[21], the peak at 1045 $cm^{-1}$ for the OH bending, while the 1200–1000 $cm^{-1}$ refers to C-O stretching[22].

Peaks coming from HAp are generally from phosphate groups, such as 1090 $cm^{-1}$, 1030 $cm^{-1}$, 600 $cm^{-1}$, and 565 $cm^{-1}$ ($PO_4$ bending), and 960 $cm^{-1}$ ($PO_4$ stretching). Carbonate ions were faintly present at 870 $cm^{-1}$[11,13]. The high calcining temperature of 1100°C in the HAp synthesis has caused the removal of water (as suggested by the absence of 3600–3200 $cm^{-1}$ OH stretch). The visibility of the structuring OH was identified at 635 $cm^{-1}$ fingerprint region, indicating a better powder-polymer

adhesion. However, the high calcination temperature might have also caused aggregation which prevented good dispersion of HAp powders in the PLA matrix[14]. The few prominent peaks of HAp were observed to be overlapped by the more intense peaks of PLA, approximately around 1100–900 $cm^{-1}$. Moreover, no new covalent bonds formed within the PLA/HAp composites, suggesting that the HAp fillers were embedded in the polymer matrix through mechanical manner rather than by chemical means.

### 3.3. Crystallinity

XRD of HAp, PLA, and the printed PLA/HAp biocomposites is shown in **Figure 5**. The HAp diffractogram displayed the crystalline nature of the powder. Prominent peaks and their corresponding planes were noted at approximately 26° (002), 33° (112), 47° (222), and 49° (213). The (211) plane at ca. 32° is inherent to and characteristic of pure HAp[12].

Pure PLA (PLA/0H) exhibited a broad spectrum indicating the amorphous structure of the polymer[23]. The composite samples exhibited diffraction peaks characterized by the presence of HAp in the polymer matrix. The peak intensity increases as a function of the increase in HAp powder loading.

### 3.4. Mechanical properties

The tensile stress-strain curve of PLA/HAp biocomposites is shown in **Figure 6A**. The HAp indeed had a reinforcing effect, as the elastic moduli and tensile strengths both increased compared to pure PLA. As the powder loading was increased, the elastic modulus increased compared to pure PLA (2.3–~3.5 GPa), but the modulus remained consistent despite the further increase in HAp loading (**Figure 6B**). Unsurprisingly, the tensile strength decreased at 15 wt% HAp loading as the powder loading increased. This may be primarily due to the HAp agglomeration and poor dispersion, as well as the formation of macro voids between neighboring filament beads. Nevertheless, HAp has shown to improve the strength of pure PLA (32.7–47.3 MPa). HAp might also act as nucleation sites where PLA molecule chains could have entangled itself through mechanical interlocking effects.

The stiffness of both PLA/10H and PLA/15H similarly generated 3.5 GPa elastic modulus which is within the range of the human cancellous bone tissue[15]; hence, these formulations have the potential for the repair of smaller bone tissues.

The fracture surface after the uniaxial tensile testing of PLA/HAp biocomposites are shown in

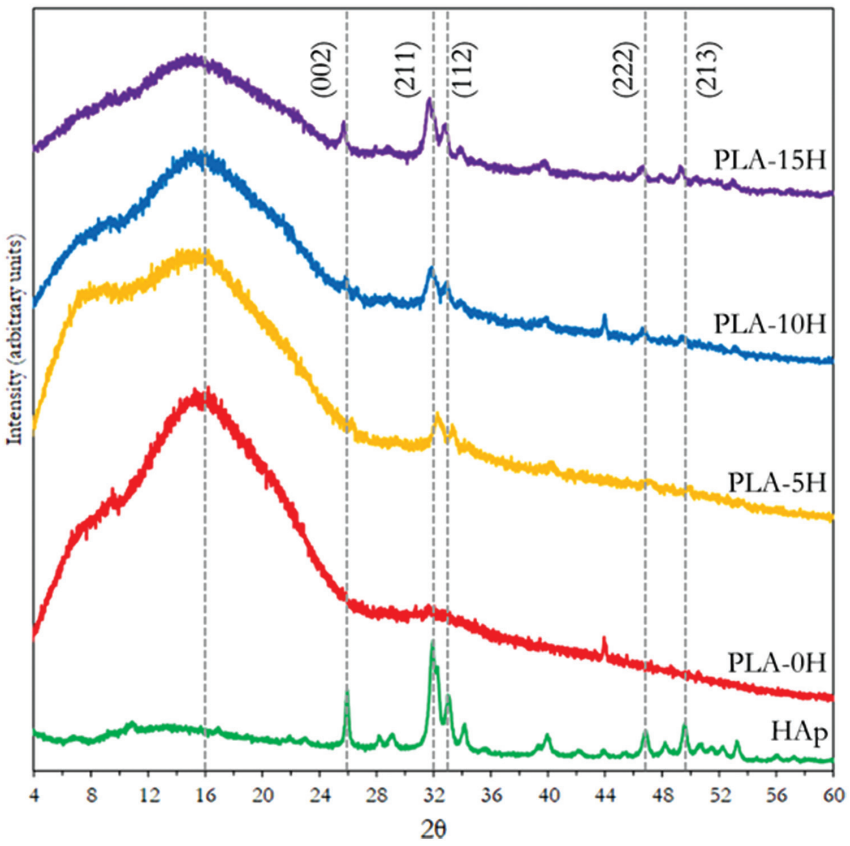


**Figure 5.** X-ray diffractograms of hydroxyapatite (HAp), and varying powder loading in 3D printed polylactic acid/HAp composites (0–15 wt. %).

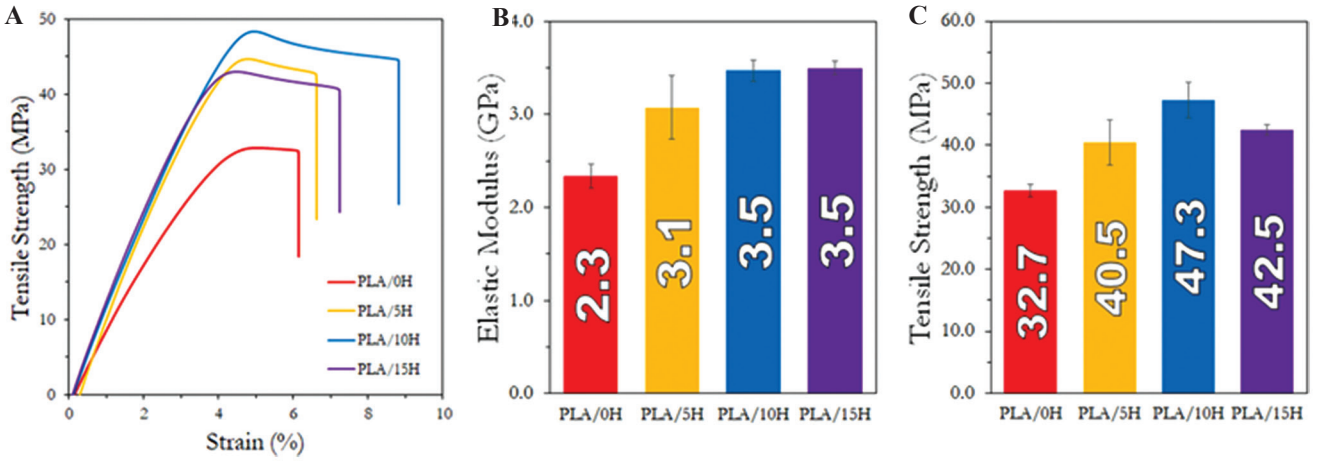


**Figure 6.** (A) Tensile stress-strain graph, (B) elastic moduli, and (C) tensile strength of the 3D printed polylactic acid/hydroxyapatite composites.

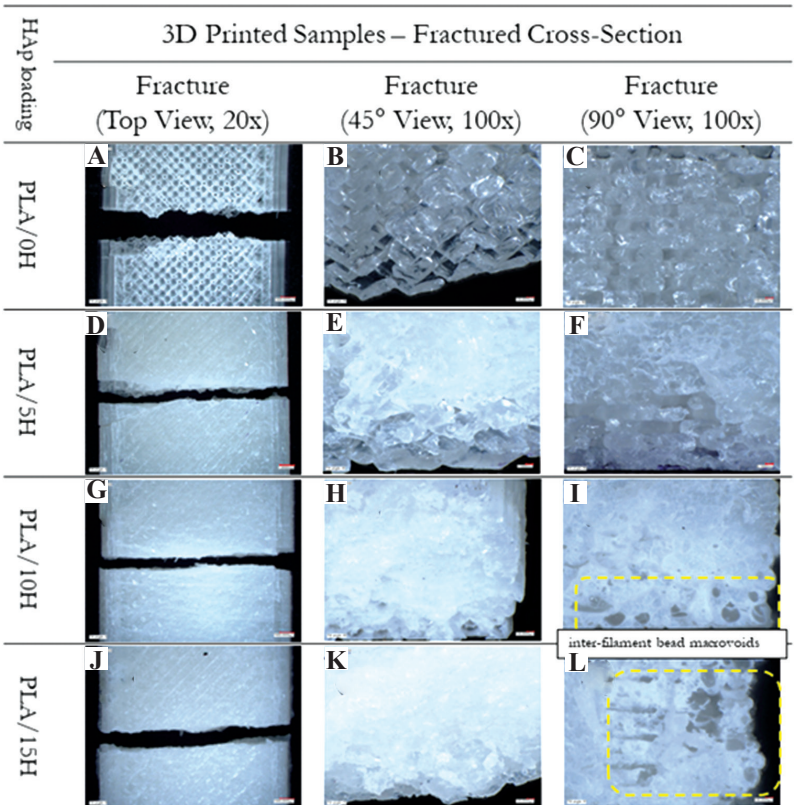


**Figure 7.** Fracture surfaces of the tensile-tested 3D printed polylactic acid (PLA)/hydroxyapatite composites. (A-C) PLA/0H; (D-F) PLA/5H; (G-I) PLA/10H; and (J-L) PLA/15H.

**Figure 7**. Fracture surfaces can provide knowledge and insight on the interaction between the matrix and reinforcement upon the application of force. The tensile-tested PLA/HAp composites exhibited linear, brittle fractures (**Figure 7D, G and J**), contrary to the somewhat irregular, moderately ductile fracture from the PLA/0H sample (**Figure 7A**). Furthermore, at higher magnifications (**Figure 7B, E and H, K**) the individual print beads were slowly disappearing as the HAp loading was increased. Evolution of macro voids or pores were also noticeable at higher magnifications (**Figure 7 I and L**). These macro voids account for the decreasing density and likewise increasing porosity from **Figure 3**. A plausible explanation can be attributed to the agglomeration of HAp particles,[15] which causes some areas to be denser and consequently

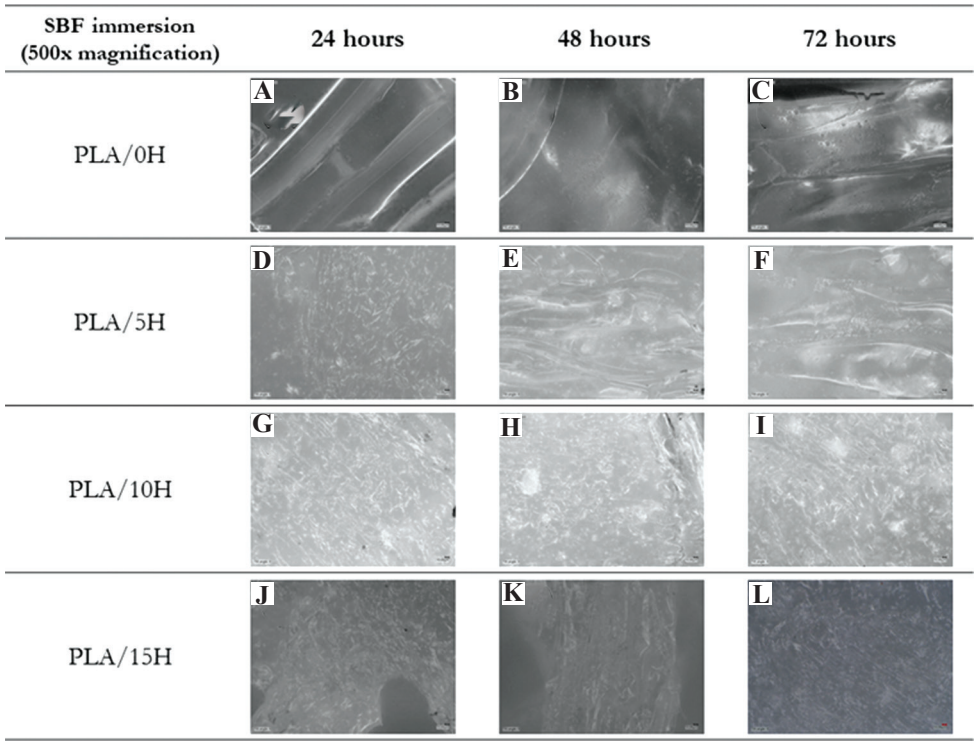


**Figure 8.** Digital micrographs of 3D printed polylactic acid/hydroxyapatite scaffolds immersed for 72 h in simulated body fluid for biomineralization activity.

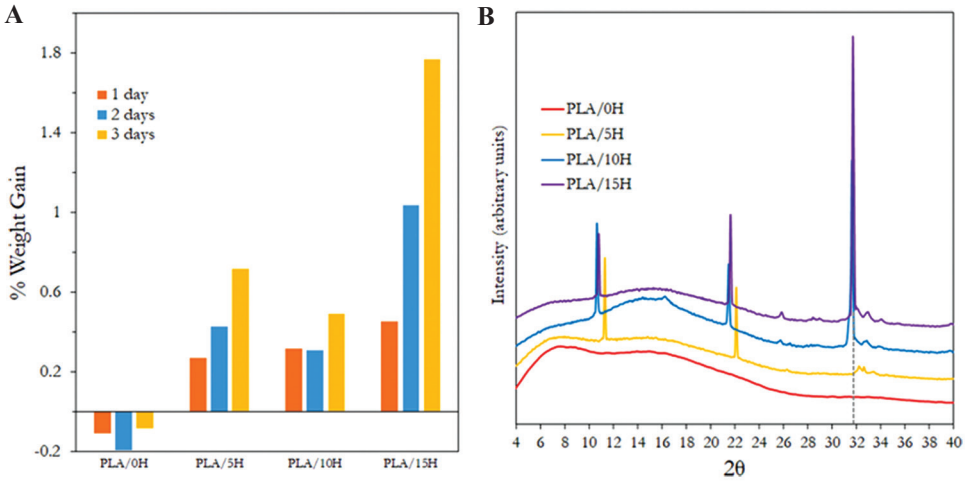


**Figure 9.** (A) Weight gain (%) and (B) X-ray diffractograms of the 3D printed polylactic acid/hydroxyapatite composites after the 72-h immersion test in SBF.

creating other sites with less material leading to void formation.

### 3.5. *In vitro* biomineralization

A preliminary *in vitro* bioactivity test was done by immersing the 3D printed PLA/HAp composite samples in SBF solutions for 24, 48, and 72 h, and the digital micrograph results are shown in **Figure 8**, while the percent weight gain and X-ray diffractograms are shown in **Figure 9A and B**, respectively. As seen on the digital micrographs, the 3D printed pure PLA (PLA/0H) exhibited an etching response to soaking in SBF. This was supported by the mass loss in **Figure 9A**. Pure PLA remains to be partly hydrophilic, and hence subjecting it to an aqueous immersion resulted to some PLA dissolving away.

The PLA/HAp composites reported varying weight gains, with the trend that was increasing. HAp particles

embedded within the PLA matrix served as nucleation sites for the deposition of calcium salts and apatite species present from the SBF solution. X-ray diffractograms shown in **Figure 9B** report of the evolution of peaks after the immersion in SBF for 72 h. The characteristic peak at 2θ ~32° confirm the growth of apatite species on the 3D printed samples during the immersion bioactivity[18]. Other well-defined peaks could be attributed to other salt species present in the SBF solution being deposited onto the 3D printed substrates.

## 4. Conclusion

The HAp used in this study was successfully synthesized as confirmed by the FTIR and XRD spectra. Pure PLA exhibited a broad infrared spectrum indicating the amorphous structure of the polymer. The 3D printed PLA/HAp composite samples exhibited XRD diffraction peaks characterized by the presence of HAp with the peak intensity increasing as a function of HAp powder loading. Moreover, composites' density decreases as the HAp loading was increased. The elastic modulus increased from 2.3 to 3.5 GPa and the tensile strength increased from 32.7 to 47.3 MPa with 15% HAp loading. The preliminary *in vitro* bioactivity test of the 3D printed PLA/HAp composite samples in SBF solutions for 24, 48, and 72 h indicated varying weight gains progressively as well as the evolution of XRD peaks. These indicate that HAp particles embedded within the PLA matrix served as nucleation sites for the deposition of calcium salts and apatite species present from the SBF solution.

## Author contributions

B.A.B. led the project and edited the paper. J.R.C., C.L.C., and P.J.M.B. designed the study. P.J.M.B. and S.R.C. performed the HAp synthesis and biomineralization, respectively. P.J.M.B. and C.L.C. performed the filament extrusion. C.L.C. performed most experiments, 3D printing, characterizations, data analysis, and wrote the paper with help from V.U. L. and J.R.C.

## Conflicts of interest

The authors declare that they have no conflicts of interest.

## Acknowledgments

We acknowledge the funding of this research project from the Department of Science and Technology – Grants-In-Aid (Department of Science and Technology [DOST]-GIA). We are also grateful for the technical support provided by the Advanced Device and Materials Testing Laboratory, and the Standards and Testing Division of the Industrial Technology Development Institute of the DOST, Philippines.

## References

1. Najmon JC, Raeisi S, Tovar A, 2019, Review of Additive Manufacturing Technologies and Applications in the Aerospace Industry. Additive Manufacturing for the Aerospace Industry. Elsevier Inc., Amsterdam, Netherlands. https://doi.org/10.1016/b978-0-12-814062-8.00002-9
2. Wiese M, Thiede S, Herrmann C, 2020, Rapid Manufacturing of Automotive Polymer Series Parts: A Systematic Review of Processes, Materials and Challenges. *Addit Manuf*, 36:101582. https://doi.org/10.1016/j.addma.2020.101582
3. Ng WL, Chua CK, Shen YF, 2019, Print Me An Organ! Why We Are Not There Yet. *Prog. Polym. Sci*., 97:101145. https://doi.org/10.1016/j.progpolymsci.2019.101145
4. Lee JM, Ng WL, Yeong WY, 2019, Resolution and Shape in Bioprinting: Strategizing Towards Complex Tissue and Organ Printing. *Appl. Phys. Rev*., 6:011307. https://doi.org/10.1063/1.5053909
5. Lao W, Li M, Wong TN, *et al*., 2020, Improving Surface Finish Quality in Extrusion-based 3D Concrete Printing Using Machine Learning-based Extrudate Geometry Control. *Virtual Phys Prototyp*, 15:178–93. https://doi.org/10.1080/17452759.2020.1713580
6. Ahmed ZY, Bos FP, van Brunschot MCA, *et al*., 2020, On-demand Additive Manufacturing of Functionally Graded Concrete. *Virtual Phys Prototyp*, 15:194–210. https://doi.org/10.1080/17452759.2019.1709009
7. Alizadeh-Osgouei M, Li Y, Wen C. 2019, A Comprehensive Review of Biodegradable Synthetic Polymer-ceramic Composites and their Manufacture for Biomedical Applications. *Bioact Mater*, 4:22–36. https://doi.org/10.1016/j.bioactmat.2018.11.003
8. Ng WL, Lee JM, Zhou M, *et al*., 2020, Vat Polymerization-based Bioprinting Process, Materials, Applications and Regulatory Challenges. *Biofabrication*, 12:022001. https://doi.org/10.1088/1758-5090/ab6034
9. Gayer C, Ritter J, Bullemer M, *et al*., 2019, Development of a solvent-free polylactide/calcium carbonate composite for selective laser sintering of bone tissue engineering scaffolds. *Mater Sci Eng C*, 101:660–73. https://doi.org/10.1016/j.msec.2019.03.101
10. Percoco G, Uva AE, Fiorentino M, *et al*., 2020, Mechanobiological Approach to Design and Optimize Bone Tissue Scaffolds 3D Printed with Fused Deposition Modeling: A Feasibility Study. *Materials* (*Basel*), 13: 648. https://doi.org/10.3390/ma13030648

11. Hassanajili S, Karami-Pour A, Oryan A, *et al*., 2019, Preparation and Characterization of PLA/PCL/HA Composite Scaffolds Using Indirect 3D Printing for Bone Tissue Engineering. *Mater Sci Eng C*, 104:109960. https://doi.org/10.1016/j.msec.2019.109960
12. Mondal S, Phuoc T, Pham VH, *et al*., 2019, Hydroxyapatite Nano Bioceramics Optimized 3D Printed Poly Lactic Acid Scaffold for Bone Tissue Engineering Application. *Ceram Int*, 46:1–13. https://doi.org/10.1016/j.ceramint.2019.10.057
13. Lopresti F, Pavia FC, Vitrano I, *et al*., 2020, Effect of Hydroxyapatite Concentration and Size on Morpho-mechanical Properties of PLA-based Randomly Oriented and Aligned Electrospun Nanofibrous Mats. *J Mech Behav Biomed Mater*, 101:103449. https://doi.org/10.1016/j.jmbbm.2019.103449
14. Pietrzykowska E, Mukhovskyi R, Chodara A, *et al*., 2019, Composites of Polylactide and Nano-Hydroxyapatite Created by Cryomilling and Warm Isostatic Pressing for Bone Implants Applications. *Mater Lett*, 236:625–8. https://doi.org/10.1016/j.matlet.2018.11.018
15. Prasad A, Bhasney S, Katiyar V, *et al*., 2017, Biowastes Processed Hydroxyapatite filled Poly (Lactic acid) Bio-Composite for Open Reduction Internal Fixation of Small Bones. *Mater Today Proc*, 4:10153–7. https://doi.org/10.1016/j.matpr.2017.06.339
16. Rodríguez K, Renneckar S, Gatenholm P, 2011, Biomimetic Calcium Phosphate Crystal Mineralization on Electrospun Cellulose-based Scaffolds. *ACS Appl Mater Interfac*, 3:681–9. https://doi.org/10.1021/am100972r
17. Hamzah MSA, Ng C, Zulkarnain NI, *et al*., 2020, Entrapment of Collagen on Polylactic Acid 3D Scaffold Surface as a Potential Artificial Bone Replacement. *Mater Today Proc*, 2020:263. https://doi.org/10.1016/j.matpr.2020.07.263
18. Alam F, Varadarajan KM, Kumar S, 2020, 3D Printed Polylactic Acid Nanocomposite Scaffolds for Tissue Engineering Applications. *Polym Test*, 81:106203. https://doi.org/10.1016/j.polymertesting.2019.106203
19. Nawawi AN, Alqap SF, Sopyan I, 2011, Recent Progress on Hydroxyapatite-based Dense Biomaterials for Load Bearing Bone Substitutes. *Recent Patents Mater Sci*, 4:63–80. https://doi.org/10.2174/1874464811104010063
20. Lizundia E, Vilas JL, León LM, 2015, Crystallization, Structural Relaxation and Thermal Degradation in Poly(l-lactide)/Cellulose Nanocrystal Renewable Nanocomposites. *Carbohydr Polym*, 123:256–65. https://doi.org/10.1016/j.carbpol.2015.01.054
21. Xu C, Chen J, Wu D, *et al*., 2016, Polylactide/Acetylated Nanocrystalline Cellulose Composites Prepared by a Continuous Route: A Phase Interface-property Relation Study. *Carbohydr Polym*, 146:58–66. https://doi.org/10.1016/j.carbpol.2016.03.058
22. Gazzotti S, Farina H, Lesma G, *et al*., 2017, Polylactide/Cellulose Nanocrystals: The *in situ* Polymerization Approach to Improved Nanocomposites. *Eur Polym J*, 94:173–84. https://doi.org/10.1016/j.eurpolymj.2017.07.014
23. Bhasney SM, Bhagabati P, Kumar A, *et al*., 2019, Morphology and Crystalline Characteristics of Polylactic Acid [PLA]/Linear Low Density Polyethylene [LLDPE]/Microcrystalline Cellulose [MCC] Fiber Composite. *Compos Sci Technol*, 171:54–61. https://doi.org/10.1016/j.compscitech.2018.11.028

RESEARCH ARTICLE

# A Novel Bespoke Hypertrophic Scar Treatment: Actualizing Hybrid Pressure and Silicone Therapies with 3D Printing and Scanning

**Lung Chow[1], Kit-lun Yick[1]*, Yue Sun[1,2], Matthew S. H. Leung[1], Mei-ying Kwan[1], Sun-pui Ng[3], Annie Yu[4], Joanne Yip[1], Ying-fan Chan[5]**

[1]Institute of Textiles and Clothing, The Hong Kong Polytechnic University, Hong Kong
[2]School of Fashion Design and Engineering, Zhejiang Sci-Tech University, Hangzhou
[3]Division of Science, Engineering and Health Studies, College of Professional and Continuing Education, The Hong Kong Polytechnic University, Hong Kong
[4]Department of Advanced Fibro Science, Kyoto Institute of Technology, Japan
[5]Department of Occupational Therapy, Prince of Wales Hospital, Hong Kong

**Abstract:** The treatment of hypertrophic scars (HSs) is considered to be the most challenging task in wound rehabilitation. Conventional silicone sheet therapy has a positive effect on the healing process of HSs. However, the dimensions of the silicone sheet are typically larger than those of the HS itself which may negatively impact the healthy skin that surrounds the HS. Furthermore, the debonding and displacement of the silicone sheet from the skin are critical problems that affect treatment compliance. Herein, we propose a bespoke HS treatment design that integrates pressure sleeve with a silicone sheet and use of silicone gel using a workflow of three-dimensional (3D) printing, 3D scanning and computer-aided design, and manufacturing software. A finite element analysis (FEA) is used to optimize the control of the pressure distribution and investigate the effects of the silicone elastomer. The result shows that the silicone elastomer increases the amount of exerted pressure on the HS and minimizes unnecessary pressure to other parts of the wrist. Based on this treatment design, a silicone elastomer that perfectly conforms to an HS is printed and attached onto a customized pressure sleeve. Most importantly, unlimited scar treating gel can be applied as the means to optimize treatment of HSs while the silicone sheet is firmly affixed and secured by the pressure sleeve.

**Keywords:** Surgical scars; Hypertrophic scars; Finite element analysis; 3D-printing; 3D-scanning

***Correspondence to:** Kit-lun Yick, Institute of Textiles and Clothing, The Hong Kong Polytechnic University, Hong Kong; tcyick@polyu.edu.hk

**Received:** November 24, 2020; **Accepted:** December 30, 2020; **Published Online:** January 25, 2021

**Citation:** Chow L, Yick KL, Sun Y, *et al*., 2021, A Novel Bespoke Hypertrophic Scar Treatment: Actualizing Hybrid Pressure and Silicone Therapies with 3D Printing and Scanning. *Int J Bioprint*, 7(1):327. http://doi.org/10.18063/ijb.v7i1.327

## 1. Introduction

Wound healing is a complicated process that can be described as the restitution of natural anatomical relationships and physiological integrity of the injured tissues[1]. The wound healing process can be divided into overlapping phases with reference to the phase of recovery, including hemostasis, inflammation, proliferation, and remodeling. Hemostasis occurs immediately after the tissue or capillary blood vessels are damaged. The platelet degranulation creates a hemostatic plug to prevent the blood loss. With aid of the coagulation factors, the plug can be further stabilized by platelet aggregation and the formation of fibrin scaffold which are driven by the enzymatic cascade[1,2]. The second phase of wound healing is inflammation which occurs around the 5 days after the injury. In this phase, the immune system is triggered to activate the inflammatory reactions to prevent infection. Neutrophils and macrophages are recruited to remove any invading bacteria or foreign debris[3]. The third phase is the proliferation which occurs around 5 – 10 days after the injury and may last for 3 – 6 weeks. The main

feature of this phase is the granulation tissue formation which includes fibroblasts, myofibroblasts, loose connective tissue, and capillaries. Extracellular matrix is excessively produced by fibroblasts and myofibroblasts for structural support for nascent capillaries which results in hypertrophic scars (HSs) formation[4-6]. At the end of this phase, the wound becomes an immature scar which is fragile and has a low tensile strength. The last phase of wound healing is the remodeling which turns the immature scar into a mature scar and this phase can last for 2 years. The excessive extracellular matrix is remodeled from the weak and disordered type III collagen into the stronger and more ordered type I collagen by matrix metalloproteinases. With the passage of time, the scar will be flattened because the newly synthesized collagen is weaved into the stable fibrils. Furthermore, the cellularity and vascularity of wound will be reduced due to the activity of matrix metalloproteinases[7].

Due to the protrude and erythematous appearance of the hypertrophic scarred skin, the quality of life of HS patients can even be significantly affected[8] as the scarring may reduce self-esteem or even affect the mental health of the patient due to their esthetically unpleasing appearance[9]. This problem is more obvious in female patients than male patients[8]. Apart from cosmetic issues, inappropriately managed HSs can cause functional difficulties; for instance, a limited range of motion is commonly found due to the reduced elasticity of the skin and HS hardened tissues[10]. The low elasticity of hypertrophic scarred skin is due to less elastin production in comparison to normal tissue[11,12]. Therefore, HSs can be said to be the most challenging problem in wound healing and rehabilitation process. In 2015, 67 million burn injuries were caused by fire and other sources of high heat worldwide and around 70% of burn patients develop an HS[13]. Another study also found that more than 70% of the patients in Hong Kong form an HS after surgery[14]. The high prevalence of HS formation with a lengthy treatment process can be a heavy burden on health care systems. In the United States, the cost for treating and managing scars is estimated at around US$ 20 billion every year[15].

Pressure, silicone sheet, and silicone gel therapies are the most common non-invasive treatments for HSs. For decades, pressure therapy has been used to accelerate the maturation of HSs and improve their appearance[16,17]. A number of studies conclude that exerting a continuous pressure of about 25 mmHg can inhibit the growth of HSs and encourage their maturation[16,18-21]. This is because exerted pressure may reduce the blood flow to the hypertrophic scarred tissues so as to limit nutrients and oxygen supply to the tissues, thereby effectively reducing the production of collagen[22,23]. Therefore, pressure garments should always be worn for optimal treatment results except when the patient is bathing or the garment needs to be washed[24]. Silicone sheet therapy is the application of a thin silicone sheet onto the HS which increases the skin temperature, hydrates the scar, and facilitates the polarization of scar tissues, thus contributing to a reduction of the HS[25-31]. Furthermore, silicone sheets can be used as a protective barrier against the external environment to prevent secondary damage or infection of the scar[27,32]. The differences between silicone sheets and silicone gel are the degree of crosslinking and polymerization. Silicone sheets have a longer and stronger polymer chain; therefore, they cannot be spread onto skin like silicone gel[26]. Although proven to be effective treatments for HSs, pressure therapy, silicone sheets, and silicone gel have their inherent limitations. For example, the complexities of the human body shape is a barrier for the pressure garments to exert pressure onto the concave parts of the body[33]. Moreover, silicone sheets do not work well on joints, such as elbows and knees, because they might debond from the body part during movement that requires joint use and a large range of motion. Although it is not a burden for the patients to apply the silicone gel twice a day, it is important to note that the gel might be easily wiped off during daily activities. Therefore, clinicians need to consider the location of the HS and determine which treatment should be used to obtain maximum treatment efficacy. In some cases, the treatments can be combined; for instance, silicone sheets and pressure therapy are often used together and proven to provide a better effect in reducing scar thickness and increasing scar pliability[26,34,35]. However, the size of the silicone sheet is usually larger than that of the HS to ensure that it is securely adhered to the skin, which may have negative impacts when covering healthy skin[26]. The negative impacts include excessive sweating, pruritus or even contact dermatitis[26,36]. To date, there have been few quantitative studies done on integrating pressure, silicone sheets, and silicone gel as a form of treatment to control the abnormal growth of hypertrophic scarred tissues.

The advancement of three-dimensional (3D) printing, 3D scanning and computer-aided design, and manufacturing software has led to a variety of applications in the medical field, such as artificial implants, orthoses, and prostheses, which can be customized and 3D printed to fit the needs of individual patients[37-39]. For example, Kang *et al.*[40] demonstrated the ability of creating vascularized cell-laden bone constructs with tunable mechanical properties using integrated tissue-organ printer. It is worth noting that the 3D printed face shields play a significant role during the outbreak of the COVID-19 in 2019[41,42]. Hale *et al.*[43] also developed bespoke orthoses for neck stability using 3D printing and scanning technologies. To improve the control over the pressure distribution or heat transfer of custom-engineered products, biomechanical

finite element models (FEMs) are commonly used to enhance the design of orthoses or prostheses through numerical simulation. For instance, Zolfagharian *et al*.[44] demonstrated the use of FE analysis (FEA) in the design of a patient-specific 3D-printed splint for mallet finger injury to ensure that the mechanical properties of the design meet the requirements but production consumes the least amount of material. These customized products first incorporated the geometric shape of the body part obtained through 3D scanning to cater to each patient based on his/her needs. After that, FEA can be adopted to modify the design to enhance the performance of the product based on the material properties of the 3D printed materials without any further trial and error fittings, thus minimizing the volume of material waste during the design process.

In this study, we propose a novel framework to manufacture a bespoke garment for HSs using a workflow of 3D scanning, 3D printing, FEA, and computer-aided design and manufacturing software. The 3D printed silicone insert which conforms to the profile of the HS is attached to a pressure garment to eliminate the problem of its displacement. Hence, scar treating gel can be applied with a silicone insert, thus helping patients toward a quicker recovery. The integration of pressure, silicone sheet, and silicone gel therapies will surely open new paths of development in HS treatment. A female participant was invited for a clinical study to observe the feasibility of the suggested therapy. Our proposed framework is also valuable for different types of customized products in the clinical field.

## 2. Materials and methods

### 2.1. Details of clinical case

A 51-year-old female patient with a body mass index of 21.5 kg/m$^2$ who has undergone surgical operation on her right wrist was recruited for the study. The patient has given her written informed consent to publish the pictures and her personal data. In December 2018, the patient suffered a radial bone fracture near her right wrist. During surgery, metal screws were applied to stabilize the radial during the healing process. About 1 month after surgery, an HS with a raised and dark red appearance developed on her hand. Afterward, she underwent silicone sheet therapy to increase scar maturation and improve the appearance of the HS. However, the silicone sheet frequently debonded. For example, the silicone sheet would debond when she sweated (wet skin), came into contact with other surfaces due to the friction (excessive friction between the silicone sheet with the desk when typing on a keyboard, or with the bed sheets while she slept at night). To address these problems, a bespoke HS treatment that combines pressure, silicone gel, and silicone sheet therapies was designed for the patient. During the study, she was ordered to wear a customized pressure sleeve with a silicone insert at all times except when she had to bathe or apply the silicone gel, which was done twice a day. The study was approved by the Human Subjects Ethics Sub-committee of The Hong Kong Polytechnic University (Reference Number: HSEARS20171214001) and Joint Chinese University of Hong Kong-New Territories East Cluster Clinical Research Ethics Committee (CREC Ref No: 2018.467).

### 2.2. Evaluation of current treatment

Current treatment with silicone sheets is problematic in that the silicone sheet debonds from the skin. To evaluate the adhesion between the silicone sheet and skin under different conditions, ASTM D5169 Standard Test Method for Shear Strength (Dynamic Method) of Hook and Loop Touch Fasteners was referenced and the Instron 5566 universal mechanical test frame was used. Pigskin was used to represent human skin, which was cleaned using a nonionic detergent and then padded dry with paper towel. The size of the specimens is 2.54 × 7.62 cm. The temperature of the wrist is approximately 34 – 36°C depending on the activity and the environment[45,46]. Testing was therefore carried out in a temperature-controlled chamber and the specimens were kept at a temperature of 35°C to simulate normal skin temperature. In the experiment, two different commercial silicone sheets, CICA-CARE and Mepiform®, were evaluated under four different skin conditions, which are normal dry skin and skin separately coated with three different types of scar care gels, which are SILBIONE BLEND 4001 (Elkem), Hiruscar®, and Contractubex®. The suggested dosage and mode of application are discussed as follows.

### 2.3. Design framework

**Figure 1** illustrates the overall design framework that involves the combination of three different types of therapies. The details will be discussed in the following sections.

#### *(1) Three-dimensional scanning and modeling*

The first and second steps of the design framework are to conduct 3D scanning and modeling (**Figures 1A and B**). The geometry of the wrist and shape of the HS of the patient was obtained using a structured light handheld 3D scanner (Artec Eva, Luxembourg). The scanner captures the texture and color of the scanned object which is convenient during the silicone insert modeling process to differentiate between the healthy skin and HS. The scanned data were registered using Artec Studio 13 and then imported into a 3D model processing software (3ds Max, Autodesk). To create a model that corresponds with the scar, a box object with a similar length and width

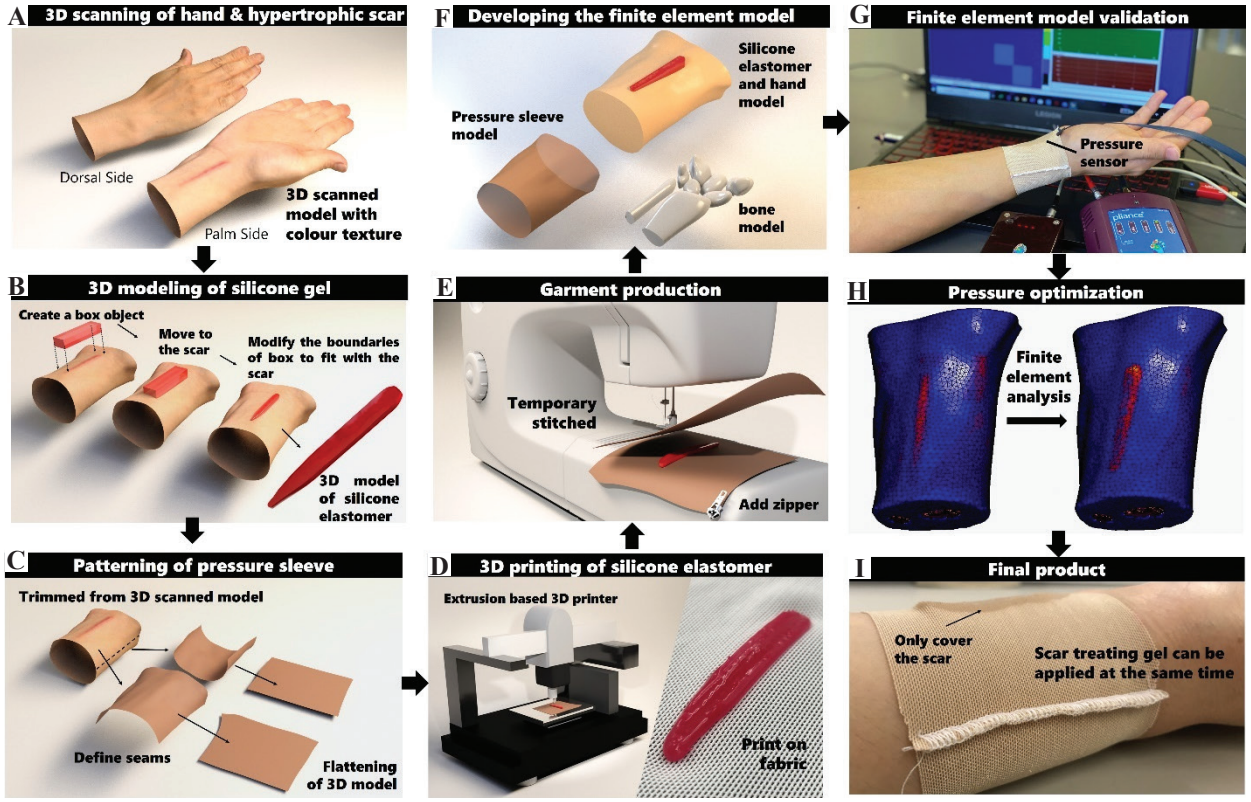


**Figure 1.** Schematic of workflow of patient specific pressure sleeve with silicone elastomer insert. (A) 3D scanning to obtain geometry and texture of hand and HS. (B) 3D modeling of a silicone elastomer which fits the HS. (C) Flattening of 3D model as pattern for pressure sleeve. (D) 3D printing of silicone elastomer on fabric by using extrusion-based 3D printer and photo of the printed silicone on fabric. (E) Producing pressure sleeve by applying stitches on the patterns. (F) Developing the FEM including the pressure sleeve, bone, silicone, and hand models. (G) Validation of the FEM for pressure through wear trial. (H) Pressure optimization through FEA. (I) Photo of the final pressure sleeve with customized silicone elastomer insert.

of the HS was first created and the thickness had to be larger than the height of the HS. Then, the box model was moved to the area where the HS was submerged into the box model. The boundaries of the box model were adjusted to the shape of the HS boundaries based on the scanned color of the HS and hand by moving the vertex or edges of the box model. Note that the number of length and width segments of the box model has to be adequate to carry out the boundary adjustment process. Once the boundaries of the silicone elastomer model fit with those of the HS, a Boolean operation can be done to subdivide the overlap volume of the silicone elastomer and hand model. The modeling process is shown in **Figure 1B**. The created model can be saved as a stereolithography (stl) file for the 3D printing process. Once the insert model was created, the coordinations of the model were rotated and adjusted to the proper position for the 3D printing of silicone onto fabric.

### *(2) 3D printing and patterning*

The third and fourth steps of the design framework are 3D printing of silicone elastomer on the pressure sleeve and the patterning of the pressure sleeve (**Figures 1C and D**). Before the silicone insert model was imported into the 3D-printer (3D-Bioplotter® Manufacturer Series), a slicing process was done to determine the number of printed layers and the path of printing for each layer. A biocompatible silicone elastomer (SILBIONE® RTV 4410 1:1 A&B) was mixed with 0.2 and 2 wt% of a silicone thickener (THI-VEXTM) and degassed respectively for the 3D printing process. The settings of the 3D printing process and the specifications of the warp knitted fabric are shown in **Supplementary Tables 1 and 2**, respectively. A multi-viscosity printing technique developed by our team was adopted. The silicone mixture with lower viscosity was extruded through the nozzle of the 3D printer and deposited onto the warp knitted fabric to improve the adhesion between the silicone and fabric. Apart from the first layer of printing, higher viscosity print mixture was adopted to maintain the form accuracy of the silicone part. The shear force of the sample constructed using the multi-viscosity technique was increased from about 10 to 60 N in comparison to normal printing approaches which should be sufficient

for the application[47]. Once the silicone insert was printed and cured on the fabric, it was ready for adherence to the pressure sleeve. The sleeve pattern was created using ExactFlat for Rhino 3D software based on the scanned geometry of the patient hand. The hand model was separated at the radial and ulnar sides of the wrist with two patterns. Since the created patterns are based on the scanned image of the hand geometry, no pressure can be exerted onto an HS and inhibit its growth. Therefore, a reduction of the sleeve circumference is required to create an effective level of pressure to treat the HS. In this study, a reduction factor of 10% was applied which is a common value for pressure garments [48,49]. After the patterns were reduced to the appropriate size, the patterns were stitched together in the fifth step of the workflow (**Figure 1E**).

***(3) Finite element analysis for pressure optimization***

After the pressure sleeve was produced, sub-models of the carpal bones, pressure sleeve, silicone elastomer, and hand were constructed using FEA software (MSC Marc/Mentat) (**Figure 1F**). The material properties of the hand, sleeve, and silicone were obtained with reference to the literature and the experimental results in Yu *et al*. and Wu *et al*.[50,51]. The material properties and parameters are listed in **Table S3**. To validate the accuracy of the FE contact model, the subject was invited to participate in a wear trial to measure the interface pressure produced by the pressure garment and silicone elastomer using the NOVEL Pliance X system (**Figure 1G**). The system has been objectively evaluated and validated for accuracy by different scholars[52,53]. In total, four positions were marked on the subject, including the center of the HS, and the ulnar, radial, and back of the hand which are horizontally aligned with the HS landmark. Through the FEA, the pressure distribution on the hand from the silicone elastomer samples with five different thicknesses of 1, 2, 3, 4, and 5 mm (the smallest thickness was considered) and two pressure sleeves with circumference reduction factors of 5% and 10% were systematically evaluated (**Figure 1H**). A pressure threshold of 25 mmHg was exerted onto the hypertrophic scarred area for effective treatment while preserving the wear comfort with the least amount of pressure on the other parts of the hand; this is as the optimal design criterion of the pressure sleeve (**Figure 1I**).

## 3. Results and discussion

### 3.1. Evaluation of current treatments

Conventionally, the silicone sheet applied onto an HSs is larger than the HS itself, especially with smaller scars. Otherwise, the silicone sheet would easily debond, causing inconvenience to the patient. Moreover, there are negative impacts, such as excessive sweating, when the silicone covers the healthy skin[26]. To minimize these unfavorable effects, we adopted 3D printing to fabricate a customized silicone elastomer so that it is the same size as the HS. The elastomer is directly attached to the pressure sleeve so that the debonding of the silicone sheet is remedied. **Figure 2A** shows the differences between a conventional silicone sheet and our 3D printed silicone elastomer.

Another issue that we observed about the silicone sheet is that it may not adhere to skin with just any type of scar treating gel. To further confirm this issue, we used ASTM D5169 to assess the adhesion between the silicone and skin under various conditions. The schematic of the test and photo of the sample are shown in **Figures 2B and C,** respectively. **Figure 2D** shows that when any random type of scar treating gel is used, lower shear forces results when compared to skin without the use of any treating gel. When comparing the effect of the three different types of gels, SILBIONE BLEND 4001 has a small effect on the shear force, while Hiruscar® has the worst performance. The pigskin samples that used Hiruscar® showed an approximately 3-fold and 8-fold reduction of the maximum shear force with the CICA-CARE and Mepiform® silicone sheets, respectively. This indicates that the application of scar treating gel can further aggravate the problem of silicone sheet debonding. The poor adhesion of the silicone sheet to gel-coated skin might be a possible challenge, so HS therapy that combines the use of a silicone sheet and silicone gel, such as an onion extract gel, has been seldom discussed in the literature. In our proposed therapy, the silicone elastomer is attached to the pressure sleeve which is secured by the corresponding pressure so that the adhesion of the silicone to the skin with silicone gel is not a problematic issue.

### 3.2. Finite element model and validation of simulated result

**Figure 3** illustrates the components of the developed FEM and the simulation process. The FEM simulates the wear process of the hand sleeve. The silicone elastomer was secured onto the model of the hand to prevent any unanticipated movement during the simulation process. Since the circumference of the pressure sleeve is smaller than that of the hand, a face load was applied on the shell elements of the pressure sleeve so that it stretched to fully fit and came into contact with the hand. During the stretching of the pressure sleeve, the sleeve was shifted toward the hand, and then the face load was applied. The pressure sleeve then recovered to its original size and came into contact with the silicone elastomer and the hand to simulate the pressure applied by the pressure sleeve. In this study, the friction between the hand and the fabric of the sleeve was neglected. The interface pressure produced by the pressure sleeve and silicone elastomer was observed at the end of the simulation. The

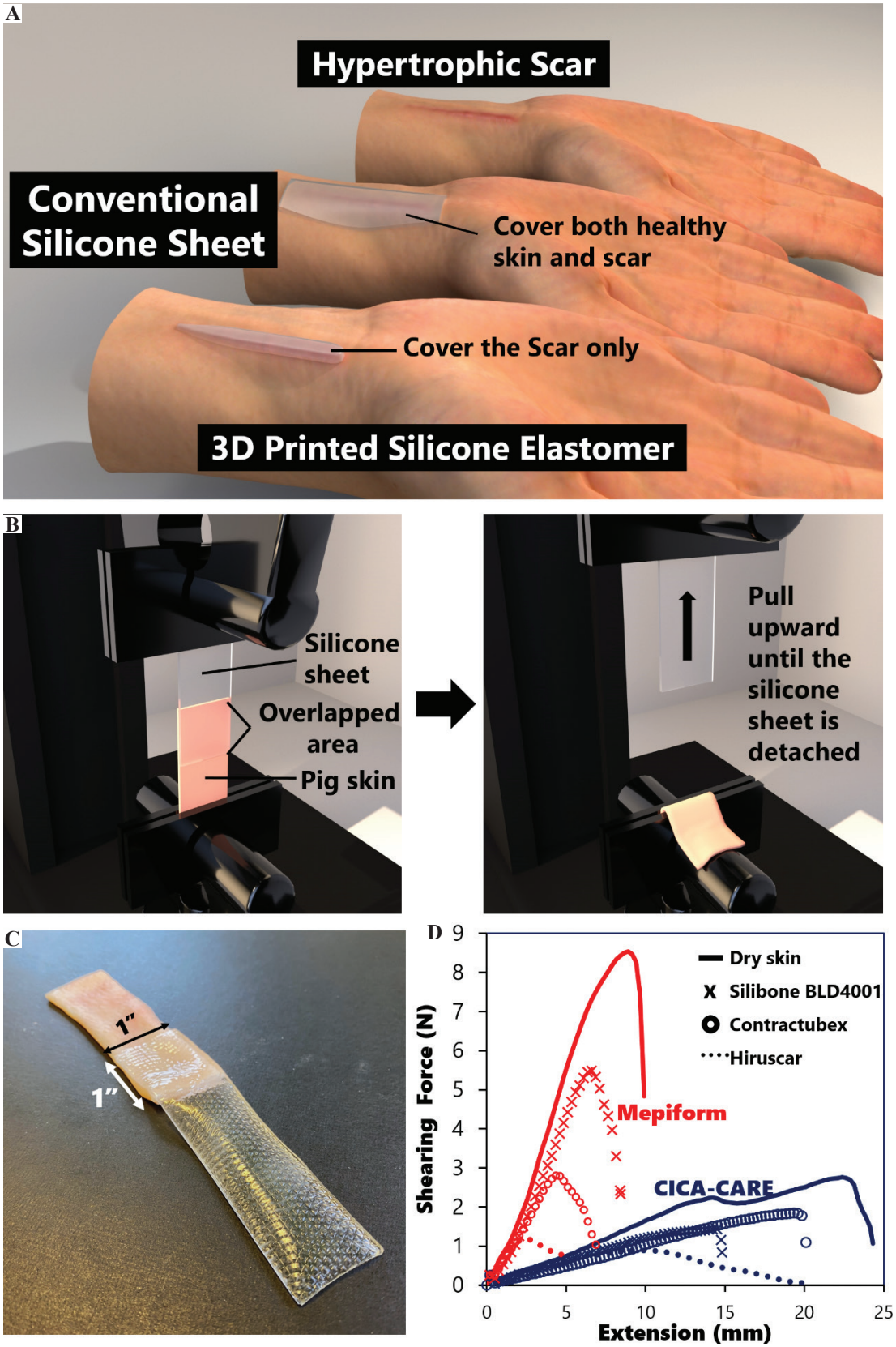


**Figure 2.** Evaluation of the silicone sheet therapy. (A) Illustration of the difference between conventional silicone sheet and 3D printed silicone elastomer on covered area. (B) Schematic of ASTM D5169 setup. (C) Photo of sample based on ASTM D5169. (D) Adhesion force of different silicone sheets (Mepiform® and CICA-CARE) under different skin conditions.

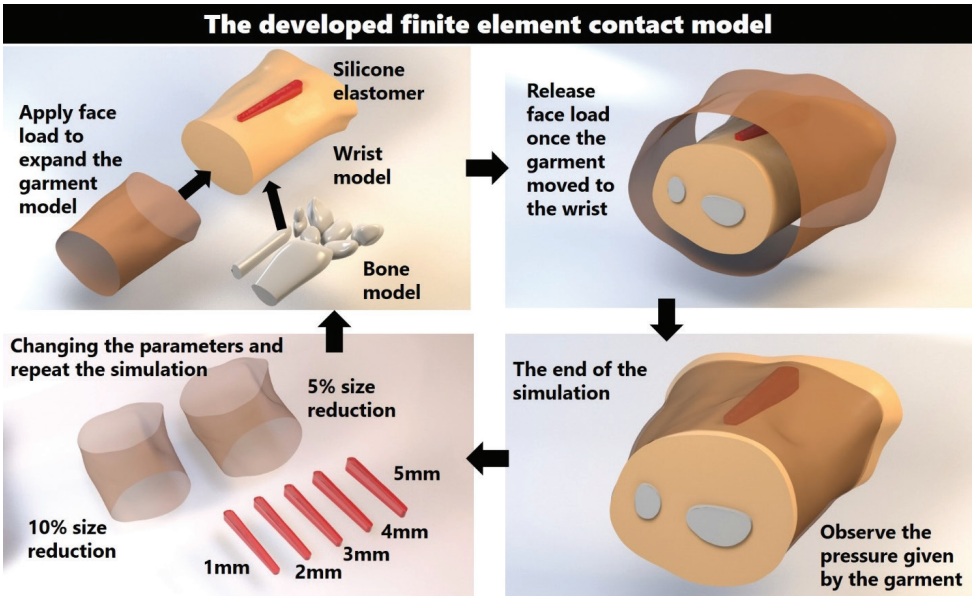


**Figure 3.** Illustration of the developed FEM for predicting the interface pressure.

sleeve size and the thickness of the silicone elastomer were adjusted before the next simulation was carried out until all the parameters were tested. To validate the accuracy of the FEM, the simulation result of a 2 mm thick silicone elastomer and a reduction factor of 10% of the sleeve were compared with the experimental result. The landmark positions are shown in **Figure 4A**. The experimentally obtained and simulated interface is compared in **Figure 4B**. The differences among the four different positions are within 5%, which is an acceptable margin of error to predict the amount of pressure.

### 3.3. Effect of silicone elastomer and garment size

The results of the simulated interface pressure that is exerted onto the HS, radial, ulnar, and back of the hand with the five different thicknesses of the silicone elastomer and two different pressure sleeve conditions are shown in **Figures 5A-D**, respectively. The interface pressure is proportional to the thickness of the silicone elastomer for both sleeve conditions (**Figure 5A**). A reduction factor of 10% in the circumference of the sleeve without the use of a silicone elastomer and a reduction factor of 5% with a 1 mm thick silicone elastomer show an exerted pressure of 20 mmHg onto the HS area. However, the pressure exerted onto the other areas with a reduction factor of 5% in the circumference of the sleeve along with a 1 mm thick silicone elastomer is significantly lower than the sleeve with a reduction factor of 10% in circumstance, with a decline of about 43% (radial and ulnar) and 50% (back). This indicates that customized 3D printed silicone elastomers can exert localized pressure onto the front side of the hand. The sleeve with a reduction factor of 5% also enables ease of wear and preserves the wear comfort in respect to the practical use of the pressure garment. When the garment size is much smaller than the body part, the patient will be not able to independently don the garment by him/herself and his/her skin might even get caught by the fastener. In considering the efficacy of treatment, we used a silicone elastomer with a thickness of 2 mm and a reduction factor of 5% of the circumference of the sleeve to exert approximately 25 mmHg of pressure onto the HS, as recommended in the literature. Compared to the treatment regimen of conventional pressure therapy that prescribes a reduction factor of 10% without the use of a silicone insert, the optimal pressure dosage applied to the HS here is on average about 20 – 25 mmHg. Furthermore, the pressure dosage on the other parts of the body is reduced by around 60%, 56%, and 80% for the ulnar, radial, and back of the hand, respectively, which result in reduced pressure discomfort. **Figure 6** shows the complete pressure distribution of the hand based on the treatment regimen of conventional therapy and the optimized parameters in this study. The literature on pressure garment therapy indicates that when the pressure dosage exceeds 30 – 40 mmHg, discomfort, and potential harm to the body part, such as maceration and paresthesia may occur[26,54-56]. To prevent these issues, the insertion of a silicone elastomer into a garment with a reduction factor of 10% and the insertion of a silicone elastomer with a thickness of 4 mm or more into a garment with a reduction factor of 5% should be avoided when the mechanical properties of the fabric used are similar to those in this study. The plotted force extension of the warp knitted fabric is shown in **Supplementary Figure 1.**

### 3.4. Demonstration of the combined therapies

**Figure 7** demonstrates the appearance of the HS before the patient underwent the prescribed combined therapy in

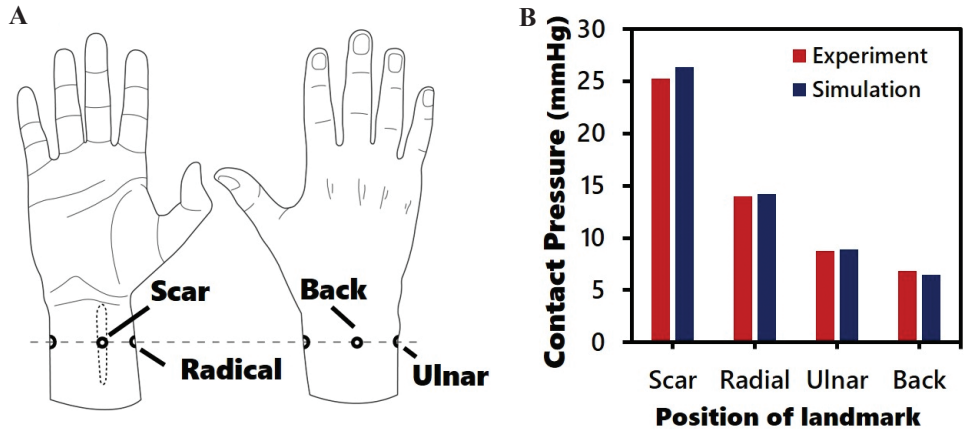


**Figure 4.** Validation of the developed FEM. (A) Illustration of the positions for pressure testing using pressure sensor. (B) Comparison of experimental and simulated results of pressure level.

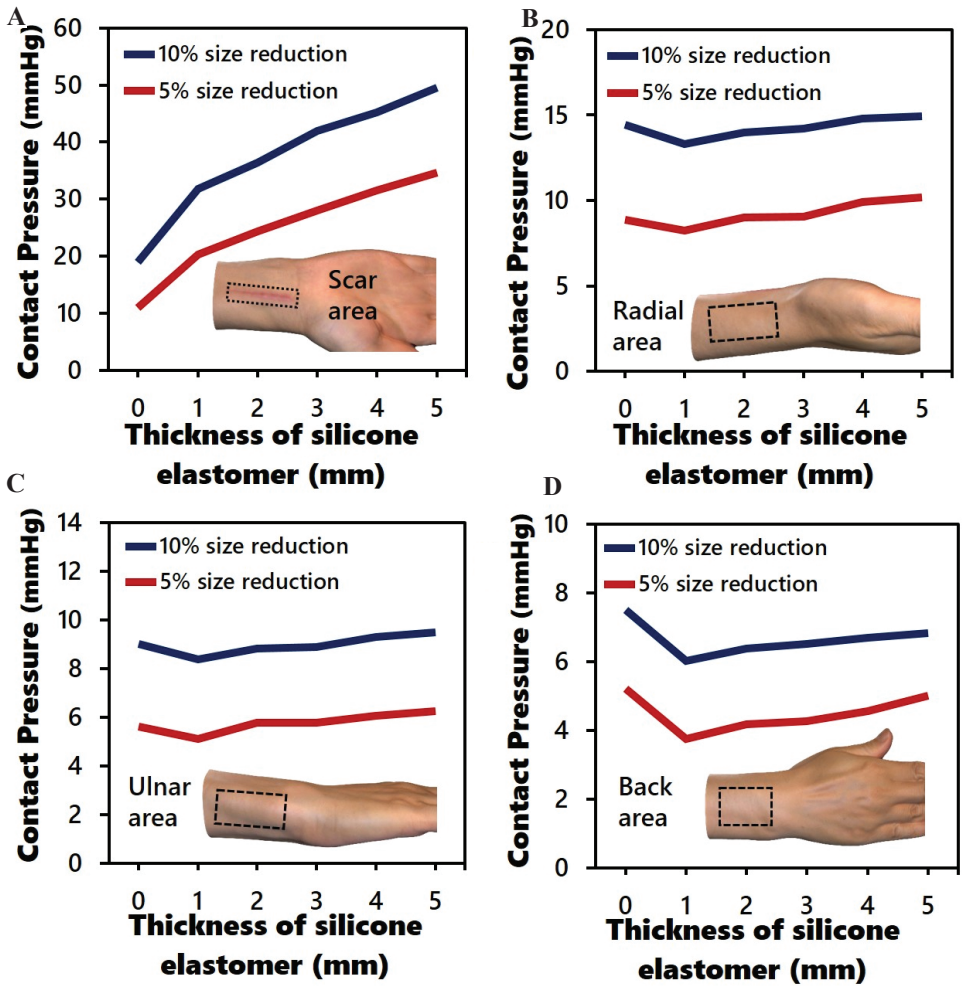


**Figure 5.** Simulated average interface pressure with different thicknesses of silicone elastomer (0 – 5 mm) and circumferences of sleeve (reduction factors of 5% and 10%) on various regions of hand: (A) scar area; (B) radial; (C) ulnar; and (D) back of hand.

this study, and after 1 year of following the therapy. The sleeve was worn for at least 23 h each day and silicone gel was applied twice a day. It can be clearly observed that the HS was reduced in thickness and pigmentation, thus showing an improved appearance. The problem of the debonding of the silicone sheet was resolved so

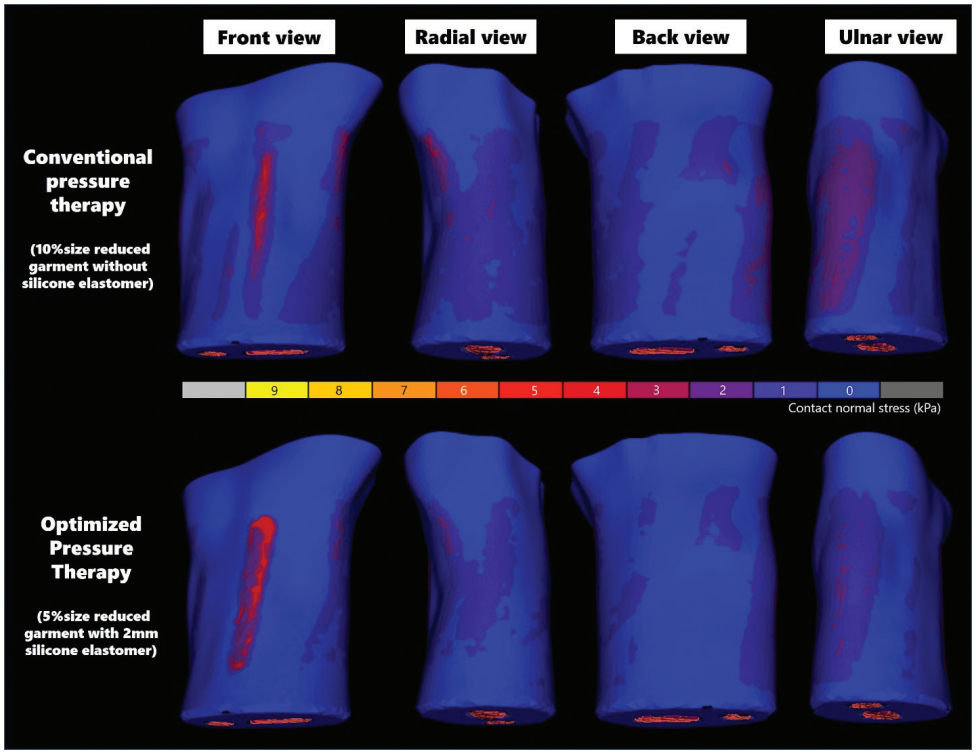


**Figure 6.** Comparison of pressure distribution provided by optimal size of pressure sleeve and silicone elastomer versus conventional pressure sleeve.


**Figure 7.** Effect of combined therapies for HS including the use of silicone sheet, silicone gel, and pressure.

that the negative effect of the treatment was minimized. The patient reported that the placement of the silicone elastomer remained securely attached even during a badminton game and she did not experience any negative impacts in comparison to conventional silicone sheet treatment. Since HS treatment usually requires more than a year, the tension of the fabric of the pressure garment can gradually decline, resulting in a lower level of pressure exerted. Therefore, it is suggested that the level of pressure should be monitored every 3 months to ensure treatment efficacy. If the amount of induced pressure significantly declines, the pressure garment will need to be adjusted or a new garment will need to be prescribed. Although the application of this combined therapy can reduce the scar thickness and pigmentation, further investigation of the effect of the use of the silicone sheet, silicone gel, and pressure as a form of combined therapy should be conducted through randomized clinical trials in the future.

## 4. Conclusion

Conventional silicone sheet treatment has a positive effect in the healing process of HSs. However, the debonding of the silicone sheet may affect the treatment compliance and therefore the treatment efficacy. In this study, we found that the scar treating gel reduces the adhesion of the silicone sheet. Therefore, using both

silicone sheet and scar treating gel is not recommended for treatment of HSs. Instead, we propose a novel bespoke HS treatment involving a combination of 3D scanning, 3D printing, FEA, computer-aided design, and manufacturing software. The 3D printed silicone elastomer that only covers the HS itself is secured to a bespoke pressure sleeve. Since the silicone sheet is secured by the pressure from the sleeve, any type of scar treating gel can be applied at the same time. Using an FEA, the pressure dosage for the HS can be accurately modified, which in this case, is approximately 25 mmHg for the effective management of HS. Most importantly, the unnecessary pressure exerted on normal skin can be reduced by approximately 60%, 56%, and 80% at the ulnar, radial, and back of the hand, respectively. In this case study, the suggested treatment provides a significant effect in reducing the scar thickness and pigmentation. Also, there is no adverse effects of the hybrid pressure and silicone therapy found. The developed design framework and production of the pressure garment can contribute to new insights for future HS therapies and new customized clinical products for scars.

## Acknowledgments

We acknowledge the financial support of the Research Grant Council for funding this research project (project account PolyU 152097/18E).

## Conflicts of interest

The authors report no potential conflicts of interest.

## Author contribution

L.C. designed the workflow, methodology, data curation and prepared the original draft of the manuscript and figures. Co-authors Y.S., M.S.H.L and M.Y.K involved in the investigation and analysis of results. K.L.Y. supervised and administered the project. K.L.Y., S.P.N, A.Y., J.Y. and Y.F.C. acquired the project funding, and reviewed and edited the manuscript.

## Ethics approval and consent to participate

This study was approved by the Human Subjects Ethics Sub-committee of The Hong Kong Polytechnic University and Joint Chinese University of Hong Kong-New Territories East Cluster Clinical Research Ethics Committee. Written informed consent was obtained from the participant before data collection.

## Consent for publication

The patient provided written informed consent to publish the pictures and her personal data.

## References

1. Ogawa R, 2020, Total Scar Management : From Lasers to Surgery for Scars, Keloids, and Scar Contractures. Springer, Singapore. https://doi.org/10.1007/978-981-32-9791-3
2. Tredget EE, Nedelec B, Scott PG, *et al*., 1997, Hypertrophic Scars, Keloids, and Contractures: The Cellular and Molecular Basis for Therapy. *Surg Clin North Am*, 77(3):701–30. https://doi.org/10.1016/s0039-6109(05)70576-4
3. Grose R, Werner S, 2004, Wound-healing Studies in Transgenic and Knockout Mice. *Appl Biochem Biotechnol Part B Mol Biotechnol*, 28(2):147–66. https://doi.org/10.1385/mb:28:2:147
4. Son D, Harijan A, 2014, Overview of Surgical Scar Prevention and Management. *J Korean Med Sci*, 29(6):751–7. https://doi.org/10.3346/jkms.2014.29.6.751
5. Enoch S, Leaper DJ, 2008, Basic Science of Wound Healing. *Surgery* (*Oxford*), 26(2):31–7. https://doi.org/10.1016/j.mpsur.2007.11.005
6. Werner S, Krieg T, Smola H, 2007, Keratinocyte-fibroblast Interactions in Wound Healing. *J Investig Dermatol*, 127(5):998–1008. https://doi.org/10.1038/sj.jid.5700786
7. Nagase H, Woessner JF, 1999, Matrix Metalloproteinases. *J Biol Chem*, 274(31):21491–4. https://doi.org/10.1074/jbc.274.31.21491
8. Bock O, Schmid-Ott G, Malewski P, *et al.*, 2006, Quality of Life of Patients with Keloid and Hypertrophic Scarring. *Arch Dermatol Res*, 297(10):433–8. https://doi.org/10.1007/s00403-006-0651-7
9. Mazharinia N, Aghaei S, Shayan Z, 2007, Dermatology life quality index (DLQI) scores in burn victims after revival. *J Burn Care Res*, 28(2):312–7. https://doi.org/10.1097/bcr.0b013e318031a151
10. Kwan P, Hori K, Ding J, *et al.*, 2009, Scar and Contracture: Biological Principles. *Hand Clin*, 25(4):511–28. https://doi.org/10.1016/j.hcl.2009.06.007
11. van Vlimmeren MA, Driessen-Mol A, van Den Broek M, *et al.*, 2010, Controlling matrix formation and cross-linking by hypoxia in cardiovascular tissue engineering. *J Appl Physiol* (*Bethesda, Md. 1985*), 109(5):1483. https://doi.org/10.1152/japplphysiol.00571.2010
12. Teekakirikul P, Eminaga S, Toka O, *et al.*, 2010, Cardiac Fibrosis in Mice with Hypertrophic Cardiomyopathy is Mediated by Non-myocyte Proliferation and Requires Tgf-[Beta]. *J Clin Investig*, 120(10):3520–9.

https://doi.org/10.1172/jci42028

13. Kassebaum NJ, Arora M, Barber RM, *et al.*, 2016, Global, Regional, and National Disability-adjusted Life-years (DALYs) for 315 Diseases and Injuries and Healthy Life Expectancy (HALE), 1990-2015: A Systematic Analysis for the Global Burden of Disease Study 2015. *Lancet*, 388(10053):1603–58. https://doi.org/10.3410/f.726827339.793524296
14. Li-Tsang CW, Lau JC, Chan CH, 2005, Prevalence of Hypertrophic Scar Formation and its Characteristics among the Chinese Population. *Burns*, 31(5):610–6. https://doi.org/10.1016/j.burns.2005.01.022
15. Block L, Gosain A, King TW, 2015, Emerging Therapies for Scar Prevention. *Adv Wound Care* (*New Rochelle*), 4(10):607–614. https://doi.org/10.1089/wound.2015.0646
16. Puzey G, 2002, The Use, of Pressure Garments on Hypertrophic Scars. *J. Tissue Viability*, 12(1):11–5. https://doi.org/10.1016/s0965-206x(02)80004-3
17. Perkins K, Davey R, Wallis K, 1983, Silicone Gel: A New Treatment for Burn Scars and Contractures. *Burns*, 9(3):201–4. https://doi.org/10.1016/0305-4179(83)90039-6
18. Leung P, Ng M, 1980, Pressure Treatment for Hypertrophic Scars Resulting from Burns. *Burns*, 6(4):244–50. https://doi.org/10.1016/s0305-4179(80)80007-6
19. Rivers E, Strate R, Solem L, 1979, The Transparent Face Mask. *Am J Occup Ther*, 33(2):108–13.
20. Staley MJ, Richard RL, 1997, Use of Pressure to Treat Hypertrophic Burn Scars. *Adv Wound Care*, 10(3):44–6.
21. Ai JW, Liu JT, Pei SD, *et al.*, 2017, The Effectiveness of Pressure Therapy (15-25 mmHg) for Hypertrophic Burn Scars: A Systematic Review and Meta-analysis. *Sci Rep*, 7(1):40185. https://doi.org/10.1038/srep40185
22. Wolfram D, Tzankov A, Pülzl P, *et al.*, 2009, Hypertrophic Scars and Keloids a Review of Their Pathophysiology, Risk Factors, and Therapeutic Management. *Dermatol Surg*, 35(2):171–81. https://doi.org/10.1111/j.1524-4725.2008.34406.x
23. Klöti J, Pochon J, 1982, Conservative Treatment Using Compression Suits for Second and Third Degree Burns in Children. *Burns*, 8(3):180–7. https://doi.org/10.1016/0305-4179(82)90085-7
24. Pratt J, 1995, In: West G, Withinshaw B, editors. Pressure Garments: A Manual on Their Design and Fabrication. 1st ed. Butterworth-Heinemann, Oxford, Boston.
25. Hoeksema H, De Vos M, Verbelen J, *et al.*, 2013, Scar Management by Means of Occlusion and Hydration: A Comparative Study of Silicones Versus a Hydrating Gel-cream. *Burns*, 39(7):1437–48. https://doi.org/10.1016/j.burns.2013.03.025
26. Van den Kerckhove E, Stappaerts K, Boeckx W, *et al.*, 2001, Silicones in the Rehabilitation of Burns: A Review and Overview. *Burns*, 27(3):205–14. https://doi.org/10.1016/s0305-4179(00)00102-9
27. Gilman TH, 2003, Silicone Sheet for Treatment and Prevention of Hypertrophic Scar: A New Proposal for the Mechanism of Efficacy. *Wound Repair Regen*, 11(3):235–6. https://doi.org/10.1046/j.1524-475x.2003.11313.x
28. Ko WJ, Na YC, Suh BS, *et al.*, 2013, The Effects of Topical Agent (kelo-cote or contractubex) Massage on the Thickness of Post-burn Scar Tissue Formed in Rats. *Arch Plast Surg*, 40(6):697–704. https://doi.org/10.5999/aps.2013.40.6.697
29. Berman B, Perez OA, Konda S, *et al.*, 2007, A Review of the Biologic Effects, Clinical Efficacy, and Safety of Silicone Elastomer Sheeting for Hypertrophic and Keloid Scar Treatment and Management. Malden, USA, pp. 1291–303. https://doi.org/10.1111/j.1524-4725.2007.33280.x
30. Saulis AS, Chao JD, Telser A, *et al.*, 2002, Silicone Occlusive Treatment of Hypertrophic Scar in the Rabbit Model. *Aesthetic Surg J*, 22(2):147–53. https://doi.org/10.1067/maj.2002.123023
31. Li-Tsang CW, Lau JC, Choi J, *et al.*, 2006, A Prospective Randomized Clinical Trial to Investigate the Effect of Silicone Gel Sheeting (Cica-Care) on Post-traumatic Hypertrophic Scar among the Chinese Population. *Burns*, 32(6):678–83. https://doi.org/10.1016/j.burns.2006.01.016
32. Puri N, Talwar A, 2009, The Efficacy of Silicone Gel for the Treatment of Hypertrophic Scars and Keloids. *J Cutan Aesthet Surg*, 2(2):104–6. https://doi.org/10.4103/0974-2077.58527
33. Yu A, Yick KL, Ng SP, *et al.*, 2016, Orthopaedic Textile Inserts for Pressure Treatment of Hypertrophic Scars. *Textile Res J*, 86(14):1549–62. https://doi.org/10.1177/0040517515573409
34. Li-Tsang CW, Zheng YP, Lau JC, 2010, A Randomized Clinical Trial to Study the Effect of Silicone Gel Dressing and Pressure Therapy on Posttraumatic Hypertrophic Scars. *J Burn Care Res*, 31(3):448–57. https://doi.org/10.1097/bcr.0b013e3181db52a7
35. Muangman P, Kongkor A, Namviriyachote N, *et al.*, 2020, Effectiveness of Silicone Gel Combined with Pressure Garment for Prevention of Post-Burn Hypertrophic Scar:

A Randomized Controlled Trial. *J Med Assoc Thailand*, 103(5):39–43.

36. Uslu A, Sürücü A, Korkmaz MA, *et al.*, 2019, Acquired Localized Hypertrichosis Following Pressure Garment and/or Silicone Therapy in Burn Patients. *Ann Plast Surg*, 82(2):158–61. https://doi.org/10.1097/sap.0000000000001686
37. Ng WL, Chan A, Ong YS, *et al.*, 2020, Deep Learning for Fabrication and Maturation of 3D Bioprinted Tissues and Organs. *Virtual Phys Prototyp*, 15(3):340–58.
38. Sun W, Starly B, Daly AC, *et al.*, 2020, The Bioprinting Roadmap. *Biofabrication*, 12(2):5158.
39. Ng WL, Chua CK, Shen YF, 2019, Print Me An Organ! Why We Are Not There Yet. *Prog Polym Sci*, 97:101145. https://doi.org/10.1016/j.progpolymsci.2019.101145
40. Kang HW, Lee SJ, Ko IK, *et al.*, 2016, A 3D Bioprinting System to Produce Human-scale Tissue Constructs with Structural Integrity. *Nat Biotechnol*, 34(3):312–9. https://doi.org/10.1038/nbt.3413
41. Oladapo BI, Ismail SO, Afolalu TD, *et al.*, 2021, Review on 3D Printing: Fight against COVID-19. *Mater Chem Phys*, 258:123943. https://doi.org/10.1016/j.matchemphys.2020.123943
42. Rendeki S, Nagy B, Bene M, *et al.*, 2020, An Overview on Personal Protective Equipment (PPE) Fabricated with Additive Manufacturing Technologies in the Era of COVID-19 Pandemic. *Polymers*, 12(11):1–18. https://doi.org/10.3390/polym12112703
43. Hale L, Linley E, Kalaskar DM, 2020, A Digital Workflow for Design and Fabrication of Bespoke Orthoses Using 3D Scanning and 3D Printing, a Patient-based Case Study. *Sci Rep*, 10(1):7028–7. https://doi.org/10.1038/s41598-020-63937-1
44. Zolfagharian A, Gregory TM, Bodaghi M, *et al.*, 2020, Patient-Specific 3D-printed Splint for Mallet Finger Injury. *Int J Bioprint*, 6(2):1–13. https://doi.org/10.18063/ijb.v6i2.259
45. Holt SG, Yo JH, Karschimkus C, *et al.*, 2020, Monitoring Skin Temperature at the Wrist in Hospitalised Patients May Assist in the Detection of Infection. *Intern Med J*, 50(6):685–90. https://doi.org/10.1111/imj.14748
46. Chen G, Xie J, Dai G, *et al.*, 2020, Validity of the Use of Wrist and Forehead Temperatures in Screening the General Population for COVID-19: A Prospective Real-World Study. *Iran J Public Health*, 49(supple 1):3670. https://doi.org/10.18502/ijph.v49is1.3670
47. Chow L, Yick KL, Kwan MY, *et al.*, 2020, Customized Fabrication Approach for Hypertrophic Scar Treatment: 3D Printed Fabric Silicone Composite. *Int J Bioprint*, 6(2):262. https://doi.org/10.18063/ijb.v6i2.262
48. Boone LA, 1995, Development of a Customized Pattern Drafting System for Interim Burnscar Pressure Garments Utilizing Fabric Properties and Circumference Measurements. University of Alberta, Edmonton, Alta.
49. Yu A, 2015, Development of Pressure Therapy Gloves for Hypertrophic Scar Treatment. The Hong Kong Polytechnic University, Hong Kong.
50. Yu A, Yick KL, Ng SP, *et al.*, 2016, Numerical Simulation of Pressure Therapy Glove by Using Finite Element Method. *Burns*, 42(1):141–51. https://doi.org/10.1016/j.burns.2015.09.013
51. Wu JZ, Dong RG, Rakheja S, *et al.*, 2002, Simulation of Mechanical Responses of Fingertip to Dynamic Loading. *Med Eng Phys*, 24(4):253–64.
52. Lai CH, Li-Tsang CW, 2009, Validation of the Pliance X System in measuring interface pressure generated by pressure garment. *Burns*, 35(6):845–51. https://doi.org/10.1016/j.burns.2008.09.013
53. Wiseman J, Simons M, Kimble R, *et al.*, 2018, Reliability and Clinical Utility of the Pliance X for Measuring Pressure at the Interface of Pressure Garments and Burn Scars in Children. *Burns*, 44(7):1820–8. https://doi.org/10.1016/j.burns.2018.05.002
54. Reid W, Evans J, Naismith R, *et al.*, 1987, Hypertrophic Scarring and Pressure Therapy. *Burns*, 13:S29–32. https://doi.org/10.1016/0305-4179(87)90090-8
55. Leung K, Cheng J, Ma G, *et al.*, 1984, Complications of Pressure Therapy for Post-burn Hypertrophic Scars: Biomechanical Analysis Based on 5 Patients. *Burns*, 10(6):434–8. https://doi.org/10.1016/0305-4179(84)90085-8
56. Miyatsuji A, Matsumoto T, Mitarai S, *et al.*, 2002, Effects of Clothing Pressure Caused by Different Types of Brassieres on Autonomic Nervous System Activity Evaluated by Heart Rate Variability Power Spectral Analysis. *J Physiol Anthropol Appl Hum Sci*, 21(1):67–74. https://doi.org/10.2114/jpa.21.67

RESEARCH ARTICLE

# Discovering the Latest Scientific Pathways on Tissue Spheroids: Opportunities to Innovate

**Marisela Rodriguez-Salvador*, Baruc Emet Perez-Benitez, Karen Marcela Padilla-Aguirre**

Tecnologico de Monterrey, Escuela de Ingenieria y Ciencias, CP 64849, Monterrey, N.L., Mexico

**Abstract:** Tissue spheroids consist of a three-dimensional model of cells which is capable of imitating the complicated composition of healthy and unhealthy human tissue. Due to their unique properties, they can bring innovative solutions to tissue engineering and regenerative medicine, where they can be used as building blocks for the formation of organ and tissue models used in drug experimentation. Considering the rapid transformation of the health industry, it is crucial to assess the research dynamics of this field to support the development of innovative applications. In this research, a scientometric analysis was performed as part of a Competitive Technology Intelligence methodology, to determine the main applications of tissue spheroids. Papers from Scopus and Web of Science published between 2000 and 2019 were organized and analyzed. In total, 868 scientific publications were identified, and four main categories of application were determined. Main subject areas, countries, cities, authors, journals, and institutions were established. In addition, a cluster analysis was performed to determine networks of collaborations between institutions and authors. This article provides insights into the applications of cell aggregates and the research dynamics of this field, which can help in the decision-making process to incorporate emerging and innovative technologies in the health industry.

**Keywords:** Scientometric analysis; Competitive technology intelligence; Bioprinting; Cell aggregates; Bioink

***Correspondence to:** Marisela Rodriguez-Salvador, Tecnologico de Monterrey, Escuela de Ingenieria y Ciencias, Mexico; marisrod@tec.mx

**Received:** December 16, 2020; **Accepted:** January 19, 2021; **Published Online:** January 29, 2021

**Citation:** Rodriguez-Salvador M, Perez-Benitez BE, Padilla-Aguirre KM, 2021, Discovering the Latest Scientific Pathways on Tissue Spheroids: Opportunities to Innovate. *Int J Bioprint*, 7(1):331. http://doi.org/10.18063/ijb.v7i1.331

## 1. Introduction

Additive manufacturing (AM), commonly known as three-dimensional (3D) printing, is a rapidly growing area that fabricates a wide range of structures and complex geometries by depositing successive layers of materials on top of each other[1,2]. In the medical field, 3D bioprinting refers to different AM techniques able to print living cells and materials, in a specified location[1]. 3D bioprinting has brought new solutions to mimic the heterogeneous and complex native tissues. Its main goal is to develop 3D living human constructs with biological and physical properties that emulate the human tissues, being a solution to repair tissue defects and restore organ structure and function[3]. Through this innovative technology, constructs, or implants tailored to the geometrically complex and irregular shapes of the native tissues can be produced using computer designs or medical images. In addition, it is also possible to create biological connectivity by embedding cells with pore networks to deliver components such as drug or nutrients[4].

Ng *et al.*[5] identify seven main technologies for 3D bioprinting: extrusion, stereolithography, laser-assisted, inkjet, microvalve-based bioprinting, two-photon polymerization microfluidic printing, and acoustic bioprinting. The main working foundation for the first five techniques is:

(i) Extrusion: pneumatic-or mechanical extrusion, loading of bio-inks into cartridges
(ii) Stereolithography: photo-polymerization of photo-initiators, loading of bio-inks into vat
(iii) Laser-assisted: localized vaporization of energy-absorbing layer, coating of homogeneous ribbon layer
(iv) Inkjet: use of actuators to overcome surface tension, loading of bio-inks into cartridges
(v) Microvalve-based bioprinting: use of actuators to overcome surface tension, loading of bio-inks into cartridges.

Extrusion, stereolithography and microvalve-based bioprinting present the less difficulties to operate while laser-assisted involves more complex process and inkjet process is even more complex.

The material that is printed is referred to as "bioink" and it consists of multiple types of cells and biomaterials. Bioinks are analyzed in terms of their printability, biocompatibility, and bioactivity[6]. The printing resolution and dimensionality contribute to the overall shape fidelity of the bioprinted construct. Its dimensionality can be represented by z-resolution in printing and it mainly depends on specific printing parameters such as printing path height, path space, and the nozzle diameter, while material properties as material contraction/swelling, thixotropy, and the crosslinking mechanism affect the z-resolution. The principle for deposition varies according to the bioprinting technology to be applied which affects the print resolution and dimensionality differently[7].

To meet all mechanical and functional requirements to produce biomimetic tissue-like constructs, multicomponent bioinks have been developed recently. Also known as multimaterials or multicelular bioinks, they include more than one biomaterial, cell, and additive material or biomolecule[3]. Multicomponent bioinks can be characterized as:

(i) Bioinks having combination of natural materials, for example, alginate with gelatin/fibrin, silk fibroin with gelatin, agarose with collagen, chitosan with gelatin, cellulose with alginate, and hyaluronan with cellulose;
(ii) Bioinks comprising natural and synthetic components;
(iii) Bioinks involving synthetic biomaterials;
(iv) Bioinks fabricated with hydrogels and particles;
(v) Bioinks for 4D printing; and
(vi) Bioinks with different type of cells and soluble factors.

Moreover, materials innano scale can also be added to improve structure and functionality[3].

One crucial element to succeed in 3D bioprinting is the right selection of cells to print. Cells can be used as individually encapsulated, as cells in scaffolds or as cell aggregates (spheroids)[3,8]. As mentioned by Hospodiuk *et al.*[9] and Rezende *et al.*[10], tissue spheroids are a type of scaffold-free bioink that has a small-sized and ideal geometric shape for bioprinting. This novel bioink enhances cell-cell interaction, growth, differentiation, and resistance to the environment because of the high cell density in the assembly[11].

Tissue spheroids consist of 3D cell clusters that represent the intricacy of healthy and unhealthy human tissues[12,13]. One important characteristic of these cell aggregates is their self-assembly, which mimics developing tissue by fusion and reorganization[14]. Conversely, a major disadvantage is that the majority of the cells do not aggregate spontaneously in culture; therefore, they need to be induced by some means[1]. These cellular aggregates can be fabricated using a scaffold or scaffold-free[12].

The first time these multicellular spheroids were created was in 2003 by Garboc Forgacs at the University of Missouri[15]. Since then, several techniques have been used for the generation of tissue spheroids. The most commonly used techniques rely solely on the self-arranging properties of cells using micromolded recessed templates prepared in a non-adhesive hydrogel[16].

In general, the use of tissue spheroids serves two main purposes, as building blocks in tissue engineering or as tissue models used in the pharmaceutical industry[9]. Tissue engineering constitutes an important field of regenerative medicine for tissue repair as it offers the potential for developing patient-specific 3D tissue constructs for the treatment of human diseases. It represents a huge potential solution to overcome the current shortage of organs or tissues for transplantation. On the other hand, 3D *in vitro* systems have significantly advanced the drug screening processes as 3D tissue models can closely mimic native tissues and, in some cases, the physiological response to the drugs, thus improving the ability to predict the efficacy and toxicity of drug candidates[17].

This study was performed to analyze and describe the development of tissue spheroids, as these cell aggregates can contribute significantly to the advancement and innovation of tissue engineering and regenerative medicine.

## 2. Methodology

A scientometric analysis was performed as part of a Competitive Technology Intelligence (CTI) process to identify current applications and newly emerging areas related to tissue spheroids for regenerative medicine and tissue engineering. CTI is a cyclical process used to collect, analyze, and interpret data from different sources legally and ethically to produce valuable information for decision-making purposes pertaining to research and development (R&D) and innovation within an organization[18]. In this research, this process was conducted using the CTI hybrid model developed by Rodríguez-Salvador *et al.*[19], which comprises ten main steps: (i) process planning, (ii) primary and secondary source identification, (iii) establishment of the information collection strategy, (iv) information collection, (v) expert validation and adjustments, (vi) scientometric analysis, (vii) expert validation and adjustments, (viii) verification of the final results, (ix) results delivery, and (x) decision-making. Execution of CTI implies the collection of the most relevant information instead of collecting the largest number of documents. From this perspective, the

identification of keywords and the design of a search query as accurately as possible is required; thereby, it involves expert consultation from the beginning through the validation of the final results[19]. Hence, the search query of this study was developed through an iterative process, to identify additional keywords, aside from the ones provided initially by experts on the topic, to improve its accuracy. The general structure of the search query employed is as follows:

((( spheroid* PRE/1 ( cell OR cellular )) OR ("3 d spheroid") OR (( 3d OR "three dimensional" OR "3 dimensional" OR "three d") PRE/1 spheroids ) OR ( cancer PRE/1 spheroids ) OR ( tumor* PRE/1 spheroids ) OR ( tumorspheres OR tumourspheres OR tumorospheres ) OR ( cell* PRE/4 spheroid*) OR ( multicell* PRE/3 spheroid*) OR ( tissue* PRE/2 spheroid*) OR (( hepat* OR liver OR pancrea* OR thyroid OR organotypic OR cardiomyocyte ) PRE/0 spheroid ) OR ("self assembl* spheroid") OR cardiosphere OR ( cell AND ( spheroid PRE/0 ( formation OR invasion OR culture )))) AND ("tissue engineering" OR "regenerative medicine") AND NOT ( plant OR graphite OR bacter* OR alga* OR "solar cell*" OR "eutectic cell*" OR yeast OR spheroidin OR alloy OR rhodopseudomonas OR phytoplankton OR mycobacteria OR larva OR protista OR volvox OR coli OR "non-spheroid*" OR anisotropic OR pollen OR coral OR biofilm OR sponge OR plankton OR microalga* OR dictyostelium OR microbial OR microbe OR phytoplankton OR saccharomyces OR eps OR candida OR sea OR food OR amoeba OR "date palm" OR kelvin OR peanut OR lanata OR yew OR roseus OR ajuga OR "protein aggregates" OR antenna OR batter* OR foam OR barnacle OR oblate OR review OR overview ))

Boolean operators AND, OR and NOT were used to include and exclude the terms and the PRE/# function that indicates the number of words that may be close to a specific term. Scopus and Web of Science (WoS) databases were selected to collect the scientific documents. Scopus contains more than 5000 publishers and 75 million items indexed dating back to 1970 across different disciplines in science[20]. In addition, WoS includes scientific documents from over 21,000 high-impact journals covering more than 100 years of scientific production[21].

Gathering scientific documents were conducted for journal articles and conference papers from both databases that were published between January 1, 2000, and June 5, 2019 (when the collection activity ended). The documents obtained from each database were exported and combined into a single list, where a manual cleaning process was performed to remove documents not complying with the purpose of the study, as well as those containing duplicated information. The resulting documents were classified according to the technological application of the tissue spheroids mentioned previously.

A scientometric analysis was applied to the collected data to identify the current and emerging areas of tissue spheroids applications. First, subject areas were identified according to the classification given by Scopus. For publications indexed in WoS but not in Scopus, their subject areas were adapted to Scopus classification to maintain homogeneity. Subsequently, the publishing growth dynamics within the time range selected (January 1, 2000, to June 5, 2019), along with the most prolific countries, cities, authors, journals, and institutions on the topic were identified. Finally, a cluster analysis was performed to determine networks of collaborations between institutions and authors.

## 3. Results and discussion

A total of 1296 scientific documents published between January 1, 2000, and June 5, 2019, were retrieved; 783 from Scopus and 513 from WoS. A deduplication and manual validation process was performed, resulting in 868 publications. These publications were classified according to the following categories.

### 3.1. Global trends

Scientific articles and conference papers retrieved in this study revealed four global trends depending on the application given to tissue spheroids. These are building blocks, drug testing and disease model, spheroid formation, and complementary studies. Each category is described in **Table 1**. The following tables (**Tables 2-5**) correspond to the most recent and representative studies from the documents analyzed for each global trend.

Results of these tables show the specific focus of the different group trends identified. There is a diversity of bioinks and cell types, ranging from healthy cells, such as human fibroblasts, human umbilical vein endothelial cells (HUVECs), human mesenchymal stem cells from bone marrow (hMSCs), human-induced pluripotent cells (hPCSs), and carcinogenic cells (e.g., human breast cancer, osteosarcoma, colon carcinoma, hepatoma, and ovarian cancer cells). Among them, the HUVECs, MSCs, and PCSs are the most used cell types. For example, stem cells offer interesting advantages as they can be obtained from various sources and differentiated into various lineages[3].

Our findings also exhibit that there is no single predominant 3D bioprinting process, this technology is evolving rapidly and different approaches exist depending on the main goal to achieve. Moreover, our results also show that spheroid resolution can be manipulated depending on the purpose of the study provided that a certain spheroid size is not yet defined.

According to Ng *et al.*,[5] a key dilemma lies in the need of obtaining a balance between achieving the nano-

**Table 1.** Tissue spheroid global trends.

| Global trend | Description |
|---|---|
| Building blocks | Tissue spheroids are used as basic units to biofabricate tissue constructs such as implants organ precursors. Tissue constructs are built placing the tissue spheroids with bioprinting or bioassembly techniques. In some cases, cells are bioprinted as bioinks to build the final tissue construct, but before its completion, cells first aggregate in spherical forms before they fusion |
| Drug testing and disease model | Cell aggregates are used as a 3D culture model for drug testing purposes or for mimicking a particular disease. The resulting model can be formed by a single tissue spheroid or by a tissue construct product of the fusion of several tissue spheroids made of one or different cell lines |
| Spheroid formation | This category is related to the improvement of the tissue spheroid formation, particularly to uniform the tissue spheroids characteristics (i.e. size and cells number) and to scale up the process for mass tissue spheroid formation. But no specific applications were discussed in documents analyzed |
| Complementary studies | Complementary studies for tissue spheroids management, such as the development of computer programs and mathematical models to simulate tissue spheroids behavior, and the production of novel accessories for imaging systems for tissue spheroids monitoring |

scale resolution that emulate the extracellular matrix (ECM) of human tissues/organs and improving the speed for fabrication of human-scale tissues/organs.

Ashammakhi *et al.*[3] published on the challenges involving multicomponent bioinks that are related to the development of appropriate materials having shear-thinning properties with cell-friendly capability and other desired biological characteristics for different tissue engineering applications. As Ng *et al.*[5] indicate, it is also important to know more about the composition and spatial arrangement of living cells and ECM within tissue constructs along with the development of advanced bioprinting strategies.

## 3.2. Scientometric analysis results

As shown in **Figure 1**, of the 868 publications obtained, 597 publications (69%) exhibited the analysis of spheroid formation, 135 publications (16%) described the use of tissue spheroids as building blocks, 100 (11%) relates to tissue spheroids for drug testing and disease model and finally, and 36 (4%) comprise complementary studies of tissue spheroids.

Subject areas were identified based on the classification of science disciplines in the Scopus database. For publications indexed in WoS but not in Scopus, their subject areas were adapted to Scopus categorization to maintain homogeneity. In this study, the analysis of all 868 publications revealed nine subjects following the distribution displayed in **Figure 2**: biochemistry, genetics and molecular biology (25%), engineering (19%), materials science (16%), chemical engineering (11%), medicine (10%), chemistry (4%), immunology and microbiology (3%), applied physics (3%), and other (9%). However, biochemistry, genetics and molecular biology, engineering, and materials science account for more than half of all the publications with 60% of all the documents.

The growth dynamics of publications on tissue spheroids were defined as shown in **Figure 3**. In terms of publications, number of papers by year of publication did not exhibit a strictly patterned behavior (e.g., linear or exponential); nevertheless, publications regarding tissue spheroids showed an increased growth from 2 publications in 2000 to 122 publications in 2018. The year 2019 was not depicted in the graph since the retrieval period ended on June 5; thus far there had been 42 overall. The biggest growth was seen from 2015 to 2016, with a 35.5% increase, going from 76 documents to 103. Of the 868 scientific documents, 51% were published in the past 5 years (2015–2019).

The affiliations of authors indexed in high-impact scientific databases are an indicator, of which countries and organizations have patterns of research concentration. The top countries and cities with the largest numbers of publications on tissue spheroids were also determined; results are presented in **Figure 4A and B**. The United States is the most prolific country with 288 publications, followed by Japan with a total of 155, China with 93, and Germany with 84 published articles. These four countries account for more than half (55%) of the total documents. The remaining countries on the top ten published between 26 and 73 scientific articles and are located either in western Europe or eastern Asia – except for Canada, which holds the ninth position.

The top cities are highly correlated with the top ten countries; however, the rankings are much closer in the total output, except Seoul, with 57 and Tokyo with 46 scientific documents which have almost twice as much as the output from other cities in the top ten. We can conclude that a significant amount (78%) of the papers produced in South Korea are centralized in Seoul, whilst in Japan, most of the papers were contributed from four

**Table 2.** Global trend: Tissue spheroids as building blocks.

| Article | Year/Journal | Impact analysis |
|---|---|---|
| Machino, R. *et al* "Replacement of Rat Tracheas by Layered, Trachea-Like, Scaffold-Free Structures of Human Cells Using a Bio-3D Printing System"[22] | 2019/Advanced Healthcare Materials | "Human cartilage cells, human fibroblasts, human umbilical vein endothelial cells, and human mesenchymal stem cells from bone marrow are aggregated into 20,000 cell spheroids and placed into a Bio-3D printing system (Regenova) with dedicated needles positioned according to 3D configuration data (Kenzan Method), to develop scaffold-free trachea-like tubes." |
| Daly, A. C., & Kelly, D. J. "Biofabrication of spatially organised tissues by directing the growth of cellular spheroids within 3D printed polymeric microchambers"[23] | 2019/ Biomaterials | "Novel biofabrication strategy that enables the engineering of structurally organized tissues by guiding the growth of cellular spheroids within arrays of 3D printed polymeric microchambers." This research used bone marrow mesenchymal stem cells (BMSC) and chondrocytes in a concentration of 20,000 and 40,000 per microchamber using inkjet printing |
| Anada, T. *et al* "Vascularized bone-mimetic hydrogel constructs by 3D bioprinting to promote osteogenesis and angiogenesis"[24] | 2019/ International Journal of Molecular Sciences | "Two-step digital light processing technique to fabricate a bone-mimetic 3D hydrogel construct based on octacalcium phosphate (OCP), spheroids of human umbilical vein endothelial cells (HUVEC), and gelatin methacrylate (GelMA) hydrogels". In this research a spheroid culture chip was used, conformed by a solution of 25×104 cells/mL |

**Table 3.** Global trend: Tissue spheroids for drug testing and disease models.

| Article | Year/Journal | Impact Analysis |
|---|---|---|
| Lee, C. *et al.* "Bioprinting a novel glioblastoma tumor model using a fibrin-based bioink for drug screening"[25]. | 2019/Materials Today Chemistry | "Printed cells spontaneously formed spheroids with upregulated levels of the proteins CD133 and DCX markers associated with cancer stem cells and metastatic invasiveness, respectively. Printed scaffolds were treated with a novel chemical treatment method previously tested in 2D culture and showed significant resistance, indicating the 3D printed glioblastoma model's potential as a more accurate representation of the in vivo response to drug treatment." Glioblastoma multiforme and human-induced pluripotent stem cells where printed using an Aspect Biosystems RX1 printer, which uses a microfluidic technology. |
| Kingsley, D. M. *et al*. "Laser-based 3D bioprinting for spatial and size control of tumor spheroids and embryoid bodies"[26] | 2019/Acta Biomaterialia | "Impact analysis of the aggregate size on the uptake of a commonly employed ligand for receptor-mediated drug delivery, Transferrin, indicating that larger tumor spheroids exhibit greater spatial heterogeneity in ligand uptake" For this research, human breast cancer cells and CCE mouse embryonic stem cells (mESCs) were printed using laser direct write (LDW) bioprinting. |
| Trisno, S. L.. *et al*. " Esophageal Organoids from Human Pluripotent Stem Cells Delineate Sox2 Functions during Esophageal Specification"[27] | 2018/Cell Stem Cell | "Dorsal anterior foregut (AFG) spheroids grown in a 3D matrix formed human esophageal organoids (HEOs), and HEO cells could be transitioned into two-dimensional cultures and grown as esophageal organotypic rafts. HEOs present a powerful platform for modeling human pathologies and tissue engineering." In this research pluripotent stem cells (PCSs) signaling pathways´ were manipulated to differentiate into esophageal organoids. Suspension method was used for spheroid formation. |

main cities, that is, Tokyo, Yokohama, Fukuoka, and Tsukuba, which are ranked in the top ten of most prolific cities.

The top authors in this study are presented in **Figure 4C**. A total of 4,069 authors were identified among all the publications. The first and second most prolific

**Table 4.** Global trend: Spheroid formation.

| Article | Year/Journal | Impact Analysis |
|---|---|---|
| Miller, A. J. *et al.* "Generation of lung organoids from human pluripotent stem cells *in vitro*"[28]. | 2019/Nature Protocols | "Protocol that recapitulates several stages like induction, patterning, lung specification, budding, morphogenesis; to differentiate human pluripotent stem cells (hPSCs) into ventral–anterior foregut spheroids and further into two distinct types of organoids: human lung organoids and bud tip progenitor organoids." |
| Lee, W. *et al.* " Dispersible hydrogel force sensors reveal patterns of solid mechanical stress in multicellular spheroid cultures"[29] | 2019/Nature Communications | "Development of ultrasoft mechanosensors that visibly deform under <10 Pascals of cell-generated stress. By incorporating mechanosensors into multicellular spheroids, the patterns of internal stress that arise during spheroid formation where captured. This technique can provide a quantitative basis to design tissues that leverage the mechanical activity of constituent cells to evolve towards a desired form and function." In this research, HS-5 fibroblasts were used as well as an aqueous two-phase droplet printing technique by an automated liquid handler in a concentration of 6×107 cells/mL. |
| Heo, D. N. *et al.* " Synergistic interplay between human MSCs and HUVECs in 3D spheroids laden in collagen/fibrin hydrogels for bone tissue engineering"[30] | 2019/Acta Biomaterialia | "To enhance stem cell function and generate pre-vascularized network, a collagen/fibrin hydrogel was employed as an encapsulation matrix for the incorporation of human mesenchymal stem cell/human umbilical vein endothelial cell (MSC/HUVEC) spheroids, and their cellular behavior (including cell viability, morphology, proliferation, and gene expression profile) was investigated and compared to that of cell suspension- or MSC spheroids-laden hydrogels." In this study, microwells in AggreWell plates were used. Cell suspension at a density of 1.2×106 cells/well was seeded. MSC-only and MSC/HUVEC (75%/25%) spheroids were used. |

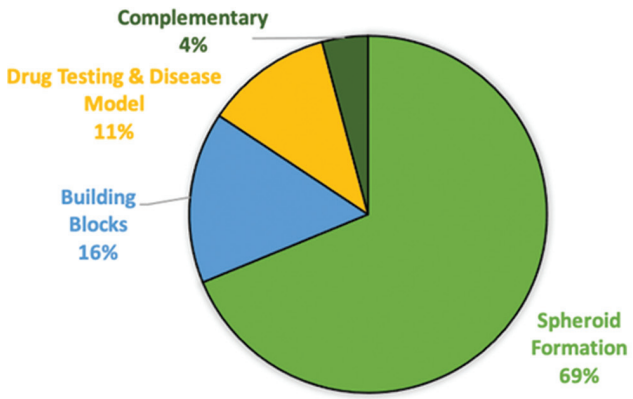


**Figure 1.** Distribution of scientific publications by categories**.**

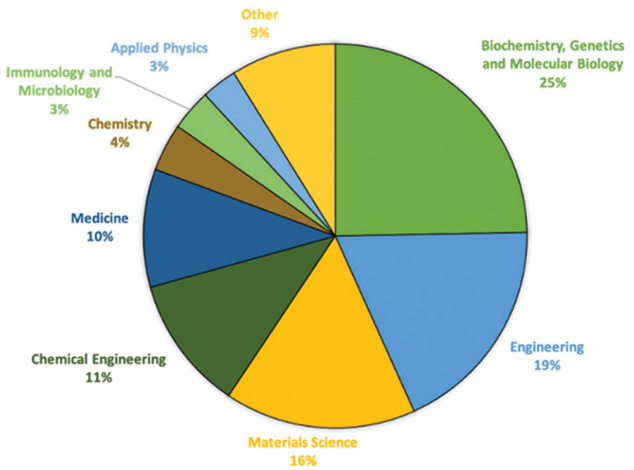


**Figure 2.** Distribution of the subject areas of publication on the use of tissue spheroids.

authors were Vladimir Mironov and Vladimir Kasyanov with 24 and 14 publications each. The third most prolific author is Gerhard Björn Stark with 13 scientific articles. These findings can correlate directly to the recently published paper "Bioprinting in the Russian Federation: Can Russians Compete?" by Peter Timashev and Vladimir Mironov in which they state five main achievements made by Russian bioprintists that have contributed to global technology in the field, such as the development of original 3D bioprinters, natural bioinks and the world's first functional and vascularized organ construct[34].

**Table 5.** Global trend: Complementary studies.

| Article | Year/Journal | Impact Analysis |
|---|---|---|
| Nakagawa, K., & Kishimoto, T. "Unlabeled image analysis-based cell viability assay with intracellular movement monitoring"[31] | 2019/Biotechniques | "Unlabeled optical metabolic imaging of cultured living cells. This imaging technique is based on motion vector analysis with a block-matching algorithm to compare sequential time-lapse images. Motion vector analysis evaluates the movement of intracellular granules observed with a phase-contrast microscope. This assay can measure cellular viability at a single-cell level without requiring any reagents". In this research, human osteosarcoma U2OS cells, human colon carcinoma Caco-2 cells and human hepatoma HepG2 cells were used. |
| Wu, H. *et al*. "Electrical impedance tomography for real-time and label-free cellular viability assays of 3D tumour spheroids"[32] | 2018/Analyst | "*In silico* and *in vitro* cell viability inside large cell spheroids can be monitored in real time and label-free with electrical impedance tomography (EIT). The results show the potential of EIT for non-destructive real-time and label-free cellular assays in the miniature sensor, providing physiological information in the applications of the 3D drug screening and tissue engineering." MCF-7 breast cancer cells were used, and the liquid overlay technique was adopted to form cells spheroids on the hydrogel surface. Cell suspension with 1×104 cells were seeded onto each microplate well. |
| Parrish, J *et al.* "A 96-well microplate bioreactor platform supporting individual dual perfusion and high-throughput assessment of simple or biofabricated 3D tissue models"[33] | 2018/Lab on a Chip | "Platform to address the experimental and *in vivo* disparity in throughput and both system complexity (by supporting multiple *in situ* assessment methods) and tissue complexity (by adopting a construct-agnostic format). It describes the potential of a scalable dual perfusion bioreactor platform for parenchymal and barrier tissue constructs to support a broad range of multi-organ-in-a-chip applications". In this research human umbilical cord-derived vascular endothelial cells (HUVEC), bone marrow-derived mesenchymal stromal cells (MSC), human ovarian cancer cells and human foreskin-derived fibroblast were used. |

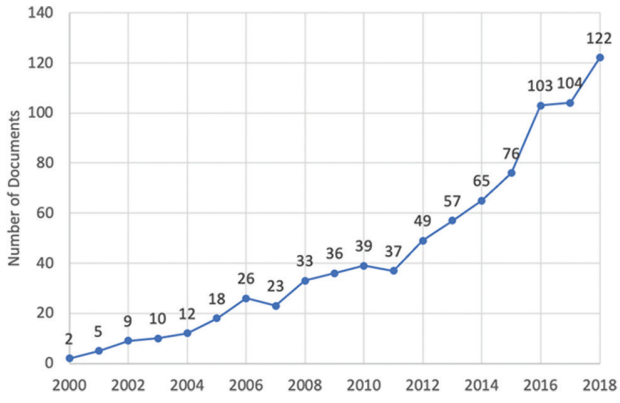


**Figure 3.** Number of documents on tissue spheroids by year of publication.

**Figure 4D** shows the journals with the highest number of publications on tissue spheroids. *Biomaterials* is the most prolific journal with 62 documents, followed by *Acta Biomaterialia* which has almost half the number of articles with 36. *Tissue Engineering – Part A* claims the third place with 32 publications. These three journals comprise 52% of all the documents in the top ten list. These journals focus on either biomaterial structure, function, and clinical application or in therapeutic strategies to regenerate tissue – the topics closely related to tissue spheroids.

Furthermore, the institutions with the highest numbers of publications were also identified, as shown in **Figure 4E**. Overall, 840 institutions were identified worldwide but the most prolific institutions are directly correlated with the most prolific countries mentioned before. Japan has the most prolific institutions with 23 publications each from Kyushu University and the University of Tokyo. The University of California in the United States published a total of 22 articles,

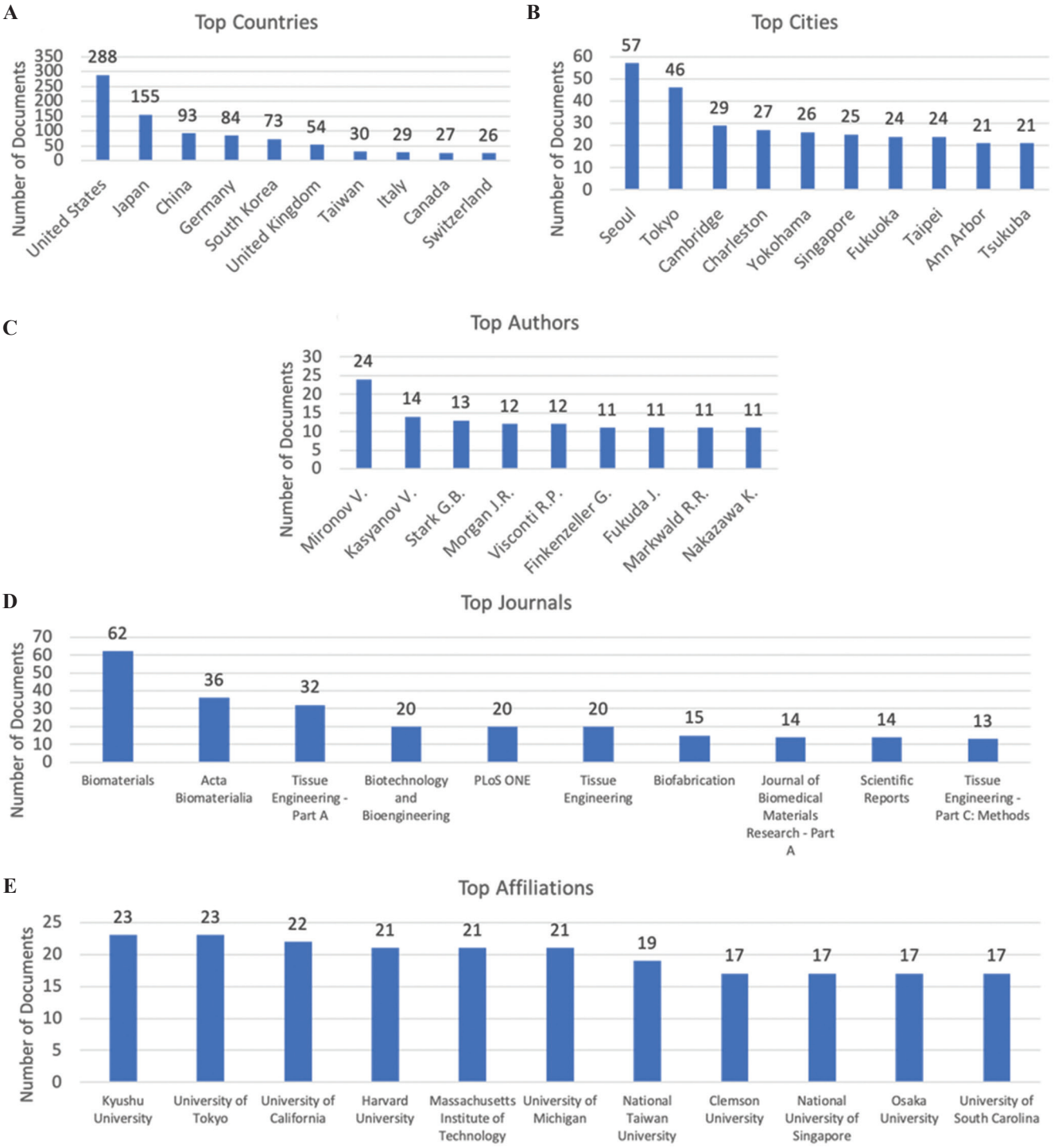


**Figure 4.** Global scientific trends in tissue spheroids. A summary of the publications that are indexed in Scopus and Web of Science according to (A) the ten most frequent affiliation countries and (B) cities of the authors; (C) the ten most cited authors (D) the ten journals with the most occurrences of the search terms; and (E) the ten most frequent organizational affiliations of the authors.

and in the same country, we found a triple tie with 21 documents: Harvard University, Massachusetts Institute of Technology, and the University of Michigan.

Finally, **Figure 5A and B** shows network maps of the authors and institutions' collaborations, respectively. In these illustrations, the nodes' size is proportional to the number of publications. Vladimir Mironov was identified as the most prolific author who engages in close collaboration with Vladimir Kasyanov, Rodrigo Alvarenga Rezende, Jorge Vicente Lopes da Silva, Roger R.

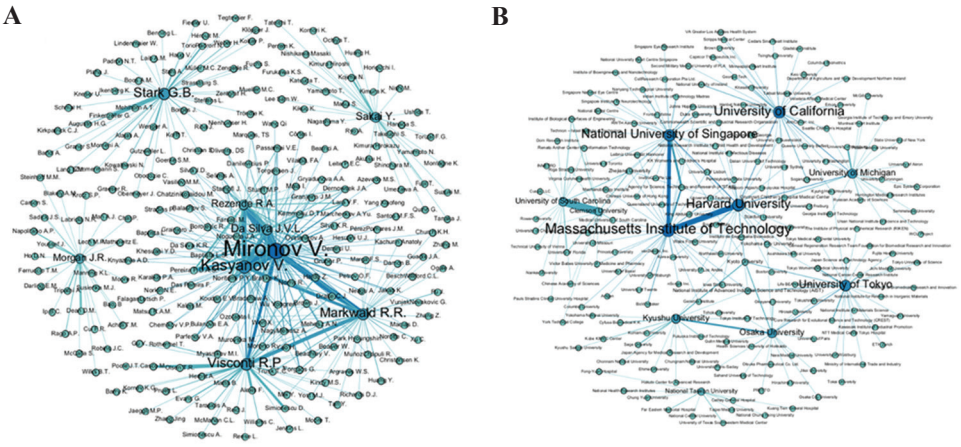


**Figure 5.** Co-occurrence network maps. (A) Top authors cooccurrence. (B) Top affiliations cooccurrence.

Markwald, and Richard P Visconti; these authors represent the biggest collaborating network. Other main authors, such as Yasuyuki Sakai, Gerhard Björn Stark, and Jeffrey R. Morgan, were also visualized working with their own research groups.

As to the institutions, we identified that the University of South Carolina has the closest collaboration with the Clemson University. Another substantial collaborator is the Massachusetts Institute of Technology with both Harvard University and the National University of Singapore. Finally, the Kyushu University collaborates closely with Osaka University.

## 4. Conclusions

This study assessed the scientific research dynamics of tissue spheroids through a CTI process using a scientometric analysis. To accomplish this, scientific publications published between January 1, 2000, and June 5, 2019, were retrieved from Scopus and WoS, before organization and analysis. Four fundamental trends were detected: tissue spheroids as building blocks, tissue spheroids for drug testing and disease models, spheroid formation analysis, and complementary studies. Different types of bioinks and cells, ranging from healthy cells to carcinogenic cells, were also identified. In addition, subject area distributions as well as the most prolific countries, cities, authors, journals, and institutions regarding this topic were identified to determine the overall research publications landscape, as well as a network of collaborations between institutions and authors.

Our results exhibit that tissue spheroids research covers nine subject areas: biochemistry, genetics and molecular biology, engineering, materials science, chemical engineering, medicine, chemistry, immunology and microbiology, applied physics, and others, with an emphasis on biochemistry, genetics, and molecular biology, engineering, and materials science that constitute 60% of the publications.

Our findings also revealed a growing interest on tissue spheroids research, evidenced by the biggest leap of scientific production particularly in the past 5 years. The United States and Japan were found to be the most prolific countries, for being ranked in the top ten positions and authoring more than half of the documents analyzed. Nevertheless, the most prolific city was Seoul, South Korea; this might be due to the centralization of the research centers in this capital. The most prolific author was found to be Vladimir Mironov, followed by Vladimir Kasyanov, probably due to the fact that they collaborate closely, representing an interesting finding in the network of authors collaboration. The top three journals identified were *Biomaterials*, *Acta Biomaterialia*, and *Tissue Engineering – Part A*. The main institutions identified are directly related to the most prolific countries. For instance, Kyushu University and the University of Tokyo in Japan were both tied at number one position, followed by the institutions in the United States: University of California in the second place whereas Harvard University, Massachusetts Institute of Technology, and the University of Michigan tied at the third place.

Insights obtained in this study show the main trends of published research in tissue spheroids. These findings may help guide research efforts in the tissue engineering and regenerative medicine, supporting the development of new technological applications that would revolutionize the health industry in the coming years.

## Acknowledgments

The authors acknowledge institutional funding received from Tecnológico de Monterrey and Consejo Nacional de Ciencia y Tecnología (CONACyT).

## Conflicts of interest

The authors declare no conflicts of interest.

## References


1. Donderwinkel I, Hest JC, Cameron NR, 2017, Bio-inks for 3D Bio-Printing: Recent Advances and Future Prospects. *Polym. Chem* , 8:4451–71. https://doi.org/10.1039/c7py00826k
2. Ngo TD, Kashani A, Imbalzano G, *et al*., 2018, Additive Manufacturing (3D Printing): A Review of Materials, Methods, Applications and Challenges. *Compos B Eng*, 143:172–96. https://doi.org/10.1016/j.compositesb.2018.02.012
3. Ashammakhi N, Ahadian S, Xu C, *et al*., 2019, Bioinks and Bio-Printing Technologies to Make Heterogeneous and Biomimetic Tissue Constructs. *Mater Today Bio*, 1:100008. https://doi.org/10.1016/j.mtbio.2019.100008
4. Schwab A, Levato R, D'Este M, *et al*., 2020, Printability and Shape Fidelity of Bioinks in 3D Bioprinting. *Chem Rev*, 120:11028–55. https://doi.org/10.1021/acs.chemrev.0c00084
5. Ng WL, Chua CK, Shen YF, 2019, Print Me An Organ! Why We Are Not There Yet. *Prog Polym Sci*, 97:101145. https://doi.org/10.1016/j.progpolymsci.2019.101145
6. Ji S, Guvendiren M, 2017, Recent Advances in Bioink Design for 3D Bio-Printing of Tissues and Organs. *Front Bioeng Biotechnol*, 5:23. https://doi.org/10.3389/fbioe.2017.00023
7. Lee JM, Ng WL, Yeong WY, 2019, Resolution and Shape in Bio-Printing: Strategizing Towards Complex Tissue and Organ Printing. *Appl Phys Rev*, 6:11307. https://doi.org/10.1063/1.5053909
8. Colosi C, Shin SR, Manoharan V, *et al*., 2016, Microfluidic Bio-Printing of Heterogeneous 3D Tissue Constructs Using Low-Viscosity Bioink. *Adv Mater*, 28:677–84. https://doi.org/10.1002/adma.201503310
9. Hospodiuk M, Dey M, Sosnoski D, *et al*., 2017, The Bioink: A Comprehensive Review on Bio-Printable Materials. *Biotechnol Adv*, 35:217–39.
10. Rezende RA, Pereira FD, Kasyanov V, *et at*., 2013, Scalable biofabrication of tissue spheroids for organ printing. In: Procedia CIRP. Vol. 5. Amsterdam, Elsevier. pp276–81. https://doi.org/10.1016/j.procir.2013.01.054
11. Sriphutkiat Y, Kasetsirikul S, Zhou Y, 2018, Formation of Cell Spheroids Using Standing Surface Acoustic Wave (SSAW). *Int J Bioprint*, 4:130. https://doi.org/10.18063/ijb.v4i1.130
12. Costa EC, Melo-Diogo DD, Moreira AF, *et al*., 2017, Spheroids Formation on Non-Adhesive Surfaces by Liquid Overlay Technique: Considerations and Practical Approaches. *Biotechnol J*, 13:1002. https://doi.org/10.1002/biot.201700417
13. Gopinathan J, Noh I, 2018, Recent Trends in Bio-Inks for 3D Printing. *Biomater Res*, 22:11.
14. Murphy SV, Atala A, 2014, 3D Bio-Printing of Tissues and Organs. *Nat Biotechnol*, 32:773–85.
15. Jose RR, Rodriguez MJ, Dixon TA, *et al*., 2016, Evolution of Bio-Inks and Additive Manufacturing Technologies for 3D Bio-Printing. *ACS Biomater Sci Eng*, 2:1662-78.
16. Mehesz AN, Brown J, Hajdu Z, *et al*., 2011, Scalable Robotic Bio-Fabrication of Tissue Spheroids. *Biofabrication*, 3:025002. https://doi.org/10.1088/1758-5082/3/2/025002
17. Peng W, Unutmaz D, Ozbolat IT, 2016, Bio-Printing towards Physiologically Relevant Tissue Models for Pharmaceutics. *Trends Biotechnol*, 34:722–32. https://doi.org/10.1016/j.tibtech.2016.05.013
18. Toit AS, 2015, Competitive Intelligence Research: An Investigation of Trends in the Literature. *J Intell Stud Bus*, 5:14–21.
19. Rodríguez-Salvador M, Villarreal-Garza D, Álvarez MM, *et al*., 2019, Analysis of the Knowledge Landscape of Three-Dimensional Bio-Printing in Latin America. *Int J Bioprint*, 5:240. https://doi.org/10.18063/ijb.v5i2.3.240
20. Elsevier, 2019, Scopus. Available from: https://www.elsevier.com/solutions/scopus. [Last accessed on 2020 Oct 20].
21. Clarivate Analytics, 2019, Databases. Available from: https://www.clarivate.com/products/web-of-science/databases. [Last accessed on 2020 Oct 20].
22. Machino R, Matsumoto K, Taniguchi D, *et al*., 2019, Replacement of Rat Tracheas by Layered, Trachea-Like, Scaffold-Free Structures of Human Cells Using a Bio-3D Printing System. *Adv Healthc Mater*, 8:1800983. https://doi.org/10.1002/adhm.201800983
23. Daly AC, Kelly DJ, 2019, Bio-Fabrication of Spatially Organised Tissues by Directing the Growth of Cellular Spheroids within 3D Printed Polymeric Microchambers. *Biomaterials*, 197:194–206. https://doi.org/10.1016/j.biomaterials.2018.12.028
24. Anada T, Pan CC, Stahl AM, *et al*., 2019, Vascularized Bone-Mimetic Hydrogel Constructs by 3D Bioprinting to Promote Osteogenesis and Angiogenesis. *Int J Mol Sci*, 20:1096. https://doi.org/10.3390/ijms20051096
25. Lee C, Abelseth E, de la Vega L, *et al*., 2019, Bioprinting a Novel Glioblastoma Tumor Model Using a Fibrin-Based Bio-Ink for Drug Screening. *Mater Today Chem*, 12:78–84. https://doi.org/10.1016/j.mtchem.2018.12.005

26. Kingsley DM, Roberge CL, Rudkouskaya A, *et al*., 2019, Laser-Based 3D Bio-Printing for Spatial and Size Control of Tumor Spheroids and Embryoid Bodies. *Acta Biomater*, 95:357–70. https://doi.org/10.1016/j.actbio.2019.02.014
27. Trisno SL, Philo K, McCracken KW, *et al*., 2018, Esophageal Organoids from Human Pluripotent Stem Cells Delineate Sox2 Functions during Esophageal Specification. *Cell Stem Cell*, 23:501-15.e7. https://doi.org/10.1016/j.stem.2018.08.008
28. Miller AJ, Dye BR, Ferrer-Torres D, *et al*., 2019, Generation of Lung Organoids from Human Pluripotent Stem Cells *in Vitro*. *Nat Protoc*, 14:518–40. https://doi.org/10.1038/s41596-018-0104-8
29. Lee W, Kalashnikov N, Mok S, *et al*., 2019, Dispersible Hydrogel Force Sensors Reveal Patterns of Solid Mechanical Stress in Multicellular Spheroid Cultures. *Nat Commun*, 10:144. https://doi.org/10.1038/s41467-018-07967-4
30. Heo DN, Hospodiuk M, Ozbolat IT, 2019, Synergistic Interplay Between Human MSCs and HUVECs in 3D Spheroids Laden in Collagen/Fibrin Hydrogels for Bone Tissue Engineering. *Acta Biomater*, 95:348–56. https://doi.org/10.1016/j.actbio.2019.02.046
31. Nakagawa K, Kishimoto T, 2019, Unlabeled Image Analysis-Based Cell Viability Assay with Intracellular Movement Monitoring. *Biotechniques*, 66(3):128–33. https://doi.org/10.2144/btn-2018-0157
32. Wu H, Yang Y, Bagnaninchi PO, *et al*., 2018, Electrical Impedance Tomography for Real-Time and Label-Free Cellular Viability Assays of 3D Tumour Spheroids. *Analyst*, 143:4189–98. https://doi.org/10.1039/c8an00729b
33. Parrish J, Lim KS, Baer K, *et al*., 2018, A 96-Well Microplate Bioreactor Platform Supporting Individual Dual Perfusion and High-Throughput Assessment of Simple or Bio-Fabricated 3D Tissue Models. *Lab Chip*, 18:2757–75. https://doi.org/10.1039/c8lc00485d
34. Timashev P, Mironov V, 2020, Bio-Printing in the Russian Federation: Can Russians Compete? *Int J Bioprint*, 6:303. https://doi.org/10.18063/ijb.v6i3.303

# INTERNATIONAL JOURNAL OF BIOPRINTING

ISSN (print): 2424-7723

## ABOUT THE JOURNAL

**International Journal of Bioprinting** is a biannual, double-blind peer-reviewed, open access journal. This journal focuses on the use of 3D printing technology with materials that incorporate viable living cells or biological elements to produce tissue or biotechnological products. Further discourses and technological advancements in bioprinting are the goals behind acceptance of high-quality basic and applied research: from concept creation to fabrication of the bioprinting process, associated clinical applications as well as social implications.


**Whioce Publishing**, official publisher for the journal welcomes researchers to submit their papers relevant to bioprinting for consideration via **http://ijb.whioce.com/** For general enquiries and order for prints and reprints, please write in to **IJB@whioce.com** for a fast response.

SUBMIT YOUR PAPERS HERE

WHIOCE
PUBLISHING PTE. LTD.

## ABOUT THE PUBLISHER

**Whioce Publishing** in Singapore is a registered publisher of excellent quality academic journals for an international readership. We deliver exceptional editorial support for the advancement and dissemination of scientific research by linking readers and researchers with networks and industries. We have ambitions to get our journals indexed in prominent databases such as EI, SCI, SSCI and AHCI, thereby aiming to be a first-class knowledge platform for researchers worldwide.

Whioce Publishing also engages in publishing e-books, organizing academic conferences and educational trainings, and providing translational services.

International Journal of Bioprinting is an
independent open access journal published
by Whioce Publishing Pte.Ltd.

WHIOCE PUBLISHING PTE. LTD.
PROVIDING
FIRST-CLASS SCIENTIFIC INFORMATION
FOR TOP SCHOLARS

Whioce Publishing Pte.Ltd.
7030 Ang Mo Kio Avenue 5
#04-15 Northstar@AMK
Singapore 569880
**Tel:** +65 65702707/65702718
**Fax:** +65 65702803

See **www.whioce.com/contact** for a full list of offices and contact information.

Whioce Publishing Pte.Ltd. is a company registered in Singapore (No. 201427293E), whose registered office is at 7030 Ang Mo Kio Avenue 5 #04-15 Northstar@AMK Singapore 569880